NEW PERSPECTIVES ON THE STYLE AND DYNAMICS OF THE 79AD PLINIAN ERUPTION AT VESUVIUS

A DISSERTATION SUBMITTED TO THE GRADUATE DIVISION OF THE UNIVERSITY OF HAWAI‘I IN PARTIAL FULFILLMENT OF THE REQUIREMENTS FOR THE DEGREE OF

DOCTOR OF PHILOSOPHY

IN

GEOLOGY AND GEOPHYSICS

AUGUST 2010

By
Thomas Shea

Dissertation Committee:

Lucia Gurioli, Chairperson
Bruce F. Houghton
Julia E. Hammer
Sarah A. Fagents
John S. Allen

We certify that we have read this dissertation and that, in our opinion, it is satisfactory in scope and quality as a dissertation for the degree of Doctor of Philosophy in Geology and Geophysics.

DISSERTATION COMMITTEE

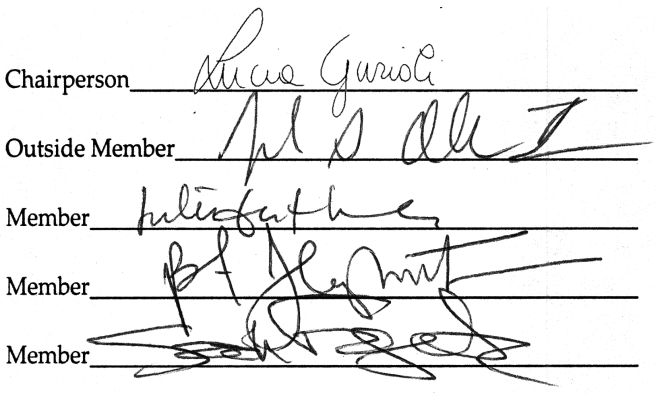

Pour Clara, Hannelore, Patrick, Erik, Eva et Punkie....

ACKNOWLEDGEMENTS

This work is dedicated to Clara and to the rest of my family in France. Your brave support has made all the difference.

I wish to thank my advisor Lucia Gurioli for bringing me here to UH over three years ago and for giving me the opportunity to fully express myself as a student and as a researcher. She has trusted me in all my ideas or decisions irrespective of how obstinate they may have been. Grazie Lucia! I also would like to thank Jessica Larsen, Bruce Houghton and Julia Hammer for truly acting as my co-advisors during this period as well as Kathy Cashman, Raffaello Cioni for their important collaborations, and Sarah Fagents & John Allen for their useful comments. Finally, extra acknowledgments are rightfully due to Andy Harris, Scott Rowland, Paul Wessel, Ken Rubin, Sarah Fagents, Julia Hammer and Bruce Houghton for the remarkable courses I took from them. I sincerely hope to keep working with, and keep learning from you all in the future as I have since 2007.

Special gracias to Ben van Wyk de Vries for allowing me to enter the world of research in the first place and for believing in me since the beginning. Salud Mincho! Clara and I are indebted to Alison Houghton for all the help in dealing with everything practical and administrative throughout our stay here.

Mahalo big time to all my friends here in Hawaii and on the other side of the planet for teaching me so much over the years.

Financial support was given by NSF grants EAR 0537950 and 0537543 and travel grants were given by the graduate student organization (GSO), NSF and IAVCEI. Additional support from the ARCS Foundation and the Toby Lee Family was immensely appreciated.

ABSTRACT

The 79AD eruption of Mt Vesuvius is one of the most studied volcanic explosive events in history. It ejected ~3 km^3 of material (dense rock equivalent DRE) in the form of thick layers of pumice and ashfall interbedded with numerous large pyroclastic density current deposits, and is responsible for the destruction of Pompeii and Herculaneum. This eruption represents a type-example of plinian eruption, where stable activity abruptly shifted to column collapse and/or phreatomagmatism.

Vesicle and crystal textures have been shown to aid greatly in deciphering some of the key physical processes that lead to their formation (e.g. storage conditions, ascent styles and rates). A new matlab-based tool (FOAMS) was developed and used to investigate the products of the 79AD eruption, which contain abundant small leucite crystals and vesicles that cover several orders of magnitude in size and number. First, laboratory experiments designed to mimic leucite crystallization and vesiculation in pumice from the opening and one of the main plinian phases (Eruption Units EU1 and EU2 of the phonolitic white magma) were performed at conditions thought relevant to the eruption. Experiments were quenched at different final pressures to investigate the evolution of textures throughout the entire decompression path. It was found that leucites do not crystallize readily during ascent, and that experimental vesicle textures do not match size distributions but do approach number densities measured in natural pumices from EU1 and EU2. Through additional isobaric-isothermal experiments, it was determined that leucites probably crystallized at depth in the reservoir, perhaps during slow decompression prior to the eruption. In particular, the causes for discrepancies

between experimental and natural textures are explored and possible ways to improve future experiments are suggested. Kinetics of crystallization and vesiculation in K-phonolites are also discussed.

The last portion of this dissertation is dedicated to finding the causes for major shifts between stable and collapsing eruptive plumes that caused the formation of multiple pyroclastic density currents (PDCs) during the magmatic phase of the eruption (EU1-EU3). PDC and pumice fall clast textures are compared to determine whether differences in conduit degassing behavior can explain the changes in column dynamics after fragmentation.

TABLE OF CONTENTS

LIST OF TABLES

CHAPTER 2:

CHAPTER 3:

CHAPTER 4:

CHAPTER 5:

LIST OF FIGURES

CHAPTER 1:

CHAPTER 2:

CHAPTER 3:

CHAPTER 4:

CHAPTER 5:

LIST OF SYMBOLS/ABBREVIATIONS

Abbreviations	**Meaning**	**Units**
EU	Eruptive Unit (Vesuvius 79AD eruption)	
FOAMS	Fast Object Analysis Measurement System	
IB-IT	Isobaric-Isothermal	
CVSD	Cumulative Vesicle Size Distribution	
CVVD	Cumulative Vesicle Volume Distribution	
DRE	Dense Rock Equivalent	
PDC	Pyroclastic Density Current	
SEM	Scanning Electron Microscope	
VEI	Volcanic Explosivity Index	
VSD	Vesicle size distribution	
VVD	Vesicle Volume Distribution	
Symbols		
dP/dt	Decompression rate	MPa s^{-1}
d	Exponent for power-law best fits	-
D	Diffusivity	m^2 s^{-1}
Y or G	Crystal or Bubble Growth rate	m s^{-1}
I or J	Crystal or Bubble Nucleation rate	m^{-3} s^{-1}
k	Boltzmann constant	J K^{-1}
L	Length/Diameter	m
N	Number density	m^{-3}
n	Number of counts/measurements	-
Ω	Volume of water molecules	m^3
ρ	Density	kg m^{-3}
P	Pressure	MPa
S	Inter-nuclei spacing	m
T	Temperature	K
T and τ	Time and Timescale	s
μ	Viscosity	Pa s
ϕ	Porosity/Vesicularity	%
Subscripts		
I or 0	Initial conditions	
A	Area	
m	Melt	
lc	Leucites	
corr	Referenced to melt fraction	
V	Volume	
HOM	Homogeneous nucleation	
EFF	Effective	
fit	Derived from best-fit curve	

CHAPTER 1. INTRODUCTION

1. Synopsis

Large explosive volcanic eruptions are highly destructive events that show extremely variable behavior, making their course difficult to predict. During a single explosive eruption, volcanoes can eject and deposit several cubic kilometers to hundreds of cubic kilometers of tephra onto and around their flanks. These deposits are most often composed of a combination of fall products that typically derive from near-vent ballistics, and convective plumes tens of kilometers in height, or pyroclastic density currents (PDCs) that travel down the edifice at high velocities and temperatures. During a single plinian eruption, the style of activity can vary substantially due to external factors such as presence of ground or external water, or intrinsic factors related to crystallization, degassing and outgassing processes that occur within the conduit during magma ascent (e.g. Sparks, 1978; Cashman and Mangan, 1994; Klug and Cashman, 1994; Jaupart, 1996; Navon and Lyakhovsky, 1998; Papale et al., 1998; Rust and Cashman, 2004). The 79AD plinian eruption of Vesuvius resulted in a complex succession of pyroclastic fall and PDC deposits that suggest several abrupt transitions in conduit and column dynamics occurred throughout the eruptive sequence (e.g. Lirer et al., 1973; Sigurdsson et al., 1985; Cioni et al., 1992). This eruption has been the subject of extensive research but the textural aspects of the various pumice clasts produced throughout the eruption have not been previously investigated even though they provide valuable information eruption dynamics. Because the crystallization and degassing histories of 79AD magmas can be compared to field, laboratory, physical and numerical investigations from the past 40 years, this eruption is the perfect candidate for detailed textural studies. Through the four main chapters of this dissertation, I (a) investigate crystallization during decompression

of the magmatic reservoir, (b) describe the methodology utilized to characterize vesicle textures in 79AD pumice, (c) compare vesicles formed experimentally to those formed during magma degassing, and (d) examine the mechanisms for the transitions between fall-producing stable eruptive columns to pyroclastic current-forming unstable collapsing plumes.

2. The 79AD eruption of Vesuvius

2.1. Geotectonic setting

Vesuvius volcano (1281 m.a.s.l.) forms part of the Somma-Vesuvius volcanic complex located in the region of the bay of Naples in Italy. Somma-Vesuvius, along with other Italian volcanoes (e.g. Campi Flegrei, Ischia, Vulture, Roccamonfina, Ernici, Colli Albani, Monte Vico, and Monte Vulsini, Fig. 1), result from the subduction of the Mediterranean seafloor under the African plate, and from the opening of the Tyrrhenian basin, west of the main compression front. Magmas erupted at these volcanic centers are dominantly alkali-rich (Savelli, 2001 and references therein).

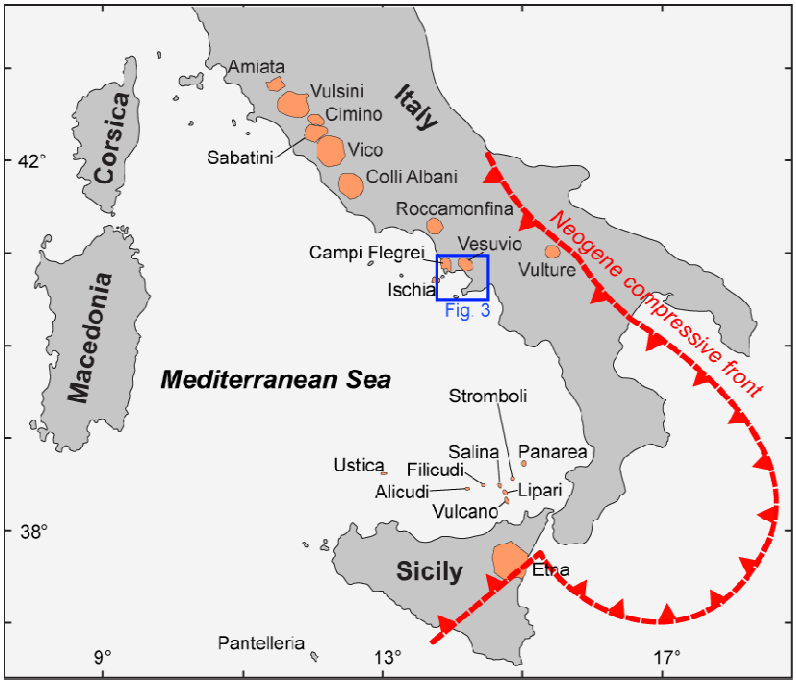

Figure 1: Geographical location of the main Italian volcanic centers along with position of the compressive front related to the subduction of the Eurasian plate under the African plate (Modified after Sigurdsson et al., 1985).

2.2. *Somma-Vesuvius*

The Somma-Vesuvius stratovolcano consists of an ancient volcanic edifice (Somma) made of accumulations of effusive lavas, welded fall deposits, and small cinder cones, which erupted over a relatively brief period (35,000-20,000BP, Santacroce et al., 2008), and were truncated by multiple caldera collapses (Cioni et al., 1999). Vesuvius grew nested within this older volcanic structure as the activity switched from dominantly effusive to dominantly explosive. The first plinian eruption (Pomici di Base) occurred about 18,000 years ago (e.g. Bertagnini et al. 1998; Santacroce et al., 2008), followed by other plinian eruptions of Mercato Pumice (~ 8,000BP, e.g. Santacroce et al., 2008; Mele et al., 2009), Avellino Pumice (~3,900BP, e.g. Santacroce et al., 2008; Sulpizio et al., 2009) and Pompeii Pumice (79AD). Sub-plinian events such as the 16,000BP Greenish Pumice (Cioni et al., 2003b; Santacroce et al., 2008), the 472AD Pollena

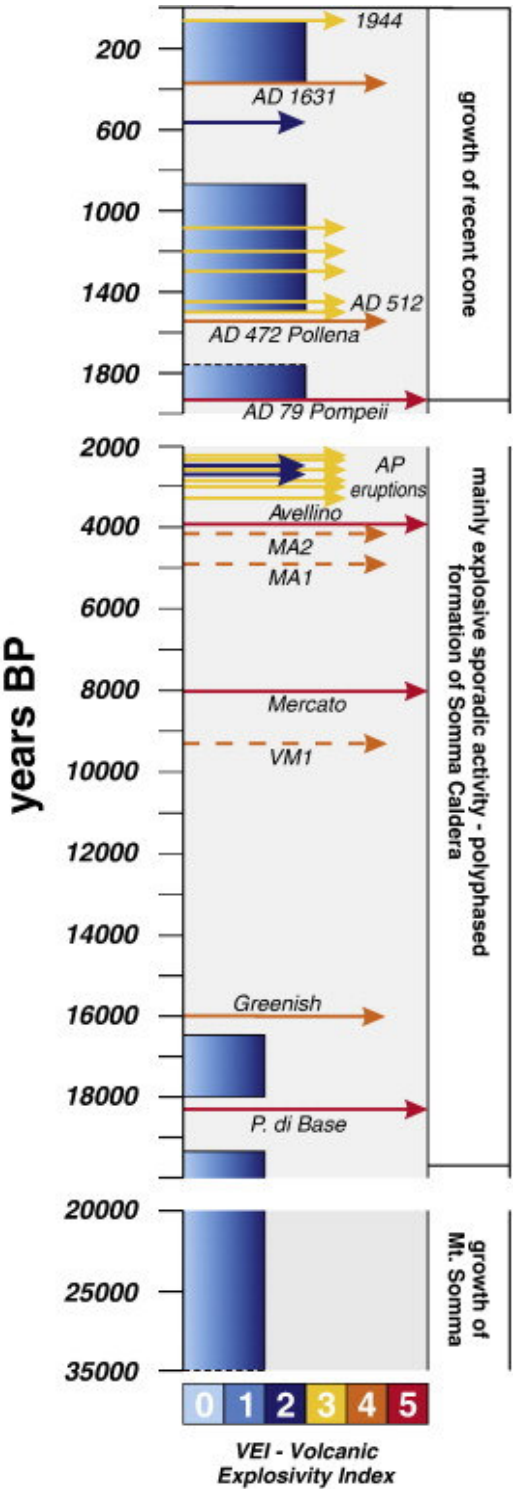

Figure 2: Somma-Vesuvius activity since formation of Mt. Somma ~35,000 years ago. Arrows show subplinian to plinian explosive events, domains represent periods of effusive activity. Colors correspond to Volcanic Explosivity Index (VEI). Dashed lines mark uncertain eruption dates. From Cioni et al. (2008).

pumice (e.g. Sulpizio et al., 2005), and the 1631AD (e.g. Rosi et al., 1993) eruption generally occurred between plinian eruptions (Fig 2). Smaller strombolian eruptions may also have been produced throughout the entire history of Vesuvius but their small dispersal and volumes could have prevented them from being identified within the deposits.

More recently, from 1631AD to 1944AD, Vesuvius has shown dominantly effusive activity punctuated by lower intensity violent strombolian eruptions (8 since 1660AD, Cioni et al., 2008). Since 1944, Vesuvius has been quiescent and shows no immediate signs of unrest. Extended periods of quiescence at Vesuvius are common, and mostly are followed by intense explosive eruptions (Cioni et al., 2008). The very high density of people living in its vicinity (Fig. 3a) makes Vesuvius one of the major volcanic threats in the world. Because 3,500,000 people inhabit the Campanian region around Vesuvius and Campi Flegrei, both volcanic centers have spawned a plethora of scientific investigations that include numerous hazard assessment studies (e.g. Carta et al., 1981; Sheridan and Malin, 1983; Barberi et al., 1990; Macedonio et al., 1990; Dobran et al., 1994; Alberico et al., 2002; Andronico and Cioni, 2002; Cioni et al., 2003a; Nunziante et al., 2003; Orsi et al., 2004; Rossano et al., 2004; Gurioli et al., 2005a; Baxter et al., 2008; Costa et al., 2009; Daniele et al., 2009; Lirer et al., 2010; Rolandi, 2010). Although speculations vary regarding the type of eruption that may occur in the future at Vesuvius, there is a general agreement concerning the urgent need to examine the range of past eruptive behavior as an indicator of what to expect in the next eruption. The 1631 event is commonly regarded as a plausible scenario for which residents of the Neapolitan region ought to prepare.

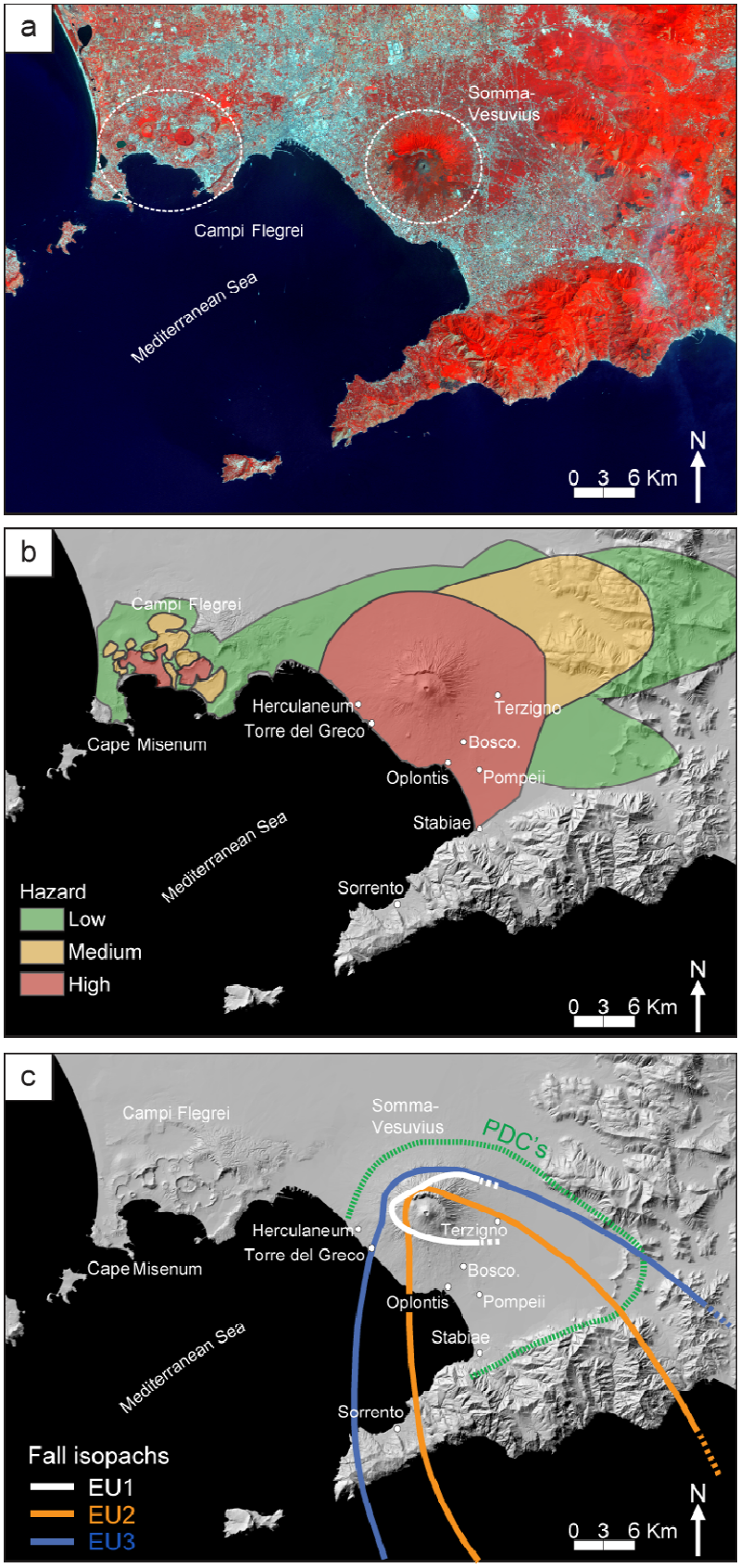

Figure 3: (a) False-color Landsat image of the Bay of Naples showing both major volcanic centers, Campi Flegrei and Vesuvius. In this image, densely urbanized areas are denoted by light blue pixels. The total number of inhabitants reaches about 3,500,000 for the entire campanian region.

(b) Hazard zone delimited by Lirer et al. (2010) based on an eruption of the intensity of 1631. About 500,000 people live in the red+yellow zones.

(c) The extent of 10 cm-isopachs for three fall deposits EU1-EU3, as well as limits of pyroclastic flow deposits, after Sigurdsson et al. (1985) and Gurioli et al. (2005a).

Recent hazards maps reveal that about 500,000 people live directly in zones possibly affected by ash and pumice fall, pyroclastic density currents and debris flows (Lirer et al., 2010, Fig. 3b).

2.3. The 79AD eruption

2.3.1. Historical and volcanological importance

Volcanological interest in Vesuvius is not recent: the first volcano observatory was built on its flanks in 1841, and several eruptions prior to 1944 were intensively studied (e.g. Heim, 1873; Hobbs, 1906, Figure A1 in appendix). However, no other eruptions have achieved the volcanological and archaeological interest that the 79AD eruption generated. The first accounts of the events that unfolded during this period came from Pliny the Younger who became one of the first eyewitnesses of a plinian eruption. He gave a detailed written report relating the course of the eruption as well as the death of his uncle, Pliny the Elder, who perished during the eruption from a heart attack (e.g. Bigelow, 1856; Ippolito, 1950). The eruption is historically famous for having caused the demise of Roman Campanian towns Pompeii (1,600 known casualties from an initial population estimated at 5,000-20,000, Luongo et al., 2003) and Herculaneum (250 casualties from an initial population of 4,000-5,000, Capasso, 2000), as well as neighboring communes, resorts and villas that included Stabiae, Oplontis, Boscoreale, along with other smaller communities located where the present towns of Torre del Greco, Terzigno, and Boscotrecase are (cf. Fig. 3c). After the eruption, these towns, as well as surrounding villas and resorts remained buried under meters of fall and PDC

deposits, and were not excavated until 1600 years later (although parts of Pompeii were unearthed briefly in the 16th century). The start of excavations in both Pompeii and Herculaneum in the 18th century, and the discovery of numerous corpses within the volcanic tephra focused the attention of a large number of archeologists and other scientists. Early studies of Johnston-Lavis (1884) and Rittmann and Ippolito (1947), suggested that Romans at Pompeii and Herculaneum died under the accumulation of ash and pumice, and that the cross-bedded portions of 79AD deposits represented either some type of remobilization of fall deposits by subsequent quarrying activity (Rittmann, 1950), or mudflow deposits (Ippolito, 1950). Merrill (1918, 1920) first made the observation that these deposits contained carbonized wood as well as partly burnt documents, and that the process responsible for the death of Romans resembled those described in 1902 at Mt. Pelee by Lacroix (1908). This view was not accepted until the pioneer field investigations by Lirer and Pescatore (1968), and Lirer et al. (1973), and comparisons with historical accounts by Sigurdsson et al. (1982). Since then much progress has been made in the characterization and interpretation of the various fall and PDC deposits that compose the 79AD stratigraphy, and on the timing of the events (i.e. edifice destruction, population evacuations, deaths) that took place at Pompeii and Herculaneum (e.g. Sigurdsson et al., 1985; Cioni et al., 1992; Gurioli et al., 2002; Cioni et al., 2004).

2.3.2. Chronology, characteristics, and stratigraphy of the eruption

Until very recently, it had been assumed that the eruption occurred on the 24th of August of 79AD. The date was derived from letters of Pliny the Younger addressed to historian Tacitus in ancient Latin. However, several translations of the texts are possible and other

authors interpreted the month to be October or November. Further evidence, including the finding of a coin relating Titus' fifteenth emperor acclamation (historically after September of 79AD, Rolandi et al., 2008), the recovery of fruit typical of the autumnal season within the remains of Pompeii, and the direction of seasonal stratospheric winds that led to the south-eastward dispersal of the eruption products, prompted the re-evaluation of the date of the eruption to October, possibly the 24rd (Rolandi et al., 2008). The time of day during which certain phases of the eruption occurred is actually better constrained (Sigurdsson et al., 1982). A series of precursory earthquakes and tremors took place throughout the four days that preceded the onset of explosive activity, probably as a fresh batch of tephritic magma intruded the reservoir where a phonolitic magma had resided and differentiated since Avellino times (~3,900 BP) (e.g. Cioni et al., 1995). The opening phase of the eruption, involving the upper phonolitic portion of the storage region, may have occurred during the night of the 23rd, or a few hours before the start of the plinian phase. This opening phase was probably associated with some degree of magma-water interaction (Barberi et al., 1989; Cioni et al., 1992), and formed a 15 km-high plume that deposited a thin layer of pisolitic ash mostly to the east of Vesuvius, notably in Terzigno (Eruptive Unit EU1, Cioni et al., 1992, Fig. 3c, Fig. 4). It has not been confirmed whether the opening phase was followed by a pause in activity. Pliny observed the rising plume corresponding to the first plinian phase EU2 at 1pm on the 24th but it remains uncertain whether the smaller plume corresponding to the opening phase would have been easily observed from his location. Nonetheless, field evidence shows that at least two small PDCs were generated at the end of EU1 (EU1pf, Fig. 4e; Cioni et al., 2000). EU2 generated a ~20-25 km-high (Carey and Sigurdsson, 1987) buoyant

column and deposited up to 1.5 m of pumice and ashfall on a much larger scale towards the south-east (Fig. 3c, Fig. 4b and d). Syn-eruptively, the batch of tephritic magma mixed with phonolitic magma from the upper portions of the reservoir (Cioni et al., 1995), and a few hours into the eruption (~8 pm), the ejected pumice changed from a phonolitic to a tephriphonolitic composition (e.g. Di Girolamo, 1968; Lirer et al., 1973). The nature of this change was mostly abrupt (Civetta et al., 1991) and may have triggered a partial collapse of the eruptive column, generating a PDC deposit containing pumices of the two end-members (EU2/3pf, Fig. 4b and e, Cioni et al., 1992). The plume became buoyant shortly afterwards and rose to over 30 km (Carey and Sigurdsson, 1987) in the stratosphere, depositing thick layers of gray pumice and ashfall (EU3, Fig. 3c, Fig. 4) over an even wider area than the white pumice fall EU2. The fall deposits EU2+EU3 alone caused the collapse of numerous roofs particularly in Pompeii (e.g. Luongo et al., 2003) where the deposit thickness reached 2.8 m, and the death of about 400 Romans (Luongo et al., 2003). Hence, of the people that had not evacuated from Pompeii, the majority did survive the fall phase. A similar extent of destruction probably occurred at Oplontis and Terzigno (Cioni et al., 1992), which may have caused most of the inhabitants to evacuate.

Figure 4: (a) Location of Roman towns around the flanks of Vesuvius, and stratigraphy of the 79AD eruption from Cioni et al. (1992) and Gurioli et al. (2002). On the map, dark gray areas represent excavation sites. (b) Outcrop at Villa Regina, near Oplontis, showing the multiple PDCs that swept past this site. (c) Photo of an outcrop at Pompeii showing some of the important spatial variations in the destruction of the various Roman towns: Pompeii was affected little by EU3 PDCs, unlike Oplontis and Herculaneum, but was devastated by EU4pf. This location shows well the destructiveness of PDCs. (d) The thick layer of fall tephra deposited at Pompeii and the clear transition between white and gray pumice. (e) The lower portions of the 79AD stratigraphy (i.e. EU1) are found only at proximal sites such as Sarcinello. Note the large ballistic lithic ejected during EU2 times that generated an impact mark into underlying EU1 and EU1pf. →

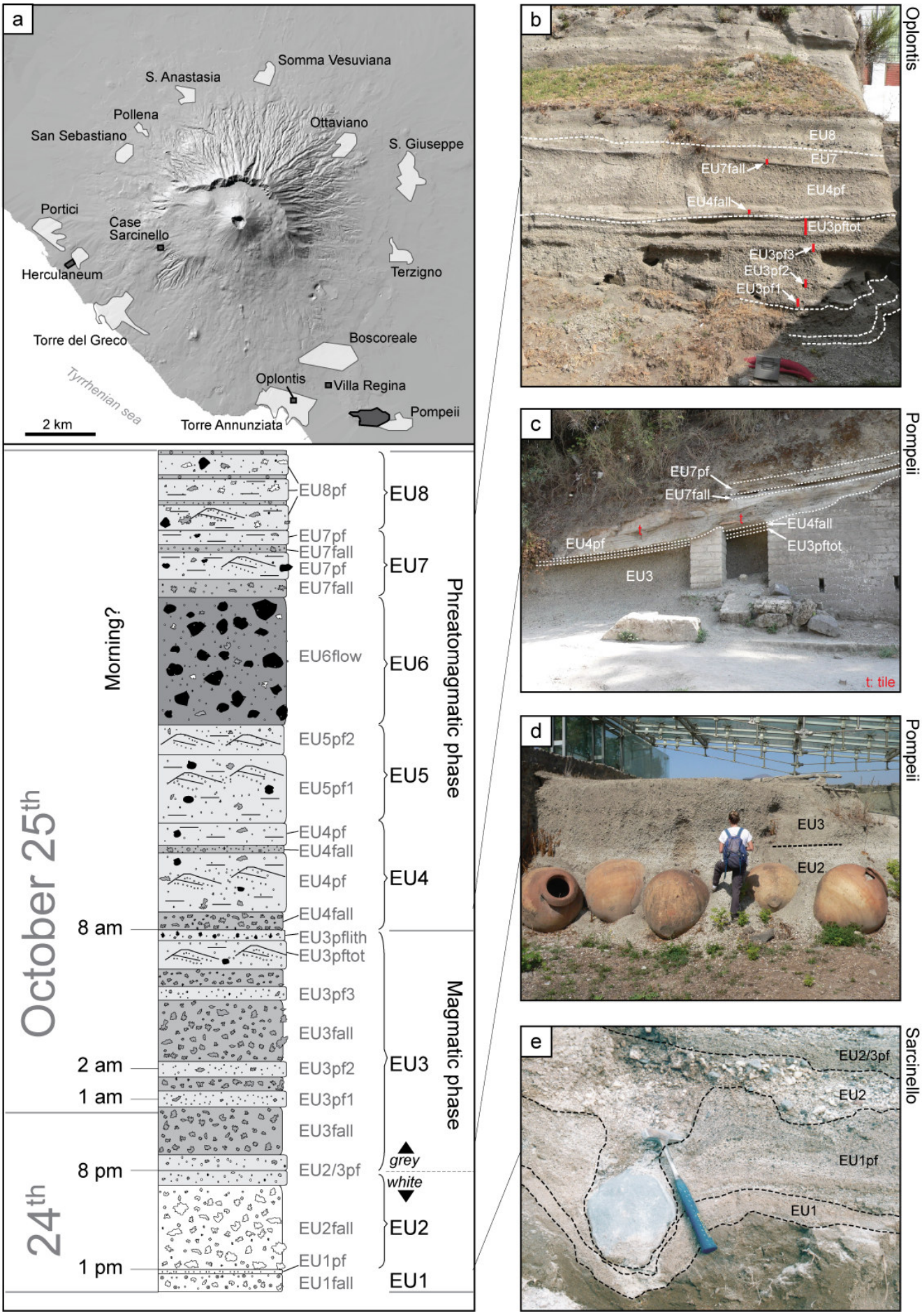
a
Somma Vesuviana
S. Anastasia
Pollena
San Sebastiano
Ottaviano
S. Giuseppe
Portici
Case Sarcinello
Herculaneum
Terzigno
Torre del Greco
Boscoreale
Tyrrhenian sea
Oplontis
Villa Regina
Pompeii
Torre Annunziata
2 km
October 25th
Morning?
8 am
2 am
1 am
24th
8 pm
1 pm
EU8pf
EU7pf
EU7fall
EU7pf
EU7fall
EU6flow
EU5pf2
EU5pf1
EU4pf
EU4fall
EU4pf
EU4fall
EU3pflith
EU3pftot
EU3pf3
EU3fall
EU3pf2
EU3pf1
EU3fall
EU2/3pf
EU2fall
EU1pf
EU1fall
EU8
EU7
EU6
EU5
EU4
EU3
EU2
EU1
Phreatomagmatic phase
Magmatic phase
grey
white
b
Oplontis
EU8
EU7
EU7fall
EU4pf
EU4fall
EU3pftot
EU3pf3
EU3pf2
EU3pf1
c
Pompeii
EU7pf
EU7fall
EU4fall
EU4pf
EU3pftot
EU3
t: tile
d
Pompeii
EU3
EU2
e
Sarcinello
EU2/3pf
EU2
EU1pf
EU1

In contrast, Herculaneum was mostly out of the main dispersal region of the fall phases EU2 and EU3 (cf. Fig. 3c); as a result, no destruction was caused during the first hours of the eruption. Nonetheless, probably alarmed by the extent of the plume, the majority of Herculaneum inhabitants evacuated (Maiuri, 1977; Sigurdsson et al., 1985). Most of the 250 people that stayed were killed by emplacement of EU2/3pf, the first PDC that reached the town (Cioni et al., 2000; Gurioli et al., 2002).

A few hours into eruption of EU3 fall, the column became increasingly unstable and partially collapsed at least three times to generate PDCs EU3pf1, EU3pf2, and EU3pf3 (Fig. 4b, Cioni et al., 1992, 2004) until total plume destabilization occurred and a powerful radially spreading PDC was produced (EU3pftot, Fig. 4b and c; Cioni et al., 1992; 2004). Although the latter phase barely reached the south-eastern limits of Pompeii and only few cm of the PDC were deposited, it is possible that EU3pftot caused the death of some of the inhabitants (Cioni et al., 2000; Zanella et al., 2007). Around 8 am on the 25th, earthquakes became increasingly frequent and violent, likely generated by the collapse of the caldera as the upper portions of the reservoir were being emptied. The subsidence and ground movements associated with the collapse may have allowed groundwater into the conduit/chamber system (Barberi et al., 1989), triggering the onset of the main phreatomagmatic phase of the eruption (EU4-EU8, Cioni et al., 1992). A new, short-lived plume was briefly stable at the beginning of this phase and deposited a thin layer of lapilli (EU4, Fig. 4b and c, Cioni et al., 1992; 2004), but then collapsed entirely to produce another radially dispersed PDC (EU4pf, Fig. 4b and c, Cioni et al., 1992; 2004) which took the lives of remaining residents at Pompeii (Sigurdsson et al., 1985; Luongo et al., 2003; Gurioli et al., 2005, 2007). After EU4 the eruptive column

entered a dominantly collapsing behavior cycle with generation of locally dispersed, valley-filling PDCs (EU5, Cioni et al., 1996; 2004), followed by production of a massive, lithic-rich PDC (EU6 Cioni et al., 1996; 2004), and the formation of another widespread PDC deposit interlayered by thin fall deposits (EU7, Fig. 4b and c, Cioni et al., 1996; 2004). The final stage of the eruption was the emplacement of pisolitic layers up to 2-3 meters in thickness (EU8, Fig. 4c, Cioni et al., 1992).

2.3.3. Context of investigation

The Somma-Vesuvius volcano has always been a popular topic in volcanology due to the unique comprehensive historical record of its past activity, the interactions of its eruptions with human settlements, as well as its location in the vicinity of over half a million people. It has been persistently regarded by the volcanology community as a type-example of explosive volcanism and was listed, along with 15 other potentially life-threatening volcanoes, in IAVCEI's "Decade Volcanoes". It produced, in 79AD, the most famous eruption in the world. In the past 40 years, this eruption has been the subject of a profusion of publications that have looked at stratigraphy, the componentry, the petrology/geochemistry, and the spatial distribution of deposits (Lirer et al., 1973; Barberi and Leoni, 1981; Barberi et al., 1980, 1989; Sigurdsson et al., 1982, 1985, 1990; Civetta et al., 1991; Lirer et al., 1993; Rosi et al., 1993; Mues-Schumacher, 1994; Marianelli et al., 1995; Cioni et al., 1992, 1995, 2000, 2004; Cioni, 2000; Gurioli et al., 2002), as well as the emplacement mechanisms and consequences of fall and PDCs associated with the eruption (Gurioli et al., 2002, 2005a, 2007; Luongo et al., 2003; Cioni et al., 2004; Zanella et al., 2007). The parameters and physical eruptive constraints

derived from these studies have been used widely in the field of physical and numerical modeling of conduit and plume processes (Sparks et al., 1976; Wilson et al., 1980; Carey and Sigurdsson, 1987; Macedonio et al., 1988, 1990; Papale and Dobran, 1993; Dobran et al., 1994; Neri and Dobran, 1994; Neri and Macedonio, 1996; Scandone, 1996; Papale et al., 1998; Rossano et al., 1998; Scandone and Giacomelli, 2001; Todesco et al., 2002; Di Muro et al., 2004, Esposti Ongaro et al., 2002, 2008; Neri et al., 1998, 2002a, 2002b, 2007). While robust models of plume formation and collapse, or studies of the emplacement of tephra deposits can be derived from field observations and constraints, conduit models require information about the processes that occurred under the surface, from the storage region(s) to the fragmentation level. Crystallization and vesiculation during ascent of magma to the surface are two major processes that are preserved to various extents in volcanic rocks (e.g. Marsh, 1988; Cashman, 1988; Houghton and Wilson, 1989; Cashman and Mangan, 1994; Hammer, 2008; Blundy and Cashman, 2008). Through the study of natural volcanic rock textures, it is commonly possible to derive crucial physical information such as magma residence time (Mangan, 1990; Cashman, 1992), magma recharge rates (Morgan et al., 2006), surface lava flow/lake/dome crystallization times (Cashman and Marsh, 1988; Cashman, 1993; Crisp et al., 1994; Hammer et al., 1999, 2000), timescales of ascent (Castro and Mercer, 2004; Noguchi et al., 2006; Polacci et al., 2009), extents of conduit-induced shearing (Burnard, 1999; Polacci et al., 2003; Wright and Weinberg, 2009), and magma properties such as crystallinity, density, viscosity and permeability (Klug and Cashman, 1994; Armienti et al. 1994; Klug et al., 2002; Formenti and Druitt, 2003; Rust et al., 2003; Armienti et al., 2007; Degruyter et al., 2010). Most importantly, if vesicle/crystal texture variations can

be characterized for an entire eruptive sequence, tracking complex shifts in the behavior of volcanic systems through time and space becomes possible (Gardner et al., 1998; Polacci et al., 2001; Gurioli et al., 2005; Adams et al., 2006; Sable et al., 2006; Lautze and Houghton, 2007, Gurioli et al., 2008; Carey et al., 2009). Since textures are a frozen record of the last thermodynamic state experienced by a volcanic rock sample, it is difficult to gain insights into the earlier phases that have brought this rock to its present state (e.g. cooling, decompression, mixing, shearing). Thus, another branch of volcanological research has focused on physical/numerical models of crystallization and vesiculation (Higgins, 1994; Toramaru, 1995, 2006; Lyakhovsky et al., 1996; Jaupart, 1996; Kaminski and Jaupart, 1997; Eberl, 1998; Llewellin et al., 2002; Lensky et al., 2004; L'Heureux, 2007), experiments mimicking ascent (Hurwitz and Navon, 1994; Simakin et al., 1999; Gardner et al., 1999, 2000; Larsen and Gardner, 2000; Mangan and Sisson, 2000; Hammer and Rutherford, 2002; Mourtada-Bonnefoi and Laporte, 1999, 2002, 2004; Martel et al., 2003; Larsen et al., 2004; Burgisser and Gardner, 2005; Szramek et al., 2006; Suzuki et al., 2007; Cluzel et al., 2008), experiments mimicking storage and crystallization conditions (Rutherford et al., 1985; Gardner et al., 1995; Hammer et al., 2002; Rutherford and Devine, 2003; Nicholis and Rutherford, 2004; Cigolini et al., 2008) as well as analogue models (Namiki and Manga, 2006; Costa et al., 2006; Okumura et al., 2006, 2008). All have provided us with the opportunity to understand and constrain the formation and evolution of a large variety of vesicle and crystal textures observed in natural rock samples.

However, the great majority of these studies have focused on rhyolitic, dacitic, trachytic, and basaltic compositions, hindering their thorough application to the potassic

magmas erupted in 79AD at Vesuvius. Larsen and Gardner (2004), Iacono Marziano et al. (2007), Larsen (2008) and Mongrain et al. (2008) provided the first detailed investigations of vesiculation in phonolitic magmas but did not aim to reproduce eruption conditions. Scaillet and Pichavant (2004), and Scaillet et al. (2008) performed phase equilibria experiments and determined possible initial storage conditions for magmas involved in several eruptions of Vesuvius. It remains unclear whether their results apply directly to the pre-eruptive conditions inferred for the 79AD eruption. In addition, while experiments have been performed to determine the kinetics of crystallization of plagioclase and potassium feldspar in magmas of various compositions (e.g. Lofgren, 1974; Muncill and Lasaga, 1988; Hammer and Rutherford, 2002; Couch et al., 2003), no similar investigation has been performed on the formation of feldspathoids (e.g. leucite) in alkalic magmas. Such magmas occur in many potentially threatening locations (e.g. Mediterranean, Malaysia, Indonesia, Canary Islands, and western United States) and there is a need for a better understanding of their crystallization and degassing kinetics. In this dissertation, two detailed investigations are presented of leucite crystallization and vesiculation applied to phonolitic magmas at conditions inferred for the 79AD eruption.

Finally, consideration of microscopic textures of products from the 79AD eruption has been initiated only recently by Gurioli et al. (2005), who examined the transitions between phases corresponding to fall layers EU1-EU4. The latter study gave a glimpse into the complexity of changes in eruptive dynamics over the course of a single eruption. However, no such study has been performed on the transitions between fall-producing and PDC-producing phases of the eruption.

3. Dissertation outline

The present dissertation contains four main sections that together aim to bring a new set of perspectives on the 79AD eruption of Vesuvius through experimental petrology and textural characterization of its products.

Chapter 2 presents some experiments that were performed to constrain the crystallization of leucite crystals in the 79AD white phonolite magma. Series of decompression experiments and isobaric-isothermal (i.e. constant conditions) experiments were performed to determine whether 79AD leucites could have crystallized during ascent – in which case the experiments could provide direct information on ascent conditions; whether they formed in the storage region – in which case the experiments yield important data on reservoir conditions, or whether they crystallized as a result of very slow decompression prior to entering the conduit. The experimentally-obtained crystals are compared to those in natural samples, to estimate eruption conditions, and derive crystallization kinetics for leucites in magmas of phonolitic composition that can be used in other comparable volcanic settings and for thermodynamic modeling.

Chapter 3 details the methodology that was used to perform the textural investigations of vesicles in Vesuvius rocks. This routine has been developed over several years by Bruce Houghton, Kathy Cashman, Lucia Gurioli, and their students. The investigation described herein tests its applicability to various settings from effusive to explosive eruptions, and presents a new software package named FOAMS (Fast Object Analysis and Measurement System) to perform most of the measurements and calculations automatically. The program along with extended guides to perform textural

characterizations in volcanic rocks have been distributed via a University of Hawaii website (http://www2.hawaii.edu/~tshea).

Chapter 4 focuses on vesiculation of the same magmas scrutinized in Chapter 2. The results of multiple series of decompression experiments are presented with the goal of replicating ascent conditions inferred for the opening and the first plinian phases of the eruption. The textures of the experimental products are compared with those of natural pumice samples to determine which parameters can be adequately reproduced by laboratory experiments and which require improved experimental setups.

Chapter 5 builds on the textural investigation of pumice from the early units of the 79AD eruption by Gurioli et al. (2005). This time, the study focuses on transitions from stable convective columns to partially or fully unstable eruptive plumes that generated the destructive PDCs during the magmatic phase of the 79AD event (EU1-EU3). This chapter tests the hypothesis put forward initially by Lirer et al. (1973), Carey and Sigurdsson (1987) and Gurioli et al. (2005), that after the transition from white to gray magma, the plume became increasingly unstable due to increases in ejected tephra density. A detailed characterization of six PDC units is introduced, and comparisons between the latter and fall-producing eruptive phases are made. We propose several mechanisms that can account for the various fall-to-PDC transitions and suggest a new conduit model that explains how density may have varied during these phases.

Chapters 2, 3, and 4 have been published in peer-reviewed journals. Chapter 5 will be submitted for review. Although only succinct essential background is given in each chapter, some information found in the various introductions may be redundant because each section is included unmodified from their original contents.

Appendix A: 18th-19th century sketches of Vesuvius

Almost every eruption since 79AD has been the subject of detailed historical writings (Arrighi et al., 2001; Principe et al., 2004; Cioni et al., 2008 and references therein), possibly making Vesuvius the best-studied volcano on Earth in terms of written eyewitness accounts. Figure A1-A3 display some early "geomorphological" sketches that show that early observers where already fascinated by the activity of Vesuvius.

Figure A1: Sketches from different 18th-19th century field observations and investigations

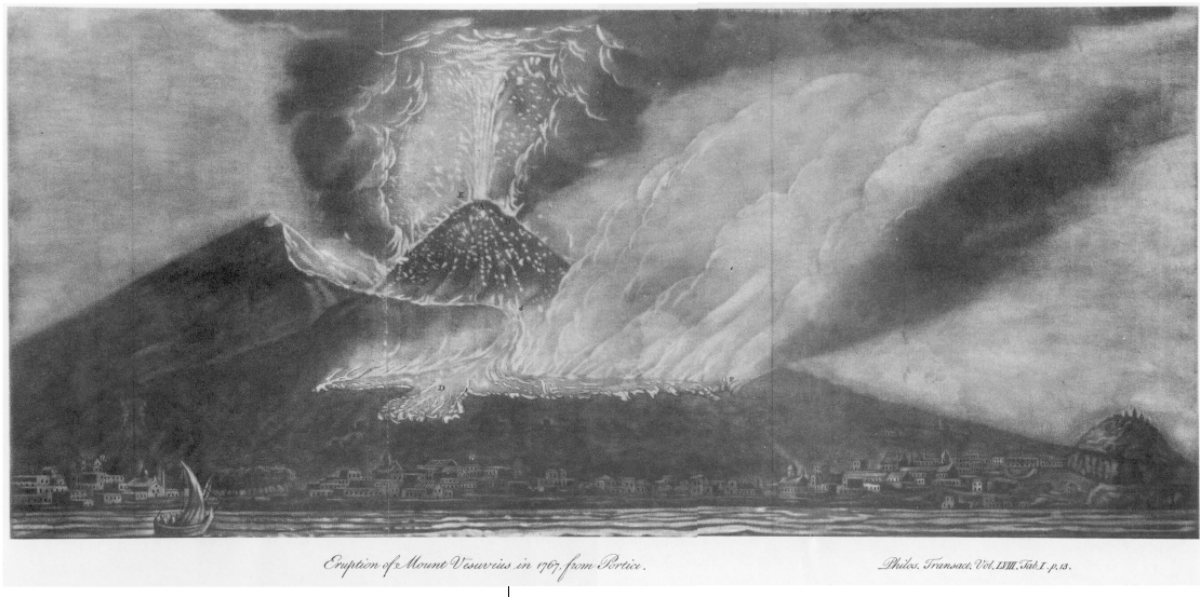

Scene from the strombolian eruption of 1767 taken from Hamilton (1768) from the town of Portici, near Herculaneum.

Figure A2: Sketches from different 18th-19th century field observations and investigations

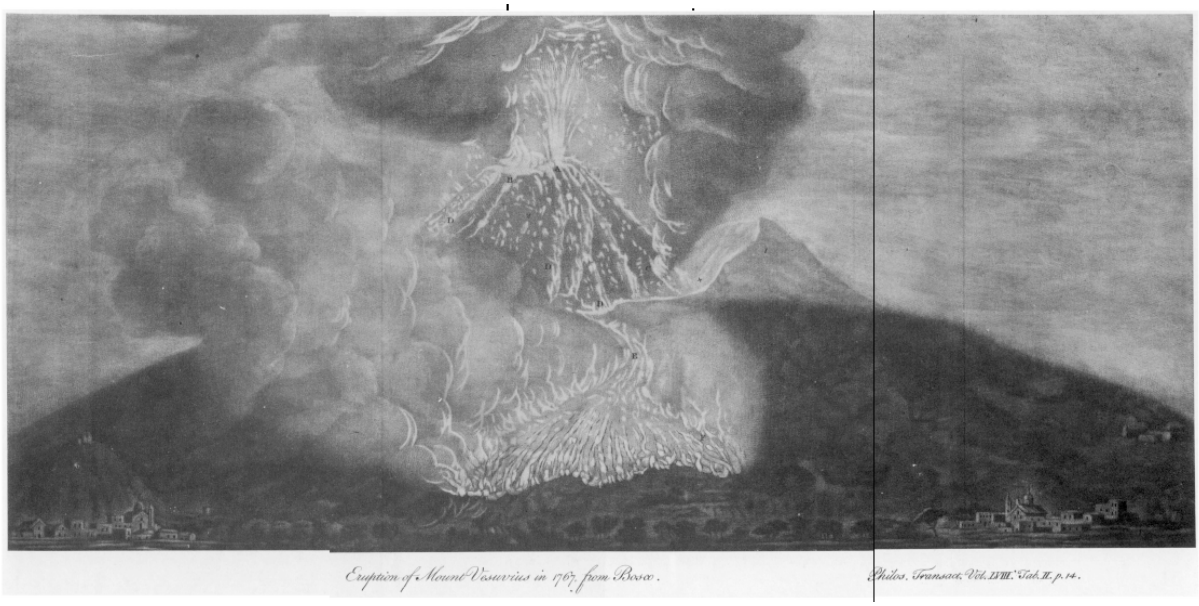

(**above**) Same scene as previous image from Hamilton (1768), here viewed from the town of Boscoreale, on the SE flank of the Vesuvius.
(**below**) Possibly some of the first interpretative geological sketches made, from Hamilton (1768), of the evolution of the summit region during the 1767 eruption.

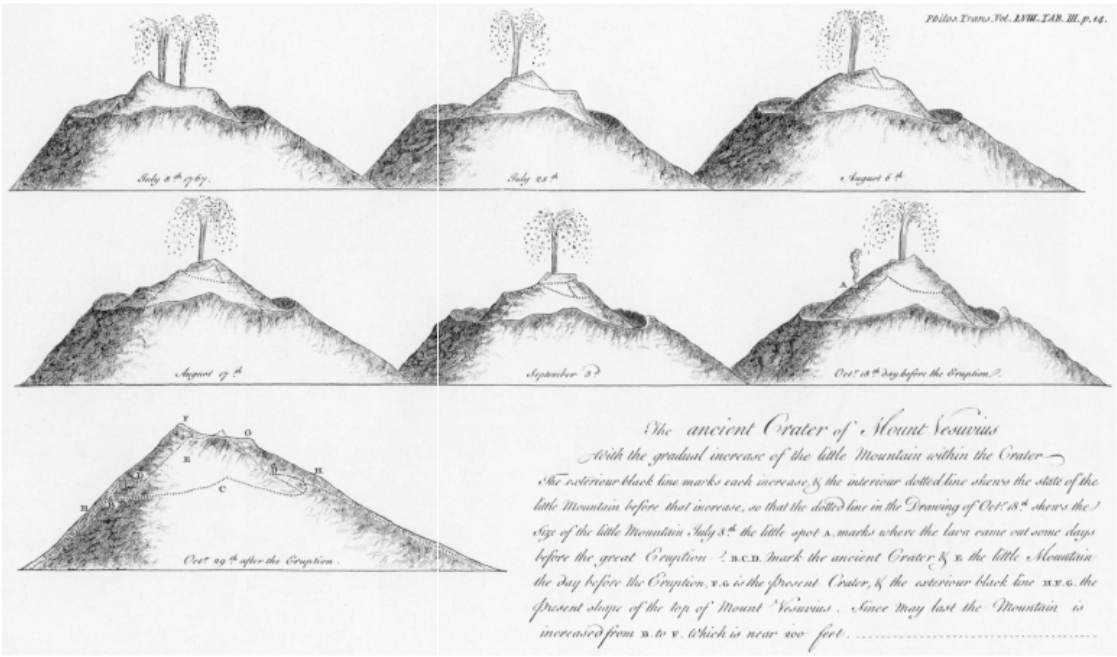

Figure A3: Sketches from 19th century field observations and investigations

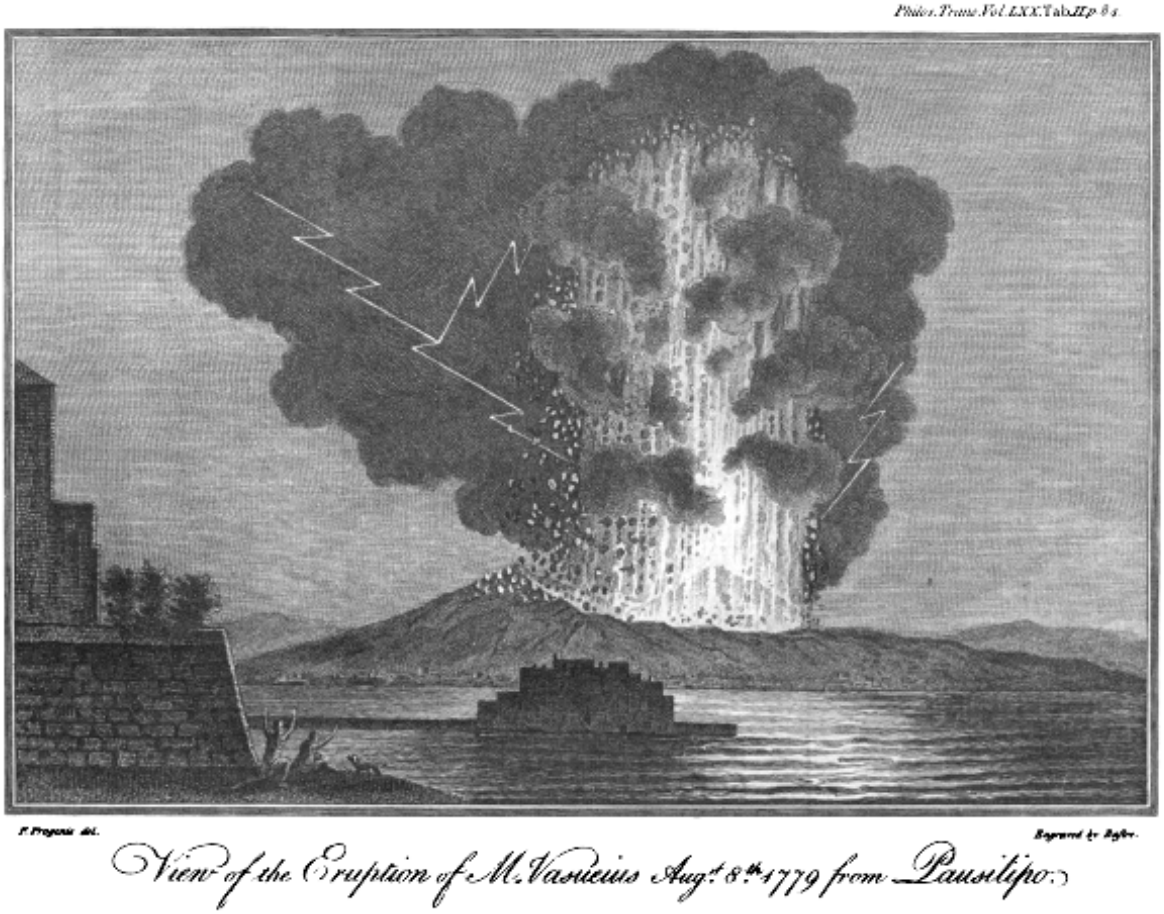

(**above**) Violent strombolian eruption of 1779 taken from Hamilton (1780), here viewed from Posillipo, about 15 km west of Vesuvius.

(**left**) Sketch of the 1872 lava flows that descended the western flanks of Vesuvius, taken from Heim (1973).

CHAPTER 2. LEUCITE CRYSTALS: SURVIVING WITNESSES OF MAGMATIC PROCESSES PRECEDING THE 79AD ERUPTION AT VESUVIUS

Published in its present form as Shea, T., Larsen, J.F., Gurioli, L., Hammer, J.E., Houghton, B.F. (2009), Earth and Planetary Science Letters, 281, 88-98. doi: 10.1016/j.epsl.2009.02.014

Abstract

Crystals in volcanic rocks are sensitive records of magma chamber and conduit conditions under volcanoes. Plagioclase is an invaluable tool to identify ascent rates for calc-alkaline magmas, but may be absent in alkaline melts. In contrast, leucite is common in alkaline magmas and is potentially useful to investigate storage and ascent conditions prior to volcanic eruptions. Leucite microphenocrysts are ubiquitous within the products from all phases of the 79AD eruption of Vesuvius. Steady-state (isobaric-isothermal) and dynamic (decompression) experiments on white phonolitic pumice from the opening (EU1) and lower Plinian (EU2) phases of the eruption were performed at temperature conditions ranging from 800 to 850ºC to test the possibility that leucites within this 'white' magma formed during ascent. However, multiple-step decompression (MSD) experiments using a decompression rate of 0.25 MPa/s failed to crystallize leucite even at pressures well below its stability domain. On the other hand, single-step decompression (SSD) experiments from 150 MPa to 25 MPa result in leucite crystallization after a ~12 h lag period, but the skeletal habit and size distribution differ from those seen in natural pumices. Instead, euhedral leucites texturally matching those observed in 79AD samples formed after 5 days under isobaric and isothermal (IB-IT) experimental conditions. Crystallization conditions derived from the latter experiments suggest the magma reservoir was thermally zoned with cooler EU1 (T=830–840ºC) overlying slightly hotter EU2 (T=850–925ºC) magma. Two models for natural crystallization conditions are consistent with the experimental data: either leucites formed at ~4 km depth (P~100 MPa) in a steady storage environment inside a magma saturated with H_2O-rich vapor, or, alternatively, the white magma was initially undersaturated with respect to H_2O and

leucites formed during a slow depressurization event prior to the eruption. Leucite crystallization seemingly adheres to the classical nucleation theory, and supports a compositional (i.e. H_2O) control on surface tension. Derived minimum leucite growth rates reach ~10^{-7} mm s^{-1}, comparable to the fastest growth rates observed for plagioclase crystals in calc-alkaline magmas.

1. Introduction

Vesuvius, Italy, entered the history of volcanology via Pliny the Younger, who documented the famous eruption that devastated the Roman towns of Herculaneum, Pompeii, Stabiae and Oplontis in 79AD (e.g. Sigurdsson et al., 1985). Because the volcano's flanks now have a population exceeding 500,000, it is a key focus of volcanology research. Despite being very well studied, the pre- and syn-eruptive magmatic processes related to the 79AD event are complex, and still poorly understood. This eruption emitted 2–2.8 km^3 DRE (dense rock equivalent) magma in less than 30 h as a complex succession of fall and pyroclastic density currents (PDCs), e.g. Lirer et al. (1973), Sheridan et al. (1981), Sigurdsson et al. (1985), designated EU1–8 from base to top (Cioni et al., 1992). During the eruption, magma composition shifted sequentially from "white" K-phonolite to "gray" K-tephriphonolite (e.g. Carey and Sigurdsson, 1987; Cioni et al., 1995). The phonolitic end-member possibly represents residual tephriphonolitic magma from the Avellino eruption (~3900 years BP), which subsequently fractionated to form the upper, compositionally layered portion of the 79AD magma chamber (Cioni et al., 1995). In contrast, the "gray" tephriphonolite erupted in

79AD is a mixture of more mafic, K-tephritic magma, periodically injected into the chamber, with the pre-existing K-phonolitic magma (e.g. Cioni et al., 1995).

The early erupted white magma deposits are divided into EU1 and EU2 fall layers, separated by proximal, locally dispersed PDC deposits. Chemically, EU1 and EU2 bulk compositions are only slightly different with respect to major elements, with SiO_2, MgO, CaO being slightly higher in EU2 and Na_2O, Al_2O_3 and K_2O higher in EU1 (Table 1). EU1 and EU2 pumices both have a complex mineralogy, with phenocrysts of alkali feldspar, clinopyroxene, amphibole, mica, garnet, and minor plagioclase and Fe-Ti oxides, in order of decreasing volumetric abundance, enclosed in a glassy groundmass with microphenocrysts/microlites of leucite, sanidine, pyroxene and amphibole (Cioni et al., 1995). Although less abundant volumetrically than sanidine, leucites are more numerous in the 79AD pumice samples and typically measure 25 μm in diameter (Gurioli et al., 2005b). In general, crystal size is intrinsically linked to nucleation and growth conditions (Cashman, 1992), with phenocrysts (>100 μm) usually forming within a magma reservoir, and microlites (<30 μm) growing during ascent or cooling after extrusion. The 25 μm size of the 79AD leucites falls between microlites and

Table 1: Major element chemistry for EU1 and EU2 natural samples.

wt. %	EU1 14-1-2	EU2 V15-2-9
SiO_2	54.91 (0.26)	55.41 (0.38)
TiO_2	0.31 (0.14)	0.26 (0.11)
Al_2O_3	22.30 (0.23)	21.97 (0.45)
FeO*	2.16 (0.13)	2.90 (0.38)
MnO	0.24 (0.08)	0.24 (0.12)
MgO	0.23 (0.03)	0.65 (0.07)
CaO	3.11 (0.22)	3.69 (0.25)
Na_2O	6.22 (0.19)	5.32 (0.21)
K_2O	9.89 (0.42)	9.17 (0.39)
Cl[a]	0.54 (0.08)	0.26 (0.14)
P_2O_5	0.09 (0.04)	0.12 (0.05)
Totals[b]	99.20 (0.41)	99.76 (0.58)
n[c]	14	19
CIPW[d]		
Or	57.0	54.2
Ab		4.6
An	3.7	9.4
Ne	28.5	21.2
Di	5.2	6.9
Lc	1.1	

[a] Cl is reported as oxide weight percent.
[b] Original totals with analyses normalized to 100%.
[c] Total number of electron microprobe analyses of glass created by melting powders in $Au_{75}Pd_{25}$ tubing for 10 minutes at 1300°C.
[d] CIPW norms, main phases wt%

microphenocrysts, a size range for which conditions of formation are equivocal. Here, we examine whether the 79AD Vesuvius leucite crystallized during rapid magma ascent akin to plagioclase microlites in other magmatic systems (e.g. Cashman, 1992; Geschwind and Rutherford 1995), or whether they formed at low degrees of undercooling in a more "static" storage environment prior to eruption.

2. Methods

2.1. Phase stability

The use of phase equilibria experiments to investigate the stability of crystals in a given magma is aided by independent knowledge of the major volatile contents and fO_2 conditions. Water saturation (i.e. $X_{H2O}^{fl} \approx 1$) was found by Rutherford (1996) to be consistent with the crystallization of the mineral assemblage present in the 79AD phonolite. The absence of measurable CO_2 in melt inclusions, also supports water saturation conditions, and was interpreted to result from CO_2 degassing at magma chamber depth (Cioni, 2000). Even if the magma was CO_2-poor immediately prior to eruption, it may have been present in the melt at an earlier stage of magmatic evolution (Scaillet and Pichavant, 2004).

All experiments used H_2O-saturated conditions and fO_2 was maintained at Ni-NiO + 0.5 to 1 log unit (Rutherford, 1996; Scaillet and Pichavant, 2004) by inserting Ni-filler rods in Waspaloy pressure vessels. The starting materials consisted of finely powdered EU1 and EU2 natural pumice, welded inside $Ag_{70}Pd_{30}$ or Au capsules with ~10% de-ionized H_2O to ensure saturation. The experiments were run at T=800-1000 °C

Table 2: Phase equilibria and reversal experimental conditions with performed leucite measurements. Reversal labels refer to starting material used.

Sample name	P	T	t at P	Lc
Phase Eq.				
EU1				
79ADEU1-2	150	850	152	no
79ADEU1-3	150	800	163	no
79ADEU1-4	150	850	163	no
79ADEU1-5	100	825	212	yes
79ADEU1-6	150	825	212	no
79ADEU1-7	50	825	212	yes
79ADEU1-8	50	850	212	yes
79ADEU1-10	100	875	164	yes
79ADEU1-11	100	850	164	yes
79ADEU1-12	200	850	164	no
79ADEU1-13	100	840	188	yes
79ADEU1-14	150	840	188	no
79ADEU1-16	175	825	166	no
79ADEU1-17	100	810	166	no
79ADEU1-18	50	800	166	yes
EU2				
79ADEU2-1	150	850	162	no
79ADEU2-2	150	800	163	no
79ADEU2-3	150	850	188	no
79ADEU2-5	125	830	120	no
79ADEU2-7	50	840	125	yes
79ADEU2-8	150	800	125	no
79ADEU2-9	50	800	120	yes
79ADEU2-10	150	825	122	no
79ADEU2-11	100	850	144	no
79ADEU2-12	150	850	137	no
79ADEU2-14	200	815	168	no
79ADEU2-15	200	850	144	no
79V1	75	880	72	yes
79V2	150	850	144	no
79V3	150	880	23	no
79VB21	200	800	23	no
79VB22	200	840	24	no
79VB24	100	800	24	yes
79VS10	50	880	28	yes

Sample name	P	T	t at P	Lc
Reversals				
EU1				
R4-EU1-10	25	880	6-7 days	yes
R4-EU1-8	25	880	6-7 days	yes
R5-EU1-13	175	800	6 days	no
R5-EU1-16	175	800	6 days	no
R6-EU1-5	125	825	5 days	yes
R6-EU1-6	125	825	5 days	yes
R7-EU1-13	115	840	5 days	yes
R7-EU1-14	115	840	5 days	yes
R8-EU1-18	125	800	5 days	no
R8-EU1-13	125	800	5 days	no
EU2				
R4-EU2-7	25	880	6-7 days	yes
R4-EU2-79VB7	25	880	6-7 days	yes
R5-EU2-5	175	800	6 days	no
R5-EU2-79VB21	175	800	6 days	no
R9-EU2-7	100	840	5 days	yes
R9-EU2-5	100	840	5 days	yes
R10-EU2-5	80	860	5.5 days	yes
R10-EU2-79V1	80	860	5.5 days	yes
R11-EU2-79VB21	125	800	6 days	no
R11-EU2-9	125	800	6 days	no

P: Pressure, MPa
T: Temperature, degrees Celsius
t at P: Time at pressure conditions, hours
Lc: Presence of leucites

and P_{H2O}= 25-200 MPa for 5-9 days (Table 2), and quenched in water. Mineral stability for all detected phases was assessed by inspection of crystal morphology and reaction/dissolution textures using SEM and EDS analysis, in order to construct phase diagrams for both EU1 and EU2 (Fig. 1). Reversal experiments (R4 to R11 in Table 2), were performed at chosen P-T conditions to refine the location of the leucite-in curves. Small capsules of material derived from phase equilibria experiments run at different

conditions (one was run at conditions above the leucite-in curve, the other one below) were placed in a same larger capsule at similar conditions to fine-tune the leucite curve.

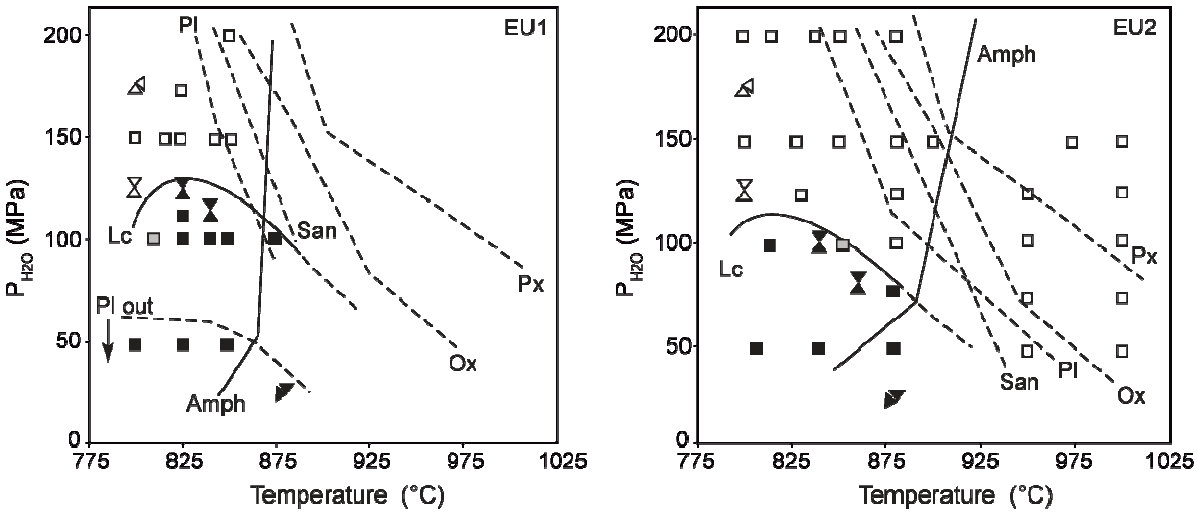

Figure 1: Phase diagram derived from IB-IT experiments. Stability curves in P_{H2O}-T space for (a) EU1 and (b) EU2; empty symbols represent leucite-free experiments, and black symbols experiments in which leucite crystallized. Double triangles symbolize reversal experiments. For most reversals, leucite stability was approached from both sides of the curve (i.e. crystallization and melting). EU1 and EU2 also crystallized garnet and mica; however, the positions of these stability curves are not well constrained.

2.2. Single and multiple-step decompression experiments

The decompression experiments were run using two approaches. Single-step decompressions were achieved through rapid decompression to 25 MPa, and holding for 5 min to 7 days before quenching, replicating integrated decompression rates of 0.0002 to 0.41 MPa/s (Table A1 in additional material). Through this method, we aimed to characterize the evolution of nucleation and growth rate following a large thermodynamic perturbation (Hammer and Rutherford, 2002). Multiple-step decompression experiments were run with 5 MPa pressure drops followed by 20-second hold times after each step, simulating a linear decompression rate of 0.25 MPa/s (Table A2). This rate was chosen to mimic a 10 m/s average magma ascent rate, calculated after models from Papale and

Dobran (1993). This value is well within the range determined for explosive Plinian eruptions (0.1 to 20 m/s, Gardner et al., 1999; Gardner et al., 2000; Rutherford and Gardner, 2000) and is conservative compared to the 30-40 m/s ascent rates required to reproduce discharge rates calculated for the 79AD eruption (CONFLOW, Mastin, 2002). Although magmatic ascent in nature is probably non-linear, use of a linear decompression rate of 0.25 MPa/s is considered an acceptable approximation given a short total magma ascent timescale of several minutes. In both cases, the experiments were conducted using run products equilibrated previously for 5-7 days at pressure conditions above the stability curve (150 MPa or 200 MPa) to obtain leucite-free starting materials (Fig. 1). The experimental temperatures of 800-850°C encompass a range determined for the 79 AD magmas from prior studies (Barberi et al., 1981; Cioni et al., 1995).

3. Results

The position of the leucite stability curves in both EU1 and EU2 bulk compositions are reported in Figure 1. The dashed curves show the approximate stabilities of major phases crystallized: plagioclase, oxides, sanidine, and pyroxene. The positions of pyroxene, sanidine and oxide-in curves are unconstrained for EU1, as no experiments were performed above 875^{o}C; they are shown as determined for EU2 and are considered very approximate. The amphibole curves are shown by solid lines to emphasize their wide stability ranges in both EU1 and EU2. The leucite stability curves are relatively constant in pressure, ranging between ~75 and 125 MPa in both EU1 and EU2 compositions at temperatures up to at least 880^{o}C. The higher temperature experiments in EU2 show no leucites at T=950 ^{o}C and P_{H2O} as low as 50 MPa.

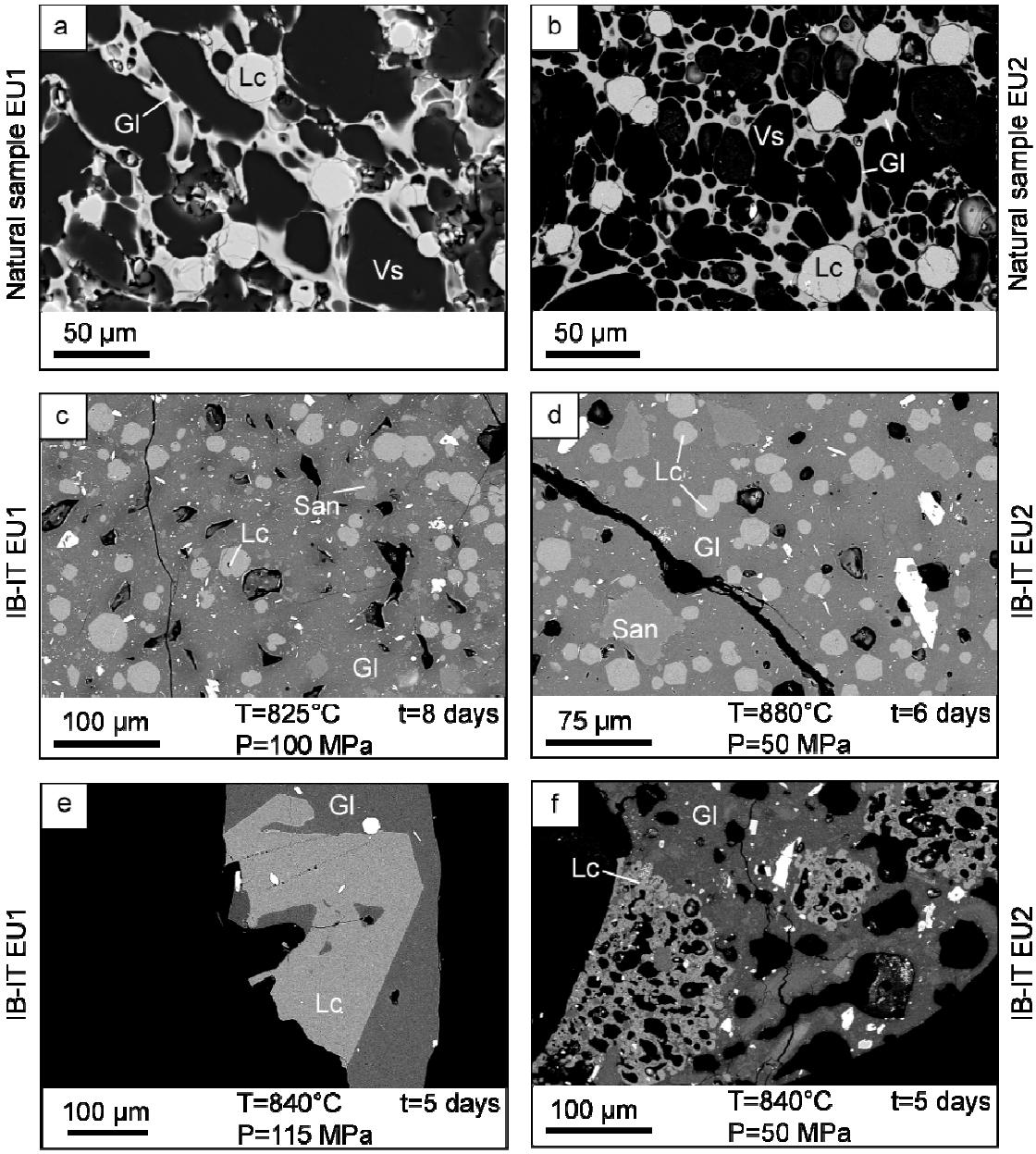

Figure 2: BSEM images of selected samples. (a) and (b) EU1 and EU2 natural samples, highly vesicular containing euhedral, homogeneously distributed leucites. (c) and (d) EU1 and EU2 IB-IT runs respectively. (e) Typical growth texture of a very large EU1 leucite which crystallized very close to the phase's stability curve. Growth of this crystal may have been limited by available space. (f) EU2 phase equilibria leucites formed at temperatures below T=850ºC are skeletal and clustered. Lc=leucite, Kfs=K-feldspar, Gl=Glass, Vesicles/pore spaces in black in the SEM images.

3.1. Leucite morphology in decompression experiments

In the natural pumices, leucites are clean, unzoned, euhedral crystals homogeneously distributed within glass (Figs. 2a and b). In contrast, the EU1 and EU2 SSD experiments produced skeletal leucites (see additional material, Fig. A1), that grew into branching clusters, irrespective of hold time and temperature. With increasing time at the final pressure (5 to 10080 min at 25 MPa), leucite shapes successively varied from small skeletal clusters to dendritic branches to massive, formless leucite domains (Fig. A1, Table A1). These complex habits and the heterogeneous distribution of leucites in EU1 and EU2 SSD are far different from those observed in the natural samples. Although the MSD series were run to approximate the average ascent rate of the 79 AD magma, none of the MSD experiments crystallized leucites, even at 25 MPa, which is well within the leucite stability field (Fig. 1). Simple textural observations from both SSD and MSD experiments show that neither decompression series replicated leucite formation in the natural magmas.

3.2. Isothermal–isobaric experiments applied to leucite formation in the 79 AD magmas

Because the decompression experiments did not yield leucites that compare well with those enclosed by 79AD white pumices, we examined the leucites that formed in the phase equilibria experiments since their textural characteristics match very well those observed in nature. In essence, the phase equilibria experiments better approximate low degrees of undercooling and crystallization at near-equilibrium conditions, more

appropriate for a magma reservoir than a conduit. The phase equilibria experiments are labeled isothermal and isobaric (IB-IT) experiments hereafter, to draw a clear distinction with the rapid changes induced during decompression. Similarly, reversal experiments provided verification of the leucite stability curves, as well as validation of the IB-IT experiments to characterize leucite textures. If the morphologies of leucites in reversal experiments are similar when approached via melting or crystallization (i.e., from either side of the curve), then these are considered path-independent.

3.2.1. Leucite morphology in IB-IT experiments

In general, natural textures were reproduced in IB-IT runs (Figs. 2c and d), with some apparent variations between EU1 and EU2 experiments. Nearly all EU1 runs produced equant, homogeneously distributed leucites. The only exception to this is experiment 79ADEU1-18, run at relatively low pressure and temperature (T=800°C, P=50 MPa), in which clusters of leucites were observed instead of free crystals. Most EU2 leucites in runs below 850°C strongly cluster around small vesicles (Fig. 2f), while above 850°C, the EU2 leucites are spatially homogeneous and equant, akin to those formed in EU1 at T>800°C. Hence, at T=800°C in EU1, and at T<850°C in EU2, IB-IT-derived leucites are texturally comparable to those formed in SSD experiments. Only above these temperatures do leucites grow similarly to their natural counterparts. Lastly, close to the inferred leucite stability boundary, EU1 experiments crystallized only a few very large individual crystals (Fig. 2e).

3.2.2. Leucite textural characterization

In using the IB–IT experiments to draw kinetic information, we assume that the mechanically as well as thermodynamically perturbed experimental system will return to chemical and textural equilibrium at the new P–T conditions. The time interval used to derive crystallization rates then becomes the time necessary to reach equilibrium. Taking into account that pulverizing the starting material in which leucites are present might have a strong influence on the experimental crystal number densities (N_V's) and derived nucleation rates, a section addresses these matters in the discussion.

Experimental and natural crystal content (vol. %), number density (N_V), and size (mean and maximum diameters, and mean diameter of 5 largest crystals in μm), are used to derive average and maximum leucite nucleation rates I (mm^{-3} s^{-1}) and growth rates Y (mm s^{-1}) (Table 3), using the 5-day run duration that was inferred to ensure near-equilibrium conditions. Experiments that were run longer (8–9 days) do not show substantial mean size differences (e.g. 79ADEU1-5). Thus, the 5 day-period is preferred over longer run times and probably represents a maximum since equilibrium conditions may have been reached earlier. The quantification task proved much more difficult for EU2 than for EU1 because half of the charges containing leucites lacked discrete crystals appropriate for size measurements (e.g. Fig. 2f).

In both EU1 and EU2, the leucite stability field is confined to pressures below ~125 MPa at a relatively wide range in temperatures. N_V, and mean sizes d_{mean}, are used to calculate the time-averaged nucleation and growth rates versus pressure (Figure 3). Although few data are available for EU2, the estimated nucleation rates I for EU1 and EU2 are indistinguishable as a function of experimental pressure below the stability limit

at 125 MPa, and increase exponentially from ~10^{-3} mm^{-3} s^{-1} at ~ 125 MPa, to 0.34 $mm^{-3}s^{-1}$ at 25 MPa (Fig. 3).

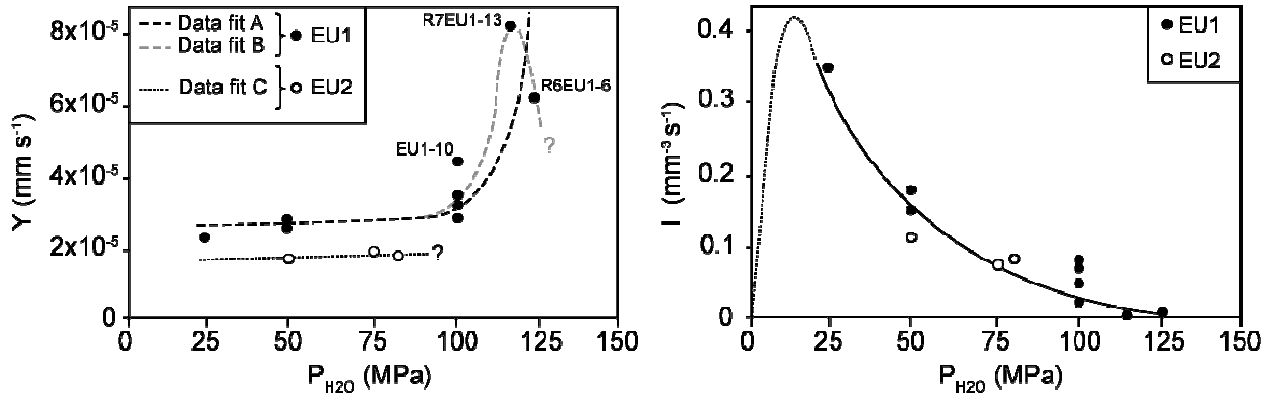

Figure 3: Rates of leucite growth and nucleation in EU1 and EU2. Around 100-125 MPa, close to the leucite-in boundary, nucleation rates are extremely low while growth rates are at their peak. As pressure decreases, growth rates stabilize while nucleation rates increase exponentially. The few experiments available for EU2 show that differences might exist only in growth rates (i.e. dotted line "Data fit C" is shifted towards lower values). Black curve in centre of the I plot shows a logarithmic fit of the form $I = -1.9325\times10^{8} \ln(P) + 9.42\times10^{8}$ (R^2=0.95) between 25 and 125 MPa, which is later used to obtain surface tension from classic nucleation theory formulations.

In contrast, leucite growth rates are highest close to the upper stability pressure (~125 MPa), with EU1 growth rates exceeding 4×10^{-8} mm s^{-1} for the three experiments closest to 125 MPa, decaying to 2-3$\times10^{-8}$ mm s^{-1} at ~100 MPa, and remaining nearly constant at lower pressures. Two fits of comparable R^2~0.90 values are proposed: in Data Fit A (Fig. 3), growth rates attain their peak near the stability limit, and, alternatively, in Data Fit B, growth rates reach a maximum before the stability pressure conditions. In both cases, the offset between nucleation and growth rate curves with respect to effective undercooling is

consistent with previous work and the classical theory (Kirkpatrick, 1981, Hammer and Rutherford, 2002, Couch et al., 2003). With the exception of the EU1 experiments run very close to the leucite stability curve (EU1-10, R6EU1-6, R7EU1-13, see Fig. 1), mean size does not vary significantly throughout the P-T domain examined. Although fewer data exist for EU2, those experiments also show consistent behavior with a shift towards smaller sizes compared to EU1 (Data Fit C).

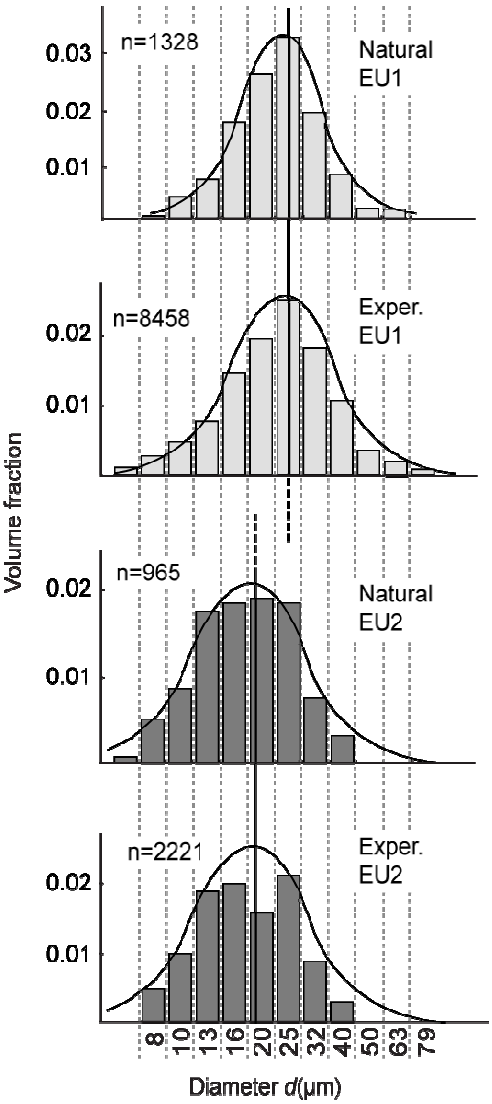

Figure 4: Comparisons between leucites formed in all static experiments and those observed in natural samples. Leucite size distribution in terms of volume for EU1/EU2 pumices and static experiments, are obtained using the stereological conversion method derived by Sahagian and Proussevitch (1998) and binned using geometric size classes. N is number of measured leucites.

Table 3: Leucite crystallization results from EU1 and EU2 experiments and natural pumice

	P (MPa)	T(°C)	[a]Lc %	[b]d mean (μm)	d mode (μm)	[c]d max (μm)	[c]d max_5 (μm)	[d]Y_{mean} $\times10^{-8}$	[d]Y_{max5} $\times10^{-8}$	[e]Nv $\times10^{-4}$	[f]I ($mm^{-3}s^{-1}$)
IB-IT											
79ADEU1-5	100	825	12.5	24.0	25	65	53.7	2.78	6.21	3.18	0.074
79ADEU1-7	50	825	23.0	22.6	25	74	62.7	2.61	7.26	7.94	0.184
79ADEU1-8	50	850	21.0	24.4	25	82	70.1	2.83	8.11	6.13	0.142
79ADEU1-10	100	875	11.5	37.1	31.5	94	84.2	4.3	9.74	1.31	0.03
79ADEU1-11	100	850	13.5	26.7	25	82	73.6	3.09	8.52	2.20	0.051
79ADEU1-13	100	840	16.7	28.8	25	102	76	3.33	9.08	3.73	0.086
79V1	75	880	14.1	17.7	16	43	38.7	2.06	4.48	3.85	0.089
79VS10	50	880	18.8	16.4	20	40	35.9	1.9	4.15	5.36	0.124
Reversals											
R4-EU1-8	25	880	30.7	21.4	20	45	44	2.48	5.09	14.70	0.34
R6-EU1-6	125	825	nd	54.0	nd	65	nd	6.25	nd	0.22	0.005
R7-EU1-13	115	840	nd	70.0	nd	140	nd	8.1	nd	0.03	0.0007
R10-EU2-5	80	860	15.2	16.5	16	27	25.9	1.9	3	4.69	0.108
EU1 Natural	-	-	17.91	24.4 (6)	25	57.6	74	-	-	3.12	-
EU1 Exp.	-	-	16.55 (5)	25.8 (5)	25	77.3 (11)	102	2.98 (0.3)	8.95 (1.1)	4.03	0.093
EU2 Natural	-	-	13.82	19.0 (6)	16-20	41.2	49	-	-	4.55	-
EU2 Exp.	-	-	16.06 (3)	19.6 (7)	16-20	33.8 (8)	43	1.95 (0.2)	3.91 (0.2)	5.63	0.107

[a]leucite volume %
[b]mean diameter (d_{mean})
[c]mean size of 5 largest crystals (d_{max5}) and size of largest crystals (d_{max})
[d]time-averaged, mean growth rates (Y_{mean}) and growth rates for 5 largest crystals (Y_{max}), in mm s^{-1}
[e]number of leucites per unit volume (N_V) corrected for vesicularity, in mm^{-3}
[f]time-averaged nucleation rate (I) derived from N_V, in mm^{-3} s^{-1}

The relatively constant average growth rates and sizes observed in both EU1 and EU2 experiments allows us to merge the crystal size distributions (CSDs), obtained from static experiments, into two size distribution plots (Figure 4; also see Table 3). We excluded the EU1 experiments EU1-10, R6EU1-6 and R7EU1-13 because their growth rates are variable, and fewer than 15 crystals were observed. Typically, EU1 and EU2 leucites in both IB-IT and natural samples show very similar unimodal distributions. However, leucites within experiments and natural pumice vary in terms of their size distributions, volume fractions, and number densities between EU1 and EU2 compositions.

EU1 experiments and natural pumices have indistinguishable mean sizes of d_{mean}=25.8±5.3 μm and d_{mean}=24.4±5.8 μm respectively (Table 3), slightly larger than those observed in EU2, in which mean sizes are d_{mean}=19.0±6.2 μm in natural samples and d_{mean}=19.6±6.8 μm in the experiments. For EU1 and EU2 experiments, calculated average growth rates are $Y_{mean}=2.98\times10^{-8}$ mm s^{-1}, and $Y_{mean}=1.95\times10^{-8}$ mm s^{-1} respectively. The mean sizes of the five largest EU1 leucites are 57.6 and 77.3 μm in experimental and natural samples respectively. Those are larger than their EU2 counterparts, with 33.8 and 41.2 μm respectively. Thus, average growth rates derived from the five largest EU1 experimental crystals are $Y_{max5}=8.95\times10^{-8}$ mm s^{-1}, nearly twice as large as those calculated for EU2 ($Y_{max5}=3.91\times10^{-8}$ mm s^{-1}). Both natural pumice and experimental leucite histograms from EU1 also possess a distinctive modal peak at equivalent diameters of 25 μm, while those from EU2 lack a clear mode. R6EU1-6 and R7EU1-13 contained the largest leucites of the experimental set (d_{mean}=54 μm and d_{mean}=70 μm respectively) and, consequently, yielded much higher mean growth rates ($Y_{mean}=6.25\times10^{-8}$ mm s^{-1} and 8.1×10^{-8} mm s^{-1}).

While leucite size is relatively invariant as a function of experimental pressure (≤ 100 MPa; Fig. 3) or temperature, crystal volume fraction increases significantly as pressure decreases. At 100 MPa, leucites comprise 11.5–16.7 vol. %, corrected for vesicularity, while at 50 to 25 MPa, they make up 21–30.7 vol. % of EU1 experiments. Therefore, as pressure decreases and crystallization advances, size remains constant while leucite volume fraction doubles. This trend is clear in the case of EU1 but unconvincing in EU2, possibly reflecting the smaller range of experimental pressures that yielded individual, euhedral leucites.

Experimental leucites have somewhat higher number densities per unit volume than the natural samples, with $N_V \approx 4.03\times10^4$ mm^{-3} in EU1 and $N_V \approx 5.63\times10^4$ mm^{-3} in EU2. In contrast, the natural pumices have $N_V \approx 3.12\times10^4$ and 4.55×10^4 mm^{-3} for EU1 and EU2 respectively. This is clearly visible in a plot of ln(n) (n is number of leucites) versus crystal size (Fig. 5a), in which the experimental samples show a consistent shift towards higher number densities compared with the natural pumices, despite similarities in the overall shapes of the curves. This is most likely an effect caused by grouping the data; while leucite size is mostly invariant throughout EU1 and EU2 and justifies using an "integrated" size distribution, number densities vary substantially in between experiments and should be treated individually. When N_V is plotted against leucite volume % (Fig. 5b), the relationship becomes quite clear: leucite volume % increases with number density. The natural EU1 pumice leucite number density and volume fraction closely matches experiment EU1–13 (P=100 MPa, T=840°C).

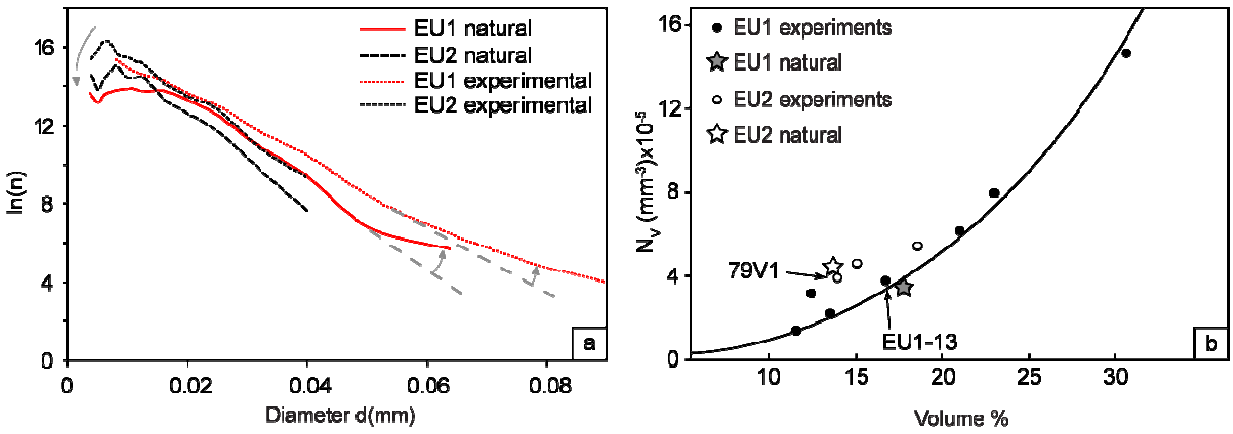

Figure 5: (a) Leucite size distribution in terms of number. Note the good correspondence in terms of curve shape between experiments and natural samples. Also, note the systematic shift towards higher N_V in both cases, probably due to grouping of the experimental data. Gray arrows illustrate the possibility of coarsening processes affecting the distribution by reducing small individuals to increase larger ones. (b) Plot of leucite number density N_V against volume fraction. The relationship indicates leucite content increases in volume dominantly by nucleation rather than by growth.

4. Discussion

4.1. Crystallization during decompression

Leucite habits in the SSD experiments are unusual compared with the natural leucites, indicating crystallization began in a nucleation dominant regime, followed by a period of rapid growth, as the crystals eventually merge and form large branched aggregates (see Fig. A1 in the additional material). Leucite nucleation in the SSD experiments occurred after an average of 1250 min at 25 MPa, indicating a substantial nucleation lag period hardly reconcilable with the ~8 min inferred for the magma to rise through the conduit (Papale and Dobran, 1993). Even the fastest-growing leucites formed only after 30 min (79ADEU1-6c, Table 3), which would imply a total ascent timescale four times slower than that postulated by Papale and Dobran (1993), and about ten times slower than that which is needed to produce the discharge rates calculated for this eruption. The complex SSD leucite shapes and the complete lack of leucites in MSD runs provide clear evidence that the decompression experiments do not replicate leucite formation in the 79AD phonolite magmas. Probably low melt viscosity fosters a very fast ascent during plinian eruptions, not allowing for leucite crystallization in the conduit. Instead, most water-saturated IB–IT experiments replicate the size ranges (15–25 μm) as well as the textural contrasts observed between EU1 and EU2 natural leucites, with EU2 containing smaller crystals on average than EU1. Most IB–IT experiments in which nature-like leucites form, were run at a lower degree of undercooling with respect to the leucite stability curve (Fig. 1). Moreover, the undercooling in the IB–IT runs is generally imposed over longer average timescales than in the decompression experiments. Hence,

the crystal-melt system was able to respond and reach a near-equilibrium state only when the imposed experimental conditions were approximately isobaric and isothermal at relatively low degrees of undercooling.

4.2. Influence of initial material on experimentally-derived textures

The starting materials used for the experiments and how they are treated prior to experimentation may influence the outcome. For example, the use of natural crushed pumices could produce different results depending on whether the powders are first fused to very high temperature and then subjected to lower temperatures, or whether unmodified powdered natural material is used. To test whether the leucites formed in IB–IT experiments bear evidence for crystal textures inherited from the starting powders, we compare features of the experimental number densities, crystal shapes, and results from the reversal experiments with those expected given completely inherited textures from the starting materials.

To test the possibility that leucites grew from a melt initially depleted in crystalline phases, we conducted four IB–IT experiments at 100 MPa and 800 to 850°C, for which the powders were first equilibrated at H_2O-saturation at 1000°C and 100 MPa for 72 hours. Those experiments were then quenched and the splits of the material were re-loaded into new capsules in the presence of H_2O and run at 800 to 850°C at 100 MPa for 90 to 120 h. These resulting experiments contained no recognizable minerals (79VB2, and 79VB9 to 13, Table 2). Instead, the melts appeared to segregate into domains that have compositions similar to sanidine or leucite (high K and high Al), but with non-stoichiometric oxide ratios. Thus, it appears that the super-liquidus pre-annealing step

disturbed the melt structure to the point where the activation energy barriers for crystal nucleation were not overcome during the experimental time-frame. Most likely, this process eliminates clusters of atoms near the critical size (Kirkpatrick, 1981) that would have otherwise grown into crystal nuclei upon decompression. Hence, because the pre-annealed samples did not produce anything that reasonably resembled the natural pumice crystal textures, we only interpret the results from experiments using natural untreated starting materials.

The use of powdered starting material, without prior fusion at super-liquidus conditions, means that the experiments contained crushed crystal fragments of all minerals in the phase assemblage (leucite, sanidine, pyroxene, etc.), in the proportions in which they existed prior to eruption. The melt is thus rich in heterogeneities, as is expected for a sub-liquidus magma. The IB-IT experiments were performed over ranges in temperature and pressure that bracket those that reproduce the major phenocryst and microphenocrysts phases found in the natural pumices (Fig. 1). About half of IB–IT experiments approached their steady-state crystallinity by melting and about half by crystallization. Coherence of textural results in runs from P-T conditions representing both lower and higher crystallinities than the starting material suggests that the direction of approach was not a factor controlling the final texture. Indeed, the effects of crushed leucite crystals from the pumices on any possible inherited experimental N_V should be random and invariant as a function of experimental pressure. Figure 3 clearly shows that nucleation rate, calculated from measured experimental N_V, varies systematically with experimental pressure, and is thus not random, but depends on the experimental conditions. The same can be said about the variation of N_V with volume fraction (Fig.

5b). This altogether supports the assertion that the experimental leucite N_V's are related to experimental conditions, and are not inherited from the starting powders.

The experimental leucites also exhibit euhedral and faceted shapes, consistent with interface-limited crystal growth textures (Kirkpatrick, 1981). Crushed leucites that had not undergone growth at experimental conditions would appear angular or even resorbed in the experiments. Thus, even if N_V had been influenced by the distribution of crystals in the starting material, leucite growth must have proceeded as a function of the experimental conditions (Fig. 3).

In summary, the measured leucite N_V, sizes and habit in the IB–IT dataset all point towards internal consistency and not inherited textures from the pre-experimental sample material. Further comparisons between initially crystal-rich and crystal-free starting materials illustrate that leucites are likely to have formed in the presence of other phases. Thus, although we acknowledge that the crushed starting material probably helped to facilitate leucite formation through heterogeneous nucleation, the effects of inherited crystal number densities and growth rates directly from the un-annealed starting powders is relatively minor.

4.3. Thermal zoning within the upper reservoir

The IB–IT experiments indicate differences in magmatic temperatures between EU1 and EU2 in the reservoir. In EU1, euhedral, individual leucites crystallize homogeneously over almost the entire temperature range examined except at T=800°C. A minimum temperature between 800°C and 825°C can therefore be inferred. Also, amphibole, present in EU1 natural samples, cannot crystallize at T>860°C at ~100 MPa P_{H2O} (Fig. 1)

Thus, the EU1 magma likely had T=800-860°C. Amphibole stability offers a good marker in the 79 AD phonolites because it crystallizes at pressures greater than P_{H2O} ~50 MPa, and is insensitive to volatile saturation conditions. The experiment which best reproduced the natural EU1 textures was run at T=840°C, and is a better match than experiments run at similar pressures at T=825°C and T=850°C. Hence, using this additional textural constraint, conditions for EU1 can be refined to T=830–840°C.

In the EU2 experiments, leucite textures comparable to the natural ones form only above 850°C. Similarly, amphibole in EU2 is found to be stable experimentally at temperatures less than 875 to 925 °C. Thus, the EU2 magma was hotter, with T= 850–925°C range. The experiment that best replicates the natural EU2 leucites is 79V1 (T=880°C). Hence, the Vesuvius 79AD phonolite magmas were not only slightly compositionally zoned, but likely thermally layered as well. The thermal differences could arise from the late arrival of the K-tephritic melt batch which mixed deep within the chamber to form the gray tephriphonolitic magmas residing beneath the EU2 magma. In this configuration, temperatures are T_{EU1}=830–840°C, and T_{EU2}=850–925°C. These conditions are corroborated by Cioni et al. (1998), who found two distinct populations of homogenization temperatures in melt inclusions for the white magma: one between 800 and 850°C, in agreement with EU1 temperatures found herein, and the other one between 900 and 950°C, slightly higher than those derived for EU2.

4.4. Leucite crystallization conditions

In this study, phase equilibria data constrain leucite crystallization at $P_{H2O} \approx 100$ MPa, and textural observations predict temperatures T=830–840°C for EU1 and T=850–

925°C for EU2. If magmas were H_2O-saturated in the Vesuvius 79AD reservoir, then leucites might have grown under relatively steady, magma chamber-like conditions at ~4 km depth. On the other hand, if CO_2 was initially present in a deeper magma chamber (Scaillet and Pichavant, 2004), leucites could have crystallized after slow depressurization or stalling during ascent. In this model, EU1 and EU2 magmas could originally have resided leucite-free at P ≥200 MPa. Slow depressurization without magmatic ascent (e.g. Scandone, 1996) could have begun at least several days before the Plinian phase of the eruption began, and gradually imposed a >100 MPa pressure drop in the reservoir. Once the leucite stability horizon was reached, the crystals grew to their final sizes in both EU1 and EU2 magmas, prior to ascent.

4.5. Leucite crystallization kinetics

4.5.1. Leucite nucleation

According to Figure 3, experimentally-measured nucleation rates for leucites are dependent on ΔP, where $\Delta P = P_{reservoir} - P_{nucleation}$, and thereby on dissolved H_2O content and effective undercooling (T_{eff}). Crystal nucleation rates (I) depend on the energy necessary to form a cluster of critical size r^*, which is generally termed the interfacial energy σ. In classical nucleation theory (CNT), I and σ are linked by the following equation (Kirkpatrick, 1981; Hammer, 2004):

$$I = \frac{A_c}{\eta} T \exp\left(\frac{-\Delta G^*}{k_B T}\right) \qquad \text{(Eq. 1)}$$

where T is temperature, η is viscosity, k_B the Boltzmann constant, $A_c = \frac{k_B n_V}{3\pi\lambda^3}$ is the pre-exponential factor with n_V volumetric concentration of reactant atoms and λ the jump distance between atoms, and $\Delta G^* = \frac{16\pi\sigma^3}{3\Delta G_V{}^2} S(\theta)$ is the free energy required to form critical nuclei having properties of the bulk solid, with θ the wetting angle between the nucleus-wall and nucleus-liquid interface. The bulk free energy change per unit volume during transformation $G_V = \frac{\Delta G}{V_M}$ encloses the volume of the crystallizing phase V_M as well as the energy change term, which can be approximated using Turnbull's equation $\Delta G = \frac{\Delta H \Delta T}{T_L}$, where T_L is the liquidus temperature of the crystallizing phase at a given pressure, and ΔH is the enthalpy of formation of the phase from elements at T. Inserting the above equalities into Eq. (1) yields:

$$I = \frac{k_B n_V T}{3\pi\lambda^3\eta} \exp\left(\frac{-16\pi\sigma^3 T_L{}^2 V_M{}^2}{3\Delta H^2 \Delta T^2 k_B T}\right) \qquad \text{(Eq. 2)}$$

The interfacial energy can then be found by re-arranging equation (1) into:

$$\sigma = \left[\frac{\left[\ln(I) - \ln\left(\frac{k_B n_V T}{3\pi\lambda^3\eta}\right)\right] \times 3\Delta H^2 \Delta T^2 k_B T}{-16\pi T_L{}^2 V_M{}^2}\right]^{\frac{1}{3}} \qquad \text{(Eq. 3)}$$

In these calculations, several assumptions are made, such as $S(\theta)$=1 (homogeneous nucleation), a compositional dependence of the interfacial energy, and the use of T_{eff} instead of ΔT (Hammer, 2004). ΔH and V_M vary with pressure and temperature, ranging from ΔH=175902 to 193686 J K^{-1} and V_M=8.93 to 8.94×10^{-5} m^3 mol^{-1} (taken from the Computational Thermodynamics Server: http://ctserver.ofm-research.org/phaseProp.html; see references therein), a jump distance $\lambda=3\times10^{-10}$ m was used (Hammer, 2004), T_{eff} and T_L were measured using phase curves from Figure 1, and viscosities were calculated following the models of Shaw (1972) and Romano et al. (2003). Nucleation rates (I) were input in two different ways:

First, and because nucleation rate seems to be mostly pressure-dependent (Fig. 3), a logarithmic best fit function applied to all experiments was inserted into Eq. (3)

$$I = -1.9325\times10^{8}\ln(\mathrm{P}) + 9.42\times10^{8} \quad \text{(Eq. 4)}$$

Because H_2O content directly depends on pressure, the equation can also be written:

$$I = -3.646\times10^{8}\ln(\mathrm{H_2O}) + 5.536\times10^{8} \quad \text{(Eq. 5)}$$

σ was then calculated using Eq. (3) for different temperatures (800, 825, 850 and 875 ºC) over the pressure range covered by the experiments (25-125 MPa). We emphasize that the calculated interfacial energy includes effects not accounted for by the CNT which reduce the nucleation barrier, and adopt σ' instead of σ (Hammer 2004).

Secondly, in an attempt to compare the interfacial energy calculated using the term *I* derived from Eq. (4) and Eq. (5), with interfacial energy calculated using nucleation rates measured in each individual run (Table 3), each experiment was plotted, along with its run conditions. Because leucite nucleation rates are pressure-dependent, co-variations between *σ'*, *P*, H_2O, and *I* are expected.

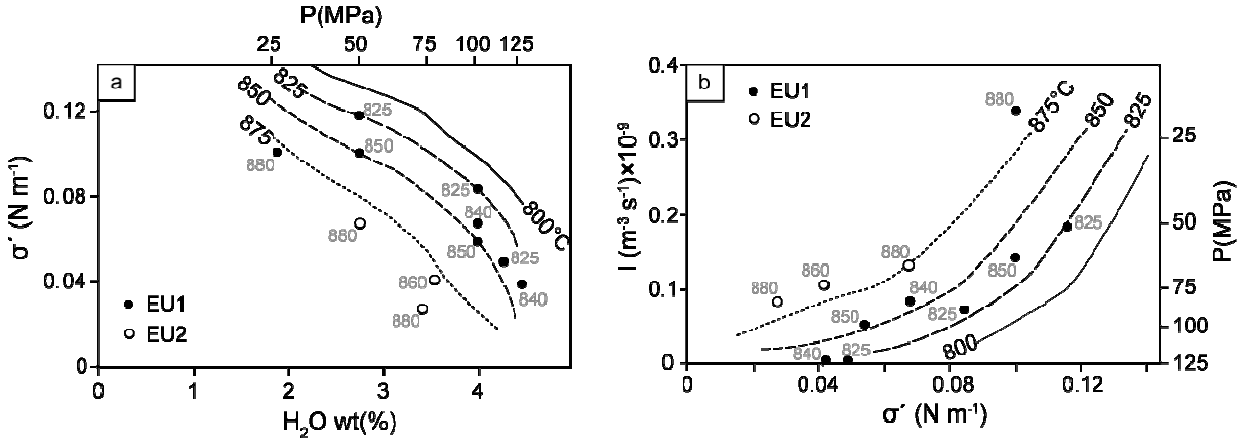

Figure 6: Link between interfacial energy σ', nucleation rates I, and intensive variables such as pressure (and thereby water content). Isotherm curves show calculated σ' in EU1 for four temperatures using Eq. (3) in the text. Note that they are *not* best-fitting curves for the individual experimental runs (temperatures displayed in gray). (a) Interfacial energy decreases with increasing water content and (b) nucleation rate (and thereby inverse pressure) increases with σ'.

As in Hammer (2004), the interfacial energy *σ'* decreases with increasing experimental H_2O pressure, suggesting a compositional control on nucleation kinetics (Fig. 6a). Hence, at the inferred temperature conditions for EU1 and EU2 and for pressures P~100 MPa, surface tension is roughly σ'≈0.07 N m^{-1} for EU1 and σ'≤0.05 N m^{-1} for EU2. Nucleation rates (*I*) show a positive correlation with increasing interfacial energy (Fig. 6b). This is expected from Eq. (3) since interfacial energy is related to the

logarithm of nucleation rate by a cubic root. The slight temperature-dependence of σ' illustrates that the interfacial energy decreases as T increases (Fig. 6a and Fig. 6b). A temperature-dependence of nucleation rate is also observed when $T_{eff.,}$ is compared to I (see Fig. A3 in the additional material). Because viscosity decreases with increasing H_2O content at fixed temperature, and since changes in dissolved H_2O strongly affect melt viscosity, the interfacial energy scales with viscosity.

Measured nucleation rates (I) and calculated viscosities (η) support the assertion that nucleation rate increases as melt viscosity increases (additional material, Fig. A3). A theoretical basis for this trend may not be obvious, since nucleation rate is inversely related to melt viscosity in Eq. (2). However, the main control on nucleation rate in Eq. (2) is the cubed interfacial energy term, which is in turn controlled by dissolved water content. Hence, the kinetic limitation imposed by increasing viscosity exerts a weaker control in leucite nucleation than surface tension, although both are intrinsically linked to water content.

A complex interplay between nucleation and growth produces the observed natural and experimental textures. The viscosity increase accompanying melt devolatilization inhibits diffusion of crystal-forming components, and this may enhance nucleation over the growth of pre-existing crystals. This hypothesis is supported by the correlation of leucite volume fraction and N_V (Fig. 5b), and lack of correlation between volume fraction and mean size. These trends suggest leucite crystallization occurs through vigorous nucleation (followed by growth) rather than by rapid growth of sparse crystals. Note that in Figure 6, individual experiments are reasonably well modeled by the calculated

isotherms, indicating internal consistency of the dataset and demonstrating the viability of our application of the classical theory of nucleation.

While the relationship between pressure and nucleation rate is clear over the examined P range, the same is not obvious for temperature (additional material, Fig. A2). Indeed, viscosity in these melts is much more influenced by P_{H2O} than by T in the studied range (also see Fig. A3). The limited dataset suggests that variations in nucleation rate as a function of P_{H2O} are larger than those caused by variations in T.

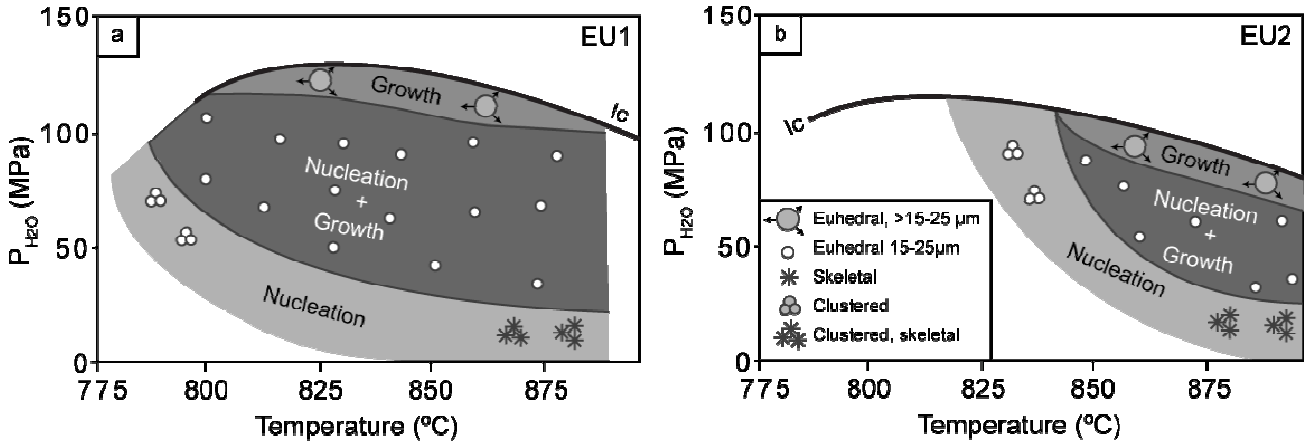

Figure 7: Interpretative diagrams of crystallization kinetics for (a) EU1 and (b) EU2 leucites. Three mainly pressure-dependent regimes are represented, *growth*, *nucleation+growth* and *nucleation*-dominated domains. Symbols are generic and do not represent specific experiments.

4.5.2. Mechanisms of leucite formation

In contrast to the clear relationship between leucite number density and pressure, the correlation between leucite size and pressure is less obvious. Size appears to be mostly affected by pressure at values over 100 MPa, close to the phase stability limit (i.e., growth rates on Fig. 3). In contrast, temperature does not affect leucite size within a large

P-T domain, but produces changes in leucite shape and arrangement, particularly at T<825ºC in EU1 and T<850ºC in EU2, below which leucites become increasingly clustered.

Based on the textural observations, and the relationships between nucleation and growth rates with varying P and T, we derive a model for leucite growth mechanisms in EU1 and EU2 phonolitic melts (Fig. 7). In the vicinity of the leucite stability curve, growth rates are much higher than at lower pressures (Fig. 3). Growth-dominant behavior is expected at low degrees of supersaturation where nucleation rates are low and nutrient transport to a few nuclei is rapid (Kirkpatrick 1981). This tendency is also observed in the experiments of Hammer and Rutherford (2002): plagioclase phenocrysts grow immediately upon decompression, while nucleation of new crystals (destined to become microlites) occurs at higher undercoolings. Near the stability curve, the experimental leucites possess sharp, faceted interfaces (Fig. 2e) and their habit is typically euhedral. Further away from the stability limit, nucleation rate increases and growth continues at a relatively high rate, producing crystallization of numerous euhedral leucites which grow to an average size of ~19 and 25 μm for EU2 and EU1 respectively. Within the "growth" and "nucleation+growth" domains, diffusion of nutrients is uninhibited by melt viscosity and growth may be interface–limited. Indeed, faceted crystal morphologies suggest that growth rate is limited by attachment of atoms and not by transport of nutrients in the melt. With increasing distance from the leucite-in curve, the "nucleation+growth" regime is replaced by the "nucleation dominated" domain in which crystals form as aggregates (Fig. 2f) or massive intergrowths very similar to those observed in the SSD experiments. Here, diffusion of nutrients to the melt-crystal interface is most likely a limiting process,

and the system responds to thermodynamic disequilibrium by vigorous nucleation. The trend is similar for EU2 compositions, except that temperatures defining the regimes are shifted upward (Fig. 7), bringing the regime of clustered crystals near the leucite-in curve at low T and high P.

4.5.3. Comparisons with plagioclase crystallization kinetics

Interesting comparisons can be made between crystallization kinetics of leucites and plagioclase in magmas of various compositions. The time-averaged leucite growth rates constrained from the present experiments vary between 2×10^{-8} mm s^{-1} and ~10^{-7} mm s^{-1}. In comparison, growth rates calculated from CSDs for plagioclase phenocrysts vary between 10^{-8} mm s^{-1} and 10^{-11} mm s^{-1} (Armienti et al., 2007; Cashman, 1988, Cashman and Blundy, 2000), and between 10^{-7} and 10^{-10} mm s^{-1} for microlites (Cashman, 1988). Thus, leucites have growth rates that are 1 to 3 orders of magnitude faster than those calculated for plagioclase. Hammer and Rutherford (2002), Couch et al. (2003), and Larsen (2005) have nevertheless demonstrated that growth rates are extremely variable as a function of experimental duration, decreasing precipitously as runtime increases, which is consistent with crystallization kinetics being slower as the system approaches thermodynamic equilibrium. Because growth rates for leucites from this study have been obtained at presumably low degrees of effective undercooling, comparisons must be made with plagioclase under similar conditions. Using asymptotes of the time-variation of plagioclase growth rate obtained from Hammer and Rutherford (2002) for dacites, and Larsen (2005) for rhyodacites, at low undercooling (T_{eff}=34–35ºC), growth rates are 2×10^{-9} mm s^{-1} and 3×10^{-9} mm s^{-1} respectively. Differences between plagioclase and

leucites could be, to a first order, attributed to viscosity differences; indeed, at similar P–T conditions, phonolites have significantly lower viscosities than dacites (see Fig. A3 in additional material) and rapid diffusion may allow for faster growth in phonolites. Even so, plagioclase growth rates estimated using CSDs from low viscosity basaltic melts (Armienti et al., 2007) are of the same magnitude as those obtained experimentally by Hammer and Rutherford (2002) in dacites after sufficiently long runtimes. Altogether, this suggests that leucites in phonolitic melts grow faster than plagioclase in other melts for reasons that cannot be attributed solely to viscosity.

Leucite nucleation rates of 0.0007 to 0.34 mm^{-3} s^{-1} from the experiments encompass those measured by Cashman and Blundy (2000) for plagioclase microphenocrysts, but are much higher than estimated for plagioclase phenocrysts, estimated to be 5-21×10^{-9} mm^{-3} s^{-1} in a Mt St Helens dacite (Cashman, 1988). On the other hand, leucite nucleation rates are much lower than the 2 to 10,000 mm^{-3} s^{-1} range observed for plagioclase microlites by Larsen (2005), and at the lower end of the 0.01-4 mm^{-3} s^{-1} interval found by Hammer and Rutherford (2002).

In terms of crystallization dynamics, low nucleation rates for leucite or plagioclase microphenocrysts (0.007-0.34 mm^{-3} s^{-1}) suggest nucleation triggered by changes in ΔT_{eff} that are slow enough for the system to respond to the thermodynamic disturbances. In contrast, the much higher plagioclase microlite nucleation rates (2-10,000 mm^{-3} s^{-1}) support a nucleation-dominant regime during rapid changes in P-T conditions, in which diffusion of crystal-forming components in the melt is rate-limiting (for additional details regarding leucite and plagioclase nucleation behavior, see also Fig. A4 and related text in the additional material).

4.5.4. Leucite size-invariance

In the above paragraphs, it appears that the observed leucite crystallization generally conforms to classical theory of nucleation and growth. At high and low undercoolings, nucleation and growth of leucites behave similarly to plagioclase, albeit at different rates (Hammer and Rutherford, 2002; Couch et al., 2003). At intermediate undercoolings, however, leucite in phonolitic melts behaves in a more complex fashion. While nucleation rates continuously increase with increasing effective undercooling, growth rates appear to decrease rapidly away from the stability curve and remain constant throughout a large P and T domain (Fig. 3). In this domain, leucites seem to reach a consistent size-distribution even as volume fraction varies significantly. Interestingly, the size attained within these conditions is larger for EU1 than for EU2 (~25 μm and ~19 μm respectively). This raises two questions: why would crystals stop growing after reaching a certain size? And why would these sizes be different in the two phonolites?

One possibility is that growth rate decreases as crystals coarsen. The final size distribution may be achieved by fast growth rates shortly after the system is thermodynamically perturbed. As chemical and thermodynamic equilibrium is approached, growth rate declines precipitously as has been observed for plagioclase and other phases forming in response to decompression (Hammer and Rutherford, 2002; Couch et al., 2003), thus preserving the size distribution that was set by the initial growth rate. A time-series of experiments is needed to test whether this is a viable explanation.

Ostwald ripening may also be important in achieving this textural invariance. Polydisperse mixtures in chemical equilibrium with melt are not at their lowest energy state due to non-zero interfacial energy expended at crystal surfaces (Voorhees, 1992).

Full textural and thermodynamic equilibrium can only be achieved through a reduction in interfacial energy. During Ostwald ripening, the total crystal-melt interfacial energy is reduced through diffusion of crystalline nutrients from zones of high interfacial curvature to zones of low interfacial curvature. Accordingly, small crystals are lost to feed larger ones until the system reaches a "textural steady-state". Although not entirely conclusive, leucite distribution curves for both natural and experimental samples (Fig. 5a) indicate this type of coarsening. However, the rate at which these processes occur is uncertain. While Park and Hanson (1999) showed that Ostwald ripening can initiate substantial textural modifications, experiments on olivine-bearing basalts and plagioclase-bearing andesites by Cabane et al. (2005) revealed that this process is only significant for one of the studied crystal phases (olivine) in one of the studied compositions (basalt). Much more work is needed to substantiate the influence of ripening processes on modifying crystal populations in volcanic rocks.

Finally, the shift in size distributions observed between EU1 and EU2 might result from small chemical variations in K_2O, Na_2O, Al_2O_3, and SiO_2 between the two magmas (Table 1). In this scenario, leucites reach ~18 μm in EU2 after 5 days compared to 25 μm in EU1. It is nonetheless hard to demonstrate how such small variations in chemistry could induce large differences in the formation of crystalline phases in magmas.

5. Conclusions

In the 79 AD magmas, leucite microphenocrysts did not crystallize during rapid magma ascent at average rates typical of Plinian eruptions. Rather, they are likely to have grown over timescales of days at lower, more slowly imposed effective undercoolings.

The study of leucite crystallization yielded not only a minimum timing for magma residence at depth, but also provided two possible scenarios yielding strong clues to magma storage and pre-eruptive dynamics occurring under volcanoes such as Vesuvius. In the first scenario, if the white magma was water-saturated, magma was stored for at least a few days at depths of ~4 km before being erupted. Alternatively, if the magma was undersaturated, leucites may have captured a slow depressurization event at greater depth prior to entering the conduit. Furthermore, at similar temperatures, EU1 and EU2 displayed different crystallization behaviors, yielding a remarkable example of how minor chemical divergences may have a measurable effect on crystallization kinetics. Although leucite crystallization is well described by the classical nucleation theory, a small complication not described by classical formulation was observed: a characteristic textural state appears to be attained over a rather large P-T domain, with invariant sizes but variable population number densities. Finally, the leucite growth and nucleation rates derived from these experiments may be used in the future as proxies to assess magma residence times or rise times in the event of eruptions involving slower ascent.

Acknowledgments

The authors wish to acknowledge NSF grants EAR 0537950 and 0537543. Kathy Cashman's input enriched this work, and comments from Bruno Scaillet, Michelle Coombs and Jon Blundy improved a previous version of the manuscript. Roberto Scandone's comments were also appreciated.

Appendix A1: Experimental conditions and leucite textures in SSD experiments

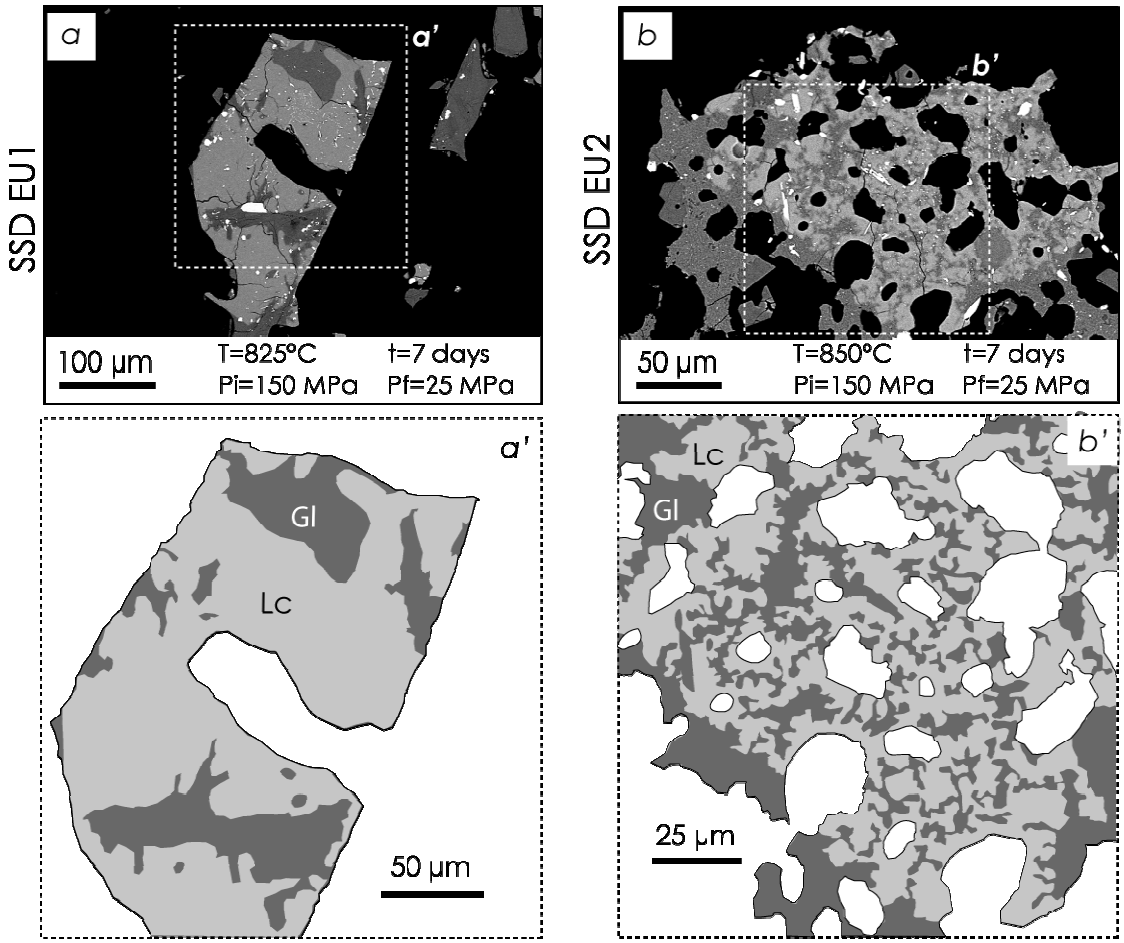

Figure A1: (a) SSD experiment in EU1 produced an entire domain of leucites (brighter areas), which nucleated in extreme numbers and progressively branched together after 7 days at 25 MPa and (b) EU2 SSD experiment shows a large skeletal leucite cluster, in which individual crystals are not discernable. (a') and (b') are close-ups of (a) and (b) sketched to ease visualization. Note the leucite "branches" typical of a nucleation dominated crystallization regime. Lc=leucite, Kfs=K-feldspar, Gl=Glass, Vesicles/pore spaces in black in the SEM images, and in white in a' and b'.

Table A1: Single step decompression experimental conditions and results

Sample name	[a]Pi (MPa)	[b]Pf (MPa)	T (ºC)	[c]t@Pf (min)	[d]IDR (MPa s^{-1})	Lc habit
79ADEU1-3a	150	25	800	5	0.4167	
79ADEU1-3b	150	25	800	15	0.1389	
79ADEU1-3c	150	25	800	30	0.0694	
79ADEU1-3d	150	25	800	60	0.0347	
79ADEU1-3e	150	25	800	720	0.0029	Skeletal/clustered
79ADEU1-3f	150	25	800	1440	0.0014	Skeletal/clustered
79ADEU1-3g	150	25	800	2880	0.0007	Skel./dendritic
79ADEU1-3h	150	25	800	5760	0.0004	massive
79ADEU1-3i	150	25	800	10080	0.0002	massive
79ADEU1-6a	150	25	825	5	0.4167	
79ADEU1-6b	150	25	825	15	0.1389	
79ADEU1-6c	150	25	825	30	0.0694	Skeletal/clustered
79ADEU1-6d	150	25	825	60	0.0347	Skeletal/clustered
79ADEU1-6e	150	25	825	720	0.0029	Skeletal/clustered
79ADEU1-6f	150	25	825	1440	0.0014	Skel./dendritic
79ADEU1-6g	150	25	825	2880	0.0007	Skel./massive
79ADEU1-6h	150	25	825	5760	0.0004	massive
79ADEU1-6i	150	25	825	10080	0.0002	massive
79ADEU1-22a	150	25	850	5	0.4167	
79ADEU1-22b	150	25	850	15	0.1389	
79ADEU1-22c	150	25	850	30	0.0694	
79ADEU1-22d	150	25	850	60	0.0347	
79ADEU1-22e	150	25	850	720	0.0029	
79ADEU1-22f	150	25	850	1440	0.0014	skel/dendritic
79ADEU1-22g	150	25	850	2880	0.0007	skel/dendritic
79ADEU1-22h	150	25	850	5760	0.0004	skel/massive
79ADEU1-22i	150	25	850	10080	0.0002	skel/massive
79V2a	150	25	850	5	0.4167	
79V2b	150	25	850	15	0.1389	
79V2c	150	25	850	30	0.0694	
79V2d	150	25	850	60	0.0347	
79V2e	150	25	850	720	0.0029	
79V2f	150	25	850	1440	0.0014	
79V2g	150	25	850	2880	0.0007	Skeletal/clustered
79V2h	150	25	850	5760	0.0004	Skeletal/clustered
79V2i	150	25	850	10080	0.0002	Skeletal/massive

[a]Pi - Initial pressure
[b]Pf - Ending pressure
[c]t@Pf: Holding time at ending pressure.
[d]IDR - Integrated Decompression Rate, obtained by dividing the total pressure drop by the hold time at final pressure

Appendix A2: Experimental conditions for MSD, and effect of temperature on nucleation rates

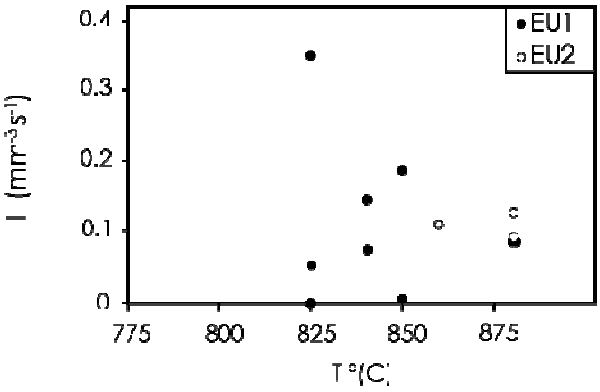

Figure A2: I versus T plot illustrating the lack of obvious control of temperature over nucleation rates.

Table A2: Details of multiple-step decompression experimental conditions. P_i: Initial pressure, P_F: Ending pressure, IDR: Integrated Decompression Rate, T_{eff}: Effective undercooling, and t/step: Holding time for each pressure step.

Sample name	Type-series	P_I (MPa)	P_F (MPa)	T (ºC)	~T_{eff} (ºC)	t/step	IDR (Mpa.s^{-1})	Lc
79ADEU1-21a	MSD	150	125	825	0	20s/5MPa	0.25	no
79ADEU1-21b	MSD	150	100	825	50	20s/5MPa	0.25	no
79ADEU1-21c	MSD	150	75	825	65	20s/5MPa	0.25	no
79ADEU1-21d	MSD	150	50	825	75	20s/5MPa	0.25	no
79ADEU1-21e	MSD	150	25	825	75-100	20s/5MPa	0.25	no
79ADEU1-19a	MSD	150	125	850	-	20s/5MPa	0.25	no
79ADEU1-4b	MSD	150	100	850	20	20s/5MPa	0.25	no
79ADEU1-4c	MSD	150	75	850	40	20s/5MPa	0.25	no
79ADEU1-4d	MSD	150	50	850	60	20s/5MPa	0.25	no
79ADEU1-19e	MSD	150	25	850	75	20s/5MPa	0.25	no
79ADEU1-2a	MSD	150	125	850	-	20s/5MPa	0.25	no
79ADEU1-2b	MSD	150	100	850	20	20s/5MPa	0.25	no
79ADEU1-2c	MSD	150	75	850	40	20s/5MPa	0.25	no
79ADEU1-2d	MSD	150	50	850	60	20s/5MPa	0.25	no
79ADEU1-2e	MSD	150	25	850	75	20s/5MPa	0.25	no
79ADEU1-2f	MSD	150	10	850	85?	20s/5MPa	0.25	no
79ADEU2-10a	MSD	150	125	825	nd	20s/5MPa	0.25	no
79ADEU2-10b	MSD	150	100	825	nd	20s/5MPa	0.25	no
79ADEU2-10c	MSD	150	75	825	nd	20s/5MPa	0.25	no
79ADEU2-10d	MSD	150	50	825	nd	20s/5MPa	0.25	no
79ADEU2-10e	MSD	150	25	825	nd	20s/5MPa	0.25	no
79ADEU2-3a	MSD	150	125	850	nd	20s/5MPa	0.25	no

Sample name	Type-series	P_I (MPa)	P_F (MPa)	T (ºC)	~T_{eff} (ºC)	t/step	IDR (Mpa.s^{-1})	Lc
79ADEU2-3b	MSD	150	100	850	nd	20s/5MPa	0.25	no
79ADEU2-3c	MSD	150	75	850	nd	20s/5MPa	0.25	no
79ADEU2-3d	MSD	150	50	850	nd	20s/5MPa	0.25	no
79ADEU2-3e	MSD	150	25	850	nd	20s/5MPa	0.25	no
79ADEU2-18a	MSD	150	175	815	nd	20s/5MPa	0.25	no
79ADEU2-14a	MSD	200	150	815	nd	20s/5MPa	0.25	no
79ADEU2-18c	MSD	200	125	815	nd	20s/5MPa	0.25	no
79ADEU2-14f	MSD	200	100	815	nd	20s/5MPa	0.25	no
79ADEU2-18d	MSD	200	75	815	nd	20s/5MPa	0.25	no
79ADEU2-14c	MSD	200	50	815	nd	20s/5MPa	0.25	no
79ADEU2-14e	MSD	200	25	815	nd	20s/5MPa	0.25	no
79ADEU2-15f	MSD	200	175	850	nd	20s/5MPa	0.25	no
79ADEU2-15a	MSD	200	150	850	nd	20s/5MPa	0.25	no
79ADEU2-17a	MSD	200	125	850	nd	20s/5MPa	0.25	no
79ADEU2-15b	MSD	200	100	850	nd	20s/5MPa	0.25	no
79ADEU2-15g	MSD	200	75	850	nd	20s/5MPa	0.25	no
79ADEU2-15e	MSD	200	50	850	nd	20s/5MPa	0.25	no
79ADEU2-15d	MSD	200	25	850	nd	20s/5MPa	0.25	no

Appendix A3: Nucleation kinetics

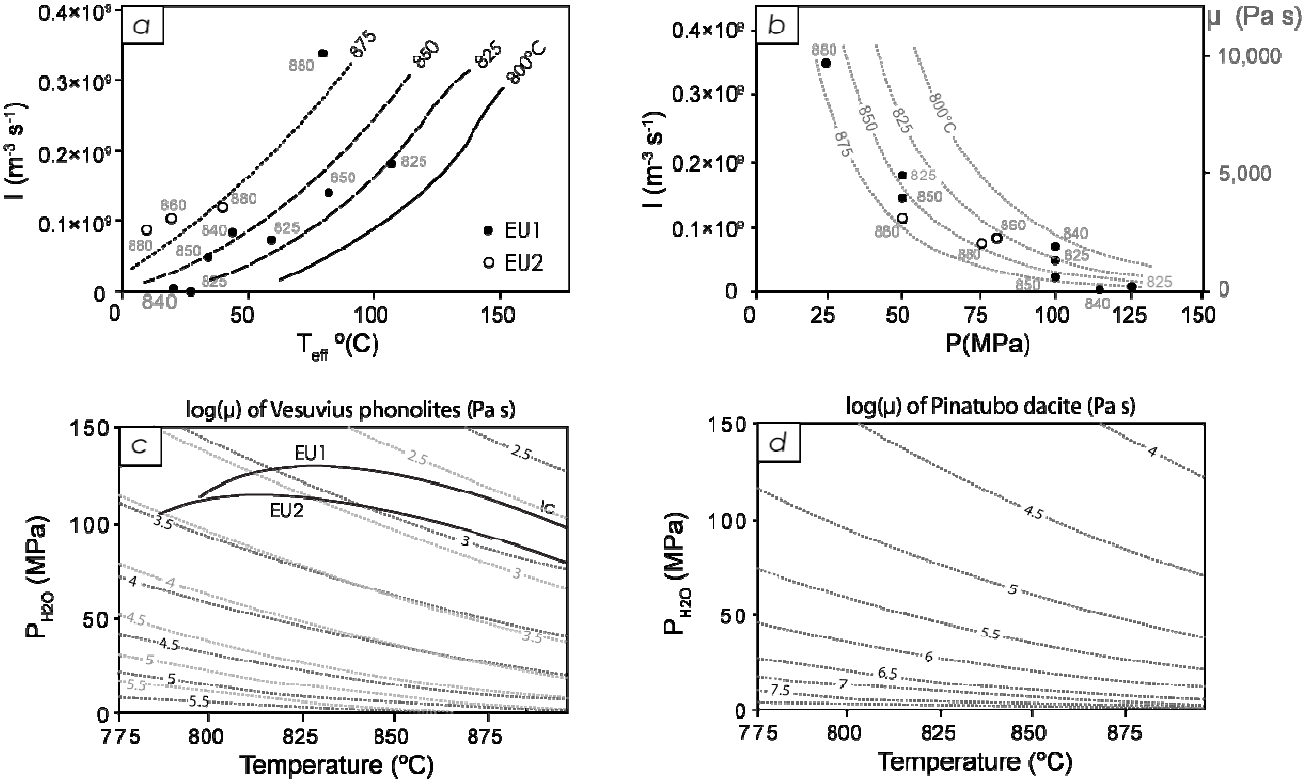

Figure A3: (a) T_{eff} and σ' covariations (b) Merged plots of nucleation rate (filled and empty circles) versus P_{H2O} and viscosity (dotted gray curves) versus P_{H2O}. Isotherm curves show calculated values for four temperatures using Eq. (3). Also reported are viscosity isokoms for the P-T space for (c) Vesuvius white phonolites (dark dotted lines calculated using Shaw (1972), gray dotted lines obtained using Romano et al. (2003), in both cases using the solubility model of Larsen, (2008)) and (d) for Pinatubo dacites (Hess and Dingwell, 1996). No distinction was made between EU1 and EU2 because the available viscosity models are unable to account for such small variations in composition.

Appendix A4: Comparisons between leucites and plagioclase behavior

Leucite nucleation rates are much lower than the 2 to 10000 mm^{-3} s^{-1} range observed for plagioclase microlites by Larsen (2005), and at the lower end of the 0.01-4 mm^{-3} s^{-1} interval found by Hammer and Rutherford (2002). Interestingly enough, while leucite nucleation rates are about one order of magnitude lower than those measured on

plagioclase microlites, their behavior is fairly similar in terms of the effective undercooling at which the two phases reach their maximum rates of nucleation. Figure A4 shows nucleation rates normalized to the measured maximum ($I_{norm}=I/I_{max}$) to facilitate comparisons without resorting to logarithmic scaling. Comparison with Pinatubo plagioclase data (Hammer and Rutherford, 2002) illustrate that the shape of nucleation rates curves is similar. Temperature (800, 825, 850 and 875 ºC) affects the undercooling at which nucleation rate peaks (Fig. 7). Otherwise, the trends are very much the same.

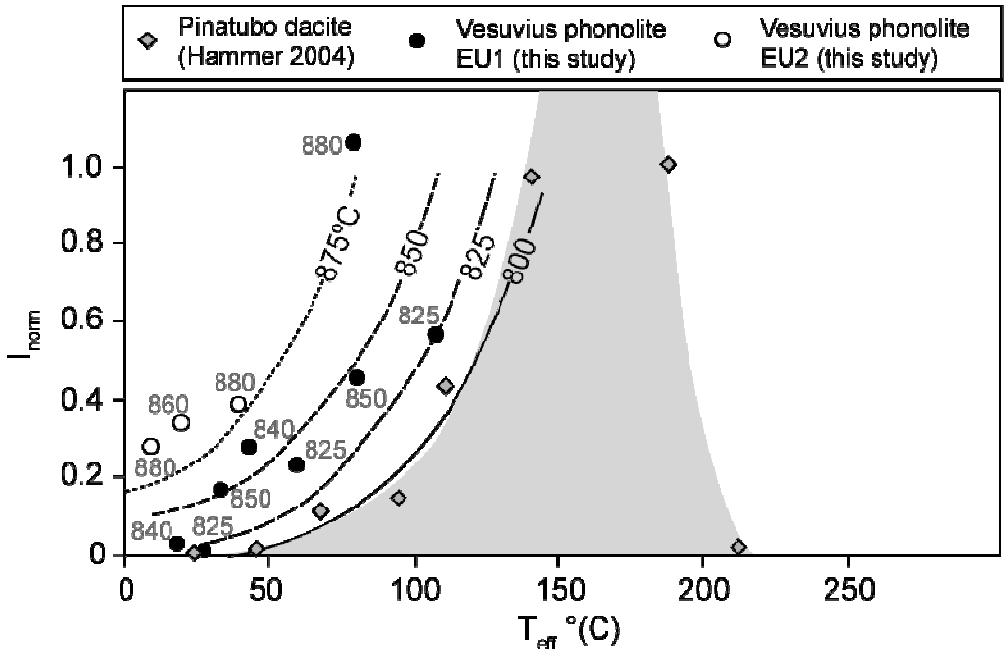

Figure A4: Comparisons between nucleation rates in Vesuvius phonolites and Pinatubo dacites (Hammer and Rutherford, 2002). EU1 and EU2 experiments are black and empty circles respectively and curves corresponding to 4 different isotherms (800, 825, 850, and 875ºC) obtained using the CNT formulations (Eq. 3) are drawn. Pinatubo data are reported as gray diamonds and the best-fit as a light gray field (from Hammer, 2004). Because plagioclase in Pinatubo dacites has higher nucleation rates than those calculated for Vesuvius leucites, rates have been normalized to the maximum. Curve shapes between Vesuvius EU1 leucites and Pinatubo plagioclase are similar and temperature changes only produce shifts along the x-axis. In most cases, leucite nucleation rates might reach their peak earlier than those of plagioclase, but this may be merely a function of temperature.

CHAPTER 3. TEXTURAL STUDIES OF VESICLES IN VOLCANIC ROCKS: AN INTEGRATED METHODOLOGY

Published in its present form as Shea, T., Houghton, B.F., Gurioli, L., Cashman, K.V., Hammer, J.E., Hobden, B.V. (2010), Journal of Volcanology and Geothermal Research, 190, 271-289. doi: 10.1016/j.jvolgeores.2009.12.003

Abstract

Vesicles in volcanic rocks are frozen records of degassing processes in magmas. For this reason, their sizes, spatial arrangements, numbers and shapes can be linked to physical processes that drive magma ascent and eruption. Although numerous techniques have been derived to describe vesicle textures, there is no standard approach for collecting, analyzing, and interpreting vesicular samples. In this chapter, I describe a methodology for techniques that encompass the entire data acquisition process, from sample collection to quantitative analysis of vesicle size and number. Carefully chosen samples from the lower, modal and higher density/vesicularity endmembers are characterized using image nesting strategies. We show that the texture of even microvesicular samples can be fully described using less than 20 images acquired at several magnifications to cover efficiently the range of existing vesicle sizes. A new program (FOAMS) was designed to perform the quantification stage, from measurement of vesicles to distribution plots. Altogether, this approach allows substantial reduction of image acquisition and processing time, while preserving enough user control to ensure the validity of obtained results. We present three cameo investigations — on basaltic lava flows, scoria deposits and pumice layers — to show that this methodology can be used to quantify a wide range of vesicle textures, which preserve information on a wide range of eruptive conditions.

1. Introduction

Volcanologists use the textures of volcanic rocks to identify processes occurring before, during and immediately after eruption of magma (e.g., Sparks, 1978; Houghton and Wilson, 1989; Cashman and Mangan, 1994). Vesicles in pyroclasts and lava flows document processes of gas exsolution, expansion, and escape that drive most volcanic eruptions. Gas exsolution is controlled by magma decompression and consequent changes in volatile saturation conditions (e.g. Papale et al., 1998). The relative rates of bubble nucleation and growth control primary vesicle textures. Nucleation and growth rates are determined by both intensive magma properties (e.g. initial volatile content and melt viscosity) and extensive properties (e.g., magma ascent rate, fragmentation and quenching). These primary textures may be further modified by bubble deformation, coalescence, expansion, or gas escape (e.g. Sparks, 1978; Cashman and Mangan, 1994, Klug and Cashman, 1994; Toramaru, 1995; Simakin et al., 1999; Klug et al., 2002; Polacci et al., 2003; Gurioli et al., 2005b; Allen, 2005; Piochi et al., 2005; Sable et al., 2006; Adams et al., 2006; Noguchi et al., 2006; Mastrolorenzo and Pappalardo, 2006; Lautze and Houghton 2007; Cigolini et al., 2008). Quantification and interpretation of vesicles have been important research topics in volcanology. However, diverse methodologies have been used to describe vesicle textures. As a result, comparisons between different studies have been hindered by differences in approaches to sampling and textural quantification. Here we present an efficient and accurate strategy for acquiring textural information from vesicular samples. We describe field sampling protocols, sample processing methods, and image acquisition and rectification techniques that employ a new Matlab-based program named “FOAMS” (Fast Object Acquisition and

Measurement System). FOAMS allows calculation of parameters that describe the spatial arrangement, as well as the size and number of vesicles in volcanic samples. Key input parameters are evaluated and tested on three examples (Makapuu lava flow, Hawaii; scoria from Villarrica, Chile; and pumice from Vesuvius, Italy), where the methodology is applied to textural characterization of samples generated by very diverse eruption styles.

2. Background

The following sections summarize the different approaches to characterizing textures in volcanic rocks and the ways in which they are commonly represented graphically.

2.1. The 3D approach: X-ray microtomography

In recent years, X-ray microtomography (XRCMT) has been increasingly applied to texture characterization in volcanic rocks. This technique allows the imaging of tens to hundreds of slices through a rock sample in a relatively short time interval. The obtained 2D slices are then merged to create a 3D representation of the sample. While Ketcham and Carlson (2001) and Ketcham (2005) introduced the many uses of XRCMT in geology, Proussevitch et al. (1998) were the first to apply XRCMT to vesicles in Hawaiian basalts. Only recently has the technique been widely applied, as Song et al. (2001) examined basaltic scoria and Polacci et al. (2006, 2009) studied scoria and pumice samples from Stromboli, Villarrica and the Campanian Ignimbrite. Polacci et al. (2008, 2009) also provided an example of how connectivity as measured by tomography can be

used to infer outgassing during ascent of Strombolian magmas. Okumura et al. (2006, 2008) exploited the ability of XRCMT to successfully measure vesicles that may be significantly deformed by shearing, and derived permeability values for rhyolitic magmas under various stress conditions. Currently, XRCMT is possibly the only viable technique to study sheared and deformed samples adequately, especially in terms of measuring key parameters such as permeability (e.g., Wright et al., 2006). Unfortunately, the technique is still not able to resolve very thin glass walls present in pumice (Song et al., 2001; Bai et al., 2008), and typically, the smallest measured objects are within the range of 10–70 µm (Gualda and Rivers, 2006; Proussevitch et al., 2007b, Degrutyer et al., 2010), which is acceptable for basaltic lavas and some scoria samples but not for pumice. Thin glass walls can be lost during imaging, and unconnected objects merged. This in turn increases apparent permeability and vesicle interconnectivity (Song et al., 2001), and causes discrepancies in vesicle number densities (N_V, mm^{-3}): for instance, Polacci et al. (2006) found N_V in the range of 10^3–10^4 mm^{-3}, about an order of magnitude smaller than values that were measured in these samples by 2D imaging and conversion to 3D (Polacci et al., 2003). In addition, reconstruction of broken or missing glass walls is much more challenging in 3D and requires automated wall reconnection routines (e.g. Shin et al., 2005) with the assumptions they entail that cannot offer the same amount of user control than in the context of 2D. Thus, while XRCMT techniques are improving and are able to resolve smaller and smaller objects, there is still a need for other robust textural characterization methods that are applicable to all sample types, from vesicle-poor lava flows to pumice and reticulite.

2.2. The 2D approach: Stereology

Studying textures in thin sections creates 2D data that ignore how particles are configured in the third dimension. Because sections through polydisperse objects are not likely to be cut routinely through their largest area (cut-effect), and since smaller objects have a lower probability of being intersected than larger ones (intersection probability), raw data from 2D images have inherent flaws. The assumption that cross-sections through particles can be used to quantify size and distribution is all the more erroneous when particles are elongate. To correct for these problems, statistical techniques to convert 2D areas into equivalent volumes were formulated early on and applied to particulate materials (e.g. Saltikov, 1967; Underwood, 1970). More recently, substantial progress has been made towards building models that account for intersection probabilities, cut-effects and variations in shape (e.g. Sahagian and Proussevitch, 1998; Higgins, 2000; Mock and Jerram, 2005; Morgan and Jerram, 2006).

In the methodology presented herein, the conversion method of Sahagian and Proussevitch (1998) is used to generate corrected vesicle size and number distributions. Their technique consists of calculating the number density of objects in given size classes (1 to i) per unit volume (N_V in mm^{-3}) by successive iterations of the number density of larger objects (N_{V1}, N_{V2}, N_{V3}, …N_{Vi}) assuming spherical geometry. The main advantages of this approach are that it is fast and does not require extensive computation. Geometric binning is employed instead of linear binning since it is more appropriate for particle sizes that are distributed over several orders of magnitude. Geometric bins allow for a much better representation of the smaller size populations, which tend not to be resolved by linear bins (Proussevitch et al., 2007a).

A major issue with this method is that it does not account for elongate shapes, since cross-section probabilities for elongate objects cannot be expressed analytically. On the other hand, assuming a given aspect ratio for vesicles implies that some process has caused them to deform uniformly (i.e. deformation is constant throughout the sample). This is the major reason why this methodology cannot be easily applied to rocks whose vesicles are intensely sheared (e.g. fibrous or tubular pumice). For the study of pyroclasts that suffered little to no shearing or did not preserve shearing textures, the spherical assumption often holds true since bubble relaxation inherently favors equal distribution of stresses at the bubble-melt interface (Rust et al., 2003). In pumice, vesicles frequently show no preferential direction of elongation or a unique aspect ratio applicable to the entire population and, though spheres may poorly define these vesicles, a set of ellipsoids with defined aspect ratios may be less accurate.

2.3. Texture representation

Because each type of distribution plot possesses its own advantages and caveats, they are all displayed and compared whenever possible. Four types of distribution plots, along with visual (i.e. texture imaging), quantitative (i.e. computation of vesicularity, total vesicle number density, and modal/mean size) and, to a lesser extent, shape data, form the end-products of the methodology presented in this contribution.

Vesicle size and number analysis: during magmatic ascent, bubbles in magma nucleate and grow as volatiles are exsolved. The final number density and size distribution of bubble populations in a volcanic rock erupted at the surface depends not

only on the available volatile concentrations, but also on the ability of this volatile phase to diffuse through the melt, as well as the time available for expansion (i.e., time spent by magma in the conduit and/or at the surface) (Toramaru, 1995; Lyakhovsky et al., 1996; Proussevitch and Sahagian, 1996). Hence, investigating vesicle sizes and numbers can prove invaluable to characterizing storage, ascent and eruption conditions (e.g. Klug and Cashman, 1994). Vesicle number densities per volume N_V (or per melt volume N_{Vcorr} when corrected for vesicularity and pre-vesiculation crystals) are typically higher in explosive eruptions than in effusive eruptions (Toramaru, 1990; Cashman and Mangan, 1994; Toramaru, 1995; Mangan and Cashman, 1996; Polacci et al., 2001; Sable et al., 2006). The tendency of N_V to increase with eruption intensity has been experimentally and numerically linked to the dependence of N_V on decompression rate, and on other properties such as diffusivity, viscosity and surface tension (Mangan and Sisson, 2000; Mourtada-Bonnefoi and Laporte, 2002, 2004; Lensky et al., 2004; Toramaru, 2006, Namiki and Manga, 2006; Cluzel et al., 2008) . Hence, N_V is expected to scale with SiO_2 content (e.g., Sable et al., 2006) and physical eruption parameters such as magma discharge rate or column height (e.g., Gurioli et al., 2008). As a consequence, obtaining accurate measurements of both vesicle size and number is crucial if valid physical comparisons are to be made between different eruptions.

Because vesicles vary significantly both in size and in number, textural data are always displayed as distributions. The four most recurrent plots in the size distribution literature are used either to display vesicle volume information (vesicle volume distributions VVD and cumulative volume distributions CVVD), or number of vesicles per class size information (vesicle size distribution VSD and cumulative size distributions

CVSD). Fig. 1 displays examples of the four categories, as well as examples of the processes that may contribute to generating or modifying them.

VVDs are generally used to infer the nature of nucleation and/or coalescence events during the vesiculation history of pyroclasts (Fig. 1a) (e.g. Klug and Cashman, 1994). Typically, each mode is interpreted to illustrate a distinct pulse of nucleation and growth (Klug et al., 2002; Polacci et al., 2003; Lautze and Houghton, 2007); coalescence tends to skew the data positively or even produce a distinct larger mode (Gurioli et al., 2008; Adams et al., 2006), ripening produces a negative skewness (Mangan and Cashman, 1996), and bubble collapse dramatically reduces total vesicle volume fraction and modal size (Burgisser and Gardner, 2005; Sable et al., 2006).

CVVD plots are complementary to VVD as they provide essential knowledge about the contribution of each size range to the total vesicularity (Fig. 1b). A unimodal distribution produces a sigmoid-shaped curve, multiple modes add bulges to the curve, coalescence tends to reduce the slope of the upper portions of the sigmoid, ripening shifts the curve to the right and accentuates the lower portion of the curve, while collapse likely results in a curve shifted towards smaller sizes, with lessened contribution of large vesicles (Klug et al., 2002, Adams et al., 2006, Mongrain et al., 2008). Apart from basic statistics such as modes, means and standard deviations, no true quantitative data can be extracted directly from VVD or CVVD plots.

VSDs (or ln(n) vs. L plots, with L equivalent diameter in mm) are used commonly to infer kinematics of nucleation density and growth rate of crystals or bubbles (e.g. Marsh, 1988, 1998). According to Mangan and Cashman (1996), linear distributions denote steady-state nucleation and growth while an upward inflexion towards smaller

sizes reflects ripening processes and a downward inflexion towards larger objects may be caused by coalescence (Fig. 1c). In turn, bubble collapse may produce a curve that plunges rapidly in the larger size classes. Hypothetically, if the data within a VSD plot follows a linear trend, growth rates (G, mm s^{-1}) can be determined from the slope of the curve and initial number density (n_0, mm^{-3}) calculated from the intercept at L=0, providing that some constraint exists on the time scale for nucleation and growth (τ). From the latter parameters, it is then possible to obtain nucleation rates (J, mm^{-3} s^{-1}). If no time constraint exists, only the total vesicle number density (N_{tot} in Mangan and Cashman, 1996; written N_{Vfit} herein to describe better its origin) and dominant diameter L_{Vfit} can be derived from the slope (see Appendix B for a brief summary of formulations).

CVSDs (or log(N_V>L) vs. log(L) plots) make use of population number density, and consider the number of objects per cubic mm with diameter greater than L. Gaonac'h et al. (1996, 2005) and Blower et al. (2001, 2002) developed the idea that power-law distributions could better accommodate certain types of vesicle size distributions produced by continuous/accelerating nucleation (i.e. data generating curves on VSD plots). Possible curve trends associated with various processes are illustrated in Fig. 1d, and important formulations are reported in Appendix B.

Vesicle shape analysis has two major functions: first, it may provide information about the sphericity of objects (which in turn serves to validate or refute the assumption used for stereological conversion) and the geometry of the bubble-melt interface (i.e., whether vesicle walls form a simple sphere/ellipsoid or whether their interfaces are complex).

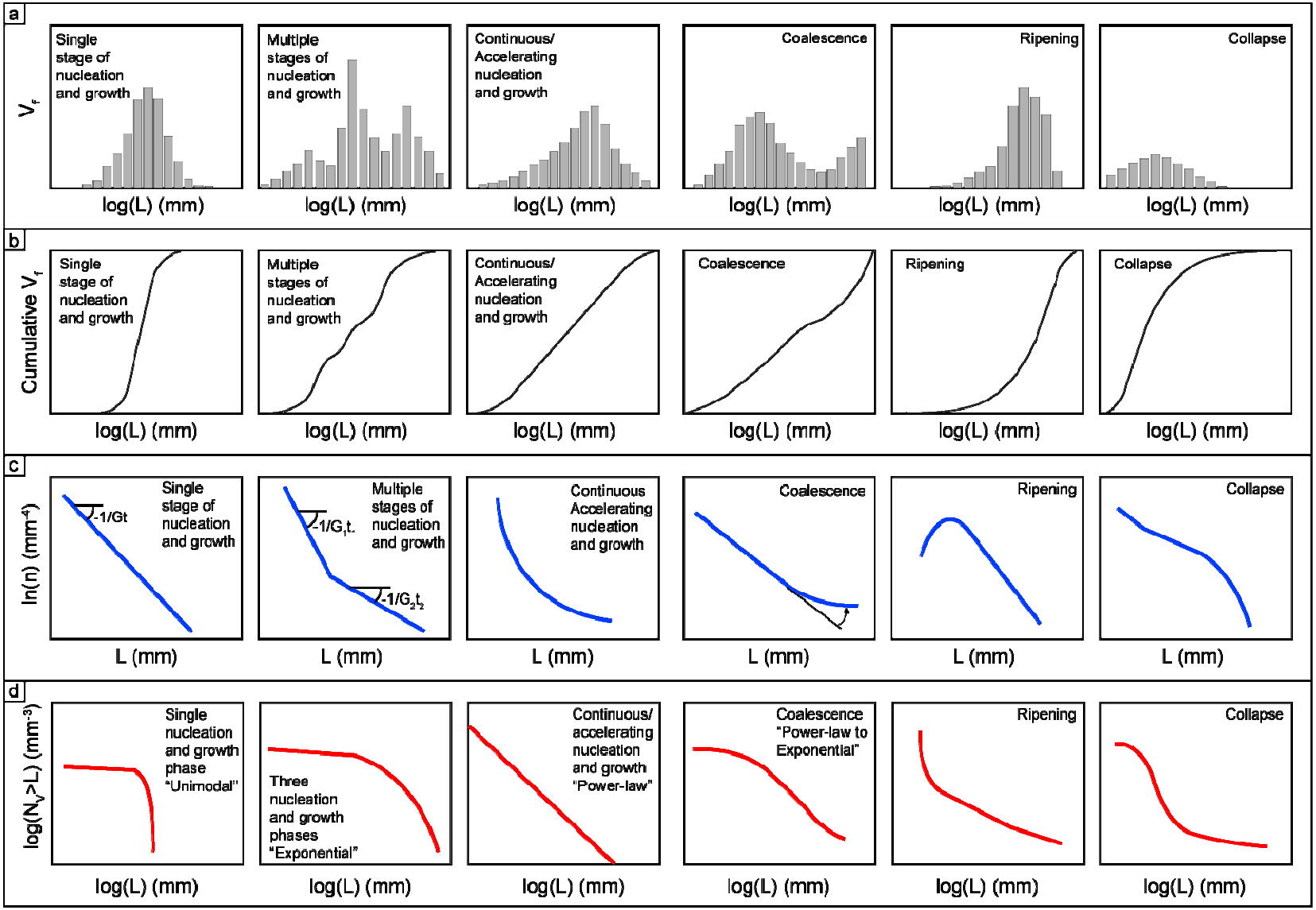

Figure 1: Various ways to display textural characteristics through size (L) and number density (n or N_V) plots, and processes that they may be associated with (single or few nucleation events, multiple nucleation and growth events, continuous nucleation and growth, coalescence, ripening, and collapse).

Several factors control whether bubbles will be preserved as spheres within a given sample, related to the timescale available for relaxation (e.g. Namiki and Manga, 2006). Providing bubbles have insufficient time to relax and minimize their surface energy, simple or pure shear may cause vesicles to be elongated (Hon et al., 1994, Rust et al., 2003), and coalescence may produce complex polylobate shapes (Klug et al., 2002; Polacci et al., 2003). Bubble collapse (Adams et al., 2006; Mongrain et al., 2008) and significant groundmass crystallization (Klug and Cashman, 1994; Sable et al., 2006) result in increasing interface complexity. Hence to fully characterize vesicle shape within volcanic rocks, two main parameters are needed: a "roundness" parameter that determines whether the vesicle has a shape closer to a circle or an ellipse, and a "complexity" parameter that measures the tortuosity of vesicle outline (Appendix C).

3. Methods

The leitmotiv behind proposing a standardized methodology lies in improving the possibilities of comparing datasets from various eruptive settings. To ensure that the textural data that is being used to infer eruptive processes is robust, sampling and sample processing need to be approached rigorously. The following paragraphs contain suggestions for field sampling, vesicularity/density determination, sample imaging (strategies of image acquisition and rectification), as well as brief description of the stereological conversion technique utilized herein.

3.1. Field sampling

Two types of samples are generally collected from the field in physical volcanology: pyroclasts such as pumice, scoria, volcanic bombs, reticulite, or Pele's hairs and tears, and more competent rocks from welded falls or pyroclastic density current deposits (PDC), lava flows, dykes and domes emplaced effusively.

Sampling of pyroclasts (fall, PDC, or ballistics) is typically conducted at well constrained proximal sites, once the physical and chemical characteristics pertaining to the eruptive layer and their spatial variations have been thoroughly investigated. For impulsive discrete explosions (Vulcanian and Strombolian explosions) clasts are collected from the deposits of single explosions (e.g. Lautze and Houghton, 2007; Gurioli et al., 2008). For pumice and small scoria from more prolonged Hawaiian through Plinian explosions, over 100 juvenile clasts of diameter 16-32 mm are collected over a narrow portion of the stratigraphic unit (Houghton and Wilson, 1989; Gurioli et al., 2005b). Where the juvenile clasts within a deposit are unusually diverse the sample size is increased to more than 200 clasts to adequately categorize the endmember textures (Polacci et al., 2003). Such a large number of clasts within the eruptive unit ensures that both the low and high end of the vesicularity range are adequately sampled (Houghton and Wilson, 1989). In the case of a fall deposits, typically a stratigraphic range of 1-3 clast diameters in thickness is selected to minimize the eruption interval that is sampled. Larger pyroclasts such as bombs are sampled individually to look for significant textural variations from core to rim, thus several thin sections are made from different internal domains within each bomb (e.g. Wright et al., 2007).

When more competent eruptive units such as lava flows (e.g. Cashman et al., 1994), welded pyroclastic deposits (e.g. Carey et al., 2008), dykes/sills or domes are sampled, several portions are usually broken from or cored through the unit in order to capture textural variations. In the case of competent rocks, it is recommended to take samples as large as 20 cm in diameter, small enough to be scanned. At even larger scales, Polacci and Papale (1997) illustrated that textural quantification can be achieved within meter-sized outcrops using reconstructive photography in the field.

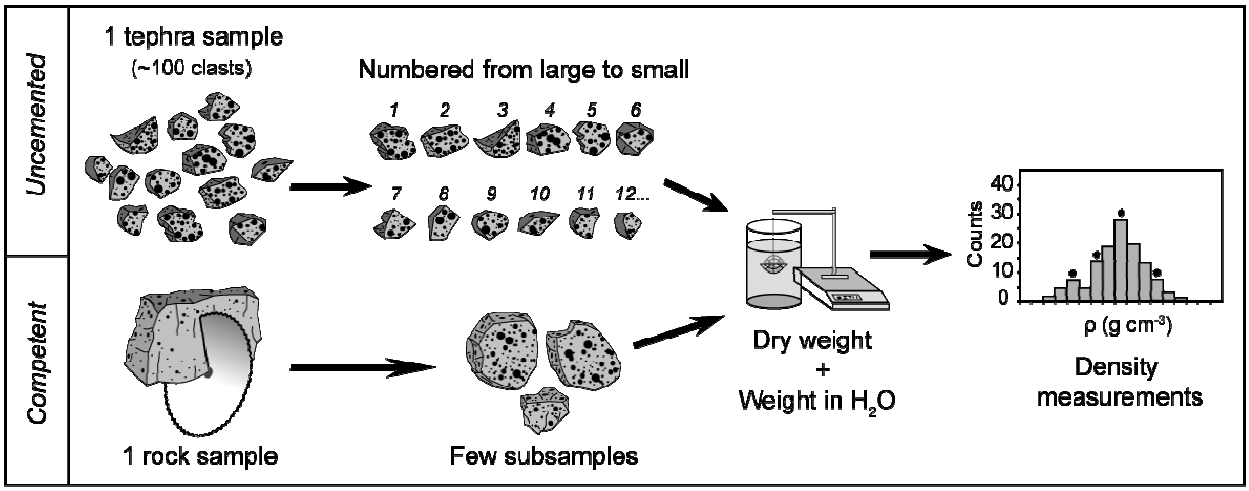

Figure 2: Illustrative cartoon of sampling procedure and density measurements.

3.2. Density/vesicularity measurements, thin sections

Prior to performing density measurements, collected samples are cleaned and dried at T>100ºC for 24 h. For pumice or scoria samples, a subset of clasts is usually ranked by decreasing size and numbered from 1-100 (Fig. 2). For other specimens, especially large ones, the rock is cut into halves, one half being kept for scanner imaging and the other

serving for density measurements and microscopic imaging. Within the half kept for density, several subsamples corresponding to distinct textural units are carefully removed (Fig. 2). If the sample is homogeneous, no further subdivision is required, provided that its size is large enough for weighing in the laboratory.

The density measurement methods described here are derived from Houghton and Wilson (1989). Clasts or sample subsets are weighed in air (mass ω_{AIR} in g), and either individually wrapped in polyethylene film (of wet weight ω_{WATER}^{film}), or made impermeable using water-proofing spray. They are then weighed while immersed within water (ω_{WATER}). Specific gravity, and thereby density is expressed as:

$$\rho_{BULK} = \frac{\omega_{AIR}}{\omega_{AIR} - \left(\omega_{WATER} - \omega_{WATER}^{film}\right)} \quad \text{(Eq. 1)}$$

For buoyant particles, e.g., pumice, the clasts are forced down using a ballast of known wet weight and volume.

Finally, the dense rock equivalent (DRE) density of the magma is used to obtain porosity (ϕ) or vesicularity ($\phi \times 100$):

$$\phi = \frac{\rho_{DRE} - \rho_{BULK}}{\rho_{DRE}} \quad \text{(Eq. 2)}$$

This technique is rapid and yields large arrays of data. Other alternatives include measuring density/porosity directly using a He-pycnometer, yielding both connected and

isolated vesicle fractions (Rust and Cashman, 2004). For pumice and scoria sample data sets, density is plotted on a histogram to choose only a few clasts that represent the different endmembers from the entire distribution (Fig. 2). In this manner, 3 to 8 clasts are typically chosen to represent low (1 to 2 clasts), modal (1 to 4 clasts) and high (1 to 2 clasts) vesicularities. For larger samples from lava flows, domes, bombs and tephra clasts showing substantial internal variability, density/vesicularity measurements are done on the sub-samples prepared for each textural zone. The chosen clasts/subsamples are made into thin sections with, in the case of pumice or reticulite, impregnation with resin to avoid breakage of thin glass walls.

3.3. Image acquisition

The largest vesicle populations can be imaged adequately by a scanner, either using a thin section or the sectioned sample itself. For thin sections, scanners possessing slide illumination functions allow better resolution. Larger magnifications (i.e. higher than 25×) are best mapped through Scanning Electron Microscopy (SEM), in back-scattered electron imaging (BSEI) mode, using chemical contrasts between phases. Before thin sections are carbon coated, it is practical to outline and highlight phenocrysts present on the scanned image, since their proportions are needed for number density corrections. In cases where the sample is very phenocryst-rich, thin sections can be scanned between two polarized foils, cut perpendicular to each other. This technique allows the operator to observe crystals in distinctive colors, as in an optical microscope (Pioli et al., 2007). The SEM working distance must be set higher for lower magnifications (e.g. 45–50 mm for 25× on a JEOL–5900 SEM) and lower for higher magnifications (e.g. 15–20 mm for

>75×), and contrast/brightness adjusted to obtain the best representation of bubbles and different crystals present in the matrix. This facilitates image processing into inputs for the FOAMS program. Details on additional SEM imaging techniques (e.g. X-ray mapping) can be found in Blundy and Cashman (2008).

3.4. Choice of magnifications

Vesicles in volcanic rocks are typically polydisperse, with sizes that range from microns to centimeters; a single clast may contain vesicles varying in size by 4–5 orders of magnitude (Klug et al., 2002). Characterizing this range of vesicle sizes requires image acquisition over a similar range of scale (e.g., Gurioli et al., 2005b; Adams et al., 2006; Sable et al., 2006; Lautze and Houghton, 2007). Accurate size data (either 2D or 3D) requires a statistically significant number of vesicles to be measured within each size range; this, in turn, requires definition of both the range of magnification needed to cover the range of vesicle sizes, and the minimum number of images per magnification required to sample each size range adequately.

The magnification range is determined by identifying the smallest and largest vesicles within the sample. For the lowest magnification, we use an area that is 1–2 orders of magnitude larger than the largest vesicle. When vesicles are $\leq$ 5mm, a thin section suffices; when vesicles exceed this size, it may be necessary to scan either a rock slab or multiple thin sections. Similarly, the highest magnification has to record the smallest vesicles at a resolution that is sufficient to represent individual vesicles. Fig. 3a shows the minimum number of pixels (in area or equivalent diameter) required to represent an object and the uncertainties associated with any pixel imaging error. For instance, in a 10-

pixel diameter object (~80 pixels in area), misrepresentation of 1 pixel will cause a 1.3% error in the measurement. Alternatively, one imperfectly imaged pixel in an object measuring 5 pixels in diameter (~ 20 pixels in area) will result in a 5% error. Fig. 3b illustrates the errors associated with the choice of minimum equivalent diameter (in µm) for a range of magnifications. The plot is used as follows: through preliminary observation (SEM or petrographic microscope), an estimate of the minimum vesicle size within samples is made. In Fig. 3b, if a 1 µm-large equivalent diameter was adequately represented by 7 pixels in area (3 pixels equivalent diameter) a maximum magnification of around 300× could be used. The uncertainty associated with one misrepresented pixel is however very high (~14%), resulting in large errors in the size distribution. A better alternative is to have a minimum area of either 80 pixels (10 pixel equivalent diameter) to ensure ~1% error or 20 pixels if the researcher accepts a larger 5% error, and choose the corresponding maximum magnification at 500×. The purpose of this choice is to ensure that the smallest vesicles are imaged adequately while minimizing the number of images to process. Very high magnifications will result in better resolutions but require many images to enclose the same number of the smallest vesicles. As we argue in the following section, a minimum of 10 of the smallest vesicles needs to be measured at the highest magnification (excluding edge vesicles) to define the size threshold and maximum magnification used. Intermediate magnifications should be chosen so that substantial vesicle size overlap occurs between each set of magnifications.

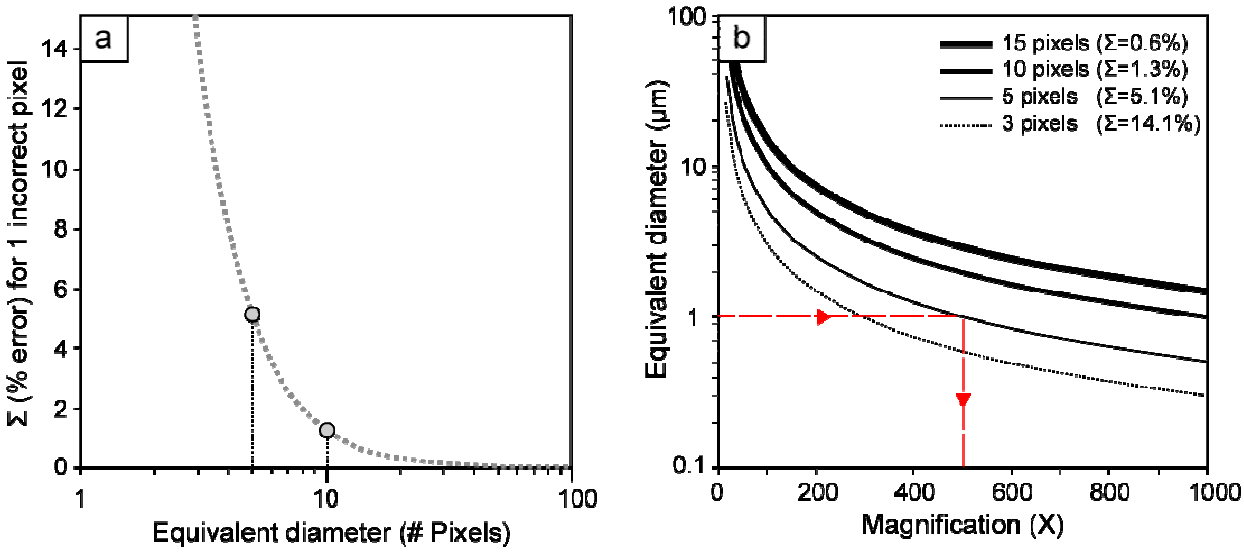

Figure 3: Resolution and magnification within imaging techniques. (a) Influence of minimum diameter. The dashed gray curve illustrates the error Σ (right y-axis) associated with misrepresentation of 1 pixel in area within a vesicle. (b) Minimum vesicle diameter measurable for various magnifications. If vesicles as small as 1 micron in diameter are present within the sample and need to be imaged, maximum magnifications of 500× are sufficient assuming a resolution of 5 pixels minimum per vesicle (arrowed dashed line).

3.5. Imaging strategy

As the area encompassed by a single image scales inversely with its magnification, the number of images needed to capture heterogeneities increases with decreasing feature size. To determine the sensitivity of the vesicle size data to the sampling strategy used, we compare data from: a 73-image grid strategy (one thin section, 24 images at each of three magnifications), a 25-image grid strategy (one thin section, 8 images at each of three magnifications), and a 15-image nest strategy (one thin section, increasing number of images at each of three magnifications) (Fig. 4). The grid strategy is similar to point counting and ensures that areas are sampled irrespective of the operator decision-making process. However, this strategy is time-consuming and may result in sampling areas

containing few or no small objects. Less time-consuming approaches include imaging 8 frames instead of 24 at each magnification (25-image nest strategy, Fig. 4b) or increasing the number of images with magnification (15-image nest strategy, Fig. 4c). These user-defined methods have the advantage of saving time but place the burden of assessing textural heterogeneity on the operator, thus introducing potential for operator-induced bias. We introduce the term Image Magnification Ratio (IMR) to designate the number of images acquired within each subsequent nest. In all grid techniques, IMR=1:1, whereas in the nested strategy, IMR>1:1. The choice of IMR values does not need to remain constant throughout the series of nests; it should promote both minimization of number of images to 20 or less as well as preservation of enough surface area to adequately represent each vesicle size range.

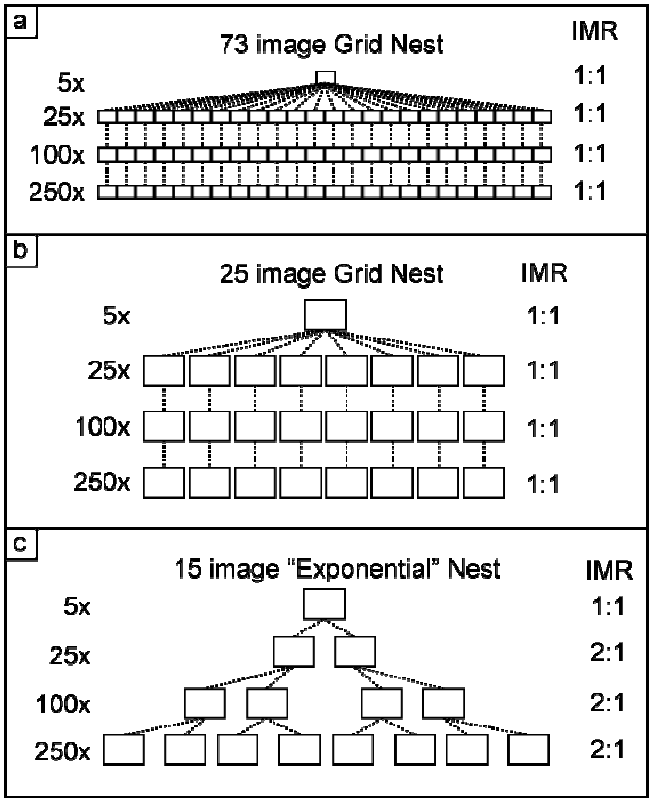

Figure 4: The three tested imaging strategies; (a) a 73 image grid nest, with one image randomly chosen within the previous magnification, (b) a 25 image grid nest of similar configuration, and (c) an example of exponential nesting, where each magnification possesses twice as many images than the previous one and chosen nests are not randomly located within each magnification. IMR: Image Magnification Ratio.

To test the relative accuracy of the three strategies, we compare the measured number density of vesicles (N_A, mm^{-2}) in a pumice sample with a wide vesicle size range that required four different magnifications. Largest vesicles were around 5 mm, thus the lowest magnification was chosen at 5× (entire thin section). Smallest vesicles measured about 5 μm, hence the largest magnification needed was around 250× (Fig. 3). Intermediate magnifications were 25× and 100×to allow sufficient size overlap between images. Fig. 5 shows that the 72-image and 25-image grid techniques produce fairly smooth decreases in number density with increasing vesicle size.

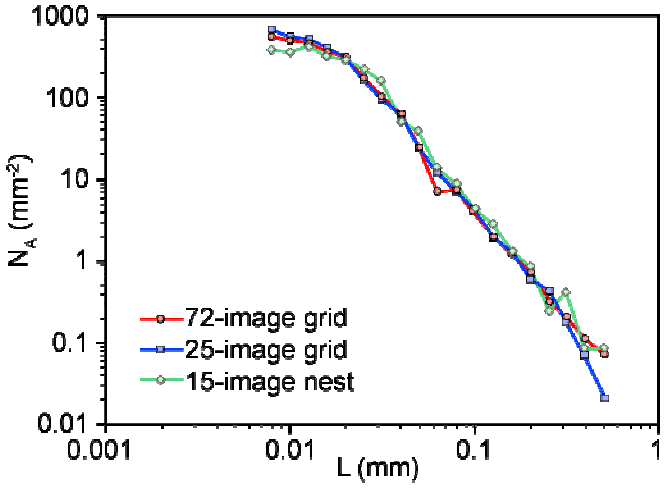

Figure 5: Number of objects per melt area for different size classes measured within pumice samples from Taupo for each of the three imaging strategies. Note the good overall correspondence between the obtained curves which allows reducing the number of images required to adequately represent the sample overall.

Number density data from the 15-image nest are somewhat noisier but still allow adequate characterization of size distributions. From this simple comparison between imaging strategies, we calculate that for a 15-image nest to adequately represent the small vesicle population (i.e. for the 15-image and the 72-image strategies to have indistinguishable N_A vs. L curves at L<0.05 mm), a minimum of 10 vesicles per image at the largest magnification must be counted (here 80 vesicles minimum for 8 images at

250×). The actual number of images used in any given nesting strategy depends on the vesicle size range and the sample heterogeneity. If both very small and very large vesicles are present and the sample displays substantial textural variations, then additional series of images are usually captured. Conversely, when samples are homogeneous and characterized by a narrow size range, fewer image nests are needed.

3.6. Image rectification

To reduce the amount of time spent performing these corrections, a detailed methodology that provides step-by-step guidelines on how to standardize and accelerate image rectification using readily available software is made available (http://www2.hawaii.edu/~tshea). Several factors are responsible for making image rectification time-consuming: first, vesicle walls in pumice or scoria clasts are often thin and may not be entirely resolved by the imaging instrument. Moreover, such walls can be destroyed as thin sections are made, and may end up as fragments within vesicles (Fig. 6a). Thus, broken walls need to be reconnected and loose fragments have to be deleted from the vesicle area. Secondly, cross-sections that have a 3D-like texture when viewed through the SEM (Fig. 6b) also require corrections. Lastly, and most importantly, imaged features (glass, vesicles, and crystals) never have truly homogeneous grayscale levels but show a spectrum of shades. Since FOAMS identifies objects based on their grayscale level, all counted features of a given type have to have uniform grayscale values (Fig. 6c). The amount of time spent preparing images will depend on the quality of the thin section, the fragility of the sample, the quality of the images (i.e. instrument), and on the number of magnifications needed to cover all vesicle size ranges.

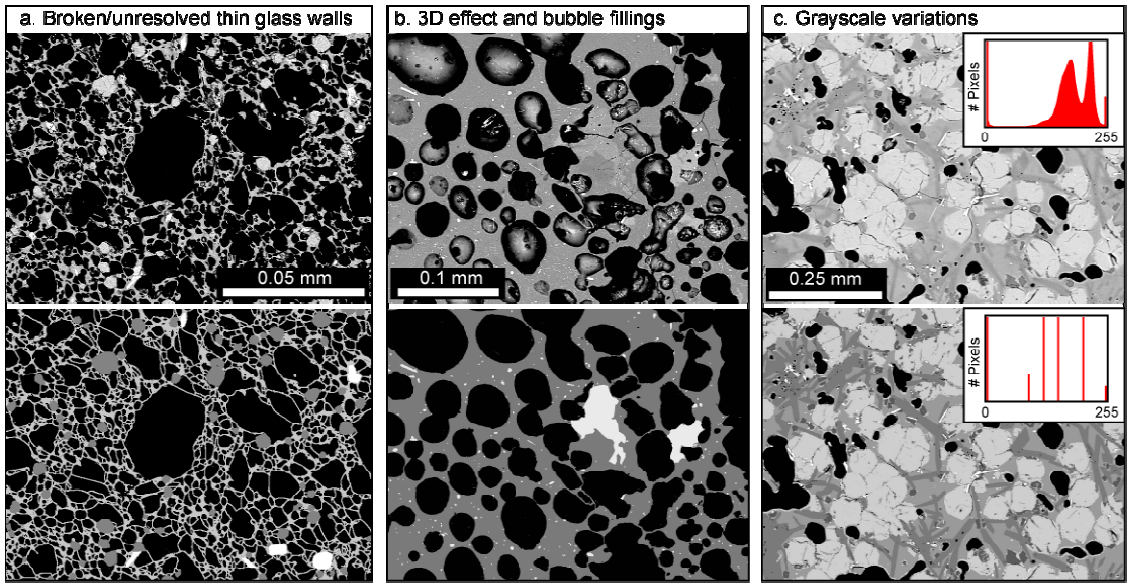

Figure 6: Common issues with SEM images obtained from thin sections (top), and grayscale image resulting from repairing and processing each image (bottom). (a) Vesuvius 79AD EU2 sample showing a significant amount of broken glass walls as well as extremely thin ones. (b) 3D effect caused by intersecting small objects within a somewhat thick section, and broken glass and crystal fillings within some vesicles. (c) Illustration of problems of heterogeneous grayscale variations within raw SEM images (top histogram), and conversion to homogenous grayscale levels after image processing (bottom histogram). For guidelines to avoid grayscale conversion issues, see manual in online additional material.

3.7. Stereological conversion and binning

Although the reader is directed to Sahagian and Proussevitch (1998) for complete details concerning this procedure, the stereological formulations used here are summarized in Appendix A. Their method consists of deriving N_{Vi}, the number density of objects of size i per unit volume from N_{Ai}, the number density per unit area via an expression of the probability of intersecting spheres of given sizes through their maximum cross-sectional area P_i. To obtain N_{Vi} from N_{Ai} (Appendix A), Underwood (1970) introduced a useful parameter called the mean projected height ($\overline{H}_i'$, mm), which represents the mean distance between parallel planes tangential to the object boundary.

For spherical particles, this equates to the characteristic diameter of each size class (L, mm). The diameter is thus used to correct N_A values for intersection probabilities on the basis of the stereological assumption $N_V = \frac{N_A}{L}$ (Underwood, 1970), and then corrected for the cut-effect (see Appendix A) to calculate final number densities ($N_{V\,i}$, mm^{-3}), and the volumes of equivalent spheres (V_i, mm^3). $N_{V\,i}$ and V_i are used subsequently to determine volume fraction for each class (Vf_i):

$$Vf_i = N_{V\,i} V_i \qquad \text{(Eq. 3)}$$

Volume fractions derived from the sum of converted N_{Vi} values are generally less reliable than those one may obtain through direct measurements of vesicularity since the former relies on the assumption of perfect sphericity for each vesicle. To correct for this, Vf_i is normalized to the measured bulk vesicularity of the clast.

Depending on whether bubble growth occurred prior to, during, or after formation of crystal phases in the melt, a number density correction may be needed ("melt-referenced N_V"). A second correction is needed to allow for the volume taken up by the vesicles themselves (e.g. Klug et al. 2002). To obtain N_V corrected for vesicularity (N_{Vcorr}), number density is divided by (1-ϕ). Both crystal and vesicularity corrections are particularly useful if one aims to investigate the actual number of bubbles that nucleated within the melt (Proussevitch et al., 2007a).

3.8. Magnification cutoffs

Overlapping size bins for adjacent magnifications ensures that all vesicle sizes are adequately represented. We illustrate a method of merging data from different magnification images using an example of pumice from Vesuvius (79AD eruption, white magma, EU2 unit; Gurioli et al., 2005b). Pumice clasts contain vesicles of sizes varying between 0.001 and about 4 mm. Four magnifications are chosen to cover this extensive size range, thus four N_A vs. L curves must be merged to generate the final size distribution (Fig. 7a). However, the transition from magnification 2 to 3 is slightly user-biased because most small vesicles were discarded from the second magnification. We have tested three different methods for merging these data. First, we applied arbitrary cutoffs at each new order of magnitude ("Magnitude jumps", Fig. 7b). The resulting size distribution is very irregular, with several apparent modes and sharp jumps between size bins. Second, we imposed a transition that minimized slope differences in the curves ("Minimized slope" in Fig. 7b), an approach that produced a smoother obtained distribution and fewer apparent modes than the first approach. Finally, we defined the shift to minimize the change in N_A values at the shift from one curve to another ("Minimized ΔN_A" in Fig. 7b). This generates smooth size distributions with 2 modes and no sharp bin transitions (Fig. 7b and c). This simple example illustrates the importance of using care when merging data across many image magnifications. The comparison between calculated N_V data shows that values are rather insensitive to merging practices so as long as the smallest (and most numerous) vesicle population is well represented.

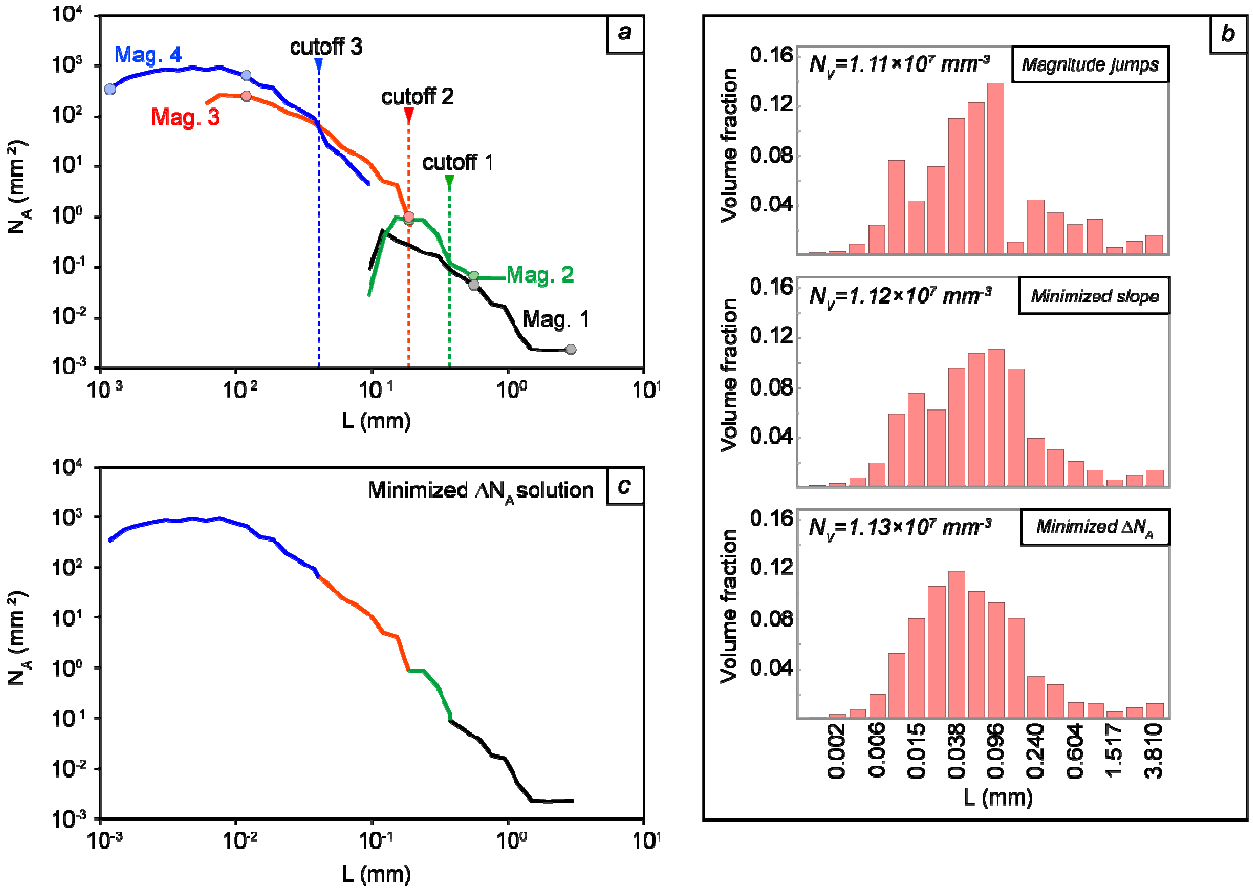

Figure 7: Illustration of the influence of how magnification cutoffs are chosen within a Vesuvius 79AD pumice. (a) A plot of N_A vs. equivalent diameter L for each magnification (1-4) results in decreasing N_A with increasing L for each decreasing magnification. A certain amount of overlap is required for the FOAMS program (or the operator) to choose the best N_A coverage per size range. (b) Vesicle volume distribution histograms resulting from several magnification cutoff trials; the first cutoff technique tested consisted in arbitrarily choosing boundaries at order of magnitude size changes, the second technique involved minimizing slope differences between the N_A curves of two overlapping magnifications (resulting cutoffs reported as round symbols), and the third method minimized N_A changes (resulting cutoffs reported as dotted lines and arrows). (c) The best result for this pumice clast was obtained using the N_A-minimizing method. Notice that there are still some irregularities in the resulting curve.

4. FOAMS: Program structure and mode of operation

4.1. Overview

FOAMS is a Matlab™-based program designed to facilitate the measurement and stereological conversion of objects within a set of one to twenty images. All the details on

the program's structure are available on the web (http://www2.hawaii.edu/~tshea/), and a simple programming flow-chart is given in the additional material. FOAMS uses Matlab™'s image processing toolbox functions and exploits simple user interfaces (GUI) operated using buttons. The function bwlabel allows grouping of objects of similar grayscale level if they are each surrounded by another shade of gray, and the function regionprops is used to measure object dimensions (area A, equivalent diameter L, perimeter p) and find the best-fit ellipse to acquire other important features (long and short axis, orientation). Edge-bordering vesicles are by definition not surrounded by any medium and are thus discarded from the subsequent measurements. Stereological conversion is applied to number density per unit area (N_A) measurements and results are plotted on a second GUI.

4.2. Modus Operandi

A detailed manual is provided with the program, and only a succinct outline is presented here. Once FOAMS is launched, a first GUI ("init") appears (Fig. 8). The user loads anywhere from 1 to 20 grayscale or binary images (number 1 in Fig. 8) all displayed in miniature windows (number 2 in Fig. 8). To allow better visualization, any image can be shown on a larger "active" window (number 3, Fig. 8).

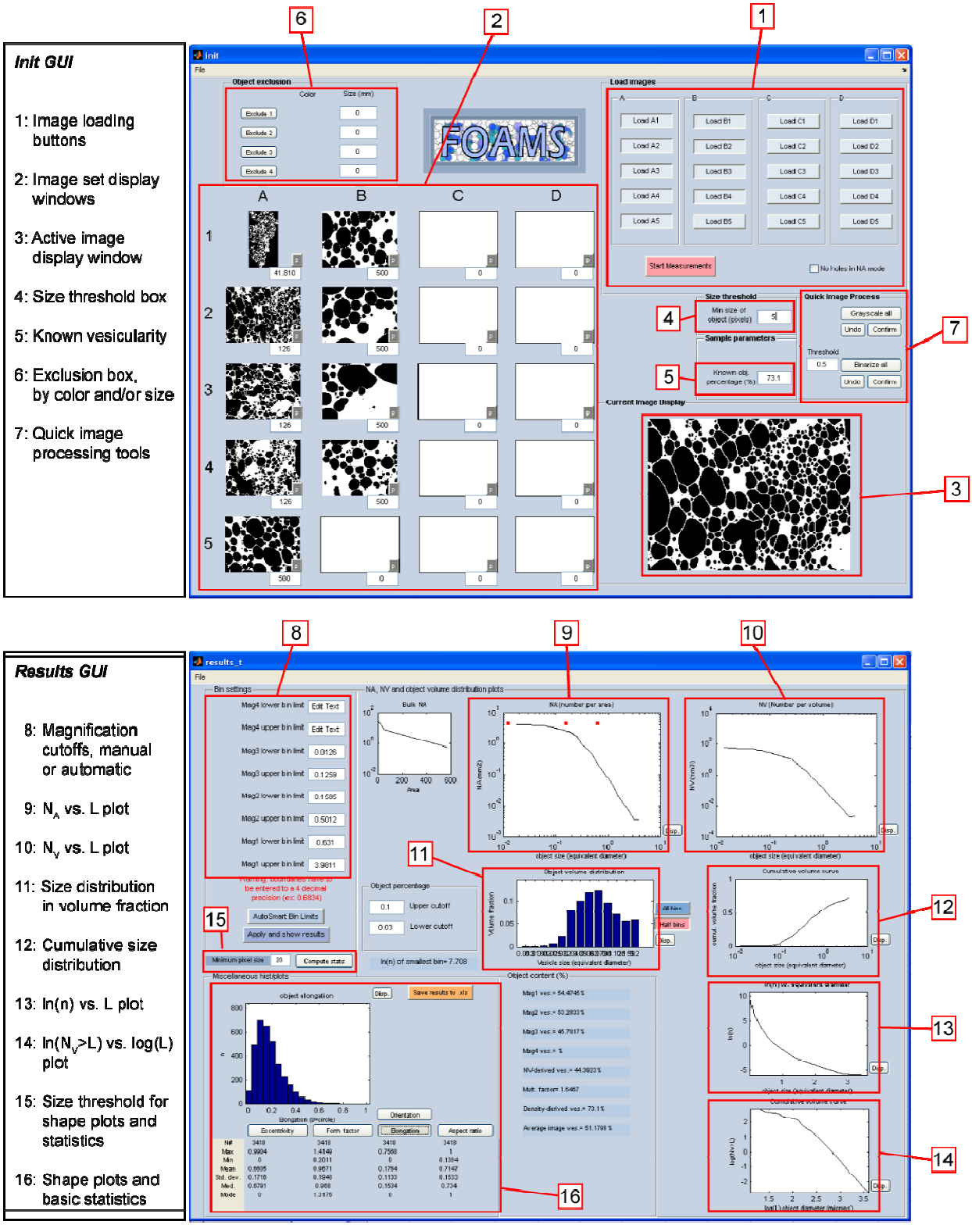

Figure 8: FOAMS "Init" (top) and "Result" (bottom) user interfaces and graphical contents.

Image scales (in pixels per mm) are inserted next to each sub-window, and the minimum diameter (in pixels) that defines the smallest measurable objects is defined by the user (number 4 in Fig. 8). The entered value defines the smallest geometric bin (in diameter units), and each subsequent bin is generated by a simple $10^{0.1}$ multiplication. Because vesicularities derived through stereological conversion may be substantially offset from the density-derived one, the known vesicularity can also be entered (number 5, Fig. 8). Prior to starting measurements, objects that need to be discarded from the analysis (e.g. phenocrysts) can be excluded from the image areas (number 6, Fig. 8) by size or grayscale-value. The quick image treatment tool (number 7, Fig. 8) simply converts all images loaded into FOAMS into grayscale or binary images; however, this is useful only when analyzed objects are homogeneous or when only two clearly distinct phases are present (e.g., crystal-free rock).

When all parameters and images are loaded, a second GUI ("results") appears (Fig. 8). A spreadsheet containing N_A vs. L data ("NA_mag") for each magnification is created and can be used to define better cutoffs. Either FOAMS computes the magnification cutoffs automatically, or the user enters their own (number 8). After stereological conversion, results are plotted within the GUI and new spreadsheets incorporating all measurements, as well as some simple 2D shape statistics, are created.

4.3. Plots and outputs

FOAMS generates a variety of plots and output files that include:

(1) N_A/N_V vs. L plots (Fig. 8, numbers 9 and 10): Raw number density plots are not useful per se for anything more than verification. Since the N_A vs. L plot was constructed

from portions of each magnification (e.g. Fig. 7), there is a risk that the transition from one to the next is not smooth and ideal. This plot allows the user to be critical about how well each size range will be represented, and whether or not some anomalies might be expected in distributions due to abrupt step-like transitions.

(2) Vesicle size distributions are plotted in terms of volume fraction (VVD, Fig. 8, number 11 and CVVD, Fig. 8, number 12), and number densities (VSD, Fig. 8, number 13 and CVSD, Fig. 8, number 14). Because magnification cutoff transitions may not be completely smooth, some unexpected spikes may appear within VVDs. In order to minimize the amount of such noise within the distribution, the number of bins is typically halved.

(3) Data files: All parameters measured and calculated using FOAMS are produced as spreadsheets (Excel® or Text format) for the user's convenience.

(4) Vesicle shape panel (Fig. 8, number 16): In FOAMS, several shape factors have been implemented including roundness parameters such as aspect ratio $AR = \frac{a}{b}$, as well as a new complexity parameter termed "regularity" $rg = \frac{A}{\pi ab}$), where a and b are best-fit ellipse semi-long and semi-short axes respectively, and A is the vesicle area (see Appendix C for more details).

5. Application to natural volcanic rocks

Three volcanic units have been selected to provide comparative examples of products of very different volcanic eruptions and to illustrate how variations within the application of the suggested methodology can affect resulting texture measurements. These three eruptions differ strongly in their volcanic explosivity indices (VEI) and show large contrasts in vesicle number, size, and distribution. Rather than reiterating existing interpretations for these deposits, we focus on how changes in chosen magnifications, magnification cutoffs, and minimum measured bubble diameter can all modify the outcome of the textural characterization procedure. Nonetheless, for context, we provide a brief summary of their volcanological setting as well as previous vesicularity studies.

5.1. Case studies, density measurements

Samples of lava flow units collected near Makapuu point in Oahu, Hawaii (USA) supply an example of vesicle textures in mostly outgassed basaltic lavas (VEI=0). At Makapuu, successions of ‘a’a, pāhoehoe, and transitional lava-flow units were erupted during the formation of the Koolau lava shield, 1.8-2.8 Ma ago (Doell and Dalrymple, 1973). We consider here a transitional unit displaying strong variations in vesicle number, size and arrangement on the scale of a single rock sample (~20 cm long) (Gurioli, unpublished data). The lower section of the samples collected from this unit possesses textural features typical of pāhoehoe, with numerous round vesicles of fairly similar sizes, whereas the upper portion resembles ‘a’a, containing mostly irregular

vesicles of varying sizes. This variation allows us to investigate the influence of merging measurements from across a heterogeneous sample.

The second study is a sample of scoria clasts collected after a Strombolian eruption (VEI=1-2) at Villarrica (Chile) in 2004 (Gurioli et al. 2008).

The third case study comprises a collection of samples from the 79AD eruption of Vesuvius from the first Plinian unit (EU2, Cioni et al., 1992) (VEI=6). These microvesicular clasts are part of an extensive dataset covering part of the 79AD eruptive stratigraphy (Gurioli et al., 2005b) and were chosen due to their relatively simple vesiculation history.

All three sample sets were processed using the guidelines described previously to derive density and vesicularity. Several pieces of Makapuu lava collected from ‘a’a, pāhoehoe and transitional units were sectioned into smaller subsamples, which were then used for density measurements. Although full textural characterization is presented only for a transitional lava, density measurements for ‘a’a and pāhoehoe are also shown in Fig. 9a for comparison. Over 100 clasts of Villarrica scoria and Vesuvius white pumice were used to obtain the density histograms shown in Fig. 9b and c. The average Makapuu transitional lava density is 1780 kg m^{-3}, and modal densities for Villarrica and Vesuvius are 900 kg m^{-3} and 600 kg m^{-3} respectively. Corresponding vesicularities are 38, 66 and 77% respectively. It is worth noting that density histograms can be broadly polymodal (Makapuu and Villarrica) or strongly unimodal (Vesuvius).

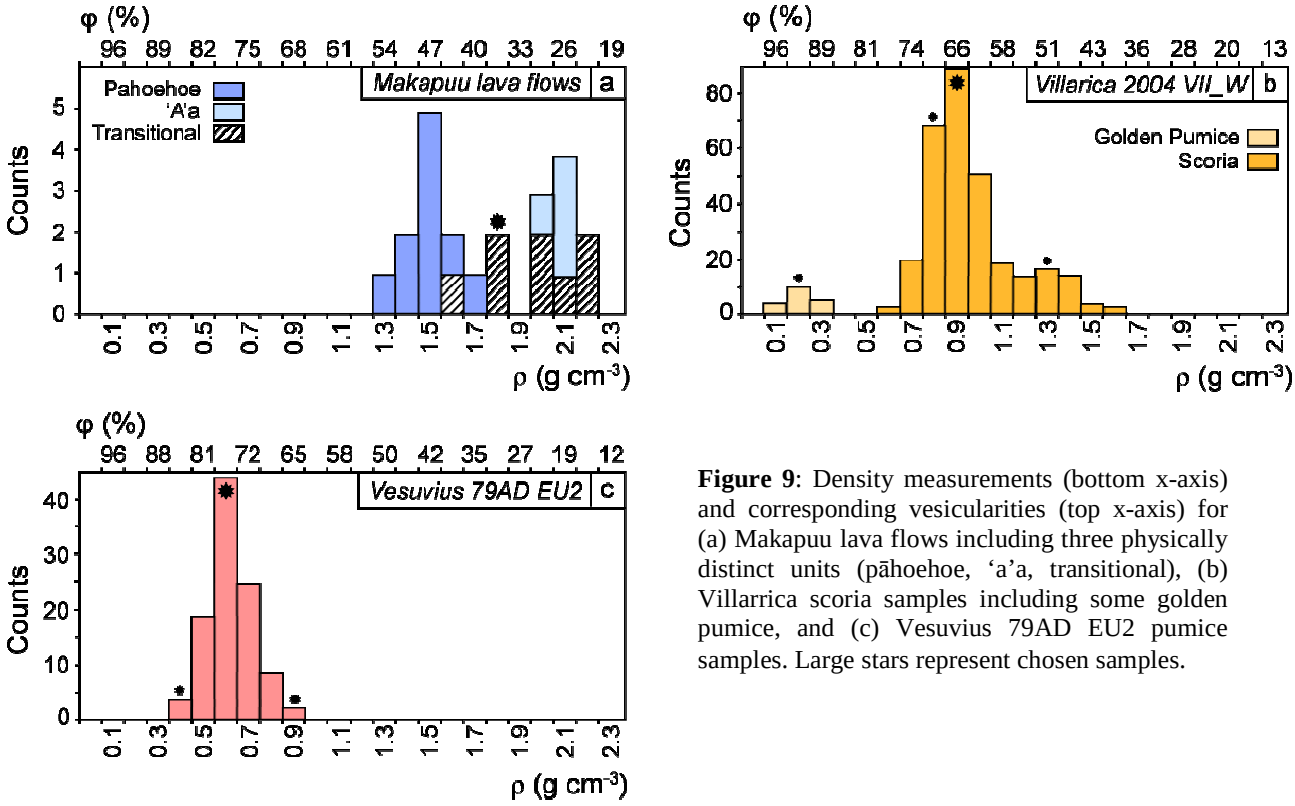

Figure 9: Density measurements (bottom x-axis) and corresponding vesicularities (top x-axis) for (a) Makapuu lava flows including three physically distinct units (pāhoehoe, 'a'a, transitional), (b) Villarrica scoria samples including some golden pumice, and (c) Vesuvius 79AD EU2 pumice samples. Large stars represent chosen samples.

5.2. Contrasting imaging strategies

We used different imaging strategies for the three sample types that reflect differences in the vesicle populations. The smallest vesicles in the Makapuu lava are ~0.1 mm and could be studied at a magnification of 25×, while the largest vesicles of ~ 5 mm required two scan magnifications (slab at 2.5× and thin section at 5×) (Fig. 10a). Measurements of vesicularity, vesicle size, and number distributions were made using the bulk sample (top+bottom) as well as the upper and lower domains individually, to address the issue of heterogeneity within a sample. Thus three magnifications (2.5×, 5×, and 25×) were sufficient to resolve all vesicle sizes; five 25× images within each 5× image allowed sufficient coverage of each textural domain.

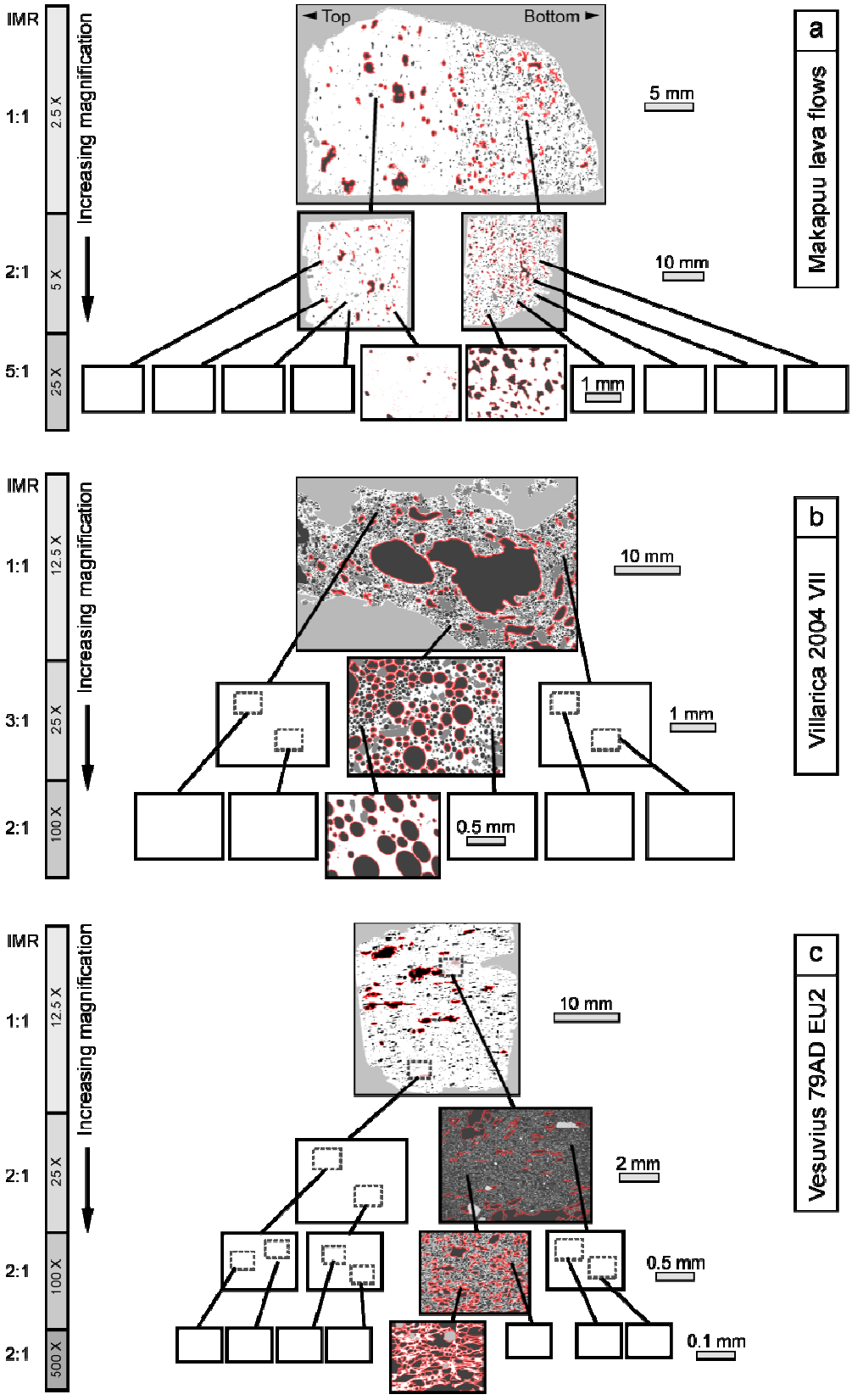

Figure 10: Nested imaging strategies chosen for the three studied eruptions. For Makapuu (a), vesicles cover a narrow size range, only three relatively low magnifications (25× at maximum) are needed. Ten images are selected for the highest magnification used so that IMR=5:1, and one nest is used for each of two distinct textural domains. Villarrica vesicles (b) also cover narrow size intervals, three magnifications are also used. Higher magnifications (100×) are required since smaller vesicles are about 0.01 mm in size. Vesuvius pumice (c) contains vesicles that span several orders of magnitude in size and four magnifications are preferred. The smallest individuals reach 0.001 mm, hence the largest magnification used was chosen to be quite high (500×). In all images, the red outlines depict the vesicles which will actually be measured in each range, after magnification cutoffs are applied.

In contrast, the smallest vesicles (~0.01 mm in diameter) in the Villarrica scoria required a maximum magnification of 100× (Fig. 10b). Thin sections (magnification 5×) were usually big enough to cover the largest enclosed vesicle, (15 mm). Three magnifications (5×, 25×, and 100×) were sufficient to include all vesicles; however, as a nesting strategy we selected three 25× images within the thin section and two 100× within each 25× image (Fig. 10b). This choice was motivated by the fact that vesicles in Villarrica samples span three orders of magnitude (0.01-10 mm) and hence each magnification is equally important to characterize the full textural domain. Finally, highly vesicular white pumice from the 79AD eruption of Vesuvius included vesicles as small as 0.001 mm, while the largest individuals reached around 2-3 mm, thus the vesicle sizes covered a total of four orders of magnitude. A magnification of 500× is required to resolve objects as small as 0.001 mm at an error of 5% for one misrepresented pixel (Fig. 2). Four magnifications were consequently used to embody all vesicles (5×, 25×, 100×, and 500×), and nests consisted of two images within each magnification (i.e. IMR of 2:1 for all magnifications; Fig. 10c).

5.3. Influence of magnification

To test the dependence of resulting size distributions and vesicle number densities on the range of magnifications used, FOAMS runs were completed using contrasting levels of nesting. For Makapuu samples, VVDs of the bottom (“pāhoehoe”) section of the subsample were calculated using two or three magnifications (2.5×, 5×, and ± 25×). Villarrica samples were run using a combination of one to three magnifications from 5× to 100×. Vesuvius EU2 pumice was tested using one to four magnifications (5× to 500×).

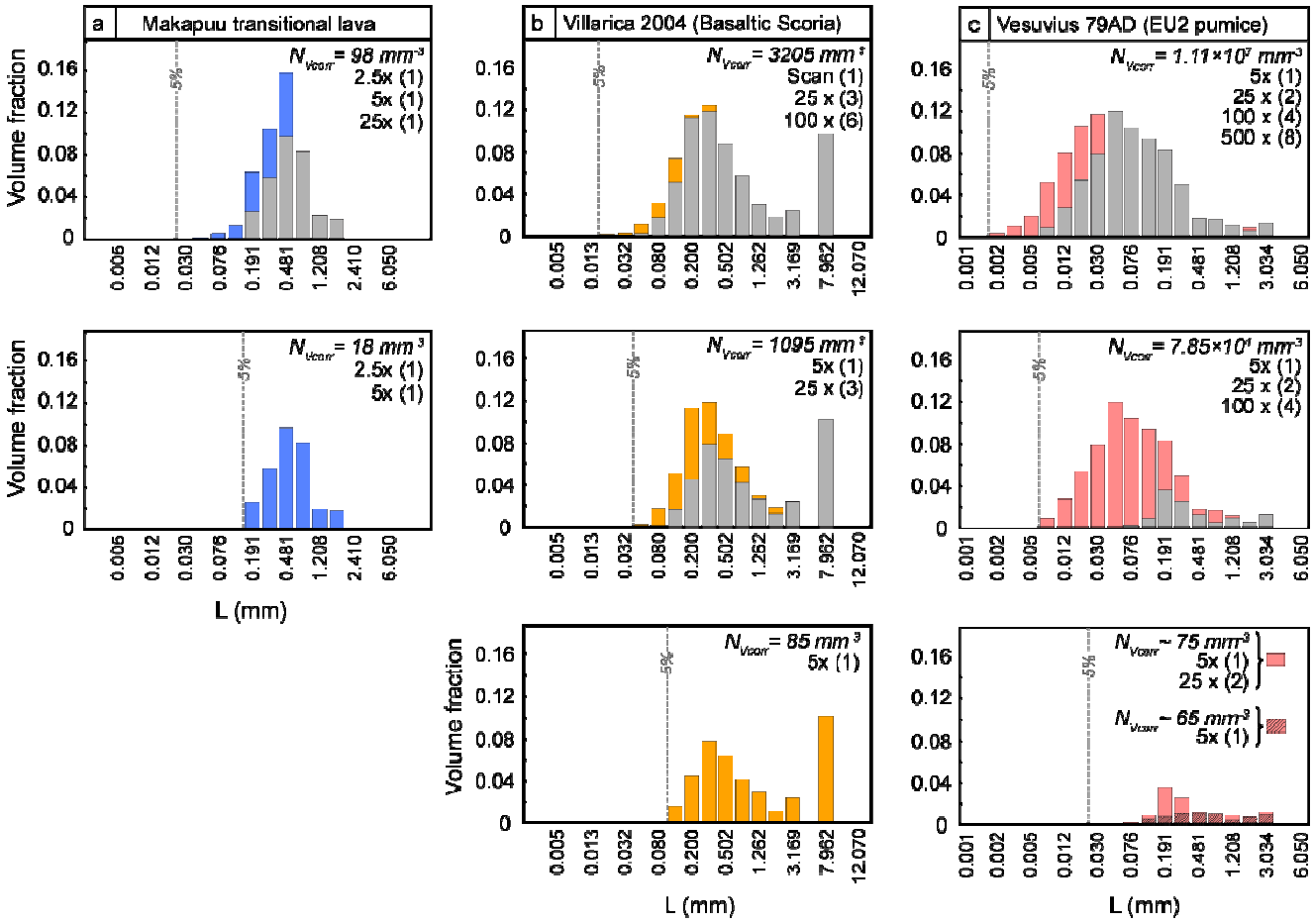

Figure 11: Influence of adding or discarding images of increasing magnifications for (a) Makapuu lavas (b) Villarrica scoria, and (c) 79AD Vesuvius EU2 pumice. The distributions from using only the lower magnifications are shown in gray. Dotted lines are the uncertainty for each misrepresented pixel is greater than 5%.

To include as many vesicles per image as possible, we set the minimum diameter to 5 pixels. Results are shown in Fig. 11. In Makapuu lavas, the distribution represented by 2.5× and 5× magnifications alone (Fig. 11a) clearly lacks the population of small vesicles. For larger bubbles, the distribution is smoother when 25× images are included. The effect of increasing or decreasing the number of magnifications also affects the

computed N_V (~20 mm^{-3} instead of ~100 mm^{-3}). In Villarrica samples (Fig. 11b), the broad shape of the distribution is also present within the first magnification (5×) but the smaller bubbles are missing. This illustrates how additional magnifications (100×) may leave volume distributions relatively unmodified, while strongly increasing number densities (from 1100 to 3200 mm^{-3}). Vesuvius pumice vesicles present an even more extreme case of how apparent number densities increase by orders of magnitude as more small vesicles are added (Fig. 11c). Overall, for all three examples, measurement of accurate number densities requires precise measurement of the smallest vesicles, while accurate measurement of vesicle volume distributions requires precise measurement of the larger vesicles. This does not imply that extremely high magnifications must always be included: while vesicles are better resolved, the area of each image is smaller and thus the risk of capturing non representative portions of a heterogeneous sample significantly increases.

5.4. Influence of minimum diameter on size distributions

Equally important to the choice of nesting strategy and magnifications, the minimum vesicle diameter, measured as number of pixels, strongly shapes the outcome of texture analysis. For each location, runs were made using six minimum diameters from 1–20 pixels (equivalent to 1–315 pixels in area), corresponding to uncertainties of 100 to 0.5% for one misrepresented pixel. The obtained N_A vs. L curves for all three samples (note: for Makapuu, only the curve corresponding to the bottom unit is reported) share a similar concave downward form for vesicle sizes greater than about 0.1, 0.01 and 0.001 mm for Makapuu, Villarrica and Vesuvius, respectively (Fig. 12).

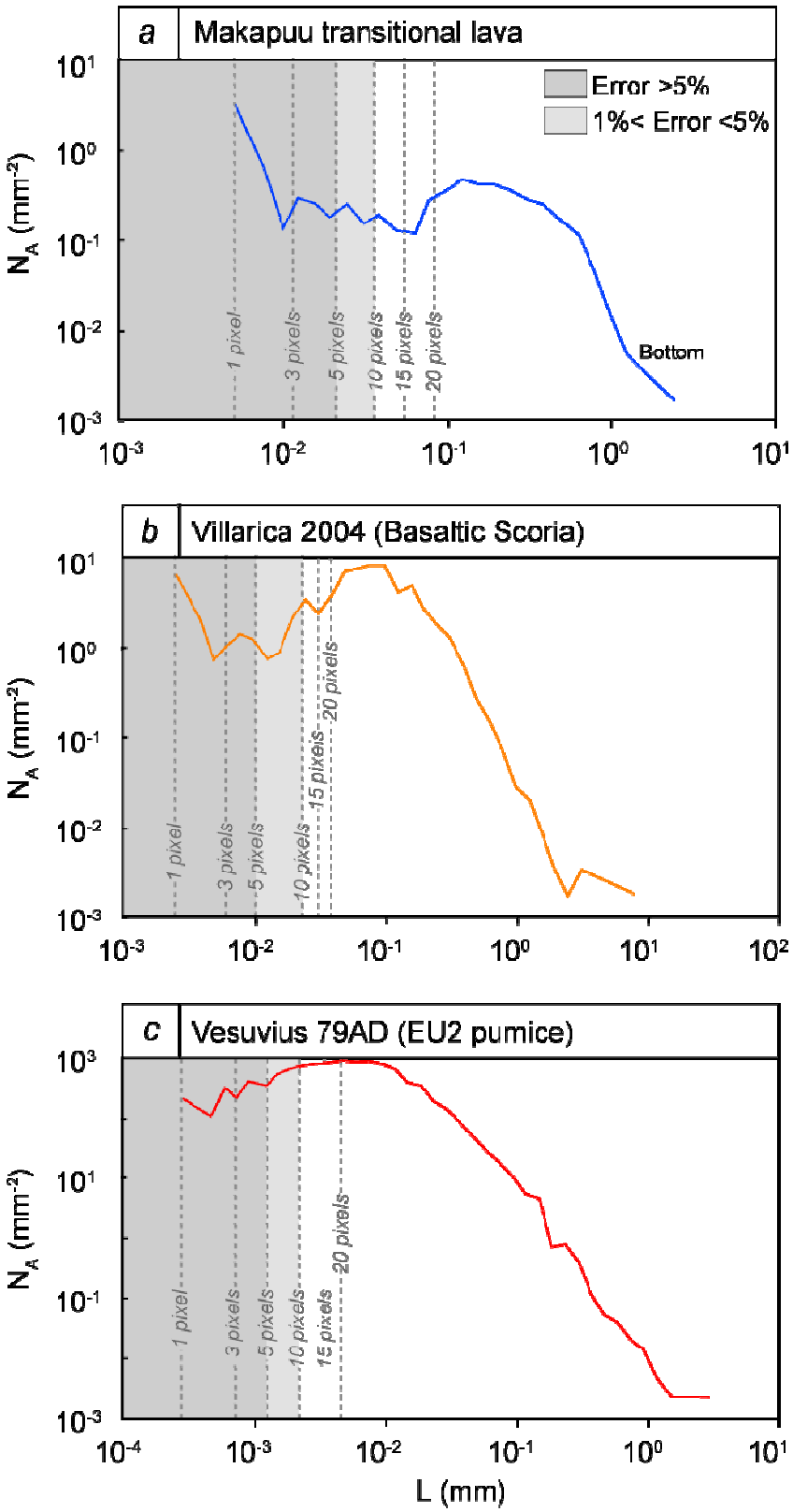

Figure 12: Vesicle number density per area (N_A) measured in the investigated samples. (a) Makapuu, (b) Villarrica, (c) Vesuvius. Gray dotted lines correspond to the resolution limit allowed by various minimum diameters. Under these boundaries, N_A values used to obtain N_V values are discarded. Typically, a maximum uncertainty of 5% is allowed. Any vesicle smaller than this is thus considered noise. For Makapuu the best choice of minimum diameter is probably situated around 15-20 pixels, for Villarrica at about 5-10 pixels, and at Vesuvius 5 pixels.

This type of hook-shaped, concave-down curve is expected for processes that generate log-normal distributions, where the number of objects scales inversely with size. The trends become horizontal as the smallest vesicles are reached. Below this size-range, trends diverge from smooth to multiple relatively saw-toothed, irregular segments. This change in behavior is a sign that a size threshold has been reached under which measurements become unreliable. The minimum diameter is thus generally chosen above this limit. For Makapuu, Villarrica and Vesuvius respectively, 15, 10 and 5 pixels allow discarding noise data that could alter the results. A preliminary run through the program using a minimum diameter of 1 pixel is therefore useful to see the full spectrum of measurements, from noise to meaningful data.

Makapuu VVDs (Fig. 13a) illustrate how merging data from regions of contrasting textures may alter the distribution. Distribution in the bulk sample is bimodal at 0.6 and 6 mm (Table 1), but the bottom pāhoehoe-like section shows only one 0.6 mm mode whereas the top ʻāʻa section has two (1.5 mm and 6 mm). Thus, interpretations have to be made after delineation of the two textural domains. On cumulative plots, the lower sample is characterized by a fairly smooth sigmoid curve that could be interpreted as one or two nucleation events, while the upper sample shows a clearer coalescence signature (cf., Fig. 8b). Ln(n) vs. L plots show less direct evidence for this merging process as both curves overlap significantly. Even though the curves reported in the log(N_V>L) vs. log(L) plot are fairly similar, an exponential trend fits the lower sample better, whereas a power-law is more appropriate for the upper section and yields d=2.54 (Table 1). The choice of a 15 pixel minimum diameter appears adequate when looking at the consequences of lowering the boundary (note: the minimum diameter test was only

applied to the bottom section). VVDs and CVVDs are unaffected at diameters below 20 pixels, whereas the CVSD curve stabilizes before the 15 pixel limit and increases again at smaller diameters.

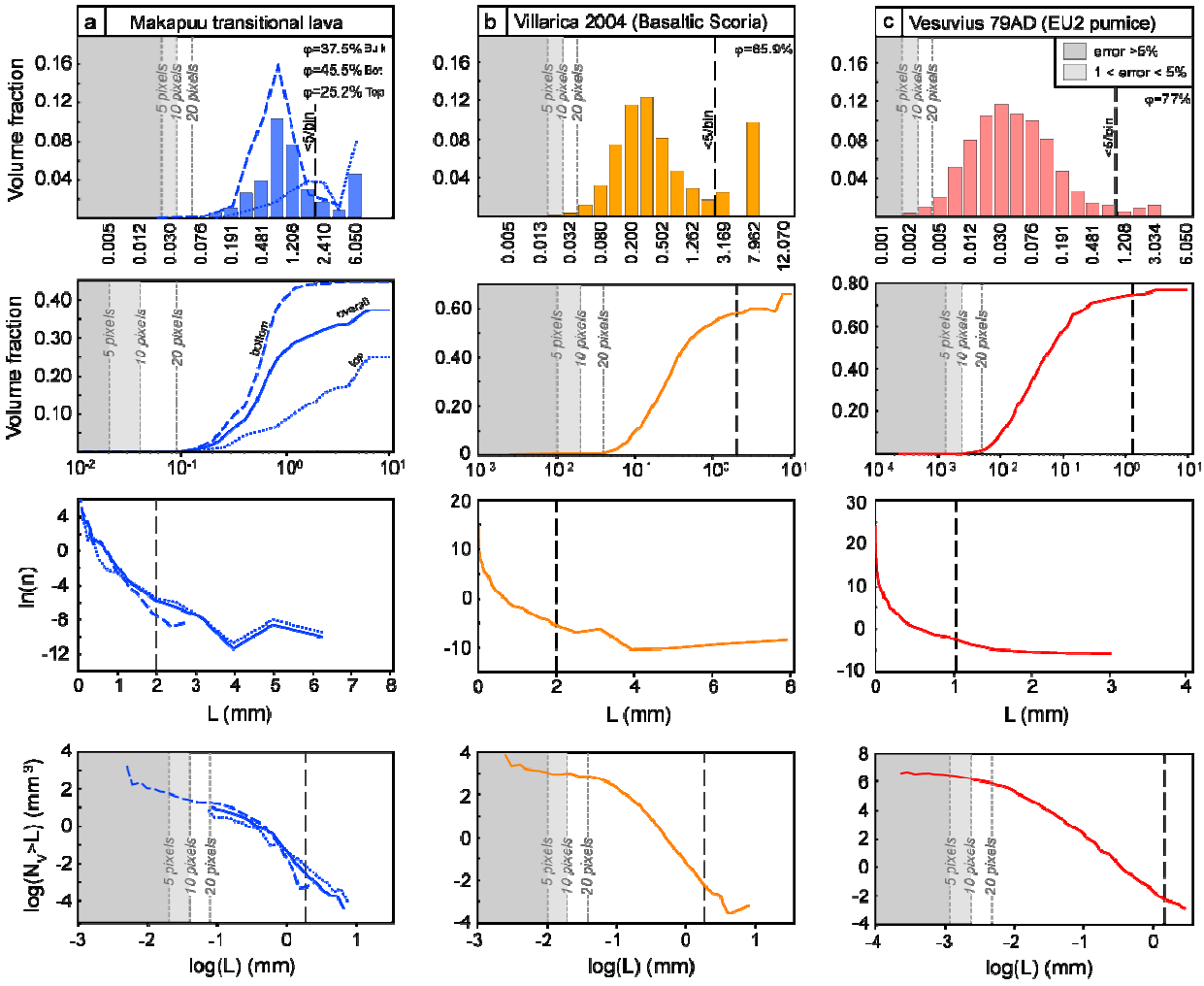

Figure 13: Vesicle size distributions in terms of volume fraction (VVD), cumulative size distributions (CVVD), size distributions in terms of number density (VSD), and cumulative number density plots (CVSD) for (a) Makapuu transitional lava, (b) Villarrica scoria, and (c) Vesuvius 79AD pumice. Vesicularities are reported in VVD plots. Gray dotted lines represent minimum diameter boundaries; i.e. the limits under which any vesicle smaller than a given diameter in pixels will be discarded. Black dashed lines are limits beyond which bins possess less than 5 vesicles each.

Table 1: Summary of main physical and textural parameters in the three samples investigated

	ρ (kg m^{-3}) [a]	ϕ (%)[b]	Diameter (pixels)[c]	Mag. (px m^{-1}) [d]	Min. size (mm)[e]	N_{Vcorr} (mm^{-3})[f]	$n=n_0e^{(-L/G\tau)}$ [g]	$G\tau$ mm [h]	N_{Vfit} (mm^{-3}) [i]
Makapuu	1780	45.5	1	252	0.00397	27.03×10^{2}	$n=(2.23\times10^{5})e^{(-203.85L)}$	0.0049	8.93×10^{2}
			3	"	0.01190	2.05×10^{2}	$n=(2.11\times10^{4})e^{(-92.05L)}$	0.0105	1.32×10^{2}
			5	"	0.01984	0.98×10^{2}	$n=(3.85\times10^{3})e^{(-39.28L)}$	0.0255	0.82×10^{2}
			10	"	0.03968	0.48×10^{2}	$n=(5.75\times10^{2})e^{(-12.62L)}$	0.0792	0.51×10^{2}
			15	"	0.05952	0.31×10^{2}	$n=(1.90\times10^{2})e^{(-7.69L)}$	0.1301	0.29×10^{2}
			20	"	0.07937	0.30×10^{2}	$n=(4.49\times10^{2})e^{(-11.67L)}$	0.0857	0.28×10^{2}
Villarica	900	65.9	1	500	0.00200	21.19×10^{3}	$n=(1.25\times10^{5})e^{(-41.00L)}$	0.0244	8.23×10^{3}
			3	"	0.00600	4.32×10^{3}	$n=(6.36\times10^{4})e^{(-35.71L)}$	0.0280	4.22×10^{3}
			5	"	0.01000	3.20×10^{3}	$n=(2.05\times10^{4})e^{(-18.06L)}$	0.0554	2.78×10^{3}
			10	"	0.02000	2.69×10^{3}	$n=(2.05\times10^{4})e^{(-17.28L)}$	0.0579	2.46×10^{3}
			15	"	0.03000	2.27×10^{3}	$n=(1.94\times10^{4})e^{(-16.71L)}$	0.0598	2.06×10^{3}
			20	"	0.04000	1.93×10^{3}	$n=(1.98\times10^{4})e^{(-17.18L)}$	0.0582	1.70×10^{3}
Vesuvius	600	77	1	4150	0.00024	1.59×10^{7}	$n=(3.87\times10^{9})e^{(-637.94L)}$	0.0016	2.26×10^{7}
			3	"	0.00072	1.56×10^{7}	$n=(2.43\times10^{9})e^{(-477.31L)}$	0.0021	1.57×10^{7}
			5	"	0.00120	1.13×10^{7}	$n=(1.88\times10^{9})e^{(-448.28L)}$	0.0022	1.06×10^{7}
			10	"	0.00241	0.76×10^{7}	$n=(1.57\times10^{9})e^{(-385.31L)}$	0.0026	0.70×10^{7}
			15	"	0.00361	0.50×10^{7}	$n=(8.89\times10^{8})e^{(-285.78L)}$	0.0035	0.48×10^{7}
			20	"	0.00482	0.37×10^{7}	$n=(8.81\times10^{8})e^{(-284.97L)}$	0.0035	0.34×10^{7}

a. Density, as measured using Houghton and Wilson (1989).
b. Vesicularity, derived from density.
c. Minimum diameter used as input to define the smallest measurable vesicle.
d. Maximum magnification used for each case study, scale in pixels per mm.
e. Minimum vesicle size analyzed as defined by (column d/ column e).
f. Vesicle number density (N_{Vcorr}) per volume melt.
g. Exponential best fit equation as measured from VSD plots; n_0 is initial number of nuclei and L is diameter.
h. Least squares goodness of fit.
i. Values of growth rate (G) times vesiculation timescale (τ) derived from column h.
j. Vesicle number density (N_{Vfit}) derived from n_0

The Villarrica sample (Fig. 13b) shows a peculiar VVD with one major mode at 0.04 mm and a secondary, widely separated mode around 8 mm. The latter mode results from the two large vesicles visible on the scanned thin section (Fig. 10b) while the first mode is generated by the bulk of the vesicle population. This bimodality is clearly seen on the cumulative plot as a step-like heterogeneity. On the VSD, within the size range defined by the bulk of the distribution, the trend is curved and shows an inflection around 3 mm. The curve then becomes horizontal as no vesicles are measured from around 2.5 mm to 8 mm. A power-law fit shows R^2=0.97, with exponent d= 3.25, higher than in most basaltic pyroclasts (Blower et al., 2002; Sable et al., 2006; Polacci et al., 2008) and close to those measured in Mt Mazama pumice (Klug et al., 2002). Unlike Makapuu, the chosen minimum diameter becomes more of an issue for Villarrica since selecting values of 15 or 20 pixels diameter leads to discarding a non-negligible portion of the VVD, CVVD and $\log(N_V)>\log(L)$ distributions. Opting for 10 pixels in this case is a better option and preserves important fractions of the distribution.

The Vesuvius 79AD EU2 pumice (Fig. 13c) shows a fairly smooth but weakly bimodal distribution with the major mode around 0.04 mm, and the minor second mode at about 3 mm. This second mode is barely visible on the CVVD plot where the curve is sigmoidal but can be inferred from the slight asymmetry of the two sigmoid tails. The trend on the ln(n) vs. L plot is very smoothly curved with no apparent break. Much like at Villarrica, a power-law fit results in a R^2 ~0.99 and yields an exponent of approximately 3.5, on the upper range of values found by Klug et al. (2002) in Mt Mazama pumice. Like at Villarrica, Vesuvius pumice VVD, CVVD and CVSD distributions are truncated with respect to the smaller vesicles if the minimum diameter is set too high. To account for the

full range of sizes, this diameter needs to be set at around 5 pixels. This choice involves a higher uncertainty (~5% for 1 incorrect pixel) than for larger diameter bubbles. As discussed previously, nonetheless, it is the only way to account for the small vesicle population at the selected maximum magnifications. As suggested earlier, the investigator might consider this uncertainty to be unacceptable and may wish to capture additional sets of images at higher magnifications to improve resolution.

5.5. Number densities

Two number density formulations have appeared throughout this methodology; N_V (or N_{Vcorr}), is obtained by counting vesicles within distinct size classes and summing them, and N_{Vfit} is the total number of vesicles derived from exponential fitting of the VSD (Appendix B) (Table 1). On the latter plots, a single exponential fit is rarely possible and only a portion of the entire curve is usually considered. The N_{Vfit} values reported in Table 1 were obtained by fitting only the smaller size fraction for all considered examples. The initial number density of nuclei n_0 used to compute N_{Vfit} is taken at the smallest measured size and not at zero. N_{Vcorr} as well as N_{Vfit} values were calculated using various minimum diameters (1, 3, 5, 10, 15 and 20 pixels) for all three deposits (Fig. 14, Table 1). A decrease in minimum diameter in all three samples results in drastic increases in vesicle number density. In Makapuu subsamples, N_{Vcorr} decreases from 3000 mm^{-3} to 30 mm^{-3} as minimum diameter increases from 1 to 20 pixels, and Villarrica number density decrease from 1×10^4 mm^{-3} to about 3×10^3 mm^{-3}. On the higher end of the number density spectrum, N_{Vcorr} values measured in Vesuvius 79AD samples decrease by about 10^6 mm^{-3}, from a maximum of 1.6×10^7 mm^{-3} (1 pixel minimum

diameter) to a minimum of 3.7×10^6 mm^{-3} (20 pixels diameter). For most tested minimum diameters, N_{Vfit} values track N_{Vcorr} surprisingly well. Discrepancies begin to appear only when very small minimum diameters are reached, and suggest that substantial noise is included in the number density data. Thus, if the minimum diameter is chosen adequately, N_{Vfit} and N_{Vcorr} should approximately coincide.

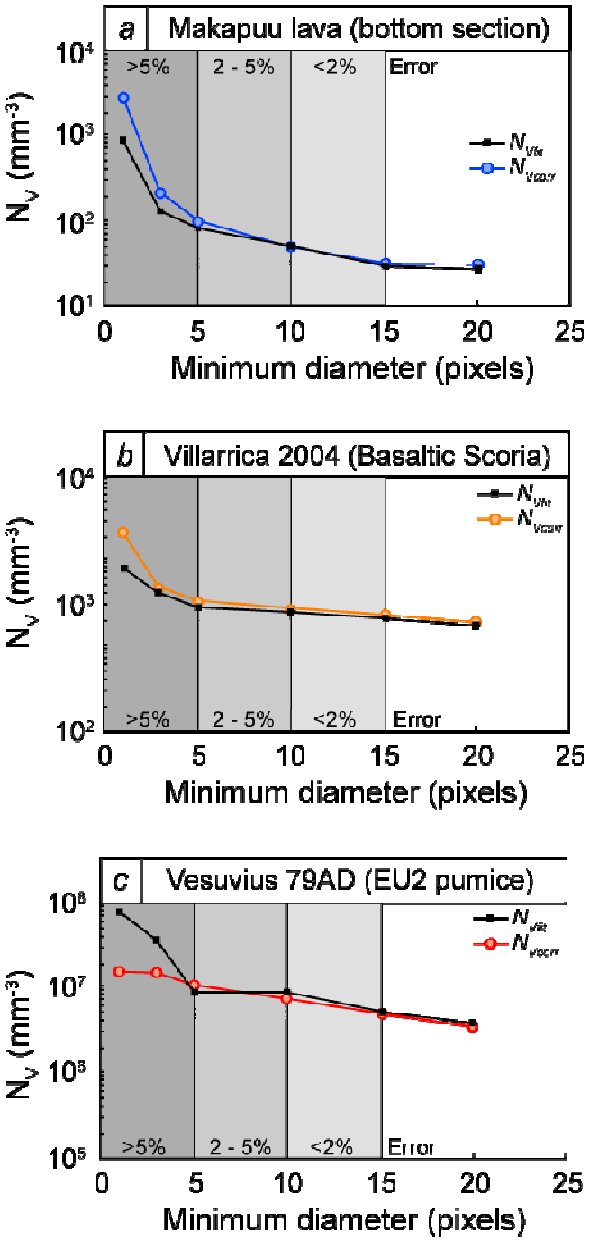

Figure 14: Influence of minimum measured vesicle size (in pixels per diameter) on the calculated N_{Vcorr} for (a) Makapuu lavas, (b) Villarrica scoria, and (c) Vesuvius white pumice. In all cases the obtained number densities are extremely dependent on the choice of the smallest resolvable vesicle size (in pixels). Number densities obtained using VSD fitted curves (N_{Vfit}) are also shown as black squares. Notice the general disagreement between the two values for samples containing a high density of vesicles (Villarrica and Vesuvius) and the good concordance with Makapuu lavas. Zones filled with increasing gray shades report errors associated with misrepresentation of 1 pixel.

6. Discussion: precautions and caveats

The vesicle texture characterization methodology presented here provides guidelines for efficient sample processing, from field collection to data representation. While applying these methods minimizes time requirements while keeping the number of analyzed objects statistically significant, there are several problems that warrant further caution. These problems include the inability to characterize elongated vesicles, the operator bias associated with the various choices needed to obtain the data, the small number of large vesicles typically present, and the difficulty of deriving statistics from the distributions.

6.1. The issue of elongated vesicles

Vesicles are often stretched either during transport (e.g. fluidal bombs), or sheared during ascent close to the conduit margins (e.g. long-tube or fibrous pumice, Klug et al., 2002; Polacci et al., 2001, 2003). Unfortunately, the current version of FOAMS does not transform 2D data adequately for vesicles that have been significantly deformed or sheared. This implies that during sample collection, clasts with very elongated vesicles must be avoided. While it may be argued that this selection might bias the textural characterization of the deposit as a whole, investigating vesicle size and number density in very deformed samples is prone to larger uncertainties associated with textural overprinting: number densities will hardly reflect conduit ascent rates and vesicle sizes will be affected by shearing-induced coalescence. Nonetheless, we acknowledge that implementation of textural quantification parameters for elongate objects is needed for investigations that may focus on the variation of shearing in lava flows or laterally across

the conduit through deformation of vesicles; for instance, tube pumice samples cut perpendicular to elongation can provide information relevant to permeability modeling. Measuring size and shape parameters of deformed vesicles within obsidian samples exhibiting low vesicularities has also proven useful to determine strain rate (Rust et al., 2003). Thus, as mentioned previously, the option to select pre-defined shapes with their corresponding intersection probabilities should be available in future versions of FOAMS. This is in part why measurements of shape parameters are already implemented into the program. Despite the problems associated with the assumption of sphericity, the size and number distributions obtained through FOAMS are shown to be reliable; indeed, our case studies (Makapuu, Villarrica, and Vesuvius) were chosen to represent complex real cases and the derived size, number and shape distributions, as well as resulting N_V values are very consistent with qualitative macroscopic observations.

6.2. Larger vesicle populations

In subsamples taken from welded/competent volcanic rocks such as Makapuu lava flows, it is fairly easy to sample a large enough area either by collecting large samples, or by using reconstructive field photography (Polacci and Papale, 1997). In scoria clasts, however, the analyzable area is typically limited to a few square centimeters. The difficulty of analyzing the larger size populations is particularly well illustrated in the case of Villarrica scoria: in all plots, the transition from the first to the second mode is abrupt because the large bubbles (most likely generated by coalescence and post-fragmentation expansion, Gurioli et al., 2008) are not present in the smaller magnification images (Fig. 13b). This is an issue which cannot readily be dealt with. To characterize

these populations under robust statistical conditions, a much larger sample would probably be needed, of which at least 10 clasts would be selected for each density mode. Due to time constraints, however, this is harder to achieve. As a result, large vesicle populations in scoria or pumice clasts are typically represented by a few individuals rather than by a statistically significant population (cf. large vesicles in Villarrica and Vesuvius samples, Fig. 10b). Hence, particularly in size distribution plots, it is advisable to determine and display sizes above which the distribution is represented by less than 5-10 individuals per bin (Fig. 13).

6.3. Minimum detectable object and statistics

We showed that the choice of the minimum number of pixels necessary to adequately represent a vesicle is crucial since it has a large influence on measured estimates of N_V. For small increases in minimum resolvable diameter, number density can drop by an order of magnitude. This decrease was observed to be stronger with increasing explosivity: each 5 pixel increase in the input threshold diameter resulted in about 5, 15, and 30% decreases in N_{Vcorr} for Makapuu, Villarrica and Vesuvius samples respectively. Thus, to obtain accurate measurements of N_{Vcorr}, it is crucial to select minimum diameters that ensure that the measured vesicles are above "noise" level. Uncertainties within N_{Vcorr} will then mostly depend on the accuracy of vesicularity measurements used to calculate number density per melt volume. The errors associated with misrepresentation (addition or omission) of 1 or several pixels during acquisition and image rectification will thereafter solely influence the precision at which small vesicle sizes are measured. On a

VVD plot, such errors will not strongly modify the shape of the distribution particularly towards smaller bins.

Another issue inherent to the acquisition of results through binning and stereological conversion to 3D is that individual data are inevitably lost in the process. This means that statistical analysis of the data will have to be done directly on distribution curves with no real decision on how large the bins are and how many objects they typically contain. Even so, distribution fitting is still possible using geometric binning, as it appears that most distributions fall within the logarithmic family (log-normal, weibull, logistic and exponential, Proussevitch et al., 2007a). Because few distributions are normal, we recommend avoiding the use of the mean and using modes instead. The actual "log-normal" mean can still be obtained through the normal mean and standard deviation derived from the geometrically binned distribution.

7. Conclusions

With increasing interest in the study of vesicles in volcanic rocks, there is a need for a standardized methodology that captures and quantifies the parameters essential for understanding the ascent and degassing of magma. By adopting a generalized procedure for textural characterization, quantification and comparison of vesicle size distributions, number densities and shapes among different eruptions become possible, and operator errors are minimized. We emphasize the need to find a certain balance between the total number of images captured and processed, and time requirements. Different nested imaging configurations are needed in the case of natural samples collected for different eruption styles. In nested-imaging configurations, the number of images required to fully

characterize most samples falls typically below 20. The textural characterization algorithm FOAMS can measure and analyze objects within these images in just seconds. Current limitations arise from lacking elongate conversion factors, which may introduce some bias in the situations where bubbles have extreme shapes. On the other hand, strengths of this methodology include the possibility of informed decision-making in all steps of the textural investigation process, while keeping time-consuming phases to a minimum. Because the entire technique from thin section to the quantification stage is based on multiscale imagery, it allows for virtually infinite vesicle resolutions, even at micrometer scale, as long as a statistically viable area is imaged. Future steps include implementing stereological solutions for ellipsoids are into upcoming versions of FOAMS, as well as achieving comparisons between XRCMT and Stereology(FOAMS)-derived distributions.

Acknowledgments

The authors wish to acknowledge NSF grants EAR 0409303, 0537950, 0537543, 0537459 and 0739060 and the New Zealand Marsden Fund. This methodology greatly benefited from discussions with Thomas Giachetti and Tim Druitt. We thank Wendy Stovall, Ian Schipper and Natalie Yakos for (very patiently!) providing much needed validation for FOAMS. Thoughtful reviews from Laura Pioli and Sharon Allen were greatly appreciated.

Appendix A: Summary of stereological conversion equations relevant to FOAMS taken from Sahagian and Proussevitch (1998)

N_{V1} and subsequent number densities can be expressed by a generalized equation of form:

$$N_{Vi} = \frac{1}{P_i \overline{H}_i'} \times \left(N_{Ai} - \sum_{j=1}^{i-1} P_{j+1} \overline{H}_{j+1}' N_{V(i-j)} \right) \qquad \text{(Eq. A.1)}$$

N_A is measured number density per unit area (mm^{-2}) for size ranges 1 to i , P the probability of intersecting particles of the same size ranges (1 to *i*), and $\overline{H}_i'$ the mean projected height.

To avoid several stages of computations, Sahagian and Proussevitch (1998) rewrite Eq. A.1) as:

$$N_{Vi} = \frac{1}{\overline{H}_i'} \times \left(\alpha_i N_{Ai} - \sum_{j=1}^{i-1} \alpha_{j+1} N_{A(i-j)} \right) \qquad \text{(Eq. A.2)}$$

where conversion coefficients $\alpha_i = \frac{1}{P_1} \left(\alpha_1 P_i - \sum_{j=1}^{i-2} \alpha_{j+1} P_{i-j} \right)$ (Eq. A.3)

For spherical particles, the probability of intersecting objects through a specific size is written:

$$P(r_1 < r < r_2) = \frac{1}{R}\left(\sqrt{R^2 - r_1^{\,2}} - \sqrt{R^2 - r_2^{\,2}}\right) \quad \text{(Eq. A.4)}$$

R is the sphere radius, r is the cross section radius, and r_1 and r_2 are the lower and upper limits of the particular size ranges considered.

Appendix B: Vesicle size distributions

B.1. Theoretical background behind VSDs

In theory, assuming that nucleation and growth rates are constant throughout the vesiculation process, numerous physical parameters can be derived from segments of VSD curves. These include nucleation rates (J), growth rates (G), number of initial nuclei (n_0), the total number of vesicles per unit volume (N_{Vfit}) and the characteristic bubble diameter (L).

These parameters are found using the steady-state conservative exponential equation:

$$n = n_0 \exp\left(\frac{-L}{G\tau}\right) \quad \text{(Eq. B.1)}$$

Then nucleation rates (J, $mm^{-3}\ s^{-1}$) are simply:

$$J = n_0 G \quad \text{(Eq. B.2)}$$

In theory, if the data are linear on an ln(n) vs. L plot, the total number density of vesicles per volume melt can be retrieved through the zeroth moment of Eq. B.2 (Cashman and Mangan, 1994):

$$N_{Vfit} = n_0 G \tau \quad \text{(Eq. B.3)}$$

In turn, the first moment gives the dominant diameter:

$$L_{fit} = G \tau \quad \text{(Eq. B.4)}$$

The value of N_{Vfit} can be compared subsequently to the N_V directly measured within the sample to test whether the trend adequately represents the actual data. If they are similar, then the fit can be considered robust.

B.2. Theoretical background behind log(N_V)>log(L) plots

Numerical models by Blower et al. (2002) demonstrate that in log(N_V>L) vs. log(L) plots, one to three nucleation events are able to generate exponential curves (Fig. 8d), of form:

$$\log(N_V > L) \propto e^{-L} \quad \text{(Eq. B.5)}$$

Whereas numerous nucleation events or continuous nucleation and growth produce power law linear trends:

$$\log(N_V > L) \propto L^{-d} \quad \text{(Eq. B.6)}$$

where d is the power-law exponent.

This type of plot was used to differentiate between exponential and power-law distributions, and between single, multiple or continuous nucleation (Gaonac'h et al., 1996; Gaonac'h et al., 2005; Blower et al., 2001, Blower et al., 2002, Polacci et al., 2008).

Power-law fitted distributions are usually only valid for a certain size range (Blower et al., 2002), and are seemingly applicable to most volcanic rocks as they represent multiple or continuous nucleation events. Gaonac'h et al. (1996, 2005) predicted that a single value of exponent d~2.5, close to the value anticipated for Apollonian packing (Blower et al., 2001), could apply to most vesicular samples, from lava flows to pumice. In the literature, however, varying d exponents have been found: d=2.5 in Basaltic scoria from Izu Oshima subplinian eruption (Blower et al., 2002), 2.8 within Stromboli basaltic scoria (Bai et al., 2008; Polacci et al., 2008; Note that their form of Eq. B.6 expresses measurements as volume instead of radius), 2.8 in Etnean basaltic scoria (Simakin et al., 1999), 2.7-2.9 in Plinian basaltic scoria (Sable et al., 2006), 3.3 in rhyodacitic pumice (Klug et al., 2002), and 3.9 in dacitic pumice (Adams et al., 2006). Thus, on the whole, it seems this exponent increases with increasing eruption explosivity, an outcome forecasted by numerical models (Blower et al., 2001).

In contrast, exponential fitted distributions are applied in $\log(N_V{>}L)$ vs. $\log(L)$ plots when the trend is nearly horizontal towards smaller class sizes and curves down towards larger objects. These fits do not seem to apply to many situations, however, and are thought to represent cases in which one or only few nucleation events have occurred (Blower et al., 2002; Bai et al., 2008). Coalescence tends to produce curves looking fairly

similar to exponential trends, with the distinction nonetheless that a more horizontal tail may exist towards large size classes (Polacci et al., 2008; Bai et al., 2008). In turn, collapse textures may produce a curve which rapidly decreases towards low N_V values and quickly becomes near-horizontal as largest sizes are approached.

Appendix C: Shape parameters

More often, the problems of shape are addressed using sphericity parameters and much less often consider complexity or both. Polacci and Papale (1997) and Rust et al. (2003) have used what is typically referred to as aspect ratio $AR = \frac{b}{a}$ where *a* is best-fit ellipse semi-long axis and *b* is semi-short axis. Circular objects possess aspect ratios of 1 while extremely stretched objects tend towards zero, however, the inverse of AR is sometimes used, where the larger the value, the more the object has an elongated form. Manga et al. (1998), Polacci et al. (2001), Rust et al. (2003) and Mongrain et al. (2008) used elongation $\varepsilon = \frac{a-b}{a+b}$, a fairly similar parameter for which values of 0 represent circular objects and values of 1 extremely elongated ones. Aspect ratio and elongation are equally adequate to characterize vesicle deformation and both are available as outputs in FOAMS. Vesicle complexity has been dealt with using the shape factor $SF = \frac{4\pi A}{p^2}$, where *A* is vesicle Area and *p* is perimeter (Orsi et al., 1992; Cashman and Mangan, 1994). In this case, a perfect circle has SF=1, and more complex shapes will have SF tending towards 0. Because the latter ratio also varies somewhat with object elongation, it is however difficult to distinguish which of the two geometrical variations (i.e. elongation

vs. complexity) is more influential. Therefore, we introduce the "regularity" parameter as the ratio of the area (A, mm^2) to the area of the corresponding best-fit ellipse $rg = \frac{A}{\pi ab}$.

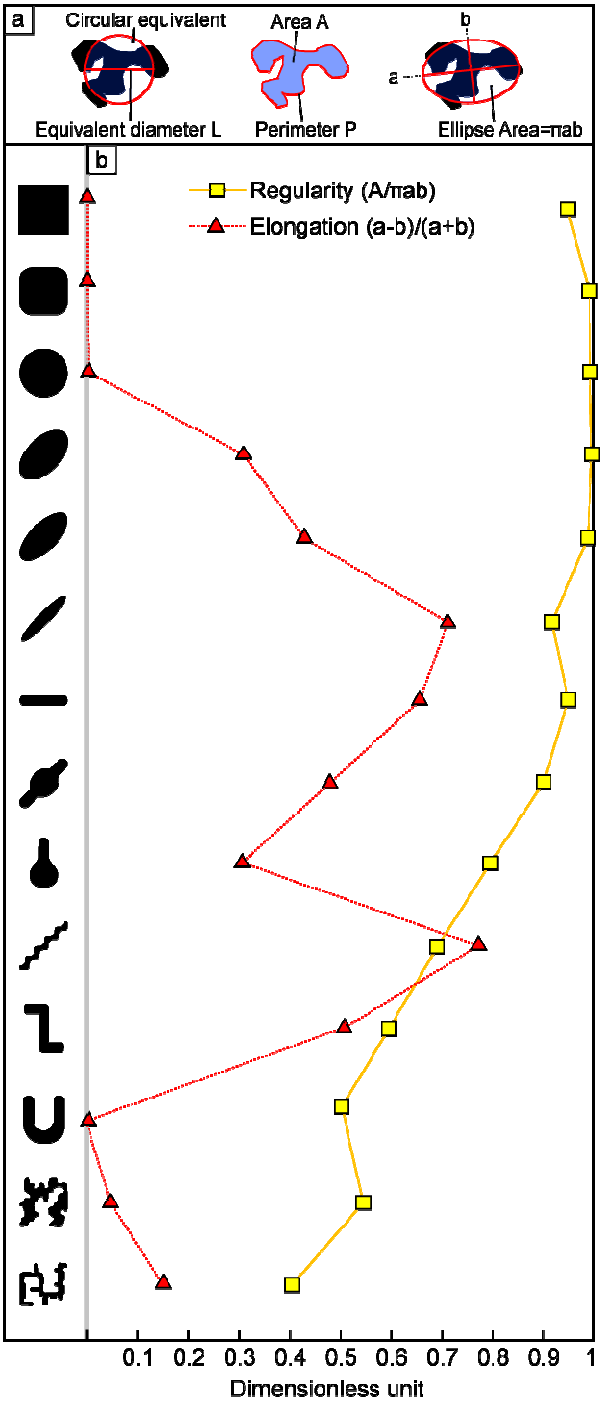

This formulation has the advantage of accounting for irregularities in vesicle outline while disregarding elongation. All measured dimensions are shown in Fig. C1 (left). To ensure the capability of elongation/aspect ratio and regularity to fully characterize vesicle shape, we ran a series of tests involving shapes of decreasing circularity and increasing complexity using binary objects of up to 300 pixels. Elongation increases along with object stretching, and, as expected, behaves more chaotically when comparing shape complexities (Fig. C1). Regularity stays constant for varying elongations and regularly decreases with increasing complexity.

CHAPTER 4. LINKING EXPERIMENTAL AND NATURAL VESICLE TEXTURES IN VESUVIUS 79AD WHITE PUMICE

Published in its present form as Shea, T., Gurioli, L., Larsen, J.F., Houghton, B.F., Hammer, J.E., Cashman, K.V., (2010), Journal of Volcanology and Geothermal Research, in press. doi: 10.1016/j.jvolgeores.2010.02.013

Abstract

Vesicle populations in volcanic pumice provide a partial record of shallow magma ascent and degassing. Here we compare pumice textures from the well-characterized 79AD Vesuvius eruption to those generated during isothermal decompression experiments. Three series of experiments were conducted using starting material from the first two phases of the eruption (eruptive units EU1 and EU2). Samples were decompressed from 100 or 150 MPa to final pressures of 10–25 MPa using conditions appropriate for simulating eruption conditions (T=850°C, dP/dT=0.25 MPa/s). The experiments differed not only in starting material but also in temperature at which samples were annealed prior to decompression, which determined the initial number of crystals present in the melt. Results show that experiments approach the vesicle number densities and sizes of pumice samples, but show narrower size distributions. The wider vesicle size range of pumice samples suggests continuous, rather than instantaneous nucleation, which may reflect non-linear rates of decompression. All experiments exhibited equilibrium degassing, a process that was probably aided by heterogeneous bubble nucleation on oxide microlites. We conclude that delayed bubble nucleation cannot explain the explosivity of the Vesuvius eruption, which instead appears to require high rates of magma decompression.

1. Introduction

Vesicles in volcanic rocks provide valuable information on the processes occurring in magma conduits and storage systems (e.g. Cashman and Mangan, 1994). Three

complementary approaches provide constraints on vesiculation in magmas: textural measurements, laboratory experiments, and physical/numerical models. Textural measurements of vesicle size, number and spatial distribution in natural samples are used to infer the processes responsible for their formation (e.g., Klug and Cashman, 1994; Klug et al., 2002; Polacci et al., 2003; Gurioli et al., 2005b; Sable et al., 2006; Adams et al., 2006, Lautze and Houghton, 2007; Polacci et al., 2007). Although natural tephra samples are the best available "tracers" of vesiculation in any eruption, they represent a frozen textural state, which might have been acquired prior to, during, and after magmatic fragmentation. Decompression experiments document processes of bubble nucleation, growth, coalescence, and collapse that may occur during magma ascent, although the small volumes of material used commonly prevent scaling of vesicle size, number and porosity to natural systems. Models of bubble nucleation and growth link experiments to conduit processes, and ultimately, shed light on conditions required to produce violent explosive eruptions (Toramaru, 1989; 1995; 2006; Lyakhovsky et al., 1996; Jaupart, 1996; Vergniolle, 1996; Lovejoy et al., 2004; Mangan et al., 2004; Massol and Koyaguchi, 2005; Yamada et al., 2005; Gonnermann and Manga, 2007).

Of the three approaches described above, laboratory experiments provide a critical link between field observations and modeling through quantification of kinetic parameters such as bubble nucleation and growth rates, volatile solubility, diffusivity, and surface tension. Most experimental vesiculation studies have examined rhyolitic magmas (Hurwitz and Navon, 1994; Lyakhovsky et al., 1996; Mangan and Sisson, 2000; Gardner et al., 1999; 2000; Mourtada-Bonnefoi and Laporte, 1999; 2002; 2004; Larsen and Gardner, 2000; Martel and Schmidt, 2003; Larsen et al., 2004; Lensky et al., 2004;

Burgisser and Gardner, 2005; Gardner, 2007; Cluzel et al., 2008) because they produce the most violent eruptions, and their high viscosity precludes problems associated with rapid microlite crystallization and bubble-melt decoupling in laboratory capsules. Sparser experimental data exist on lower viscosity melts such as basalts (Bai et al., 2008), dacites (Mangan et al., 2004; Suzuki et al., 2007) and phonolites (Larsen and Gardner, 2004; Larsen et al., 2004; Iacono Marziano et al., 2007; Larsen, 2008; Mongrain et al., 2008).

Here, we examine the decompression and vesiculation of phonolites at conditions relevant to the 79AD eruption of Vesuvius, and compare experimental textures to those of pumice deposited during the opening and first Plinian phases of the eruption. Both natural and experimental data are then compared to models of bubble formation to determine (1) limiting conditions of equilibrium H_2O exsolution, (2) the correspondence between number densities, modal vesicle size, and size distribution of pumice and experimental samples, and (3) the influence of microlites on nucleation. We find that 79AD K-phonolites nucleate heterogeneously on microlites, exsolve efficiently even at low temperatures, and produce number densities close to those measured in natural samples. On the other hand, bubble size distribution comparisons between experimental and natural samples suggest that natural ascent processes are probably more complex than the simulations performed to date in the laboratory environment. We suggest that the most viable way to mimic natural bubble size populations through experiments is to apply non-linear decompression pathways, possibly resulting in multiple nucleation and growth pulses.

2. The 79AD eruption of Vesuvius

Nearly 2000 years ago, Vesuvius volcano produced one of the largest and deadliest historical eruptions, burying the Roman towns of Herculaneum, Pompeii, Oplontis and Stabiae under meters of both fallout tephra and pyroclastic density current (PDC) deposits (e.g. Lirer et al., 1973; Sigurdsson et al., 1982, 1985; Cioni et al., 1992). The eruption (volcanic explosivity index VEI=6, Cioni et al., 2008) lasted over 20 hours and produced a total of 2–3 km^3 of deposits, calculated as dense rock equivalent (DRE). Pumice composition and color varied from a white phonolitic to a gray tephri-phonolitic composition during the course of the eruption, which is thought to reflect pre-eruptive zoning of the magma reservoir (Sigurdsson et al., 1990; Cioni et al., 1995). According to this model, the magma that produced white pumice (hereafter referred to as "white" magma) was an un-erupted remnant from the ~3900 BP eruption of Avellino, which had differentiated and cooled to ~850 ºC (Cioni, 2000) over about 2000 years (Lirer et al., 1973, Cioni et al., 1995). During the 79 AD eruption, batches of hotter tephritic magma intruded the storage region, heated the lower portion of the white magma to $\leq$ 925˚C (Shea et al., 2009) and mixed with white magma to produce the tephri-phonolite, which produced the later gray pumice deposits.

Herein, we focus on the white magma and, more specifically, on the opening sub-plinian (EU1) and plinian (EU2) stages. Our objective is to characterize vesiculation processes from the onset to the sustained plinian phase of the eruption. The opening phase (EU1) formed a ~15 km-high buoyant column that was advected eastward by lower tropospheric winds (Sigurdsson et al., 1985) and deposited fine-grained pumice tens of kilometers from the vent (Fig. 1a and 1b).

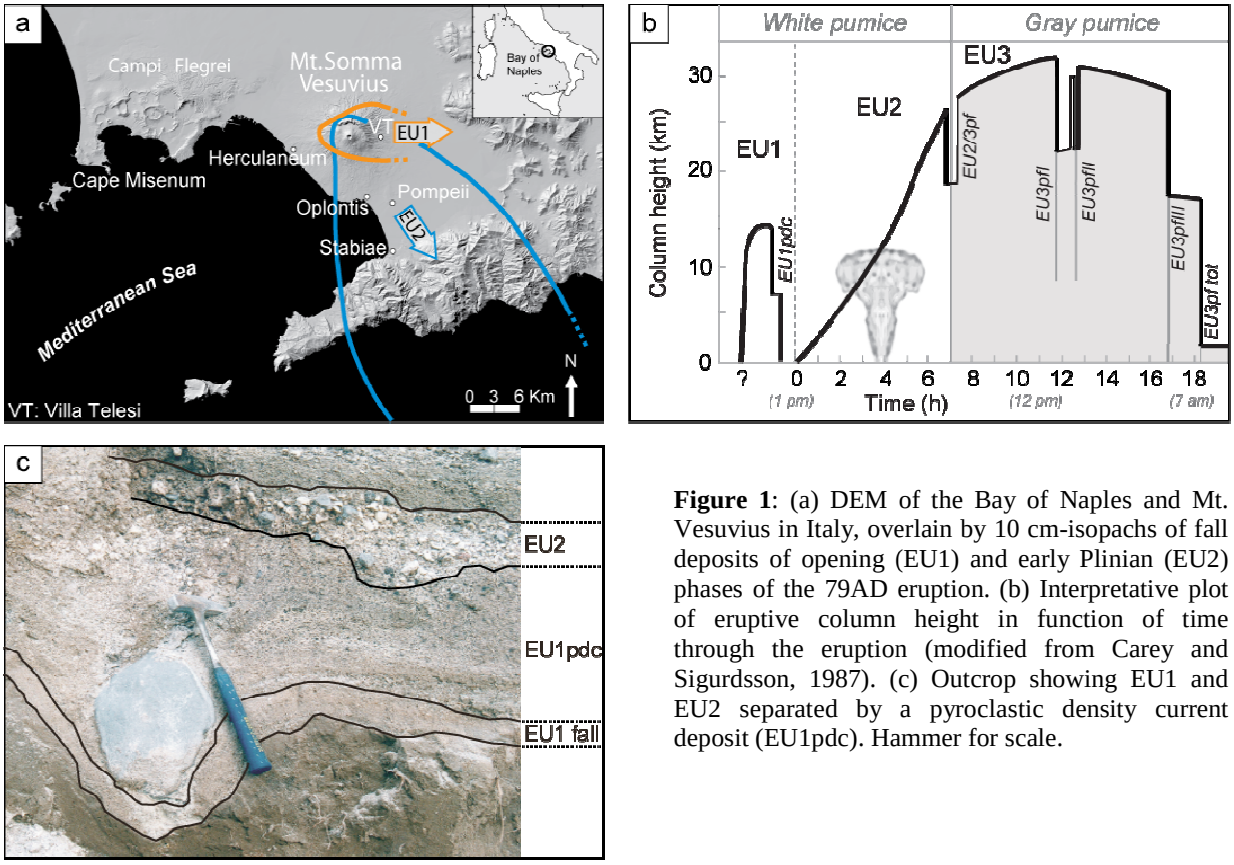

Figure 1: (a) DEM of the Bay of Naples and Mt. Vesuvius in Italy, overlain by 10 cm-isopachs of fall deposits of opening (EU1) and early Plinian (EU2) phases of the 79AD eruption. (b) Interpretative plot of eruptive column height in function of time through the eruption (modified from Carey and Sigurdsson, 1987). (c) Outcrop showing EU1 and EU2 separated by a pyroclastic density current deposit (EU1pdc). Hammer for scale.

The unit varies from 0 to 15 cm in thickness (Fig. 1c) and blankets the flanks of the volcano. After a small column collapse event generated a poorly dispersed PDC (EU1pf, Cioni et al., 2000), the sustained activity increased in intensity and a much higher ~25–30 km plume formed (Fig. 1b), was carried south-east by stratospheric winds (Rolandi et al., 2008), and deposited EU2 pumice hundreds of kilometers from the eruptive center (Sigurdsson et al., 1985). EU2 is ≤ 140 cm thick at the base of Vesuvius (Cioni et al., 1992), thins outward and then thickens again (>100 cm) towards the Sorrento peninsula (Sigurdsson et al., 1985; Fig. 1a, 1c).

3. Background: Textural investigation of products from the 79AD eruption and vesiculation experiments in phonolites

The products of the 79AD eruption of Vesuvius have been characterized by Gurioli et al. (2005b), who examined textural evidence for the origin of changes in eruptive behavior during two important transitions (i.e. white to gray pumice EU2-EU3 and sustained plinian activity to caldera collapse EU3–EU4) using vesicle and crystal textures. We focus on conditions related to the onset of eruptive activity (EU1) and subsequent transition to the first Plinian phase (EU2). In particular, we used decompression experiments to explore the effects of varying starting conditions (composition and microlite content) on conditions of vesicuation and, by inference, on the course of the eruption. Textural data for EU2 is presented in Gurioli et al. (2005b); textural data for EU1 is presented here.

Previous decompression experiments that use Vesuvius phonolite starting compositions have explored conditions that allow equilibrium degassing to be maintained. Iacono Marziano et al. (2007) used superliquidus melts (1050˚C) to determine limiting decompression rates of $\geq$ 1.7 MPa/s for homogeneous nucleation, and $\leq$ 0.0028 MPa/s to maintain near-equilibrium conditions of degassing. Larsen (2008) started experiments at subliquidus temperatures (900 and 950˚C) where bubble nucleation appeared heterogeneous even at high decompression rates (3–17 MPa/s), requiring $\Delta P \leq$ 50MPa to trigger vesiculation. These experiments indicated, however, a big contrast in the degassing behavior between the higher temperature experiments, where equilibrium volatile contents were maintained during decompression, and the lower temperature

experiments, where experiments deviate strongly from equilibrium trends. Our experiments extend the range of experimental conditions to lower temperatures (850˚C) and slower decompression (0.25 MPa/s); these conditions lie within the estimated temperature and decompression rate for the early phase of the 79 AD eruption, thereby allowing us to link the experiments to the natural environment.

4. Methods

4.1. Decompression experiments

We used multiple-step decompression (MSD) experiments to investigate bubble nucleation and growth in Vesuvius phonolites at conditions relevant to the 79AD eruption. Pressure drops of 5 MPa were followed by 20-second holding periods to replicate a linear, integrated ascent rate of 10 m/s (0.25 MPa/s), which represents the average ascent velocity derived from the numerical model of Papale and Dobran (1993). It is a conservative estimate considering that input rates of 20–40 m/s are required to reproduce the high mass discharge rates calculated for the EU2 phase of the eruption (Carey and Sigurdsson, 1987) in other numerical ascent models (e.g. CONFLOW, Mastin and Ghiorso, 2000). Although magma ascent during eruption is non-linear (e.g. Neri et al., 2002b), the use of a linear decompression rate of 0.25 MPa/s was most practical in the laboratory environment.

4.2. Starting material and experimental setup

Starting material for decompression experiments are 2–3 cm-sized EU1 and EU2 pumice clasts (see Fig. 1 for sampling locations) that show minor differences in composition (Table 1), with slightly lower SiO_2, FeO, MgO, and CaO and higher Al_2O3, Na_2O, and K_2O in EU1 compared to EU2. Two sets of experiments using powdered pumices from EU1 and EU2 were placed at the initial pressure (P_I=150 MPa) and temperature (T=850ºC) for 5–7 days under water-saturated conditions (a_{H2O}=1) inside Au, Ag, or Ag-Pd capsules loaded into Rene-style Waspaloy vessels pressurized with H_2O. This step ensured that the material would reach near-equilibrium starting conditions, and that pore space was minimized (Larsen and Gardner, 2004; Larsen, 2008). A series of prior MSD runs with initial pressure P_I=100 MPa and temperature T=850°C (Larsen, unpublished data) was also available to compare with series at P_I=150 MPa. Those MSD experiments underwent an additional annealing step at 1000°C prior to re-equilibration at 850°C that initially served to eliminate most microlites that might modify nucleation behavior, thus allowing us to assess the effect of crystal content. Hereafter, the 150 MPa series for EU1 and EU2 are labeled "series A and B" respectively, and the annealed 100 MPa series available for EU2 is labeled "series C".

Table 1: Major element chemistry for EU1 and EU2 natural samples.

wt. %	EU1 14-1-2	EU2 V15-2-9
SiO_2	54.91 (0.26)	55.41 (0.38)
TiO_2	0.31 (0.14)	0.26 (0.11)
Al_2O_3	22.30 (0.23)	21.97 (0.45)
FeO*	2.16 (0.13)	2.90 (0.38)
MnO	0.24 (0.08)	0.24 (0.12)
MgO	0.23 (0.03)	0.65 (0.07)
CaO	3.11 (0.22)	3.69 (0.25)
Na_2O	6.22 (0.19)	5.32 (0.21)
K_2O	9.89 (0.42)	9.17 (0.39)
Cl[a]	0.54 (0.08)	0.26 (0.14)
P_2O_5	0.09 (0.04)	0.12 (0.05)
Totals[b]	99.20 (0.41)	99.76 (0.58)
n[c]	14	19

[a] Cl is reported as oxide weight percent.
[b] Original totals with analyses normalized to 100%.
[c] Total number of electron microprobe analyses of glass created by melting powders in $Au_{75}Pd_{25}$ tubing for 10 minutes at 1300°C.

Oxygen fugacity (fO_2) was maintained at Ni–NiO ±0.5 to 1 log unit (Rutherford, 1996; Scaillet and Pichavant, 2004) in saturation experiments by inserting nickel filler rods into the vessels. Capsules were placed on a hot plate at 150 ºC and weighed before and after each saturation run to ensure that no water had been lost. Splits of resulting glass slabs were then reloaded into several capsules 30 mm in length and 4 mm in diameter, each crimped and welded. Each capsule was then placed into rapid quench-capable cold-seal vessels at T=850ºC, P_I=150 MPa for 1–2 hours, then decompressed stepwise and quenched at ending pressures (P_F) between 125 and 25 MPa. In general, decompression to lower pressures resulted in foam collapse or fragmentation although one successful run at P_F=10 MPa was integrated into the experimental dataset.

4.3. Experimental conditions

The experimental temperature of 850°C is within the range determined for the 79 AD magmas from prior studies (Barberi et al., 1981; Cioni et al., 1995) and at the lower bound of the 850–925°C found by Cioni et al. (1998) and Shea et al. (2009). Storage pressures have been constrained at 100–150 MPa by Cioni (2000) on the basis of volatiles in melt inclusions although Scaillet et al. (2008) and Iacono Marziano et al. (2007) have inferred pressures of 200 MPa using phase equilibria and water solubility experiments, respectively. We used P_I=150 MPa for both EU1 and EU2 runs. Finally, although CO_2 might have been present during earlier stages of magma storage (Scaillet and Pichavant, 2004), absence of CO_2 within melt inclusions indicates that the magma was H_2O-saturated ($H_2O \leq 6.5$ wt%) immediately prior to ascent (Cioni, 2000). Water-saturation was consequently assumed for all decompression experiments.

4.4. Textural characterization

Measurements of sample vesicularity, vesicle size distribution (VSD), vesicle volume distribution (VVD), and number density per unit volume melt (N_V) were obtained using methods described in Shea et al. (2010a). Sample vesicularity is determined by measuring sample weight in air and water, assuming a fixed solid fraction density (Houghton and Wilson, 1989). Density/vesicularity histograms were used to select three samples representative of the low, modal and high-density end-members for further textural characterization (Fig. 2).

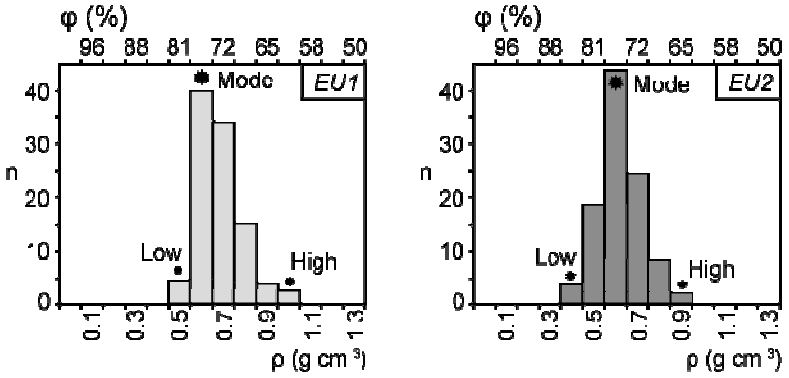

Figure 2: The density variations for pumices sampled from EU1 and EU2 (from Gurioli et al., 2005b). Representative samples (low, modal and high density) were chosen within the distribution. Vesicularities are also reported on top of each plot. n=number of clasts.

While density measurements are easily achievable for cm-sized pumice clasts, they are not feasible for experimental samples that have volumes of a few cubic mm. Thus, experimentalists often choose to consider the 2D vesicularity as representative of the 3D vesicularity (e.g. Gardner, 1999; Gardner et al., 2000; Martel and Schmidt, 2003; Mangan et al., 2004; Mourtada-Bonnefoi and Laporte, 2004; Burgisser and Gardner, 2005; Cluzel et al., 2008), or derive vesicularity using stereological corrections methods

(e.g. Mourtada-Bonnefoi and Laporte, 2002; Larsen and Gardner, 2004). In an attempt to estimate how 2D (i.e. "image vesicularity", ϕ_{2D}) compares to true vesicularity ("density-derived vesicularity", ϕ_{3D}), we gathered data from five explosive and one effusive eruptions, and derived a best-fit equation (see Appendix A for a full description):

$$\phi_{3D} = -6.762\times10^{-2}\,\phi_{2D}{}^{2} + 1.5574\phi_{2D} + 2.5 \qquad \text{(Eq. 1)}$$

VSDs, VVDs and N_V values were derived via a Matlab®-based algorithm (cf. FOAMS, Shea et al., 2010a) based on formulations by Sahagian and Proussevitch (1998). Vesicle number densities were corrected for calculated vesicularities (N_{Vcorr}, Table 2) to provide information on the number of bubbles that nucleated and survived coalescence and collapse. Finally, to test the influence of microlites on vesiculation, oxide number densities N_{Vox} per unit volume were also measured in decompression experiments.

5. Results

5.1. Textural characterization of Vesuvius 79AD white pumice

Detailed descriptions of EU2 textures can be found in Gurioli et al. (2005b); new measurements concern EU1 only. Nonetheless, to facilitate comparison, both EU1 and EU2 textural features are summarized in the following paragraphs.

5.1.1. Observations

Textural measurements for both EU1 and EU2 are reported for clasts that represent the mode and extremes of the density distribution for each deposit (e.g., Shea et al., 2010a). Progressing from low to higher densities (Fig. 3a, c, d and Fig. 3b, d, f), large (>0.5 mm) vesicles become sparser and glass walls thicken. In all samples, larger vesicles have complex shapes while smaller ones (i.e. <0.1 mm) are round. Vesicle walls are smooth, and bubbles are either located away from large crystals or arranged as intricate radial webs around leucites (Fig. 3g and h). Tiny ~1–3 μm oxide microlites (dominantly titanomagnetite) are abundant and homogeneously distributed within the glass of all natural samples. While the low and modal density end-members in both EU1 and EU2 display similar textures and vesicularities, EU1 high-density clasts are less vesicular (~62% for EU1 high and 71% for EU2 high) because of alternating dense and vesicular regions (Fig. 3e) that may be associated with shear-bands. In contrast, the high-density end-member of EU2 (Fig. 3f) is relatively homogeneous. EU2 also contains more minute (i.e. <0.01 mm) vesicles than EU1 (e.g. compare Fig. 3g with 3h). Neither EU1 nor EU2 show evidence of post-fragmentation expansion (e.g., breadcrusting, differential bubble expansion, Polacci et al., 2001; Klug et al., 2002), which may affect the interpretation of measurements. Throughout this contribution, we therefore assume that the textures by EU1 and EU2 pumices are frozen records acquired during or prior to fragmentation.

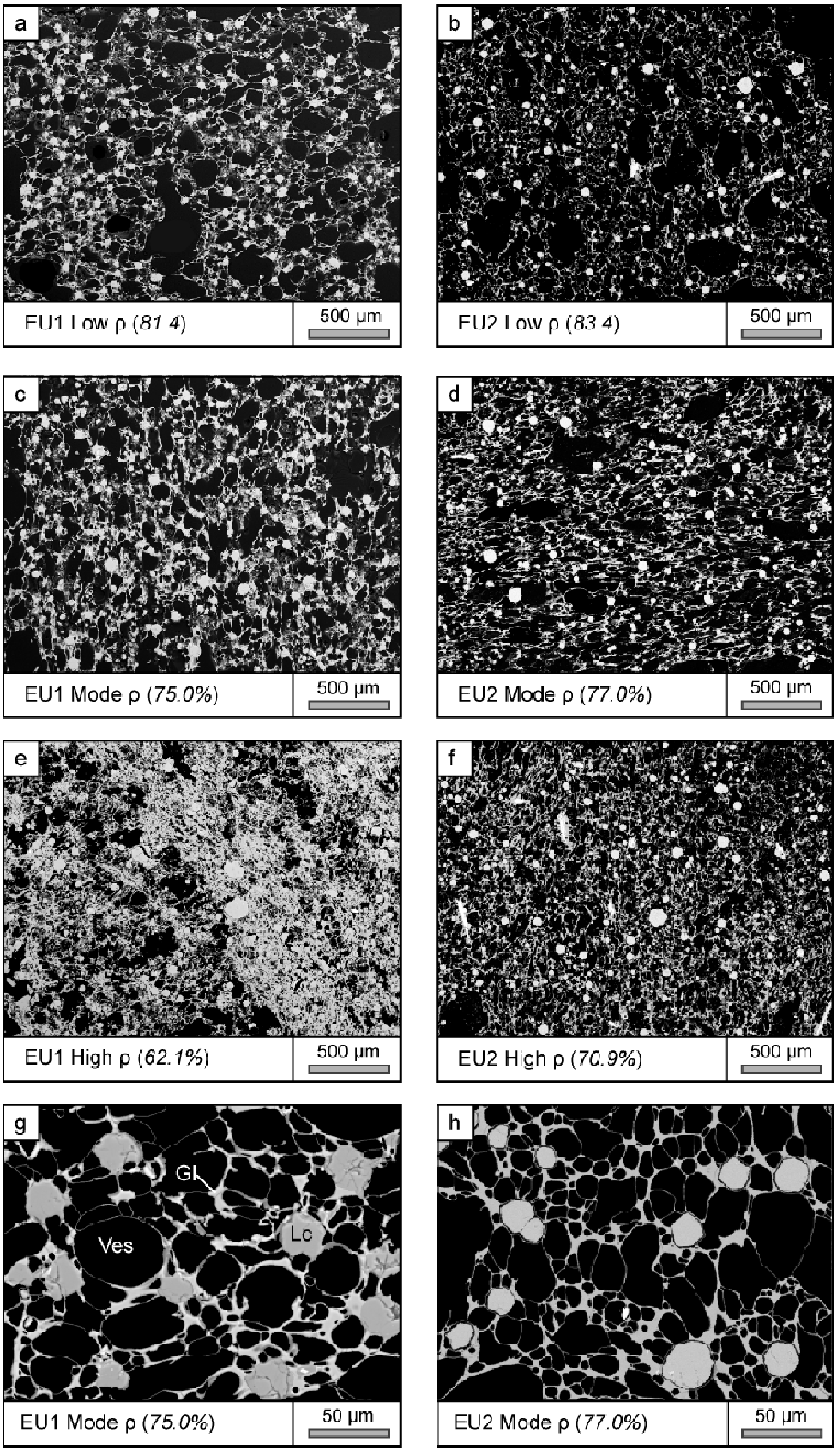

Figure 3: SEM images of EU1 and EU2 natural pumice samples. (a) low, (c) modal and (e) high density clasts chosen within EU1, and (b) low, (d) modal, (f) and high density clasts from EU2. Walls are somewhat thicker in EU1 and the high density end-member (e) possesses different textural zones. (g) and (h) are close-ups of modal density clasts from EU1 and EU2 respectively. Note in (h) the slightly higher proportion of very small bubbles in between glass nodes compared to (g).
Ves=vesicle, Gl=glass and Lc=leucite

Table 2: Summary of textural measurements performed in Natural and Experimental samples

	P_I [a]	P_F [b]	ΔP [c]	t [d]	ϕ_{2D} [e]	ϕ_{3D} [f]	$\phi_{L<0.01}$ [g]	L_{mean} [h]	$L_{maj\text{-}mode}$ [i]	$L_{min\text{-}mode}$ [j]	N_V [k]	N_{Vcorr} [l]	*D.Type* [m]	N_{Vox} [n]	J [o]	G_{mode} [p]
Natural samples																
$EU1_{low}$	-	-	-	-	73.8	81.4	2.9	0.27	0.03	0.381	0.63×10^{6}	3.4×10^{6}	*p* (3.42)	-	-	-
$EU2_{low}$	-	-	-	-	82.1	83.4	7.3	0.289	0.019	2.403	1.4×10^{6}	8.7×10^{6}	*p* (3.44)	-	-	-
$EU1_{mean}$	-	-	-	-	64.7	75	2.8	0.099	0.076	-	0.64×10^{6}	2.6×10^{6}	*p* (3.39)	-	-	-
$EU2_{mean}$	-	-	-	-	67.5	77	8.1	0.171	0.038	3.026	2.5×10^{6}	11×10^{6}	*p* (3.50)	-	-	-
$EU1_{high}$	-	-	-	-	51.1	62.1	7.9	0.108	0.048	0.604	2.9×10^{6}	7.8×10^{6}	*p* (3.47)	-	-	-
$EU2_{high}$	-	-	-	-	61.9	70.9	12.1	0.087	0.015	1.517	3.5×10^{6}	12×10^{6}	*p* (3.63)	-	-	-
Series A																
1-2a	150	125	25	100	3.8	8.3	3.48	0.009	0.005	-	0.75×10^{6}	0.82×10^{6}	*e/p*	9×10^{6}	8.21×10^{3}	5.10×10^{-5}
1-2b	150	100	50	200	6.3	12.1	5.12	0.017	0.013	-	0.95×10^{6}	1.1×10^{6}	*e* (376)	16×10^{6}	1.31×10^{3}	7.49×10^{-5}
1-2c	150	75	75	300	11.8	19.9	4.15	0.031	0.05	-	0.64×10^{6}	0.8×10^{6}	*p* (2.42)	11×10^{6}	0	37.53×10^{-5}
1-2d	150	50	100	400	23.2	35	2.82	0.09	0.158	-	0.22×10^{6}	0.34×10^{6}	e (187)	-	0	107.48×10^{-5}
1-2e	150	25	125	500	49.5	63	0.56	0.154	0.25	-	0.08×10^{6}	0.23×10^{6}	e (63)	-	0	92.19×10^{-5}
Series B																
2-3a	150	125	25	100	1.7	5.2	2.54	0.002	0.006	-	3.4×10^{6}	3.6×10^{6}	*e* (752)	44×10^{6}	36.2×10^{3}	6.31×10^{-5}
2-3b	150	100	50	200	5.6	11	10.18	0.006	0.008	-	5.2×10^{6}	5.9×10^{6}	*e* (712)	52×10^{6}	51.1×10^{3}	1.63×10^{-5}
2-3c	150	75	75	300	15.5	25.1	7.48	0.028	0.02	-	7.4×10^{6}	9.9×10^{6}	*e* (164)	45×10^{6}	11.2×10^{3}	12.01×10^{-5}
2-3d	150	50	100	400	22.4	33.9	8.73	0.035	0.05	-	4.5×10^{6}	6.8×10^{6}	*p* (2.51)	-	0	30.17×10^{-5}
2-3e	150	25	125	500	43.4	57.3	7.88	0.053	0.079	-	3.7×10^{6}	8.6×10^{6}	*e* (143)	-	0	29.48×10^{-5}
Series C																
26a	100	75	25	100	4.9	10	3.02		0.016	-	0.23×10^{6}	0.26×10^{6}	*e* (245)	3.3×10^{6}	2.56×10^{3}	15.76×10^{-5}
26b	100	50	50	200	16.3	26.1	3.14	0.038	0.05	-	0.27×10^{6}	0.36×10^{6}	*e* (144)	3.4×10^{6}	0.54×10^{3}	34.08×10^{-5}
26c	100	25	75	300	45.1	59	0.23	0.07	0.079	-	0.07×10^{6}	0.17×10^{6}	*e* (64)	-	0	29.15×10^{-5}
26d	100	10	90	360	76.5	82	0.05	0.193	0.252	-	0.01×10^{6}	0.08×10^{6}	*e* (22)	-	0	288.00×10^{-5}

a: Starting experimental pressure (MPa)
b: Final quench pressure (MPa)
c: Total decompression (MPa)
d: Total decompression time (s)
e: 2D-vesicularity obtained by area measurements (%)
f: 3D-vesicularity obtained by density-derived measurements (%)
g: Vesicularity for vesicle populations with diameters <0.01 mm (%)
h: Mean vesicle diameter (mm)
i: Major mode of size distribution (mm)
j: Minor mode of size distribution (mm)

k: Vesicle number density (mm^{-3})
l: Vesicle number density corrected for vesicularity (mm^{-3})
m: Type of distribution: *p:* power-law distribution of form $N_V(>L)\sim f(L^{-d})$ with corresponding exponents *d* in parentheses. *e*: exponential distribution of form $N_V\sim f(e^{-aL})$ with corresponding exponents *a* in parentheses. *e*/*p*: undetermined, both show good fit.

n: Oxide microlite number density corrected for vesicularity (mm^{-3})
o: Nucleation rates ($mm^{-3}\ s^{-1}$)
p: Growth rates calculated using modal sizes ($mm\ s^{-1}$)

5.1.2. Measurements

Measurements of natural and experimental vesicle sizes, numbers, and other relevant parameters are reported in Table 2. Vesicularities for the two sets of natural samples are 62, 75, 81% low, modal and high densities respectively for EU1, and 71, 77, 83% for EU2 (Fig. 2). Vesicle size distributions (VSD, Fig. 4a) differ in that the modal sample of EU1 lacks the larger portion of the population visible in EU2 modal. Both EU1 and EU2 low density clasts show extended tails towards large vesicles (> 1.5 mm) while the high density end-members contain only vesicles < 1.5 mm. VSD curves, which are used to infer the steadiness of the vesiculation process (e.g. Cashman and Marsh, 1988; Mangan and Cashman, 1996, Klug et al., 2002; Adams et al., 2006), show gradual rather than abrupt changes. Kinks within the larger populations (>500 μm) are artifacts of lower sampling frequency associated with geometric binning.

Size distributions expressed as volume fraction histograms (Vesicle Volume Distributions "VVD", Fig. 4b) provide a more detailed view of the larger (and less numerous) vesicles. Low density clasts have a dominant mode at 20–30 μm, and a secondary mode at larger sizes caused by coalescence (e.g. Klug et al., 2002). EU1 and EU2 mean density clasts show minor differences at comparable vesicularities (75 and 77% EU1 and EU2 respectively); EU1 is unimodal whereas EU2 could be bimodal. Lastly, EU1 and EU2 high density distributions both have one dominant mode. For high-density samples, in contrast with low and mean density pumices, vesicularities differ strongly (62% and 71% for EU1 and EU2 respectively) probably due to shearing-induced bubble collapse within narrows zones of EU1 (Fig. 3e).

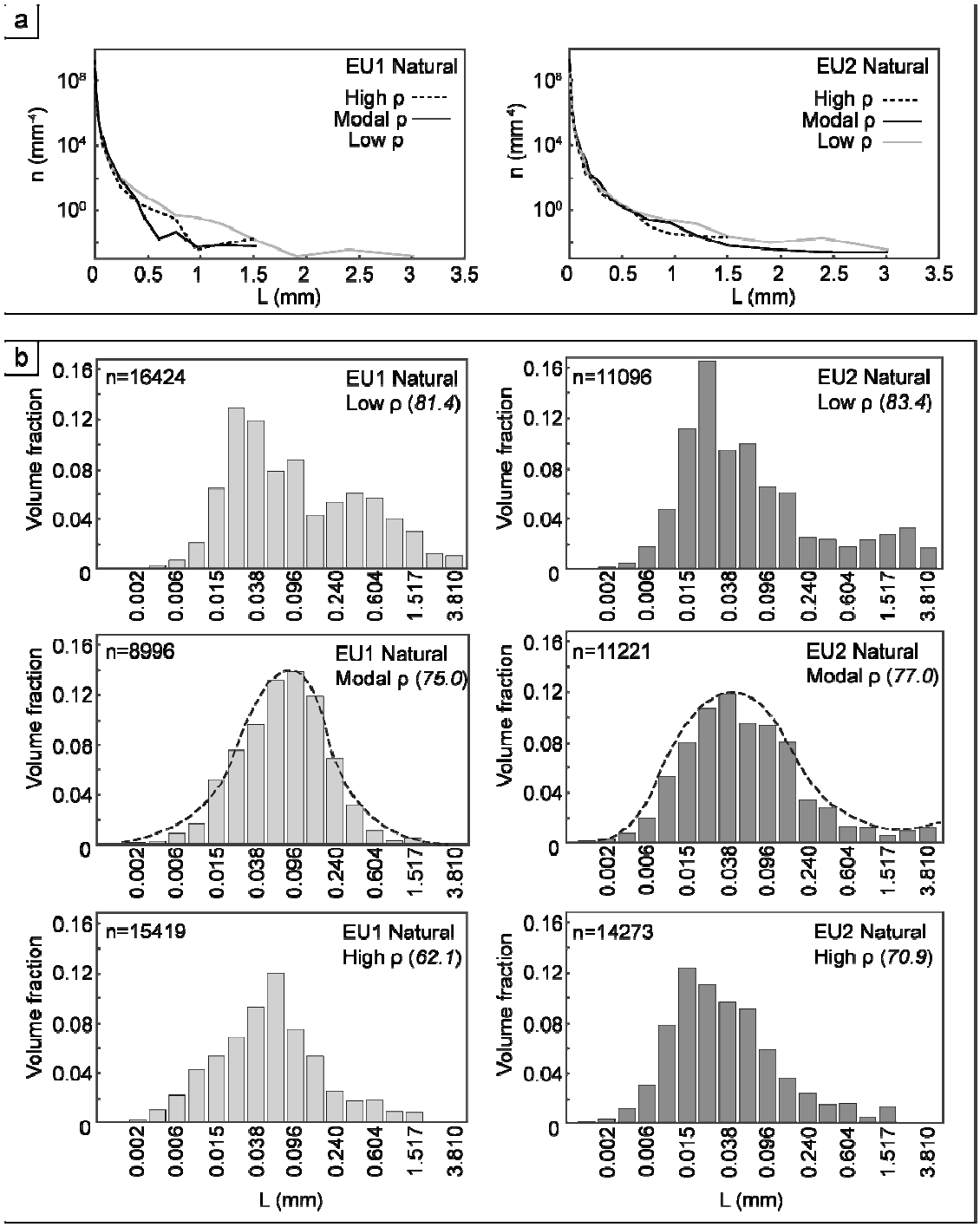

Figure 4: (a) Vesicle size distributions for EU1 and EU2 vs. equivalent diameter (*L*, linear scale). (b) Vesicle size distributions in terms of volume fractions vs. equivalent diameter (*L*, geometric scale) display different modes. Note that volume fractions sum to vesicularity values for each sample. Fitted curves in modal clasts are used in Fig. 6 to compare with experiments. n=number of vesicles analyzed.

In general, dominant modes are about two to three times larger in size in EU1 compared to EU2 (Table 2), irrespective of clast vesicularity. Calculated N_{Vcorr} values are systematically higher in EU2 than in EU1 for all clast densities (close to 3×10^6 mm^{-3} for EU1 and around 1×10^7 mm^{-3} for EU2). The smallest vesicles (L<0.01 mm) are the most numerous (VSDs, Fig. 4a) and their contribution to total porosity is non-negligible (~3 to 12% vesicularity $\phi_{L<0.01}$, Table 2).

Gurioli et al. (2005b) interpreted EU2 to have undergone continuous nucleation and growth. Additional information is provided by comparison with EU1 data; EU1 vesicle modes (0.03, 0.08, and 0.05 mm, cf. Table 2) are slightly larger than EU2 (0.02, 0.04, and 0.015mm), which could indicate more time in the conduit after nucleation of late-stage bubble populations or simply differing ascent rates in the upper regions of the conduit prior to fragmentation. In all pumice samples analyzed, cumulative VSDs are best characterized by power-law distributions (cf. Blower et al., 2001) with exponents d>3 (Table 2).

5.2. Textural characterization of laboratory experiments

To provide direct comparison between natural samples and experiments, observations of the development of vesicle textures during decompression are followed by descriptions of textural measurements made within each experimental series.

5.2.1. Vesiculation during experiments: observations

The evolution of the exsolution process in series A and B (P_I=150 MPa) and C (P_I=100 MPa) is illustrated in Fig. 5 by SEM photos of experimental charges (see Table 2

for measurements). Bubbles nucleate soon after decompression (Fig. 5a,b,c), indicating that a large supersaturation is not required to initiate vesiculation in H_2O-saturated Vesuvius phonolites. As expected, bubbles grow larger at lower ending pressures and start to coalesce at the lowest pressure reached (P_F=25 MPa in series A and B, and P_F=10 MPa for series C).

At P_F=125 MPa, the numerous small bubbles present within series A and B experiments appear homogeneously distributed within the melt (Fig. 5a and b), often associated with oxides (titanomagnetite ±hematite, Fig. 5d, e, f). At P_F=50 MPa, vesicles have grown much larger, although EU2 samples retain smaller bubbles. After decompression to P_F=25 MPa, series A is dominated by closely-spaced large bubbles separated by thin walls, whereas series B contains fewer but larger bubbles separated by thick glass walls. Coalescence areas appear more dominant within series B. At the lowest final pressure, series A and B have calculated vesicularities of 63 and 57% respectively, which are lower than in most natural 79AD samples, and are likely a consequence of incomplete decompression. The most apparent differences can be expressed in terms of bubble shape and outline: large series A vesicles are mostly round with smooth walls, whereas series B vesicles show irregular shapes with ragged walls. Even at very low ΔP (P_F=125-100 MPa), tiny series B vesicles show faceted outlines whereas series A vesicles are round (Fig. 5a and b). This striking difference can be attributed to the high numbers of 1–3 μm-sized sanidine microlites within series B glass (Fig. 5e), whereas series A glass lacks microlites other than oxides (Fig. 5a).

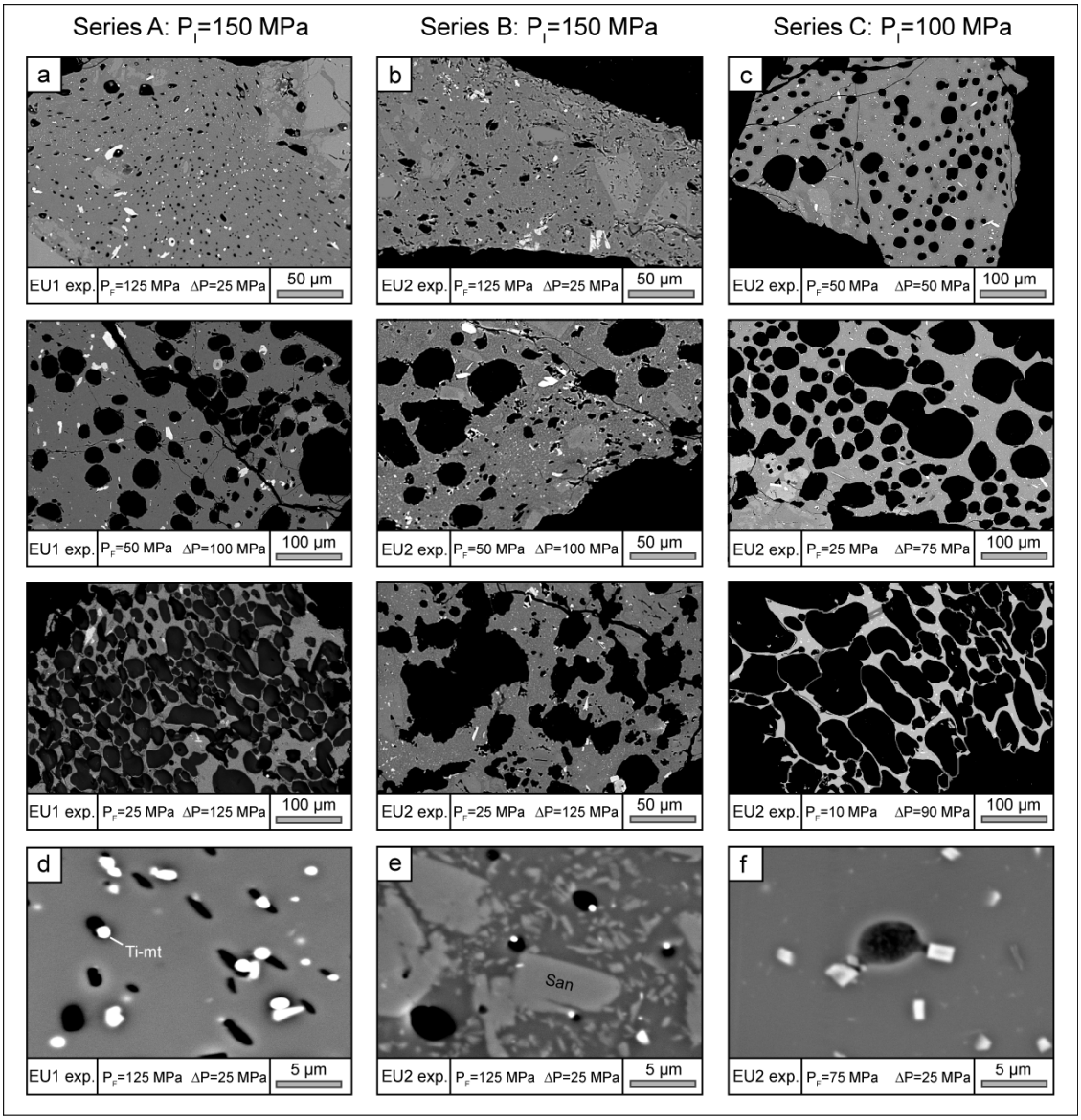

Figure 5: SEM images of experimental samples quenched at different pressure conditions. (a) Series A and (b) Series B started at P_I=150 MPa and quenched at P_F=100, 50 and 25 MPa, and (c) Series C started at P_I=100 MPa and quenched at P_F=50, 25 and 10 MPa. Vesicles in Series B have fairly distorted shapes and ragged glass walls compared to Series A and C or natural samples. (d), (e), and (f) are close-ups (5000X magnification) of groundmasses from all three series showing bubbles often nucleate on titanomagnetites. Note the numerous sanidine microlites within series B compared to series A and C. Black=vesicles, dark gray=glass, white=oxide microlites.

Series C experiments involved the same EU2 starting material used for Series B experiments, but the results differ considerably. Much like in Series A, vesicles are dominantly round, their boundaries smooth, and the surrounding glass is clear and homogeneous containing fewer oxide microlites (Fig. 5f). At a similar ending pressure of P_F=25 MPa, vesicularity is comparable to series A and B (59%) and at P_F=10 MPa attain 82% as vesicle walls become extremely thin (Fig. 5c). Judging from vesicle shape, coalescence appears to be more dominant in series C than in other series: glass walls are often deformed and seem to be on the verge of rupturing (Fig. 5c).

In terms of general appearance, EU1 and EU2 natural samples more closely resemble series A and C than series B. Compared to series A and C, however, vesicle walls are typically thinner in natural samples and glass nodes are less prominent. In addition, the number of small vesicles between large bubbles is much higher in natural samples, where configurations closer to Apollonian packing (i.e., minimization of space by packing spheres of varying radii) are reached. In contrast, experimental samples have a limited size range, even after extensive decompression.

5.2.2. Measurements

Quantification procedures identical to those used for natural samples were employed to characterize decompression experiments. Unfortunately, due to the reduced sample volume within experimental capsules, observations are limited to about 4 mm^2 in area and measurements are restricted to a 0.001–0.240 mm interval. Because modes are not well depicted by VSDs, the distributions are reported only as VVDs (Fig. 6), with EU1 and EU2 mean density distributions shown for comparison.

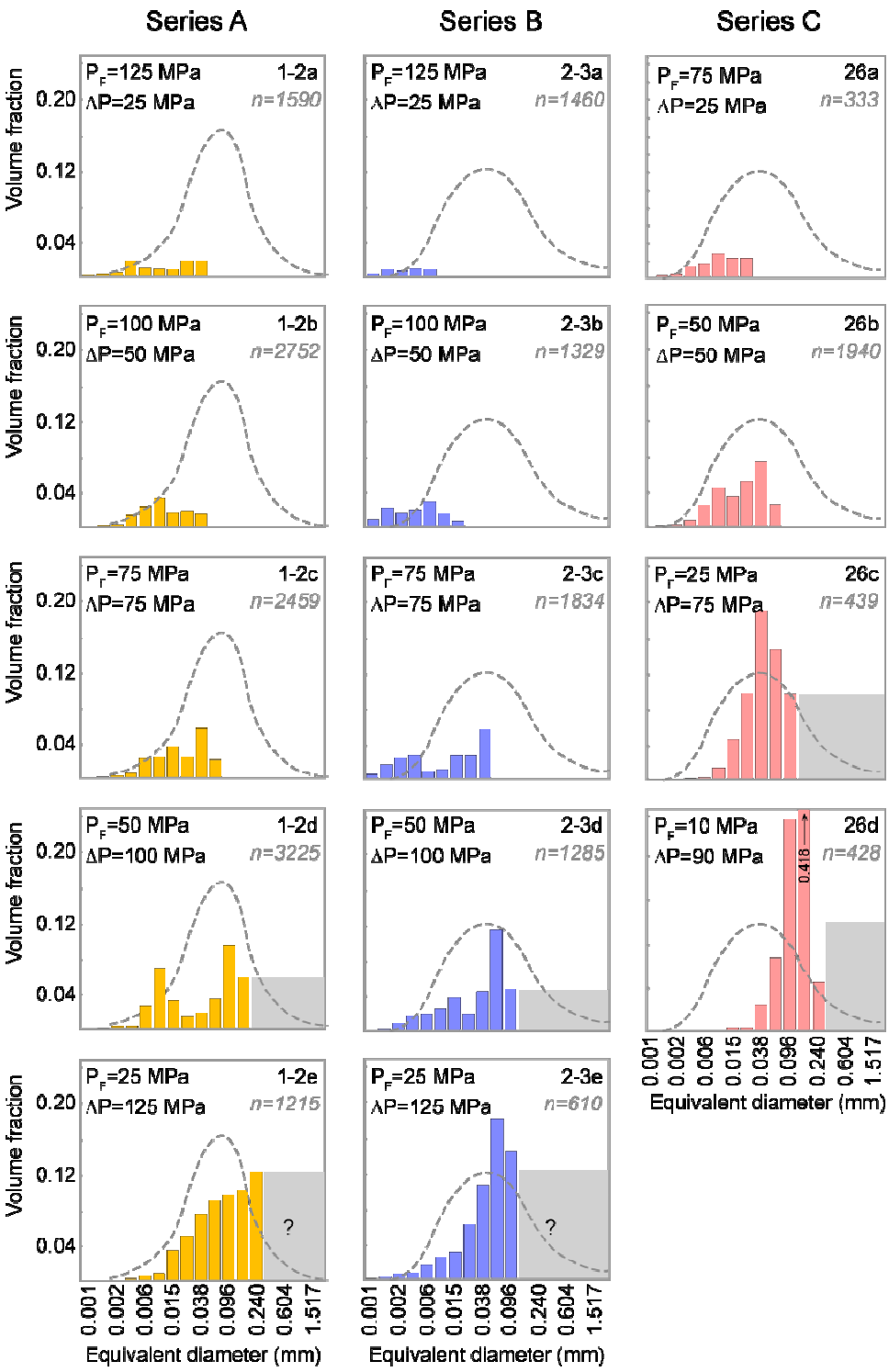

Figure 6: VSDs for Series A, B and C at different final pressures. Vesicles larger than 0.240 mm are not accounted for. The shaded region represents the portion of the size distribution for which we cannot make inferences. Size distribution curves (dashed lines) for EU1 and EU2 modal densities are reported along with their corresponding series. Note that volume fractions sum to vesicularity values for each sample.

Inspection of the smaller size range (0.001–0.010 mm) reveals that both series A and B possess small vesicles throughout decompression, in contrast to series C, where they disappear with decompression. All three series have dominant modes that increase in size with decompression, but do not achieve the size range seen in pumice samples (Fig. 6). Interestingly, series A and B VVDs are polymodal until P_F=25 MPa, where only one mode remains, although the limited measurable size range may mask secondary modes associated with coalescence. Series C preserves only one mode and has larger modal sizes than Series B.

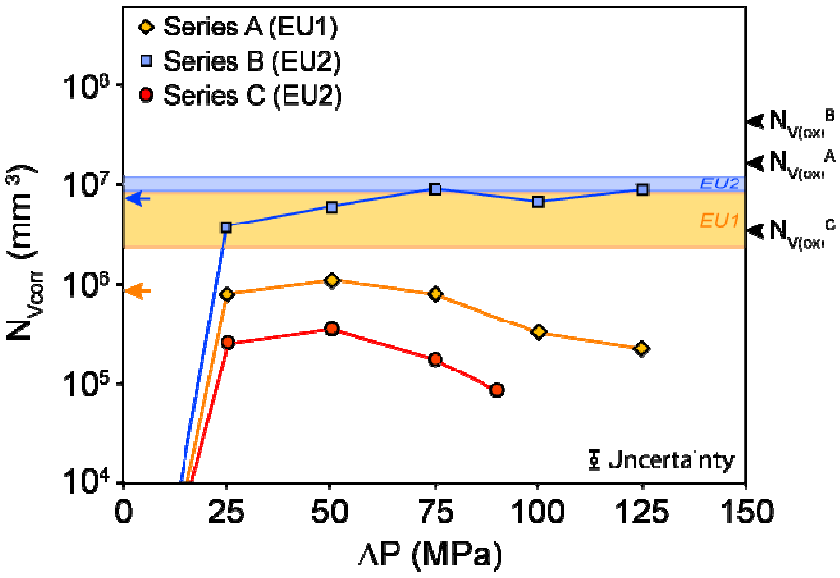

Figure 7: Vesicle number density (N_{Vcorr}) variations within experiments as a function of the amount of decompression undergone (ΔP). Number density ranges measured in natural pumice from low to high density clasts are also included on the y-axis. The maximum uncertainty is reported on the bottom right. The two arrows on the y-axis show values taken for calculations leading to Fig. 11 (see text).

Vesicle number densities (N_{Vcorr}, Table 2) in all three series show rapid increases before reaching a plateau (Series B) or declining (Series A and C; Fig. 7). Series A reaches a maximum of $N_{Vcorr} \approx 10^6$ mm^{-3}, which drops to 10^5 mm^{-3} at ΔP=125 MPa (P_F = 25 MPa). In contrast, Series B attains values of 10^7 mm^{-3}. Series C N_V values are significantly lower than series A and B, reaching a maximum of 4×10^5 mm^{-3}. These

experimental number densities barely reach the range of N_V values measured in natural samples, with the exception of Series B, where number densities overlap with the most vesicular EU2 sample. Most experimental cumulative VSDs show distributions that follow exponential functions (Table 2) with exponents decreasing with increasing decompression.

6. Discussion

6.1. Assumptions inherent to experimental procedure

Before laboratory experiments can be compared to the natural samples, several underlying assumptions need further consideration. Initial materials used for these experiments were crushed into fine powder and then either annealed at 1000°C or inserted directly into experimental capsules for equilibration at high pressure and temperature prior to decompression. Using powders without fusing them at high temperatures (i.e. series A and B) presents the disadvantage that pore spaces or hydration bubbles may be present at the onset of decompression (Larsen and Gardner, 2000, 2004). In series A and B samples, a few hydration bubbles can be observed but are in such small numbers that their contribution is considered insignificant (cf., Gardner et al., 1999). In comparison, fusing samples prior to equilibration (i.e. series C) reduces pore spaces, but has the drawback of annealing some microlites that might otherwise be present within the natural melt stored in the crust prior to eruption.

6.2. Heterogeneous nucleation in 79AD Vesuvius phonolites

Our experiments show that <25 MPa of decompression was required to initiate vesiculation in all experiments, in contrast to the high degrees of supersaturation typically necessary to trigger homogeneous nucleation in rhyolites (Mangan and Sisson, 2000; Mourtada-Bonnefoi and Laporte, 2004) or phonolites (Iacono Marziano et al., 2007). The low pressure drop required to generate bubbles reflects heterogeneous nucleation, as pre-existing microlites provide surfaces on which bubble embryos can form (Hurwitz and Navon, 1994; Navon and Lyakhovsky, 1998; Gardner et al., 1999; Mangan and Sisson, 2000, Cluzel et al., 2008). Larsen (2008) reached a similar conclusion for K-phonolites at higher temperatures and, like Hurwitz and Navon (1994), suggested microscopic crystalline phases as potential nucleation sites.

In our experiments, bubbles nucleate both on and away from microlites (e.g. Fig. 5d, e, f); Furthermore, as seen in other experiments, only oxides serve as bubble nucleation sites (Fig. 5e; Hurwitz and Navon, 1994; Navon and Lyakhovsky, 1998; Cluzel et al., 2008). To investigate the relationship between vesicles and microlites in more detail, oxide number densities N_{Vox} were measured in experimental series. In series A, B, and C, resulting N_{Vox} are 1×10^7, 5×10^7, 3×10^6 mm^{-3} respectively, five to ten times higher than their corresponding vesicle number density (Table 2, Fig. 7). Thus, for each series, there are more available nucleation sites than there are nucleating bubbles. Series A and B used slightly different compositions but identical experimental procedures. Series B and C used identical starting compositions but different pre-decompression treatment (Series C samples were annealed at high temperature). From this we infer that nucleation is limited by properties of the melt (water diffusivity and/or surface tension)

and the time scale of decompression. As oxides are already present in the melt before decompression, oxide number density should be controlled by pre-eruptive composition and temperature rather than decompression rate. Differences in measured vesicle number density between the three series (cf. Fig. 7) are thus only partially related to the number density of oxide phases since all available nucleation sites are not utilized.

6.3. Equilibrium exsolution

To verify whether our experiments followed equilibrium exsolution paths, vesicularities measured in Series A, B, and C are shown in Fig. 8 along with equilibrium curves given by Gardner et al. (1999) as:

$$\phi = \left[\frac{\frac{\rho}{Z}\overline{V}_{H2O}\left(w_I - w_F\right)}{1+\left(\frac{\rho}{Z}\overline{V}_{H2O}\left(w_I - w_F\right)\right)} \right] \qquad \text{(Eq. 2)}$$

where ρ is magma density in kg m^{-3}, Z is molecular water weight in kg, w_I and w_F are the weight fractions of dissolved water at initial and final pressures determined using the solubility model of Larsen (2008), and $\overline{V}_{H2O}$ the molar volume of water (in vapor phase) at the final pressure in m^3.

Within uncertainty, experimental porosities follow the equilibrium line very closely for all series, attaining about 60% at P_F=25 MPa, and 82% at P_F=10 MPa in Series C. Thus, the experiments not only nucleated bubbles rapidly at low ΔP, but

maintained equilibrium degassing paths during decompression. When compared with Larsen's (2008) results, which show disequilibrium degassing at T = 900˚C and decompression rates ≥ 3 MPa/s, this illustrates the sensitivity of degassing trends to both magma properties and decompression conditions (see also Larsen and Gardner, 2004).

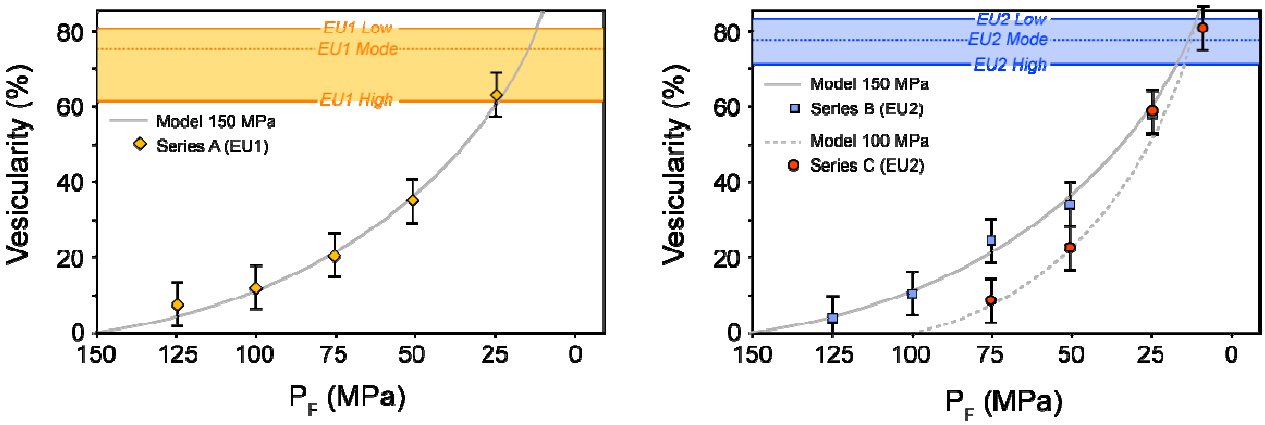

Figure 8: Variations in vesicularity shown by experimental samples from Series A, B and C compared to predicted equilibrium vesicularities following the model of Gardner et al. (1999). Vesicularities within low, modal and high density natural clasts are also reported on the y-axis for comparison. Maximum uncertainties reported are associated with vesicularity correction scheme imposed (see Appendix A for details).

6.4. Evolution of vesicle size during decompression

To investigate bubble growth, we compare vesicle sizes measured within experiments to those found in natural pumice. We compare modal sizes for samples representative of each final pressure achieved in series A, B and C with the ranges measured within EU1 and EU2 low, mean and high densities (Fig. 9). All series reach modal sizes measured in natural samples by $P_F \approx 75$ MPa regardless of starting pressure, which indicates that pressure exerts the primary control on bubble size. However, quenching at this pressure is unrealistic for the Vesuvius eruption. For this reason, we

infer that at least one experimental variable strongly differs from 79AD eruption conditions. The most likely is decompression rate, as more rapid magma ascent and decompression implies less time spent within the conduit, and consequently smaller bubbles.

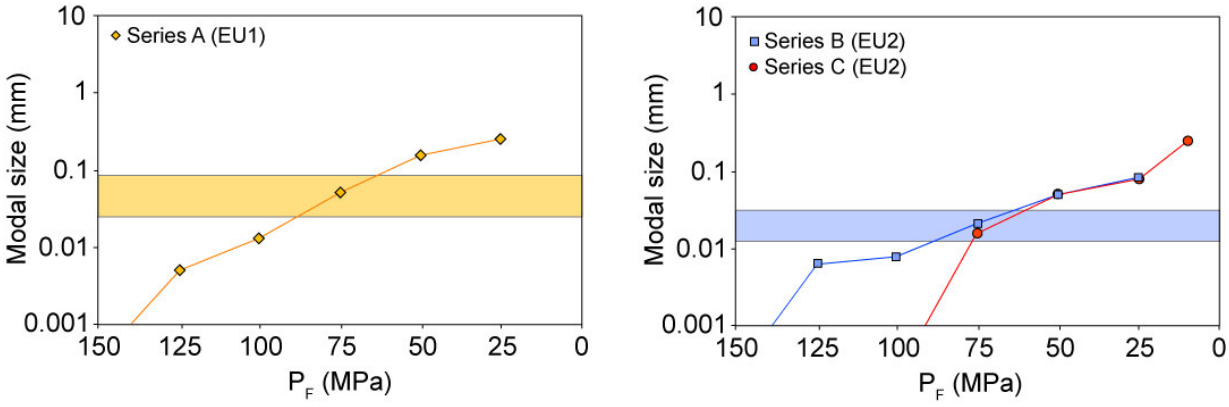

Figure 9: Modal sizes of experimental samples obtained from size distributions from all three series. Ranges of modal sizes measured in natural samples (low, modal and high densities) are also plotted on the y-axis for comparison. Experimental samples all reach modal sizes measured in natural pumice at P_F=75MPa.

6.5. *Evolution of nucleation and growth through decompression*

Modal growth rate (G_{mode}) variations during decompression can be calculated directly at each 25 MPa step using modal sizes and experimental times. We consider only additional growth at each step of decompression (Table 2 and Fig. 10a). Although series A shows higher growth rates than Series B, both have growth rates that increase slowly until P_F=90–100 MPa, after which values increase abruptly to achieve maximum values at P_F=50 MPa. Series C has maximum growth rates at lower P_F, with growth rates escalating at P_F=25 MPa, most likely due to the onset of coalescence.

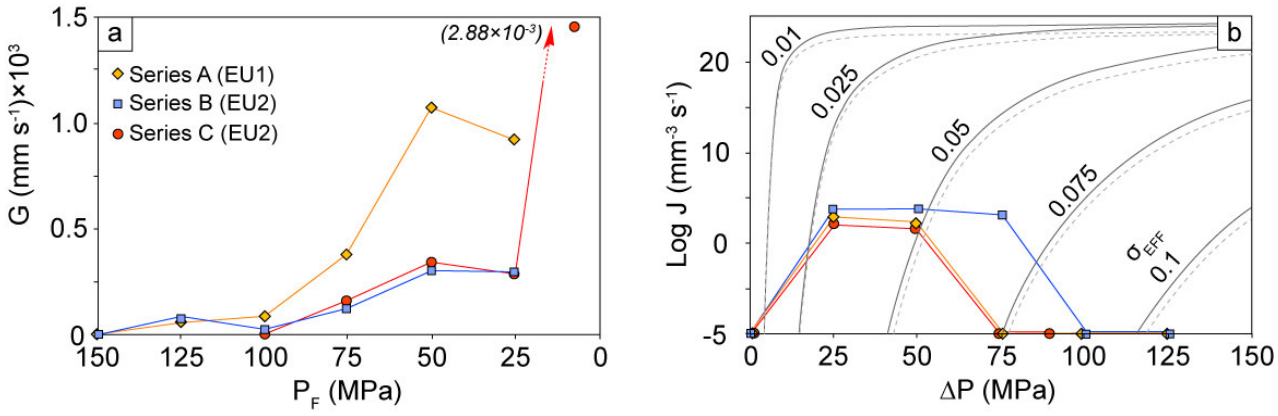

Figure 10: (a) Growth rates *G* measured within experimental samples. Because G_{mode} strongly depends on final pressure rather than ΔP, growth rates are plotted against P_F. (b) Nucleation rates J are a direct function of ΔP, and values measured in experiments are compared to curves obtained from the classical nucleation theory (gray curves) for various values of effective surface tension σ_{EFF} (N m^{-1}) and a diffusivity D=10^{-12} m s^{-2}. Similar curves calculated using diffusivity values D=10^{-11} m s^{-2} are also shown for comparison (dotted lines). Exsolution in series A and B is first dominated by bubble nucleation and then subject to prevailing growth as no new bubbles are formed. In series C, growth is more influential at the onset of vesiculation. Notice that nucleation occurs through a wide range of effective surface tension values as samples are decompressed.

Nucleation rates were calculated using differences in N_{Vcorr} between successive experiments divided by the decompression time interval. We compare them to those derived from classical nucleation theory (CNT). Nucleation rates depend directly on the free energy change required to form a cluster and are expressed as (Turnbull and Fisher, 1949; Hurwitz and Navon, 1994; Mangan and Sisson, 2000, 2005; Mourtada-Bonnefoi and Laporte, 2002, 2004; Cluzel et al., 2008):

$$J = J_0 \cdot e^{-\frac{16\pi\sigma_{\text{hom}}^{\ 3}}{3kT(P_V - P_M)^2}} \qquad \text{(Eq. 3)}$$

where J and J_0 are nucleation rate and a pre-exponential parameter respectively, in m^{-3} s^{-1}, σ_{hom} is melt-bubble surface tension for homogeneous nucleation in N m^{-1}, k is the Boltzmann constant in J K^{-1}, T is temperature in K, and P_V and P_M are critical nucleus and melt pressures respectively.

In turn, J_0 is expressed as:

$$J_0 = \frac{2\Omega_M n_0^2 D}{a_0}\sqrt{\frac{\sigma}{kT}} \qquad \text{(Eq. 4)}$$

where Ω_M is volume of water molecules in the melt in m^3, D is water diffusivity in m^2 s^{-1}, n_0 is the number of water molecules per unit volume of melt in m^{-3} calculated as $n_0 = \Pi_A X_M \frac{\rho}{m}$, with Π_A being Avogadro's number, ρ the melt density in kg m^{-3}, X_M the mass fraction of water within the melt, and m the molar mass of water; finally, $a_0 \approx n_0^{-\frac{1}{3}}$ is the mean distance between neighboring water molecules (Cluzel et al., 2008). In heterogeneous nucleation, the activation energy is reduced by a factor φ expressed as (Hurwitz and Navon, 1994; Navon and Lyakhovsky, 1998):

$$\varphi = \frac{(2-\cos\theta)(1+\cos\theta)^2}{4} \qquad \text{(Eq. 5)}$$

where θ is the wetting angle between bubble and crystal. Because we do not know θ for the oxides that serve as nucleation sites, we replace σ_{HOM} by an "effective" surface tension σ_{EFF} that incorporates the activation energy reduction term expressed as $\sigma_{EFF} = \varphi^{1/3}\sigma_{HOM}$ (Cluzel et al., 2008). This term thus incorporates all parameters that facilitate nucleation (e.g. microlites). Our observation that there seems to be no barrier to nucleation supports the assumption that the number of nucleation sites is larger than the total number of vesicles and that $P_V \approx P_{SAT}$, where P_{SAT} is the saturation pressure and P_V the critical nuclei pressure. Thus, $P_{SAT} - P_M = \Delta P$ in nucleation rate calculations. Water diffusivity is assumed to be D=2×10^{-12} m^2 s^{-1}, based on D=2×10^{-10} m^2 s^{-1} for Vesuvius phonolites at T=1050°C (Iacono Marziano et al. 2007) and a factor of 100 correction to account for the temperature difference (Watson, 1994; Larsen, 2008).

Eq. (3) was solved for various effective surface tensions ranging from 0.01 to 0.1 N m^{-1}, and results are plotted along with experimental data (Fig. 10b). As expected, experiments indicate a low effective surface tension (<0.075 N m^{-1}) at 25≤ ΔP≤75 MPa and nucleation rates drop to 0 at ΔP=50-75 MPa. Prolonged nucleation in Series B experiments is indicated by the presence of small bubbles at ΔP=75 MPa (Fig. 6). In all series, nucleation rate trends traverse a range of effective surface tensions, as observed by Mangan and Sisson (2005) for dacites and rhyolites. After 25 MPa of decompression, all three series plot close to effective surface tensions as low as 0.030 N m^{-1} (Fig. 10b). Similar values of σ_{EFF} were found by Mourtada-Bonnefoi and Laporte (2004) in dacites using data from Gardner et al. (1999).

A comparison of growth and nucleation rates (Fig. 10a and b) reveals that nucleation is dominant for the first 50-75 MPa of decompression in series A and B, after which growth takes over. Thus, equilibrium vesicularities are maintained first by vigorous nucleation and then by diffusive growth with no addition of new bubbles. In series C, growth is much more rapid at the beginning of decompression. In all series, bubble numbers decrease at low pressures as smaller bubbles coalesce.

6.6. Comparisons with numerical models

We use the numerical models of Toramaru (1995, 2006) to predict vesicle number densities (N_{const}) as a function of decompression rate, diffusivity, and the surface tension between melt and bubbles (Yamada et al., 2006; Toramaru, 2006). For comparison with pumice samples, we use number densities $N_{Vcorr}\approx 3\times10^6$ mm^{-3} and $N_{Vcorr}\approx 11\times10^6$ mm^{-3} measured in EU1 and EU2 modal density samples respectively (Table 2). Similarly, experimental plateau values are used, that is, $N_{Vcorr}\approx 1\times10^6$ mm^{-3}, 6.5×10^6 mm^{-3}, and 0.3×10^6 mm^{-3} in series A, B and C respectively.

The number density predicted by Toramaru's model, here labeled N_{const} for constant number density, is written (Toramaru, 2006):

$$N_{const} = 34 X_0 \alpha_1^{-2} \alpha_2^{-\frac{1}{4}} \alpha_3^{-\frac{3}{2}} \qquad \text{(Eq. 6)}$$

Here X_0 is the initial water concentration at the saturation pressure, and α_1, α_2, α_3 represent dimensionless parameters (Toramaru, 1995) that are defined as:

$$\alpha_1 = \frac{16\pi\sigma_{HOM}^3}{3kTP_0^2} \quad \text{(Eq. 7)}$$

$$\alpha_2 = \frac{\Omega_M P_0}{kT} \quad \text{(Eq. 8)}$$

$$\alpha_3 = \frac{kTX_0 DP_0}{4\sigma_{HOM}^2 \left|\frac{dP}{dt}\right|} \quad \text{(Eq. 9)}$$

As in earlier calculations, σ_{HOM} is replaced by σ_{EFF} to account for activation energy reduction during heterogeneous nucleation.

Figure 11 shows the influence of both decompression rate (*dP/dt*) and effective surface tension (σ_{EFF}) on the maximum stable value of N_{const}. Experimental number densities agree well with the model if σ_{EFF} = 0.02, 0.035 and 0.045 N m^{-1} for series A, B and C respectively. These values are similar to effective surface tensions estimated for small ΔP experiments using Eq. (3) (Fig. 10b) and with estimates by Mourtada-Bonnefoi and Laporte (2004) and Mangan and Sisson (2005) for dacites. We also compare the numerical results with measured number densities (N_{Vcorr}; Table 2) for EU1 and EU2 samples. Assuming that experimental surface tensions of 0.035 N m^{-1} calculated from series A can be extrapolated to both EU1 and EU2, decompression rates of ~0.5 and 1.0 MPa/s could produce the N_{Vcorr} measured in EU1 and EU2 natural samples respectively. If, however, effective surface tension in EU2 was closer to series C values (i.e. 0.045 N m^{-1}), decompression rates of about 2 MPa/s are needed.

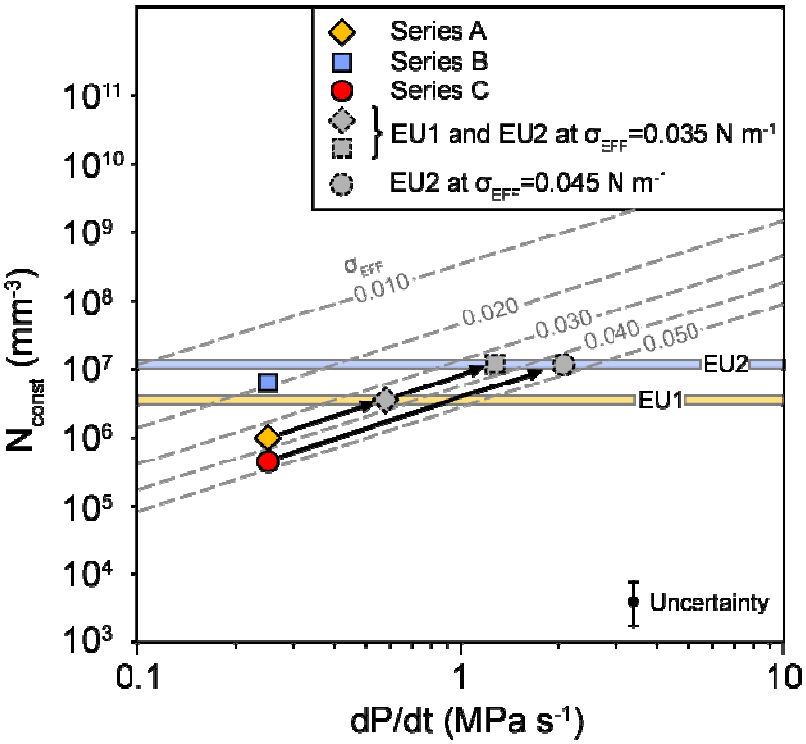

Figure 11: Number densities in function of ascent rate log(*dP/dT*) as predicted by the model of Toramaru (1995, 2006) for varying effective surface tensions σ_{EFF}=0.01-0.05 N m^{-1} (dashed gray lines). Values measured in natural samples are also reported for comparison along with corresponding experiments (plotted according to their N_{Vcorr} and for *dP/dt*=0.25 MPa/s). Arrows and dotted gray symbols represent increases in *dP/dT* required to attain values measured in natural samples if σ_{EFF}=0.035 N m^{-1} is adopted (see text). Uncertainty on N_V is displayed at the bottom right.

6.7. Volcanological implications

Our comparison of pumice samples, experimental charges and numerical models raises several questions. The first relates to differences in the vesiculation characteristics of EU1 and EU2 magmas. EU1 natural samples and series A experiments have larger but fewer vesicles than EU2 natural samples and series B experiments. If the differences in natural samples were solely a function of varying decompression rates, then the experiments should have yielded identical results. Shea et al. (2009) show that the compositional difference between the two eruptive units caused shifts in phase equilibria curves for leucite and other phases. Indeed, sanidine microlites crystallized vigorously within series B but not series A experiments. The textures show that the presence of sanidine affected the form, if not the rate, of vesiculation in the experiments. However

EU2 pumice clasts show no evidence of sanidine. Thus, the experimental conditions chosen for replication of EU2 vesiculation failed to adequately reproduce natural conditions. The recent results of Shea et al. (2009) suggest that higher experimental temperatures are necessary to prevent sanidine crystallization.

A second question relates to the observed form of the vesicle size distributions. Vesicle number densities measured within experimental samples are only slightly lower than those found in pumice. Our calculations show that decompression rates two to eight times faster would better replicate observed number densities. It follows that two hypotheses can be put forward to explain differences in number densities between the opening and the Plinian phase of the 79AD eruption: either that EU1 and EU2 melts, although chemically related, are different enough that their physical properties (particularly microlite concentrations) promote bubble nucleation in EU2 magma, or that EU2 erupted more rapidly than EU1. Whereas experiments suggest that the presence of oxides could significantly influence the outcome of vesiculation, field evidence supports differences in ascent rates between eruption of EU1 and EU2. Calculations of column height and discharge rate for the eruption (Carey and Sigurdsson, 1987) demonstrated that the column height increased along with discharge rate during eruption of the white magma (c.f. Fig. 1). Hence, it is likely that ascent rates within the conduit were higher during emission of EU2 than they were during the opening phase EU1.

Vesicle size variability is much broader in nature when compared to experiments (cf. Fig. 3 and Fig. 5). This variability can be quantified by comparing VVDs (Fig. 6). Additionally, it appears that modal sizes measured in EU1 and EU2 are attained too early in the inferred (experimental) decompression history (Fig. 9). This is a strong indication

that vesiculation undergone by natural magmas is more complex than in simple decompression experiments. Natural pumice shows near-Apollonian packing configuration predicted for continuous nucleation (Blower et al., 2001; 2002), with VSDs that follow power law distributions (exponents d=3.4–3.6 Table 2). In contrast, experimental samples show thinner glass walls and VSDs that follow exponential distributions, indicating one or few pulses of nucleation (Blower et al., 2002). Experiments show that nucleation is not steady for a constant decompression rate (Fig. 10b) but rather peaks and drops fairly rapidly. Hence, the pressure perturbation responsible for continuous nucleation during ascent of natural magmas is unlikely to be generated by a steady decompression rate, as in the experiments. This confirms that magmas such as those involved in the 79AD eruption have more complex ascent and vesiculation histories than simple "continuous nucleation and growth" models often proposed to account for vesicle textures observed in pyroclasts.

6.8. Comparisons with other magmas and implications for the style of ascent

Larsen's (2008) experiments run at EU2 temperatures (T=900°C) and $dP/dT \geq 3$ MPa/s, did not show equilibrium degassing. Experiments on rhyolitic magmas show similar disequilibrium at decompression rates >0.025 MPa/s, due to much slower diffusion and resulting build-up of high supersaturation levels (Gardner et al., 1999; Mangan and Sisson, 2000; Mourtada-Bonnefoi and Laporte, 2004; Cluzel et al., 2008). A common conclusion is that impeded nucleation may be the key to generating the extreme

explosivity of silicic magmas. In most models, because diffusion is slow in rhyolites or rhyodacites, bubbles nucleate in numbers reaching 10^6–10^7 mm^{-3} (Mourtada-Bonnefoi and Laporte, 1999, 2002; Gardner and Denis, 2004) only after the critical supersaturation pressure is exceeded. In microlite-bearing K-phonolites, no supersaturation is needed for bubbles to nucleate; nevertheless they attain numbers similar to those measured in more silicic magmas (Larsen and Gardner, 2004; Iacono Marziano et al., 2007; Larsen, 2008; this study).

The difference in vesiculation behavior between more evolved silicic and less evolved alkalic magmas has important implications for the style of volcanic eruption. If rhyolitic melts are brought to extremely unstable thermodynamic states by build-up of oversaturation, they may fragment as a consequence of sudden nucleation and growth (e.g. Cluzel et al., 2008). In contrast, phonolitic melts tend to track equilibrium water contents and vesicularities along the decompression path, as long as decompression rates are lower than 5 MPa/s. It is thus much more likely that fast ascent is the main fragmentation-triggering mechanism in phonolite systems, ultimately responsible for initiating and sustaining the Plinian eruption of Vesuvius in 79AD.

6.9. The uses and limits of linear laboratory vesiculation experiments

We have illustrated how textures observed in experimental runs are a subtle balance between nucleation and diffusive growth of bubbles. When abundant nucleation sites are available (series A and B) nucleation dominates, and as the space between bubbles is reduced, diffusive growth becomes dominant (Fig. 10). However, as mentioned previously, this behavior (i.e. one pulse of nucleation and growth) occurs only

in systems undergoing linear, constant decompressions through time. While this condition may be satisfied for certain phases of magmatic ascent, studies have shown that magma likely ascends in a non-linear fashion, entering the conduit rather slowly and accelerating until the fragmentation level (e.g. Neri et al., 2002b). In this model, primary nucleation events form fewer large bubbles when decompression rates are slow enough, and countless smaller bubbles form following secondary nucleation events towards the upper regions of the conduit due to substantial acceleration (Mourtada-Bonnefoi and Laporte, 2004; Massol and Koyaguchi, 2005; Cluzel et al., 2008). This non-linearity is thought to be responsible for the bi-modality of vesicle size distributions often measured in natural pumice (Cluzel et al., 2008). In 79AD white pumice VSDs, bi-modality is not ubiquitous (Fig. 4). High density clasts for both EU1 and EU2 do not record a clear bi-modal distribution and the second mode observed in EU1 and EU2 low density clasts, as well as the population in the EU2 modal density clast, may result from coalescence or could have formed deeper in the conduit. Assuming that bubbles do not have time to entirely decouple from the melt, the superimposition of size ranges resulting from each nucleation events could then generate the wide and complex size distributions typically measured in natural pumice. It is difficult to assess in detail the effects of non-linear ascent rates on textures at the laboratory scale, and such experiments have not been yet attempted. In the future, non-linear vesiculation experiments involving either numerous pressure drops with decreasing hold times or involving continuously increasing decompression rates need to be tested in order to evaluate the influence of variations during the decompression path on resulting vesicle textures.

7. Conclusions

Experiments involving decompression of K-phonolites were compared to natural samples erupted during the opening and plinian phases of the 79AD eruption of Vesuvius. At conditions initially inferred for ascent of the Vesuvius 79AD white magma (100 MPa < P_I < 150 MPa, T=850°C, dP/dT=0.25 MPa/s), experimental samples produce vesicle number densities within the same order of magnitude of those measured in EU1 and EU2 pumices, and bubbles of equivalent sizes at final pressures that are unrealistically high for the natural environment. Experimental samples exsolve their water in equilibrium with the melt at the applied decompression rates; however, vesicle size distributions are somewhat different from those shown by natural EU1 and EU2 samples. Number densities rapidly reach their maximum and stabilize (around 10^6 and 10^7 mm^{-3} in EU1 and EU2 respectively), as predicted by Toramaru (2006), and low effective surface tensions (σ_{EFF}~0.035 N m^{-1}) are needed to generate such high values at ascent rate conditions suggested for the 79AD eruption. In nature and within the experiments, EU1 shows fewer but larger vesicles than EU2; this can be related both to small differences in ascent rates (EU2 faster than EU1) and compositional differences within the melts (i.e. influence of microlites).

From this study, we infer that the wide and often polymodal size distributions measured in natural samples can be obtained if magma endures non-linear pressure perturbations and if nucleation pulses are triggered at various levels in the conduit. In this model, modal sizes observed in EU1 and EU2 samples result from bubble growth in the upper part of the conduit as ascent accelerates, as opposed to being generated throughout decompression. In turn, experiments show that the high number densities measured in

natural samples can be reached as long as decompression rates of the order of 0.5-1 MPa/s are attained during ascent.

Finally, comparisons made between K-phonolites and more evolved silicic magmas such as rhyolites illustrate how diverging ascent histories may result in similar catastrophic plinian eruptions. Through detailed investigations of natural pumice and laboratory vesicular samples, therefore, significant progress is being made towards understanding how complex textures observed at the surface may form. Future experiments should perhaps include the possibility of exploring non-linear decompression rates in the laboratory in order to even better replicate natural pumice textures.

Acknowledgments

The authors wish to acknowledge the NSF grants EAR 0537950, 0537543, and 0511070 (J. Larsen). We thank Clara Margalef and Leslie Almberg for help in the lab. Thomas Giachetti, Tim Druitt, Nicolas Cluzel, Didier Laporte, Carrie Brugger, Owen Neill and Lisa Petrochilos are thanked for the helpful discussions. Reviews and suggestions by Alain Burgisser and Jacopo Taddeucci considerably improved the quality of this manuscript.

Appendix A

In an attempt to estimate how 2D (i.e. "image vesicularity", ϕ_{2D}) compares to true vesicularity ("density-derived vesicularity", ϕ_{3D}), we gathered data from five explosive

and one effusive eruptions including Mt. St Helens (Washington, USA) (Klug and Cashman, 1994), Vesuvius (Naples, Italy) 79AD white and gray pumice (Gurioli et al., 2005b), 1912 AD Novarupta (Alaska, USA) (Adams et al., 2006), Makapu'u lava flows (Hawaii, USA, Gurioli, unpublished data), Kilauea Iki (Hawaii, Stovall et al., in prep.), and Villarica (Chile) (Gurioli et al., 2008). To provide a useful value applicable to experiments, 2D vesicularity was measured at the highest image magnification used for each individual study. This means that much like in the experiments, large bubbles are often discarded and image vesicularity tends to be lower than true vesicularity. Indeed, Fig. A1 shows that while "image" and "true" vesicularities compare well at very high values (i.e. >70-75%), image vesicularity tends to underestimate the true vesicularity at lower values. The fitted 2nd degree polynomial curve is given in the main text (Eq. 1).

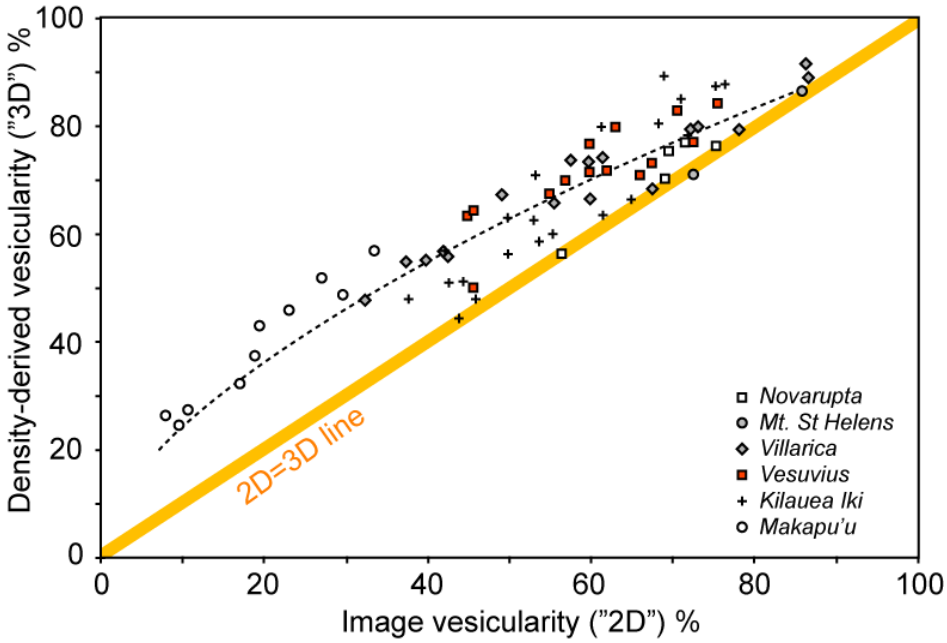

Figure A1: Comparisons between vesicularities measured in thin sections (ϕ_{2D}) with those derived from density measurements (ϕ_{3D}). Note the limited agreement between the data and the orange 1:1 line.

Despite the fairly good fit (R^2=0.85), a typical spread of about ±5–10 % (mean error=4.3% with 1σ=3.08) is to be expected if the relationship is to be used to derive "true" 3D vesicularities from 2D image fraction area measurements. These uncertainties most likely originate from the frequent non-sphericity of vesicles in volcanic pyroclasts, and, more importantly, from the lower probability of encountering smaller objects when performing cross-sections within samples (Sahagian and Proussevitch, 1998). Although difficult to quantify due to the lack of data at ϕ_{3D} <30% in Fig. A1, uncertainties will inherently be much larger for samples with low vesicularities (i.e. less probability of encountering fewer large vesicles or numerous very small ones), than for high vesicularity ones. Hence, even if it is far from perfect, extrapolation of vesicularities using Eq. 1 provides a better alternative than simply reporting 2D measurements of vesicle area within experimental samples.

CHAPTER 5. TRANSITIONS FROM STABLE TO COLLAPSING COLUMN DURING THE 79AD ERUPTION OF VESUVIUS: MECHANISMS INFERRED FROM TEXTURAL INVESTIGATIONS OF PUMICE FROM PYROCLASTIC DENSITY CURRENT AND FALL DEPOSITS.

To be submitted in its present form to Bulletin of Volcanology as Shea, T., Gurioli, L., Houghton, B.F., Cioni, R., Cashman, K.V., (2010).

Abstract

The plinian column formed during the magmatic phase of 79AD eruption of Vesuvius alternated several times between stable, buoyantly rising convective regimes and unstable, collapsing regimes. The pyroclastic density currents (PDCs) produced during the latter transitions were responsible for most Roman deaths around the volcano. We performed a full textural characterization of pumice samples from multiple fall and PDC deposits and found that vesicle textures are comparable in both cases, preserving a full spectrum of degassing and outgassing processes, from bubble nucleation to collapse. While vesicle textures show there is no fundamental difference in the kinetics of degassing during the passage from fall to PDC-producing plumes, a combination of phenomena are required to explain the transitions; the production of denser clasts through increased shearing and outgassing at the conduit margins ultimately caused several of the partial collapses (eruptive units EU2/3pf, EU3pf2, EU3pf3). Another partial column collapse (EU3pf1) was generated by a combination of high discharge rates and high clast densities. Finally, the total collapse of the eruptive plume (EUpftot) occurred in response to a widening of the conduit, and a last small lithic-rich PDC (EU3pfLith) was produced as decompression rates waned. We propose a conduit model that satisfies all the textural and physical observations made for this phase of the eruption where lateral and vertical vesicularity/density stratifications are produced by maturing of bubble textures as well as localized shearing of bubble-rich magmas, eventually supplying the plume with dense clast end-members having lower vesicle number density, and vesicular clasts having higher number densities.

1. Introduction

Pyroclastic density currents (PDCs) are among the deadliest hazards for populations living around volcanoes, resulting in at least 59,000 deaths in the past 230 years, over 25% of the total number of victims from all volcano-related phenomena (Blong 1984; Tanguy et al. 1998). They are generated by several mechanisms including dome collapse (e.g. Unzen, Japan in 1995; Nakada et al. 1999), lateral cryptodome depressurization (e.g. Bezymianny, Russia in 1955; Gorshkov 1959) or complex transitions from stable to collapsing eruption columns during the course of highly explosive eruptions (e.g. Tambora, Indonesia in 1815; Sigurdsson and Carey 1989).

Early one-phase steady-state numerical models of eruption column dynamics suggest that dominantly buoyant plumes can partially or fully collapse following increases in mass discharge rate (MDR) and/or vent radius, or decreases in exit velocity and/or initial dissolved water content (e.g. Sparks and Wilson 1976; Wilson et al. 1980). While this approach has been applied to several eruptions (e.g. Carey and Sigurdsson 1987; Sigurdsson and Carey 1989; Carey et al. 1990), there is little knowledge of the specific physical conditions that lead to column collapse. Discharge rates can increase as a result of conduit/vent widening by erosion or vent wall collapse (Walker 1981; Woods and Bower 1995) or simply due to the tapping of magmas with varying compositions and physical properties (Carey et al. 1990). Increases in MDR lead to a decrease in the efficiency of air entrainment in the eruptive column and, ultimately, to reduced overall buoyancy and collapse. On the other hand, transitions from volatile-poor to volatile-rich magmas can occur when magmas of varying compositions (and varying gas solubilities) are tapped (Dobran et al. 1994, Neri and Dobran 1994), or when the portions of an

ascending magma body have been partially outgassed. Two-dimensional, transient models (e.g. Valentine and Wohletz 1989; Dobran et al. 1993; Neri and Macedonio 1996) have demonstrated the occurrence of a full spectrum of behaviors between fully collapsing and fully stable columns. Transitional to fully collapsing eruptive columns have been generated in numerical simulations by using particles of multiple sizes (i.e. where larger particles tend to segregate from the main plume and concentrate into flows, Clarke et al. 2002; Neri et al. 2003), by applying non-equilibrium exit pressure conditions (Neri et al. 2002a; Di Muro et al. 2004), by increasing microlite content (Neri et al. 2002b), or by modifying the opening angle of the vent/crater (Esposti Ongaro et al. 2008). While these plume collapse mechanisms may apply to some eruptions, it is unclear whether they can be applied to the 79AD eruption of Vesuvius which switched multiple times between fully convective, transitional, fully collapsing, and fountaining or boiling-over behaviors. Sigurdsson et al. (1985) suggested some of these shifts could be caused by increases in magma discharge rate or tapping of volatile-depleted magmas but values for 79AD magmas (cf. Sigurdsson et al., 1985) plot far away from the collapse threshold proposed by Wilson et al. (1980). Other models illustrating the influence of different particle sizes in generating PDCs may apply but only offer a phenomenological explanation; they do not provide any direct information on the causality of the changes in the physical conditions of conduit ascent or fragmentation that produced the modifications in particle sizes or density within the plume. Belousov et al. (2002), through measurements of clast vesicularity and crystallinity, hypothesized that transitions in column behavior during the 1997 Bezymianny eruption were triggered by changes in the density of erupted material, which were brought about by temporal variations in

magma degassing and crystallization. Although textural investigations of clasts from the 79AD eruption were initiated by Gurioli et al. (2005a), the variations in ascent parameters below the fragmentation level are still largely unknown, particularly during unstable column phases. In this contribution, we argue that temporal and spatial changes in the style of degassing may have sufficed to generate several shifts in plume conditions, and ultimately produced the multiple devastating pyroclastic density currents that destroyed the Roman towns around Vesuvius.

1.1. Generation of PDCs during the 79AD Vesuvius eruption

In 79AD, Vesuvius produced the grandest, most lethal and destructive explosive eruption of the past 3000 years of Somma-Vesuvius activity. This eruption lasted over 20 hours and deposited in excess of 3 km^3 (dense rock equivalent, Cioni et al. 2008) of volcanic material around the Bay of Naples (Fig. 1a). A few hours into the eruption, the feeding magma abruptly shifted from a phonolite to a tephriphonolite composition, emitting dominantly “white” then “gray” pumice (Lirer et al. 1973; Sigurdsson et al. 1982; 1985). During the course of the eruption, the behavior of the eruptive column switched multiple times from fully buoyant to transitional, fully collapsing and fountaining or boiling-over conditions (Cioni et al., 2004). These phases generated successions of fall and PDC deposits (Fig. 1a), termed EU1-EU8 by Cioni et al. (1992) (Fig. 1b). The same terminology is employed here, but for clarity, we designate PDC units according to their inferred collapse style (“Partial Collapse” PC, “Total Collapse” TC, “Boiling-over” BO, see below).

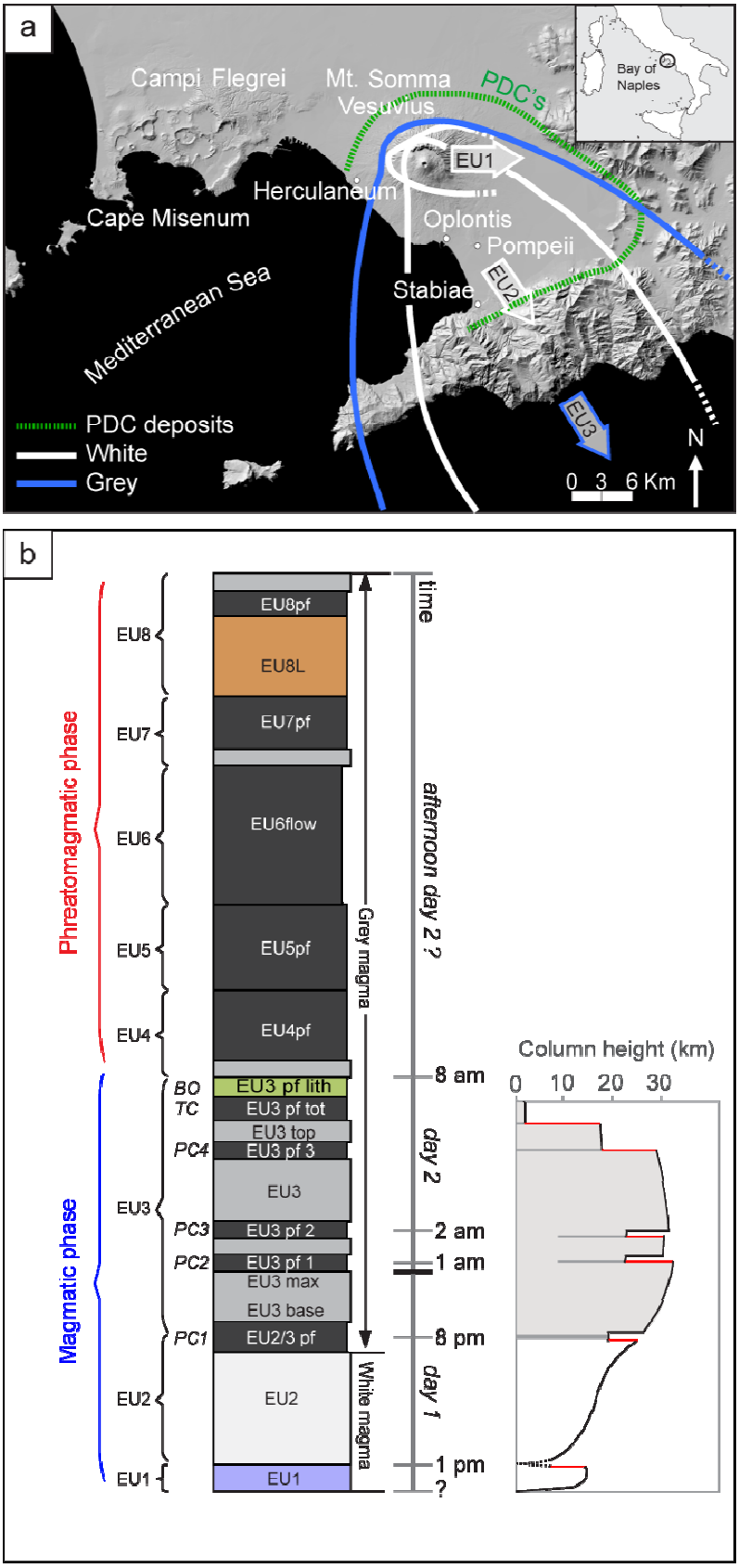

Figure 1: (a) DEM of the bay of Naples with Campi Flegrei and Vesuvius. 10 cm-isopachs for both white (EU1+EU2) and gray (EU3) magmatic phases of the 79AD eruption are shown, along with the distribution of the various PDCs (Gurioli et al. 2005b). (b) Simplified idealized stratigraphy (unit thicknesses are relative) of the 79AD eruption deposits modified from Cioni et al. (1992, 2004). The variation of column height for the first 19 hours was modified from Carey and Sigurdsson (1987). Estimates for the remainder of the eruption are not easily obtainable due to the lack of prolonged building of a convective column.

The eruption started with an opening weak phase (EU1), followed by the rise of a stable plinian column to heights of ~25 km (EU2) (Carey and Sigurdsson 1987). During the transition from white to gray magma, the established column became partly unstable, and the passage between EU2 and EU3 was marked by the partial collapse of the column margin and the production of the first PDC (EU2/3pf, here "PC1"), which took the life of most Romans in the towns of Terzigno and Herculaneum (Cioni et al. 1992; 2000). A fully convective plinian column was then restored for the first 3-4 hours of gray pumice fall (fall samples EU3base-EU3max) until the column shifted back to a transitional behavior, partially collapsing and generating at least three PDCs (EU3pf1, EU3pf2 and EU3pf3, here labeled "PC2, PC3" and "PC4" respectively) that destroyed several surrounding villas (Cioni et al. 2000, 2004; Gurioli et al. 2002). PC2 was produced during the peak in discharge rate (sample EU3max) inferred by Carey and Sigurdsson (1987) from column height, while PC3 and PC4 were generated as the column height decreased (Fig. 1b). The eruptive plume fully destabilized shortly after, forming a radially dispersed PDC (EU3pftot, here unit "TC") that partly destroyed Herculaneum (Gurioli et al. 2002) and reached Pompeii, probably killing unsheltered people (Zanella et al. 2007). The magmatic phase of the eruption (EU1-EU3) ended with the production of a "boiling-over" fountain (i.e. a low column that was never buoyant) that deposited a poorly dispersed, massive, lithic-rich PDC (EU3pfLith, here unit "BO") (Cioni et al. 2004). The phreatomagmatic activity (EU4-EU8) started with the short-lived reestablishment of a convective plume and deposition of a thin fall blanket (EU4). The collapse of this short-lived plume produced the most widespread, lethal PDC (EU4pf) that destroyed Pompeii and took the lives of all remaining survivors around Vesuvius

(Cioni et al. 1992, 2004; Gurioli et al. 2005b). The phreatomagmatic phase ended with multiple PDCs generated by low fountaining (EU5, EU8L, EU8), caldera collapse (EU6) and column collapse, (EU7pf) (Cioni et al. 2004). This paper focuses only on the six major PDCs generated during the magmatic phase of the eruption, PC1 to PC4, TC, and BO (Fig. 1b).

Early on, Lirer et al. (1973) noticed that the transition from white to gray pumice is marked by an abrupt increase in juvenile clast density. Additional measurements by Carey and Sigurdsson (1987) led them to hypothesize that this increase could be linked to the change in column behavior during the eruption. Gurioli et al. (2005a) provided a detailed investigation of fall units EU1-EU4, as well as a nearly complete record of clast density variations throughout the entire stratigraphy, further substantiating a possible relationship between column collapse and an increase in the density of clasts in the column. To test this hypothesis, we introduce new density measurements made on pumice from each PDC of the magmatic phase, and complement them with a comprehensive textural investigation. The comparison of new PDC data with fall tephra data from Gurioli et al. (2005a) sheds light on the processes that triggered the transitions from convective to collapsing plume during the first 7-15 hours of the 79AD eruption.

1.2. Pumice textures in Vesuvius 79AD deposits and shear-localization

This work was in great part stimulated by our previous textural investigations (Gurioli et al. 2005 and Shea et al. 2009, 2010b), in which we focused on vesicle and crystals from 79AD pumice collected within tephra fall deposits.

Through comparisons between experimental and natural samples we deduced that vesiculation had occurred continuously during ascent of magma that produced fall phases, and that decompression rates probably accelerated during ascent, resulting in increasingly vigorous nucleation. It was also noted that small-scale shear bands containing deformed vesicles were present within some pumice clasts. Populations of deformed vesicles within pumice from trachytic or rhyolitic eruptions are often linked to stress variations within the conduit during magma ascent (Heiken et al. 1978; Klug and Cashman 1996; Marti et al. 1999; Polacci et al. 2001, 2003; Mastin 2005; Wright et al. 2006). Tube or fibrous pumice clasts have extremely elongated vesicles. They are often found within deposits of highly explosive silicic eruptions, and are commonly associated with greater shearing of ascending magma along conduit walls (e.g. Polacci et al. 2003). Smaller-scale, microscopic shear zones have also been reported within rhyolitic pumice (Wright and Weinberg 2009) and highly crystalline andesites with residual liquids of rhyolitic composition (Sparks et al. 2000; Le Pennec et al. 2001). Little is known, however, about where these shear-zones form in the conduit and how they evolve through magma ascent to imprint the pumice textures we observe at the surface.

The presence or absence of shear-localization textures in 79AD pumice, together with the continuous nucleation they experienced, suggests different scenarios of bubble evolution throughout magma ascent (Fig. 2). At the onset of volatile exsolution, decompression rates are slow, nucleation rates are low, and vesiculation is dominated by bubble growth/expansion (Fig. 2a). Two diverging vesiculation paths are explored. In both cases, nucleation intensifies throughout ascent, coalescence occurs as expanding bubbles cause the thinning of melt films, and bubble connectivity increases until gas

escape becomes possible. In the first scenario (Fig. 2b to e), the magma is not affected by shear localization along conduit walls. Vesicularity reaches peak values when most bubbles have coalesced before gas is able to escape. Once partial outgassing occurs, vesicularity decreases. In the second scenario, the magma is affected by small shear zones (Fig. 2b' to e').

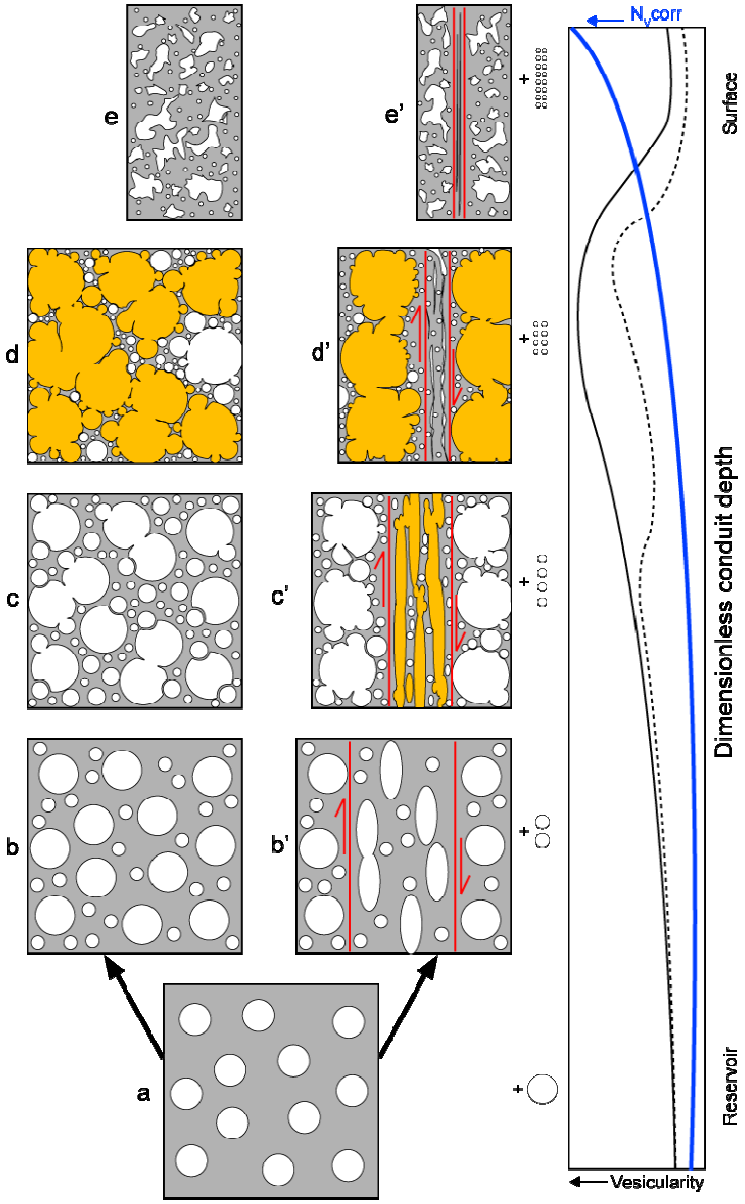

Fig. 2 Models of degassing and outgassing in Vesuvius 79AD magmas. Magma vesicularity and bubble number density referenced to melt fraction (N_{Vcorr}) are plotted approximately as a function of depth in conduit. Orange fill in vesicles denotes connectivity from one side of the image to the other. The solid curve represents the scenario where magma is not affected by shear localization while the dotted curve shows the scenario where shear zones affect the magma. In tboh cases, the number density increases in a similar fashion. While vesicularity easily mimics the processes affecting medium and large bubbles, number densities remain mostly unmodified because they are controlled dominantly by the small bubble population that forms continuously throughout decompression. The loss of a limited number of bubbles through coalescence and collapse is considered less influential on N_{Vcorr}.

Larger bubbles are more deformed by shearing and are rapidly forced into coalescence within the shear zone. While undeformed zones outside the shear area start to coalesce, bubbles may be fully connected within the shear zone allowing partial outgassing, and resulting in a decrease in vesicularity. As the areas outside the shear zone still expand and coalescence, vesicularity increases and reaches maximum values. A second collapse and outgassing event unaided by shear may finally occur (Fig. 2d') causing a new decrease in the magma vesicularity. These two examples offer a glimpse of some of the complications that may ultimately be frozen within pumice clasts during fragmentation: lower vesicularities are not necessarily associated with early stages of degassing (and thereby low N_V) and a comprehensive spectrum of vesicle sizes, shapes and numbers needs to be described in order to decipher the stages undergone by individual clasts. Note that throughout this contribution, we refer to 'mature' textures as textures that contain substantial evidence of high vesicle connectivity (through coalescence) and/or collapse.

Shea et al. (2009) demonstrate that the numerous leucite microphenocrysts (~20-30 µm) present in all clasts of the 79AD eruptive stratigraphy did not form during fast ascent like plagioclase in magmas of other compositions (e.g. Mt St Helens, Geschwind and Rutherford 1995). Rather, they crystallized during initial slow decompression of the reservoir and/or during storage. Their textural characteristics argue for a thermal zoning of the upper reservoir containing the white magma, EU1 being stored at slightly colder conditions than EU2 prior to the eruption.

Aside from the crucial information on the mechanisms responsible for transitions from stable to collapsing columns that the study of vesicle and leucite textures within pumice from the PDC-producing phases of the eruption offers, we are presented with a

unique opportunity to validate degassing and crystallization models proposed previously for the 79AD eruption (Shea et al., 2009; Shea et al., 2010b).

2. Methods

2.1. Textural characterization

Characterization of pumice textures from PDCs was carried out following Shea et al. (2010a). Briefly, samples of a few hundred 16-32 mm juvenile clasts were collected for each PDC unit, and the largest hundred were selected to perform density measurements. Density histograms were produced, and clasts representative of the mode, the low and the high end-members were chosen. Vesicularities were calculated by mass balance using individual clast densities and values of magma density ρ_M=2600 kg m^{-3} (Barberi et al. 1989).

Thin sections made from selected clasts were imaged using a scanner and the scanning electron microscope (SEM), using magnification of 5×, 25×, 100×, and 500× to cover a range of vesicle sizes of $0.001 < L < 10$ mm. In this fashion, for each thin section, a total of 15 images were acquired. The latter were used to derive vesicle size distribution (VSD), vesicle volume distribution (VVD), and number density per unit volume melt (N_V) via Matlab®-based "FOAMS" (Shea et al. 2010a), based on stereological conversion methods by Sahagian and Proussevitch (1998). Vesicle number densities can provide essential information on the style of ascent and allow the derivation of magma decompression rates (Toramaru 2006). In pumice, nucleation is often inferred to be continuous throughout ascent (e.g. Blower et al. 2001; Klug et al. 2002; Gurioli et al.

2005; Shea et al. 2010b); hence the total number of vesicles measured within a clast reflects a range of nucleation periods. Because we aim to utilize number densities to derive maximum decompression rates experienced during ascent (see below), total N_V cannot be used because a cumulative rate is calculated. To avoid this problem, we preserve only number densities calculated in the size range 0.01-0.001 mm to capture the decompression rates corresponding to the final stages of rapid ascent prior to fragmentation. These number densities are labeled N_{Vf} to denote their correspondence to only the final accelerating portions of the ascent path.

Because leucite crystals are ubiquitous within 79AD products and may provide valuable information on magma storage and ascent conditions (Shea et al. 2009), crystal volume distribution (CVD) and leucite number density ($N_{V\text{-}lc}$) were also acquired through FOAMS, under the justifiable assumption that leucite shapes are nearly spherical. All vesicle and leucite number densities are normalized to melt volume (N_V^{corr}, N_{Vf}^{corr}, N_{V-lc}^{corr}, Table 1).

Lastly, a new program module ($FOAMS_{film}$) was utilized to measure glass wall thickness between vesicles. The algorithm identifies vesicles, finds the coordinates of their centroid, and counts glass pixels within lines that connect the centroids of two vesicles.

Table 1: Textural properties of both fall and PDC samples from the 79AD eruption.

	Sample	ϕ [a] %	ρ [b] (g cm^{-3})	N_{vf}^{corr} [c] (mm^{-3})	N_{Vf}^{70} [d] (mm^{-3})	dP/dt [e] (MPa s^{-1})	d [f]	X_{corr} [g] %	Lc_{corr} [h] %	V_{glass} [i] %	$N_{V\text{-}lc}^{corr}$ [j] (mm^{-3})
EU1 fall	14-1-1	81.4	0.48	(4.7) 2.8×10^6		0.38	3.43	6.1	22.0	11.5	
	14-1-10	75	0.87	(3.3) 3.3×10^6	5.5×10^6	0.40	4.03	4.1	18.0	17.0	3.1×10^4
	14-1-52	62.1	0.98	(8.3) 8.0×10^6		0.66	3.85	5.8	14.0	27.7	
EU2 fall	15-2-11	83.4	0.41	(13) 11.3×10^6		0.98	3.39	4.1	13.0	10.9	
	15-2-3	77	0.60	(16) 15.2×10^6	17×10^6	1.13	3.57	6.1	14.0	15.6	4.6×10^4
	15-2-5	70.9	0.76	(17) 16.0×10^6		1.15	3.67	5.4	17.5	20.5	
EU3 base	12-8-29	76.9	0.6	(7.9) 7.1×10^6		7.78	3.21	3.5	28.7	15.7	19×10^4
	12-8-13	64.5	0.92	(2.7) 2.4×10^6	5.0×10^6	3.17	3.14	6.2	21.2	25.8	15×10^4
	12-8-37	50.1	1.3	(2.2) 2.0×10^6		2.35	3.56	6.0	19.3	37.3	29×10^4
EU3 max	12-9-42	67.4	0.85	(7.0) 6.4×10^6		6.63	3.8	3.4	17.7	25.7	7×10^4
	12-9-16	59.6	1.05	(6.7) 6.4×10^6	7.0×10^6	6.20	3.41	3.7	20.8	30.5	23×10^4
	12-9-37	52.2	1.24	(4.9) 4.7×10^6		4.65	3.6	3.6	35.1	29.7	32×10^4
EU3 top	20-1-31	80	0.52	(13) 11.7×10^6		11.53	3.34	5.0	22.3	14.6	25×10^4
	20-1-4	72	0.72	(14) 12.2×10^6	10×10^6	11.07	3.44	9.0	34.6	15.8	19×10^4
	20-1-05	55.7	1.16	(6.5) 6.2×10^6		5.83	3.52	4.3	35.9	26.5	11×10^4
EU4 fall	12-10-10	82.8	0.45	(12) 10.4×10^6		11.10	3.42	7.0	40.7	9.0	32×10^4
	12-10-27	73.1	0.7	(9.7) 8.8×10^6	8.2×10^6	8.89	3.55	4.3	33.6	16.7	24×10^4
	12-10-15	62.4	0.98	(7.4) 6.9×10^6		6.74	3.57	5.9	28.4	24.7	17×10^4
EU2/3 pf	26-1-5	77.9	0.57	(5.7) 4.9×10^6		3.19 [k]	4.01	5.4	28.4	14.6	17×10^4
	26-1-7	70.8	0.76	(7.3) 6.8×10^6	8.5×10^6	3.77 [k]	3.49	4.8	15.9	23.2	8.0×10^4
	26-1-11	67.9	0.83	(11) 10.6×10^6		5.01 [k]	3.86	5.3	21.1	23.6	11×10^4
EU3 pf1	27-1-9	83.7	0.42	(12) 10.3×10^6		10.95	3.47	8.0	17.5	12.1	18×10^4
	27-1-30	66.2	0.88	(4.3) 3.7×10^6		4.38	3.77	6.8	17.8	25.5	13×10^4
	27-1-22	60.6	1.02	(7.2) 6.5×10^6	8.3×10^6	6.29	4.00	4.1	27.0	27.2	17×10^4
	27-1-4	52.6	1.23	(6.7) 6.2×10^6		5.70	4.01	7.2	32.8	28.4	16×10^4
EU3 pf2	28-1-32	74.1	0.67	(9.3) 8.4×10^6		8.45	3.81	5.0	18.4	19.9	18×10^4
	28-1-12	67.6	0.84	(7.0) 6.3×10^6	7.4×10^6	6.59	3.78	5.9	16.1	25.3	5.3×10^4
	28-1-1	52.8	1.23	(8.8) 6.0×10^6		5.54	3.77	5.5	34.8	28.2	24×10^4
EU3 pf3	19-1-21	74	0.68	(11) 9.7×10^6		9.55	3.58	7.7	24.2	17.7	19×10^4
	19-1-4	67.9	0.83	(10) 8.7×10^6	9.3×10^6	8.08	3.62	7.2	32.3	19.4	20×10^4
	19-1-10	51.9	1.25	(9.9) 9.7×10^6		7.72	3.79	4.8	25.0	33.8	14×10^4
EU3 tot	21-1-52	82.4	0.46	(17) 12.7×10^6		12.75	3.56	8.5	35.6	9.8	44×10^4
	21-1-10	73.4	0.69	(9.1) 8.4×10^6	8.0×10^6	8.55	3.49	7.1	22.6	18.7	14×10^4
	21-1-2	58.1	1.09	(5.0) 4.3×10^6		4.46	3.54	7.2	22.9	29.3	18×10^4
EU3 lit	22-4-8	77.5	0.59	(5.3) 4.4×10^6		5.53	3.57	6.7	23.4	15.7	4.5×10^4
	22-4-17	33	1.74	(4.2) 0.4×10^6	3.4×10^6	0.60	3.95	5.5	42.8	34.6	47×10^4
	22-4-35	62.1	0.99	(3.7) 2.2×10^6		2.84	3.96	5.3	27.2	25.6	5.1×10^4

2.2. Vesicle connectivity

Vesicle connectivity provides first-order information on the outgassing potential of the magma near fragmentation (Klug et al. 2002; Rust and Cashman 2004), providing that vesicle walls were not broken by clast transport during the eruption or during sample collection and preparation. To test whether fall tephra and PDC deposits show differences in vesicle connectivity, a total of 17 large (i.e. >3 cm) EU2 and EU3 pumice clasts were collected, along with 16 PDC pumices from EU3pftot. Pumices were cut into cubes of easily measurable volume, and bulk density was calculated both by cube dimensions and by methods of Houghton and Wilson (1989). Connected vesicularities (Table 2) were obtained using He-pycnometry, following procedures described in Formenti and Druitt (2003) and Giachetti et al. (in press).

← (p. 172)

a. Clast vesicularity
b. Clast density
c. Vesicle number density for vesicles <0.01 mm normalized to sample glass content. The total number density including all vesicle sizes N_V^{corr} is reported in parentheses.
d. Vesicle number density normalized to sample glass content extrapolated to φx100=70% vesicularity
e. Decompression rate calculated from vesicle number densities and formulations of Toramaru (2006)
f. Exponents derived from best-fit power law curve within N_V>L plots
g. Crystal content of non-leucite phases (microphenocrysts+phenocrysts) normalized to glass
h. Leucite content normalized to glass content
i. Volume of glass after vesicularity and crystal contents have been removed.
j. Leucite number density normalized to glass content.
k. Values of dP/dt for EU2/3pf are displayed for nucleation parameters intermediate between a 900˚C phonolite (EU2 end-member) and a 1050˚C tephriphonolite (EU3 end-member), assuming the two magmas were mixed at this transitional stage.

Table 2: Pumice connectivity data obtained from He-pycnometer measurements.

	$\rho_{melt+crystals}$ [a]	φ_{bulk} [b] %	$\pm\sigma$ [c]	φ_{conn} [d] %	$\pm\sigma$	φ_{isol} [e] %	$\pm\sigma$
EU2 fall	2550±15 kg m^{-3}						
K1a1	2554	79.71	0.44	79.59	0.42	0.12	0.86
K1a2	2538	81.95	0.43	82.23	0.35	-0.29	0.78
K1a3	2564	78.68	0.46	78.59	0.71	0.09	0.46
K1a4		76.60	0.58	71.74	1.04	4.86	1.61
K1a6		83.54	0.49	82.00	0.66	1.53	1.15
K1a7		85.89	0.41	85.20	0.74	0.69	1.16
K1b1		70.23	0.83	63.89	1.27	6.35	2.10
K1b2		80.26	0.57	70.17	0.76	10.09	1.33
EU3 fall	2620±10 kg m^{-3}						
K2a1	2606	75.52	0.51	75.57	0.29	-0.04	0.80
K2a2		82.75	0.41	83.57	0.27	-0.82	0.69
K2a4		64.42	1.03	64.24	1.44	0.18	2.46
K2a5		75.99	0.49	77.04	0.68	-1.05	1.16
K2a6		77.01	1.00	75.49	1.47	1.52	2.47
K2b1	2617	66.59	0.76	69.01	0.59	-2.42	1.36
K2b1bis		56.43	1.00	57.57	1.64	-1.14	2.63
K2b2		62.79	0.84	63.51	0.81	-0.72	1.64
K2b3		62.08	1.24	64.90	1.33	-2.82	2.57
EU3 PDC	2620±10 kg m^{-3}						
K3a1		69.67	0.89	70.96	0.90	-1.30	1.79
K3a1bis		73.91	0.57	74.41	0.52	-0.49	1.08
K3a1bis2		66.53	1.36	67.62	1.27	-1.10	2.63
K3a1bis3		77.14	0.55	77.57	0.47	-0.43	1.03
K3a2	2622	70.64	0.65	71.67	0.46	-1.03	1.12
K3a2bis		72.49	0.64	73.74	0.67	-1.25	1.31
K3a2bis2		72.59	0.64	73.59	0.57	-1.00	1.21
K3a2bis3		74.49	0.71	75.68	1.04	-1.18	1.76
K3a3		69.06	1.08	69.66	0.94	-0.60	2.02
K3a3bis		68.99	0.67	70.03	1.53	-1.04	2.20
K3a4	2616	62.08	1.00	60.38	0.78	1.70	1.78
K3a4bis		61.49	1.61	61.76	1.61	-0.27	3.22
K3a5	2621	70.96	0.60	71.74	0.41	-0.78	1.01
K3a6		58.39	1.19	57.42	1.00	0.98	2.19
K3a7		70.28	0.78	71.33	0.68	-1.05	1.45
K3a8		70.02	1.51	67.90	1.52	2.12	3.03

← (p. 174)

a. Density of powdered samples (i.e. glass+crystals) measured by pycnometry. A few samples were measured to ensure that density was similar throughout, and an average value was adopted for the rest of the pumice measured.
b. Bulk vesicularity.
c. Standard deviation on the vesicularity measurement.
d. Connected vesicularity.
e. Isolated vesicularity.

2.3. Decompression rate calculations

Vesicle number densities depend strongly on magma properties such as surface tension (melt-vapor and crystal-vapor) and volatile diffusivity, as well as on the timescale available for vesicles to nucleate (i.e. decompression rate) (e.g. Hurwitz and Navon 1994, Toramaru 1995). If magma properties are known, vesicle number densities can be translated directly into decompression rates. As in Mourtada-Bonnefoi and Laporte (2004), Cluzel et al. (2008) and Shea et al. (2010b), this conversion is achieved by using the equations presented in Toramaru (2006):

$$N_{V\,calc} = 34 X_0 \alpha_1^{-2} \alpha_2^{-\frac{1}{4}} \alpha_3^{-\frac{3}{2}}, \quad (1)$$

where X_0 is the initial water concentration at the saturation pressure, and α_1, α_2, α_3 represent dimensionless parameters (Toramaru 1995) defined as:

$$\alpha_1 = \frac{16\pi\sigma_{HOM}^3}{3kTP_0^2}, \quad (2)$$

$$\alpha_2 = \frac{\Omega_M P_0}{kT}, \quad (3)$$

$$\alpha_3 = \frac{kTX_0 DP_0}{4\sigma_{HOM}^2 \left|\frac{dP}{dt}\right|}, \quad (4)$$

where k is the Boltzmann constant, Ω_M is volume of water molecules in the melt taken as 2.6×10^{-29} m^3, P_0 is initial pressure, and X_0 is 4.9 wt% and 3.5 wt% for the white and the gray magma respectively (Cioni et al. 1995, 1998; Cioni 2000; Larsen 2008; Shea et al. 2009, 2010b). The temperature T is set at 850˚C for EU1, 900˚C for EU2, 975˚C for EU2/3 (PC1), and 1050˚C for all other gray magma products. For similar magma compositions, the water diffusivity D depends primarily on temperature and dissolved water content in melt (e.g. Zhang and Behrens 2000). Larsen (2008) and Shea et al. (2010b) used values of 2×10^{-12} for the 79AD white magma (i.e. EU1 and EU2). For the gray magma, we use values of 2×10^{-11} m^2 s^{-1} an order of magnitude higher, to account for the temperature difference and the lower initial H_2O contents (e.g. Watson 1994). These diffusivity values assume water saturation at the initial pressure (X_0=4.9 wt% and 3.5 wt% for the white and gray magmas, respectively). However, the values of N_{Vf}^{corr} replaced with N_{Vcalc} in Eq. (1) to derive dP/dt only represent the small vesicle populations, and thereby the last stages of nucleation. Because a fraction of the initial water was used for vesiculation of earlier vesicle populations, the diffusivity values need to be modified to account for this. Thus, in all equations, the initial pressure and water contents need to be set at values corresponding to late-stage nucleation. Because we

possess measurements of porosity for each vesicle size category (i.e. through FOAMS outputs), we can calculate the predicted water content at a given porosity by rearranging the equilibrium model presented in Gardner et al. (1999):

$$X_F = X_I - \frac{\phi}{\frac{\rho}{Z}\overline{V}_W(1-\phi)}, \quad (5)$$

where X_I and X_F are initial water content and final water content at porosity ϕ, Z is molecular weight of water, $\overline{V}_W$ is the molar volume of water in the vapor phase, and ρ the magma density. For each measured clast, we used the porosity value obtained by summing the contributions from all vesicles with sizes $L \geq 0.01$ mm to derive X_F. The latter value replaces X_0 in Equations (1) to (4). New initial pressures P_0 were also calculated using X_F based on solubility models experimentally calibrated by Larsen (2008) for the white magma, and calculated from the macro H2OSOLvX1 by Moore (2008) for the gray magma. Typically, calculated water contents X_F were ~2 wt% lower than the initial pre-vesiculation values of 3.5 and 4.5 wt%. Hence, to mimic D vs. H_2O relationships measured in other magmas (e.g. Watson 1994; Zhang and Behrens 2000), diffusivity was lowered by a factor of ~5 to account for the lower water content.

Because nucleation is inferred to be heterogeneous in 79AD Vesuvius magmas (Larsen 2008; Shea et al. 2010b), we replace σ_{HOM} in Eq. (1) by an "effective" surface tension σ_{EFF} that incorporates the activation energy reduction term φ, expressed as $\sigma_{EFF} = \varphi^{1/3}\sigma_{HOM}$ (Cluzel et al. 2008). Since bubble nucleation is strongly controlled by the presence of tiny oxide microlites, σ_{EFF} is set at 0.035 N m^{-1} for both the white and the gray magma, similar to values found by Mangan and Sisson (2005), as well as by

Mourtada-Bonnefoi and Laporte (2004) for dacites, and by Shea et al. (2010b) for phonolites.

After all necessary parameters were obtained, curves of dP/dt vs. N_{Vcalc} were used to determine the decompression rate that best matched N_{Vcorr} measured in natural samples from both fall and PDC phases of the eruption. For layer EU2/3pf (transition from white to gray pumice), dP/dt (Table 1) was calculated using both intermediate values of diffusivity and temperature and properties of white and gray magma, individually.

3. Results

3.1. Density variations throughout the magmatic phase of the 79AD eruption

Juvenile clast density histograms obtained for both fall and PDC samples (Fig. 3) reveal several key features of the magmatic phase of the 79AD stratigraphy. First, pumice samples EU1 and EU2 show narrow, unimodal distributions with low density modes (ρ ~ 600 kg m^{-3}) while samples from the gray pumice layers have wider distributions and modal densities that are commonly shifted towards higher values. Second, there is a tendency for distributions from gray fall layers to maintain a nearly constant modal density around ρ ~ 700 kg m^{-3} throughout the stratigraphy, while PDC samples are more variable both in modal density and breadth of distribution. The transitions from fall layers EU2, EU3, EU3top, to subsequent PDC samples PC1, PC3, PC4 all correspond to increases in both modal clast density and in the abundance of mean and high density clasts.

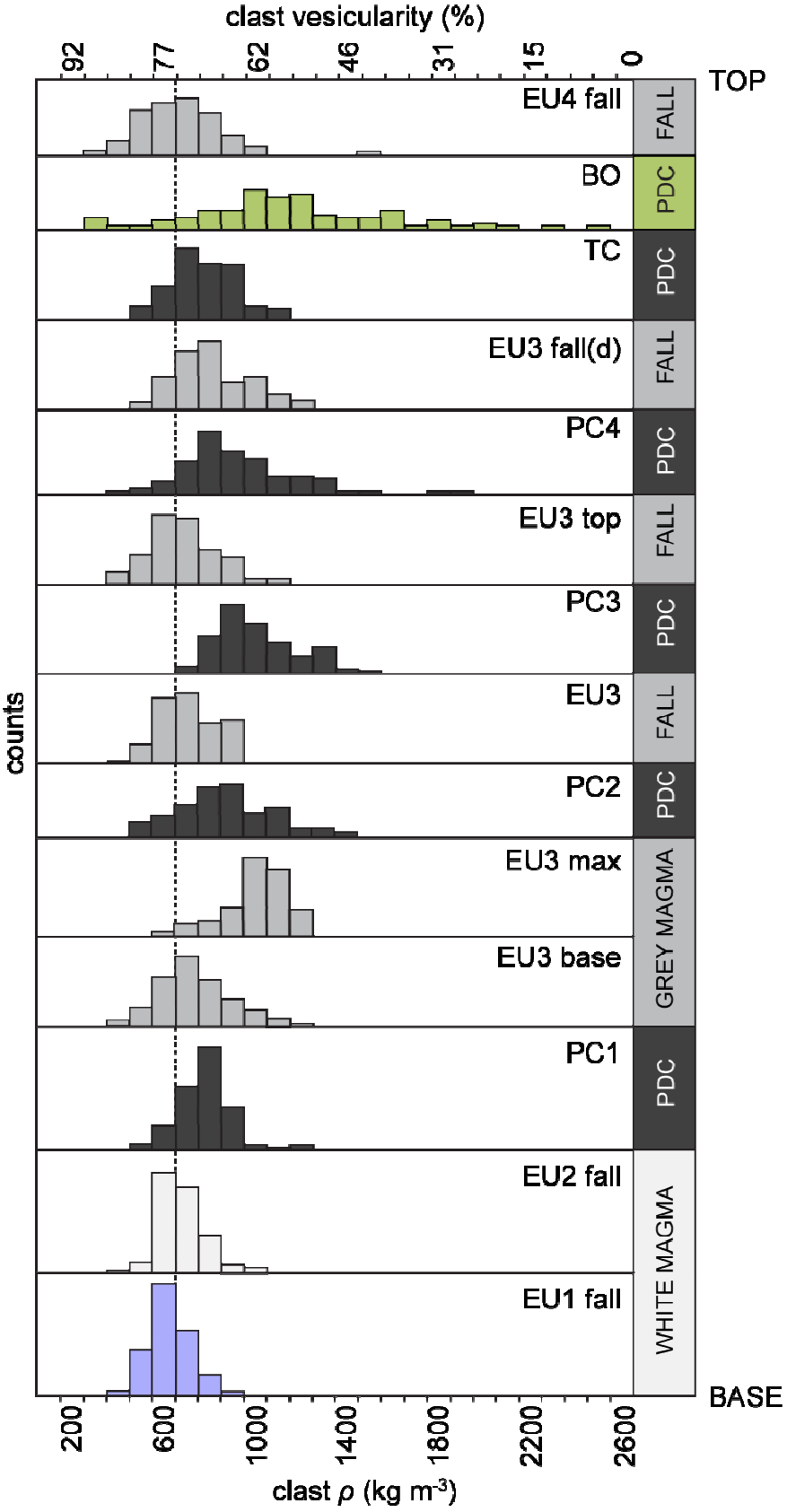

Figure 3: Histograms of clast density distribution shown for selected samples from the magmatic phase of the eruption. Distributions are typically broader in gray pumice samples than in white pumice, and PDCs frequently involve a greater fraction of high density clasts.

In contrast, the transitions from EU3max to partial collapse deposit PC2 and from EU3top to TC (total column collapse) depart from this trend, having either comparable density distributions (EU3top-TC), or higher density modes for fall samples (EU3max-PC2). Finally, unit BO is very different from the other samples and displays the broadest and most complex distribution with a high proportion of clasts of ρ > 1200 kg m^{-3}.

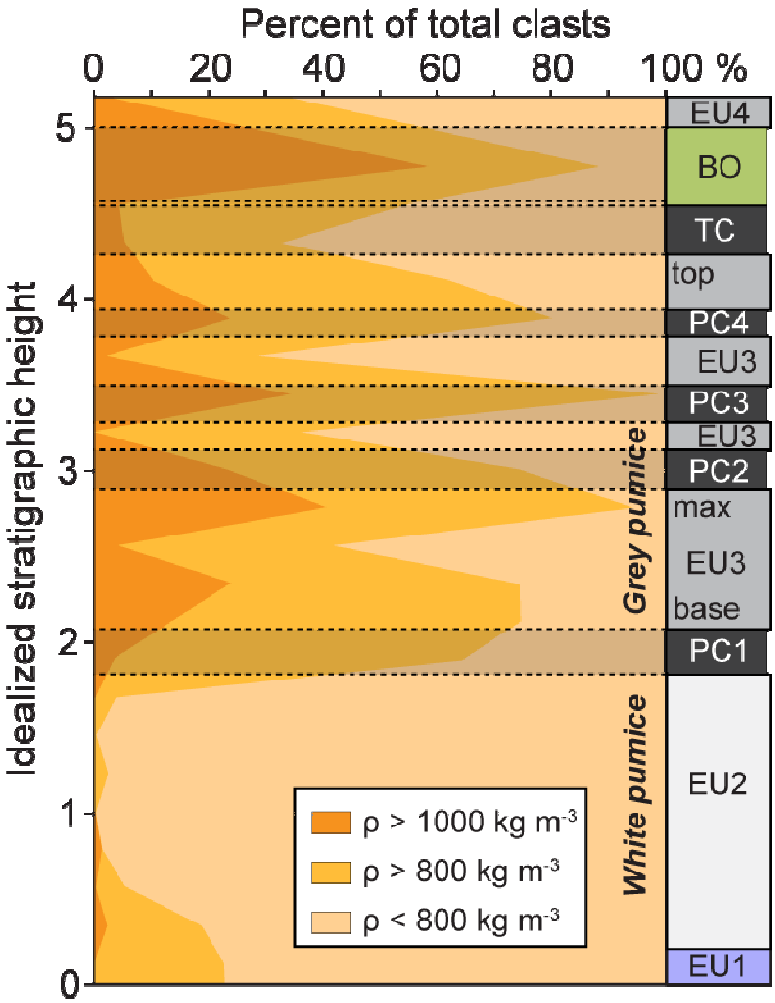

Figure 4: Variations in density displayed as fractions of low, medium and high density. Note the well defined density peaks associated with PC1, PC3, PC4 and BO and the absence of any peak for TC. In comparison, sample PC2 was preceded by a peak in dense clasts.

There is a general tendency for the fraction of dense clasts present in PDC deposits to increase compared to fall units (Fig. 4). For example, the fraction of clasts with ρ > 800 kg m^{-3} reaches 70-98% of total clasts in PDC deposits PC1, PC3, PC4 and

BO. In contrast, most fall phases are marked by proportions of clasts with $\rho > 800$ kg m^{-3} of 0-35%. TC is the only deposit that does not follow this tendency, with 45% low density clasts. As in density histograms, EU3max departs from the general tendency with subsequent PC2 deposit containing a slightly lower fraction of dense clasts (Fig. 4).

3.2. Textural observations

Vesicles: Certain textural features are recurrent within the entire series of PDC samples. Small vesicles (i.e. $L < 50$ μm) are typically round, medium-sized vesicles ($50 < L < 200$ μm) are round-to-irregular in shape, and large vesicles ($L > 200$ μm) are both fairly irregular and slightly elongate (Fig. 5). From low to high density clasts in each PDC, glass walls become thicker (1 μm to 100 μm in the case of BO), large vesicles progressively disappear and vesicle shapes become more irregular and elongate. The presence of retracted walls within low density clasts suggests most large vesicles suffered at least some degree of coalescence. The influence of coalescence appears to increase with increasing clast density; vesicle shapes become more complex, broken glass extremities appear increasingly rounded, and thin glass walls disappear entirely, indicating bubble collapse has occurred. More specifically, in high density samples (i.e. low vesicularity), glass walls tend to thicken PC1 and TC; medium and large vesicles also become less abundant. Within high density clasts of the last PDC sample (BO), numerous tiny vesicles remain, while medium to large vesicles have disappeared (Fig. 5).

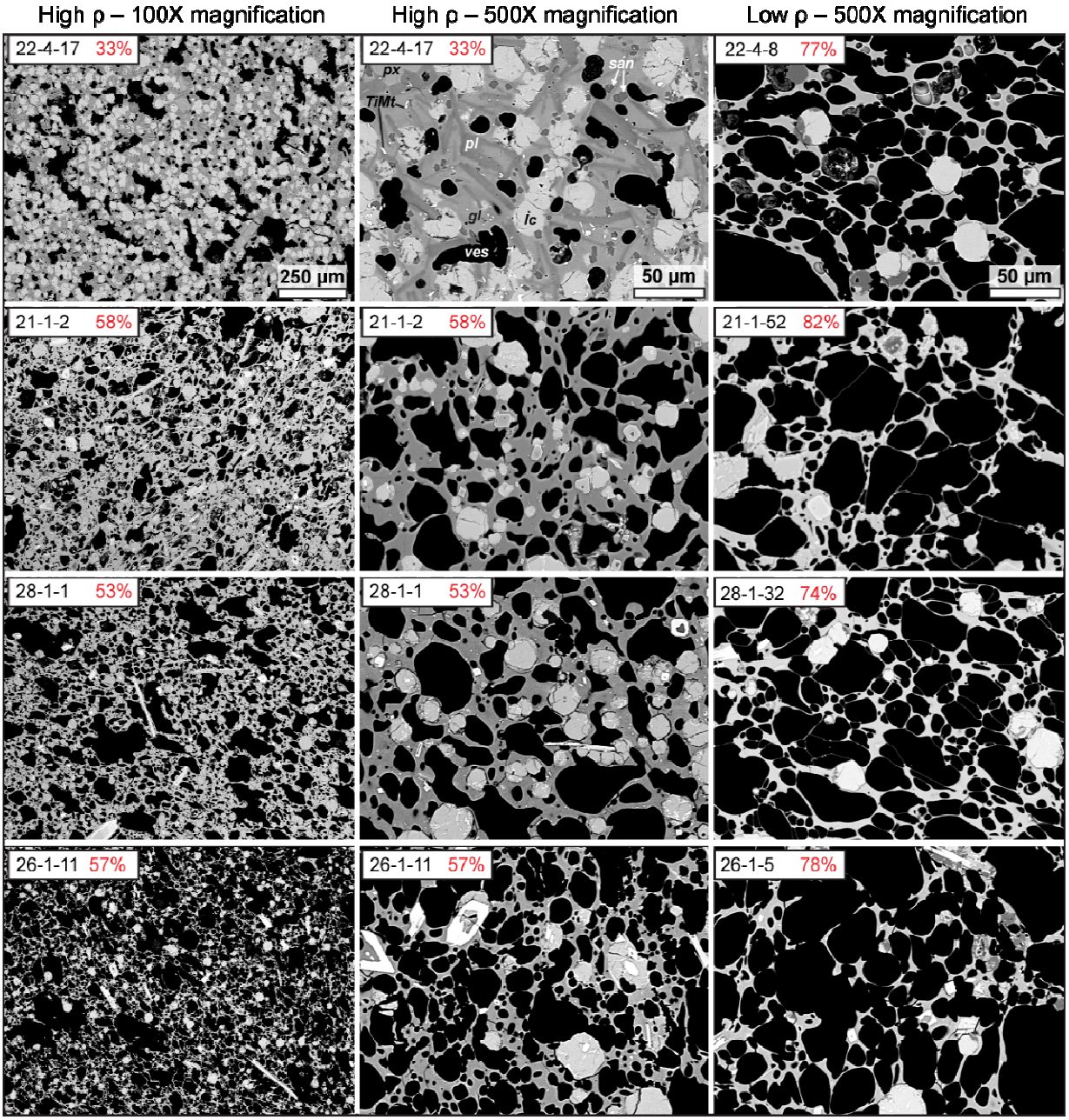

Figure 5: Selected 100× and 500× SEM images of PDCs associated with partial column collapses PC1, PC3, the total collapse TC, and the last lithic-rich low velocity PDC BO. High and low density end-members are shown for comparison. Clast 22-4-17 is the only one in our sample sets that contains microlites of plagioclase and sanidine in addition to usual leucite microphenocrysts. Note the collapse textures in high density clasts and the thin or absent glass walls associated with bubble expansion and coalescence in low density clasts (compare with Fig. 2).

In comparison, low and modal density clasts are fairly similar in appearance among PDCs, with low density PC2 and TC end-members showing the highest proportions of large vesicles.

A striking feature observed in most pumice clasts throughout the eruptive stratigraphy is the recurrence of combinations of dense, vesicle-poor bands (Figs. 6a, 6b, 6e, and 6f), trains of irregular (Fig. 6c), and/or elongate (Fig. 6b) vesicles, and smooth or abrupt transitions from rounded to sheared vesicles (Figs. 6d and 6e). These features appear in nearly all clasts, and their distribution does not seem to follow any particular pattern other than they appear more numerous in higher density clasts. Nonetheless, even in low density populations, on the scale of one clast, several sub-millimetric dense bands and vesicle trains can be observed (Fig. 6a). Within a few dense bands, populations of numerous tiny vesicles also appear to have escaped any kind of deformation (Fig. 6f).

Crystals: Leucite crystals are present within all samples (Fig. 5) and visually seem to preserve similar sizes throughout the PDC sequence. Sanidine, clinopyroxene, amphibole and mica phenocrysts are also present, though in lower proportions. The glass phase is typically clear and contains mostly oxide microlites (Fig 7). BO is the only imaged clast suite that contains sanidine and plagioclase as groundmass microlite phases. In the high-density clast, sanidine appears as equant 5-10 μm crystals whereas plagioclase has more tabular 20-50 μm (long axis) habits (Fig. 5).

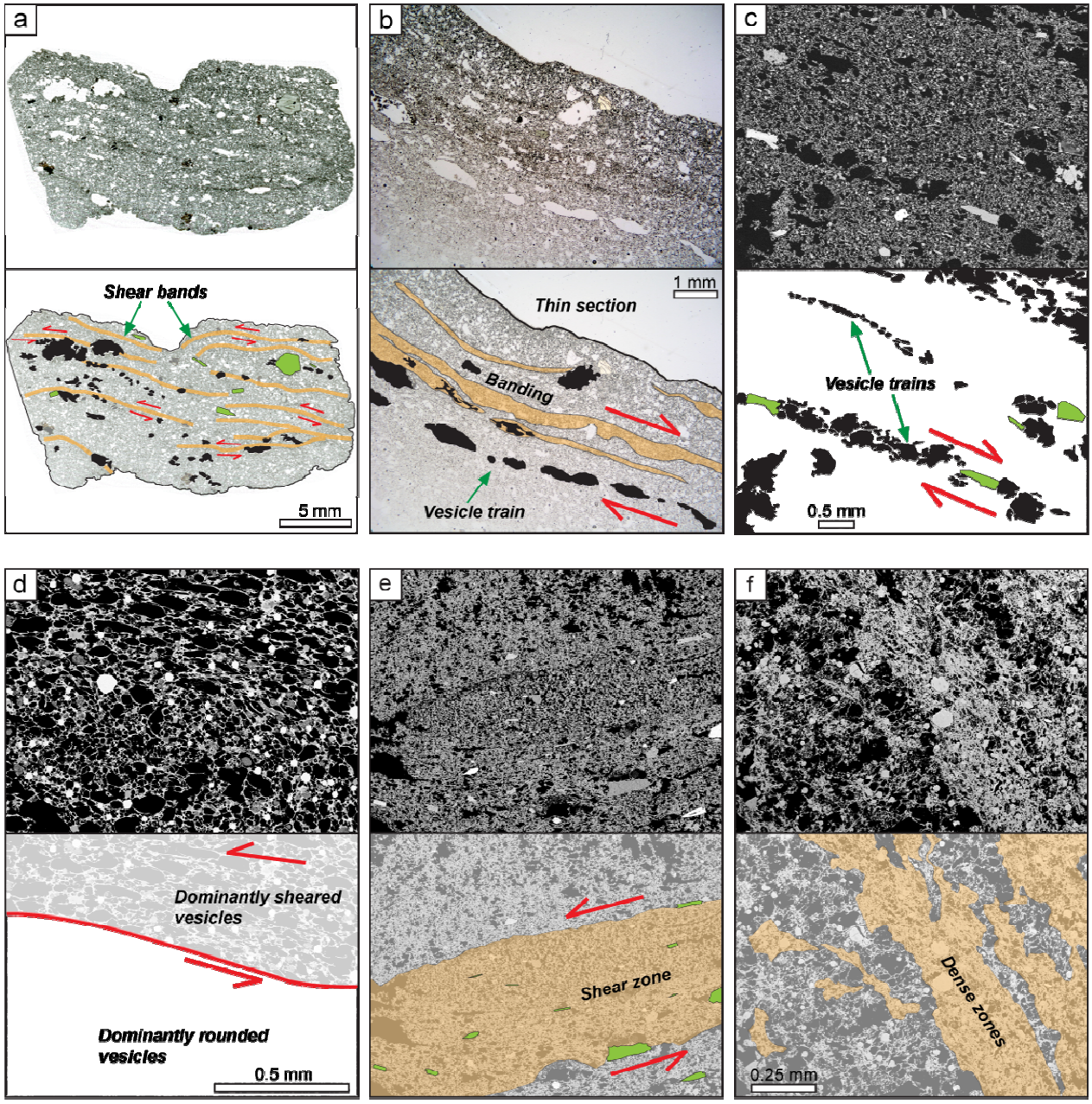

Figure 6: Shear zones and bands in 79AD pumice clasts. (a) Scanned thin section from a high vesicularity (~80%) fall clast from EU3base with tens of shear bands and vesicle alignments. (b) Image of a low vesicularity (~68%) clast from PC1 with combinations of dense bands and elongated vesicle trains. (c) Train of non-elongate vesicles displaying irregular margins (bottom) near a smaller train of elongate vesicles (top-left) in a high vesicularity (~74%) clast from PC4. (d) Progressive transition from undeformed vesicles (bottom) to increasingly sheared vesicles (top) in a high vesicularity (~77%) pumice from BO. (e) Shear band observed in PC4 (vesicularity ~52%). This shear-zone encloses some remnants of collapsed vesicles, and has been repopulated by smaller vesicles. Note the irregular vesicles on top, and the abrupt transition to the shear-zone. (f) Dense bands in fall pumice EU1 alternating with high vesicularity zones. Again, smaller round vesicles are present within the shear bands. In images (c) and (e), elongate phenocrysts shown in green appear aligned with shear-zones or vesicle trains.

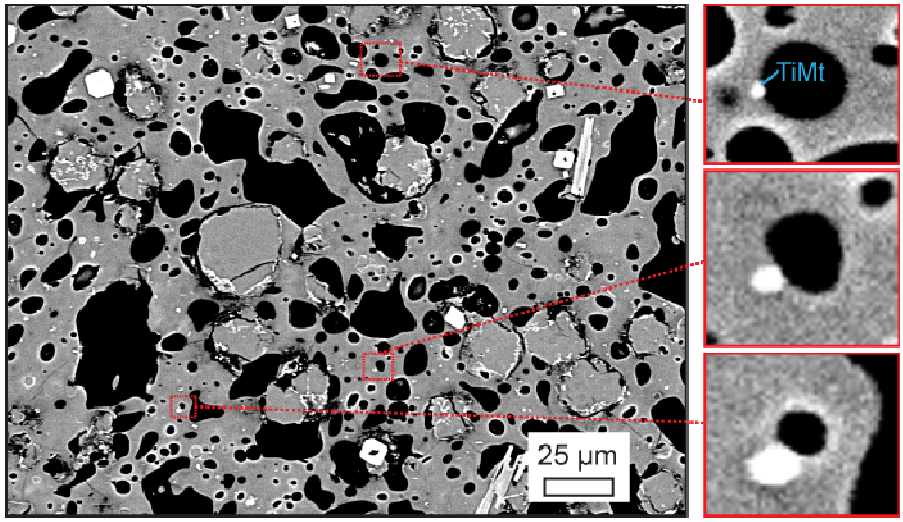

Figure 7: 500× SEM image of sample 19-1-10 from PC4 showing clear glass full of tiny oxide microlites that served as nucleation sites for bubbles during magma decompression. Several grains are enlarged to show the relationship frequently encountered between vesicles and oxides.

3.3. Textural measurements

Vesicle volume distributions: VVDs from selected low and modal density PDC clasts (Fig. 8) vary little throughout the EU3 phase of the eruption. The dominant mode in vesicle size remains at 25-35 µm (equivalent diameter) for the entire PDC and fall succession. All modal and low density pumice show extended distribution tails towards large vesicles (positive skewness), and some possess possible secondary modes of larger (i.e. L > 200 µm) vesicles (e.g. 22-4-8, 21-1-10, 19-1-4, 27-1-9). In contrast, high density clasts have distributions that vary significantly from the base to the top of the stratigraphy. Excluding TC, high density clasts from PC1 to BO have distributions that progressively broaden, and distribution amplitudes that decrease (i.e. lower kurtosis). These distributions also become more irregular, particularly towards small and medium vesicle populations. BO illustrates the extreme case of this pattern with a ragged distribution shape possessing no well-defined mode, as well as much lower peak frequencies. The high density PDC pumice associated with the total collapse of the column (TC) departs from this trend of increasing distribution complexity, with a distribution similar to PC1 and most modal density clasts.

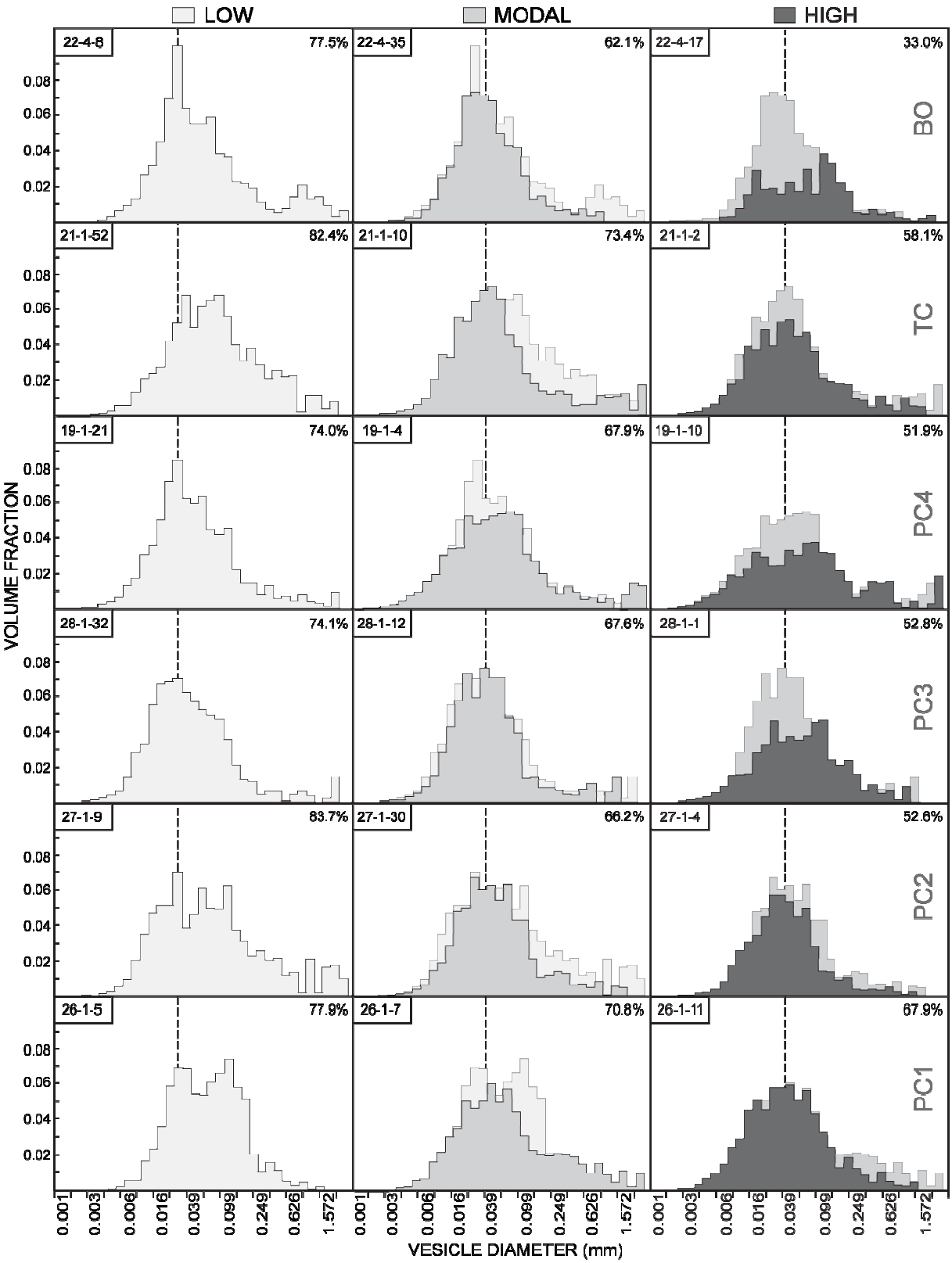
LOW
MODAL
HIGH
22-4-6
77.5%
22-4-35
62.1%
22-4-17
33.0%
BO
21-1-52
82.4%
21-1-10
73.4%
21-1-2
58.1%
TC
19-1-21
74.0%
19-1-4
67.9%
19-1-10
51.9%
PC4
28-1-32
74.1%
28-1-12
67.6%
28-1-1
52.8%
PC3
27-1-9
83.7%
27-1-30
66.2%
27-1-4
52.6%
PC2
26-1-5
77.9%
26-1-7
70.8%
26-1-11
67.9%
PC1
VOLUME FRACTION
0.02
0.04
0.06
0.08
0.001
0.003
0.006
0.016
0.039
0.099
0.249
0.626
1.572
VESICLE DIAMETER (mm)

← **Figure 8:** Vesicle volume distributions for the six main PDC deposits of the magmatic phase. Distributions are shown for low, modal and high density endmembers. Dashed lines mark the dominant modes. Size distributions for high density clasts are shown in the background of distributions obtained for modal density clasts, and distributions of modal clasts are reported with distributions for high density pumice for comparison. Jagged distributions in high density clasts mark the influence of bubble collapse and outgassing. From low to high density clasts, size distributions show loss of medium and large vesicles.

Globally, from low to modal density clasts, distributions show progressively a disappearance of large and medium size vesicles, and from modal to high density pumice, distributions lose medium vesicle populations mostly.

Cumulative vesicle size distributions: VSDs measured in PDC and fall pumice are all curved; consequently, CVSDs are typically preferred since they also provide useful information on nucleation behavior (e.g. Blower et al. 2001). Most CVSD curves on log-log plots follow similar trends with simple power-law behavior from 0.01 to 2 mm (Table 1), and a curved exponential-like behavior for smaller vesicles.

Vesicle connectivity: Connected and bulk vesicularities (Fig. 9, Table 2) obey a straightforward 1:1 relationship for nearly all fall and PDC clasts measured from the gray magma phase of the eruption. Hence, vesicles within gray pumice are for the most part interconnected. The white pumice clasts from EU2 diverge slightly from the 1:1 trend as lower vesicularity samples show a significant proportion of isolated vesicles (5-10% in volume). Higher vesicularity EU2 clasts, like EU3 fall and PDC pumice, appear entirely connected. However, as the numerous very small vesicles (< 0.01 mm) comprise less than 1-2% of the total volume, our data do not provide sufficient resolution to determine the connectivity of the small vesicle population.

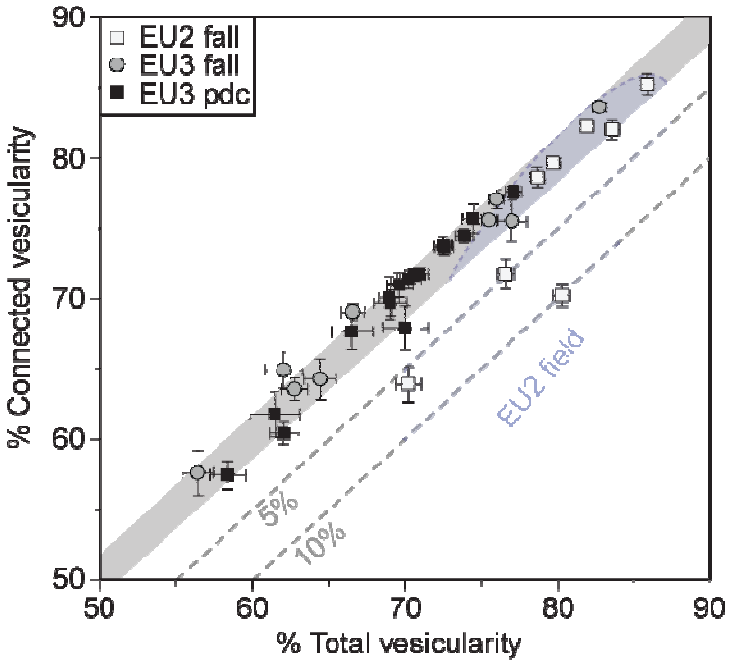

Figure 9: Vesicle connectivity plot obtained from He-pycnometer measurements. All gray pumice samples and over half of white pumice clasts plot on the 1:1 array, implying that their medium and large vesicles are fully connected. Three samples from EU2 show a larger fraction of isolated vesicles, particularly in high density clasts. Dashed lines represent lines of equal fraction of isolated vesicles.

Vesicle number density: Vesicle number densities are referenced to the melt fraction (N_{Vf}^{corr}) to correct for volume changes because of gas expansion. We observed, nonetheless, that gray pumice clasts have N_{Vf}^{corr} values that vary systematically with vesicularity even after normalization (Fig. 10a). To examine variations in mean number density throughout the stratigraphy, we normalized N_{Vf}^{corr} to a common vesicularity of 70% (N_{V70}^{corr} , Table 1 and Fig. 10a) by fitting straight lines through N_{Vf}^{corr} values obtained for the high, modal and low density clasts from each sample. Using a normalized value allows us to compare between the different units while avoiding the intrinsic relationship between vesicularity and number density. We also reported N_{Vf}^{corr} for all clasts to illustrate the range of number densities present in a single unit.

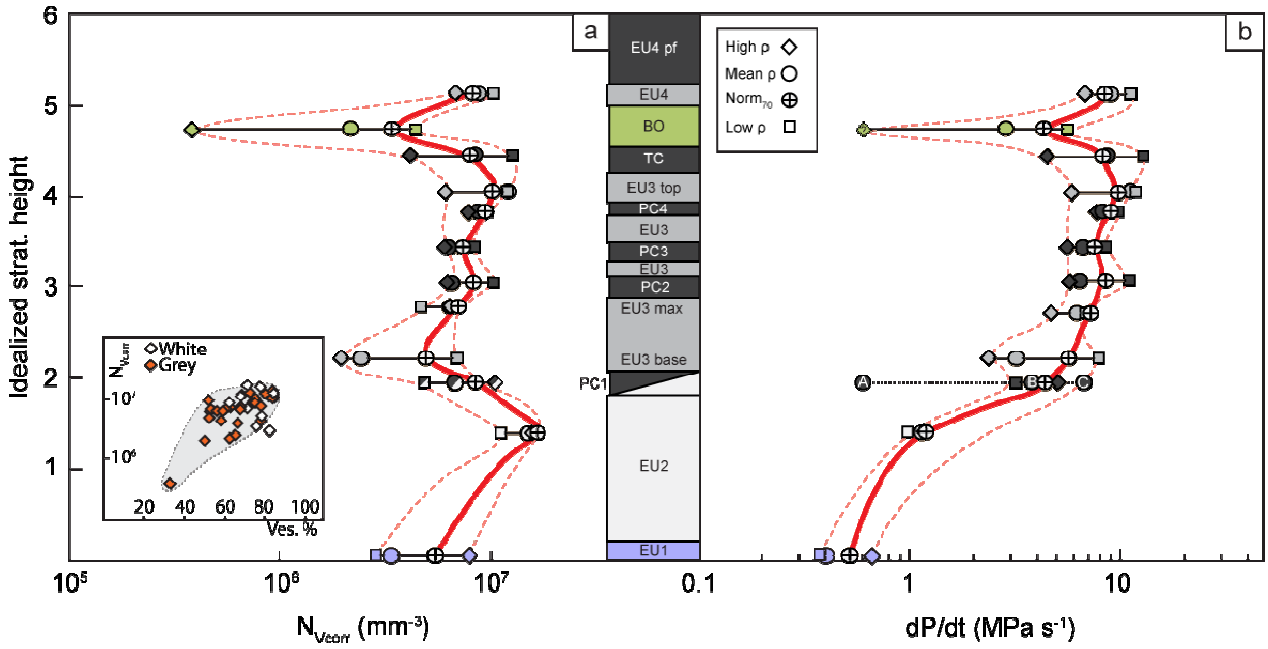

Figure 10: (a) Variations in vesicle number densities $N_{Vf}{}^{corr}$ throughout the stratigraphy. Inset shows that a relationship between number density and vesicularity exists for most gray pumice clasts whereas white pumice shows no well defined behavior. (b) Evolution of decompression rates calculated to match measured number densities. Due to differing compositions and properties (mainly temperature and diffusivity), the white magma nucleates higher numbers of vesicles at lower decompression rates. For layer PC1, kinetic properties of the phonolitic magma (EU2 white) result in decompression rate "A"; those of the tephriphonolitic magma (gray) yield "C", and intermediate values give "B". Thick red lines marks the evolution of average values, while dotted envelopes show the entire range. Crossed circles are average values.

N_{V70}^{corr} increases strongly from EU1 to EU2, reaching a maximum of 1.7 x 10^7 mm^{-3} (Table 1). N_{V70}^{corr} decreases at the transition between white and gray pumice PC1, then increases slightly from EU3base to TC in both fall deposit and PDC samples. Only unit BO displays significantly lower number densities (3.4×10^6 mm^{-3}). Low density gray pumice clasts also show a slight increase in N_{Vf}^{corr} with time, peaking at PDC pumice TC. Values of N_{Vf}^{corr} in high density pumice, which are typically lower than those measured in lower density clasts, remain constant throughout EU3 after an initial increase from EU3base to the first collapse PC2. Interestingly, these trends are reversed in EU1, EU2, and PC1, where high density clasts have higher N_{Vf}^{corr} than low density clasts.

3.4. Evolution of decompression rate during the magmatic phase of the eruption

Due to different magmatic properties (i.e. mainly *T* and melt composition), decompression rates inferred for the white magma are much lower on average than those obtained for the gray magma (0.4-1.2 MPa/s and 0.6-12.8 MPa/s respectively, Fig. 10b, Table 1). Note that for PC1, decompression rates calculated using magma properties intermediate between white and gray end-members fall between values of EU2 and EU3base. Inferred decompression rates are initially low at ~0.5 MPa/s during EU1, and increase to ~1.1 MPa/s during EU2. Much higher inferred decompression rates of 2.3-7.8 MPa/s are reached during initial eruption of gray magma (EU3base). Peak values of ~12.8 MPa/s are calculated for the low density pumice of TC, while BO suggests diminished rates of decompression.

3.5. Crystal textures

Leucite number densities: $N_{Vcorr\text{-}lc}$ values (Fig. 11a) measured in white pumice (cf. Gurioli et al. 2005a; Shea et al. 2009) reach ~ 5×10^4 mm^{-3} and are typically lower than number densities from gray clasts. Within gray pumice deposits (PDC and fall samples), N_{V-lc}^{corr} values stay within one order of magnitude but show a two-fold increase from PC1 to EU4 (12×10^4 $mm^{-3}$and 24×10^4 mm^{-3} respectively, values averaged over low+modal+high density clasts, Table 1). No obvious correlation is observed between leucite number density and clast vesicularity.

Leucite size: For brevity, only dominant modes of leucite volume distributions are shown (Fig. 11b). Leucite modes in PDC clasts investigated show a small but noticeable size increase throughout the eruptive stratigraphy. From the bottom to the top of the succession, average sizes increase from 25 μm to around 30-35 μm by the end of the magmatic phase, implying 5-10 μm total growth.

Crystal volume fraction: As expected from the moderate increase in size and number (Fig. 11a and b), the melt-referenced leucite content (Figure 11c) also increases throughout the magmatic phase of the eruption, from 13-17% for EU2 and EU1, to about 35% within EU4, although there is a wide range of leucite content for each unit. In contrast, phenocryst and microphenocryst contents (leucites excluded) do not show significant changes over the investigated eruptive phases. Importantly, there is no substantial difference between fall units from the gray magma and PDC units in terms of crystal content, size or number.

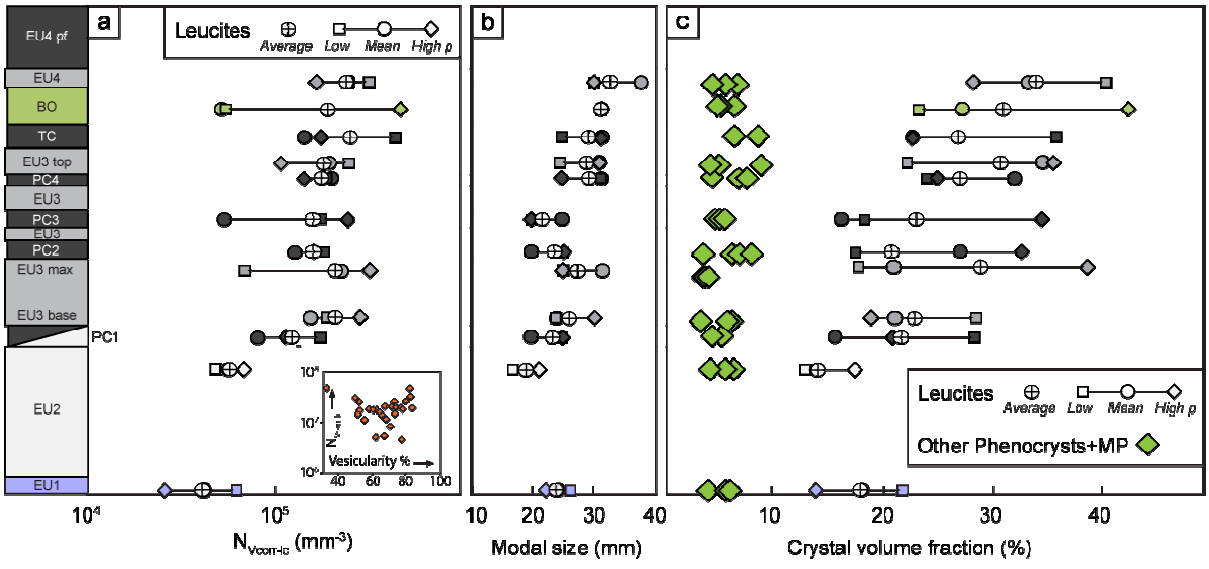

Figure 11: Textural data for leucites and other crystals. (a) Number densities, (b) modal sizes, and (c) resulting volume fraction. Leucites tend to continue forming during the eruption, while other phases stay mostly constant.

4. Interpretation

The following paragraphs give first order interpretations of the textural data measured from fall and PDC units. We elucidate whether magma density variations could have played a part in the formation of PDCs, and attempt to clarify how these density variations were brought about within the conduit by interpreting vesicle textures (vesicle appearances, sizes, numbers, connectivity, glass wall thicknesses). We invoke the potential role of shear localization in decreasing the vesicularity of magma, and try to explain the meaning of the variations in crystallinity observed.

4.1. Pumice density

Variations of clast density throughout the entire magmatic phase of the eruption (EU1-EU4, Gurioli et al. (2005a) and measurements herein) reveal some consistent changes during transitions from fall deposits to PDC units. Most PDCs sampled contain clasts that are, on average, denser than pumice within fall deposits (Figs. 3 and 4) and their distributions are broader with coarser tails (i.e. positive skewness). In comparison, fall layer EU3max has a higher fraction of dense clasts than subsequent PC2, and TC shows density histograms indistinguishable from most fall samples (i.e. mode at $\rho \sim 700$ kg m^{-3}, narrow distribution with no coarse tail). To a first order, density is thus a viable candidate for partial destabilization of the eruptive column and the ensuing production of PDCs, although there is a need to elucidate why the column could stay stable during eruption of EU3max prior to PC2. Furthermore, an alternative mechanism for the formation of TC (total collapse of the column) must be invoked.

4.2. Vesicle textures

Qualitative observations of vesicle shape and size reveal that clasts from PDCs in the gray pumice differ only slightly from fall clasts investigated previously by Gurioli et al. (2005a). Low and modal density clasts from PDC units display a subpopulation of large vesicles (coarse tails within distributions, Fig. 8), thin glass walls (Fig. 5), extensive coalescence, and trains of sheared or non- to lightly-sheared vesicles. High density PDC samples show an increasing thickening of glass walls through time (i.e. from PC1 to BO, Fig. 5) and increasing evidence of partial bubble collapse (cf. Fig. 5, and high density VVDs in Fig. 8). In general, vesicle textures within PDC pumice are similar to those in fall samples, and textures reflect the vesicularity of the imaged clasts more than their stratigraphic location or depositional origin.

White EU1 and EU2 pumice have textures that are distinct from those of gray pumice. Bubble collapse textures were detected only within narrow (i.e. 0.1-0.5 mm) shear zones in EU1 and EU2, whereas they occur both in shear zones and in undeformed areas in EU3 high density clasts. Measurements of glass thickness (Fig. 12a) also confirm that both fall and PDC samples have undergone phases of coalescence and collapse. Initial glass thickness can be calculated from the total vesicle number density as $S_0 = (3/4\pi N_V^{corr})^{1/3}$ (Lyakhovsky et al. 1996). In high vesicularity (i.e. >65%) pumice, the calculated S_0 is typically thicker than the glass thickness measured, suggesting that expansion has stretched bubble walls.

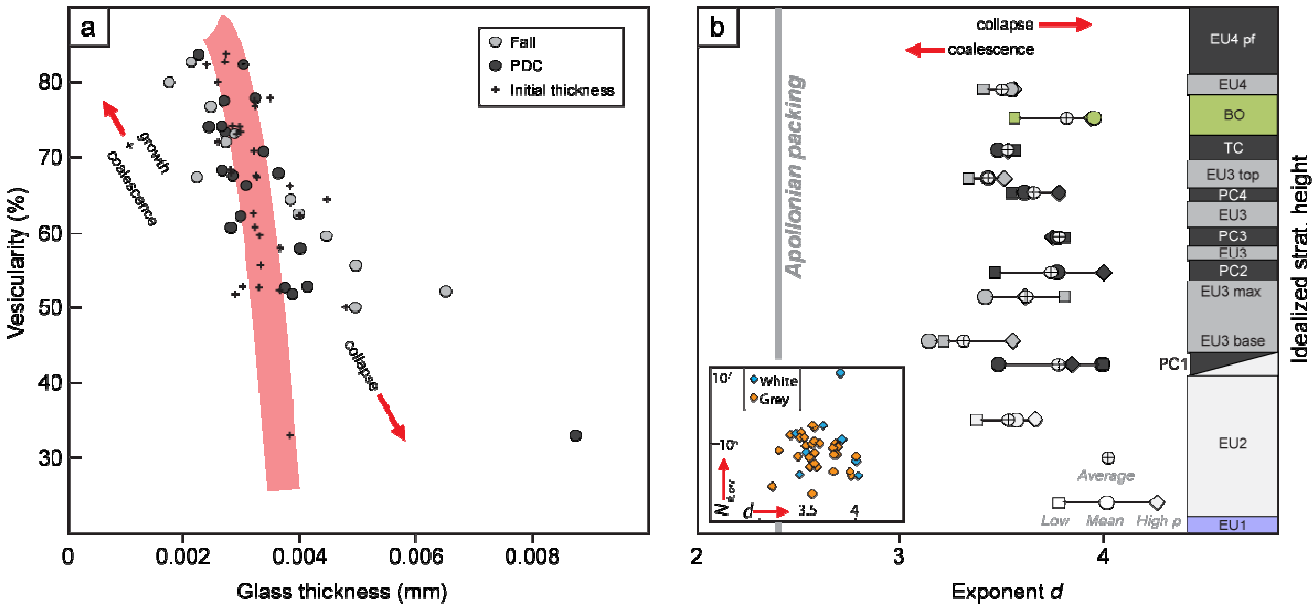

Figure 12: (a) Glass wall thickness vs. vesicularity in fall and PDC samples. Black crosses represent calculated initial wall thickness from number densities. The thick array is the best fit through these crosses, the array width representing the typical standard deviation in thickness. Data located to the upper left of the array have stretched vesicle walls and high vesicularities (i.e. bubble expansion and coalescence), data positioned to the lower right show thicker walls and lower vesicularities (i.e. bubble collapse). (b) Power-law exponents from CVSD curves. To a first order, high nucleation rates produce high exponents (d>3). Second order variations (3<d<4) cannot be attributed solely to intense nucleation (i.e. lack of correlation between d and N_{Vcorr} in the inset). Rather, coalescence processes tend to increase the participation of larger vesicles thus reducing the slope/exponent, while bubble collapse increases the exponent. As a result, PDC samples ttypically have higher exponents suggesting more mature vesicle textures.

In contrast, glass walls in low vesicularity pumice are much thicker than values predicted for initial glass meaning that the latter samples likely underwent outgassing by collapse.

All clasts show power-law relationships for most of the measured size range (Table 2). This behavior probably reflects continuous nucleation of bubbles during ascent (e.g., Blower et al. 2001) although it also represents a geometric constraint on highly vesicular samples (e.g., Klug and Cashman 2002). Power-law exponents for the different fall and PDC samples (Fig. 12b) obtained from fitting the coarser part of the curves (0.01-3 mm) lie between 3.3 and 4, well above the value inferred for Apollonian packing (d ~ 2.45). Higher exponents can be obtained by increasing the small vesicle populations

(i.e. through intense nucleation), and/or by decreasing the number of medium-to-large vesicles (i.e. through coalescence and collapse). In fact, exponents higher than 3 are extremely common in tephra from highly explosive eruptions (e.g. Gaonac'h et al. 1996; Klug et al. 2002; Adams et al. 2006) because they typically produce clasts with high vesicle number densities. Thus, nucleation rates were likely to be high in 79AD magmas to generate values of $d > 3$, both during eruptive phases producing fully stable columns (EU1-EU4 fall, Gurioli et al. 2005a) and during phases generating PDCs. In detail, however, d is typically higher during PDC phases ($d \sim 3.7$-3.9) than in fall-producing phases ($d \sim 3.4$-3.5) with the exception of TC, which has d values that resemble fall samples, and EU3max, which has an elevated d (3.8). These high exponents are not directly correlated to vesicle number densities (Fig. 12b), hence supporting the alternative explanation, which is that PDC samples have suffered more vesicle loss by bubble collapse than fall samples.

Analysis of vesicle connectivity within fall deposits from the white (EU2) and the gray (EU3) magmas compared to PDCs (EU3pdc) suggests that vesicles within pumices produced by the eruption are for the most part connected. EU2 is the only unit containing clasts that display a high proportion of isolated vesicles (Fig. 9). These observations agree well with textures being in earlier stages of vesiculation in white pumice than in gray pumice. As coalescence begins, connectivity is promoted and magmas lose their isolated vesicles. Note that maturing of high density clast textures in Figure 8 removes medium and large-sized vesicles from the distribution. Small-vesicle populations are unaffected, which explains why pumice samples can maintain high vesicle number

densities (controlled mostly by small vesicle populations) while being nearly fully connected in terms of vesicle volume fraction.

PDC vesicle number densities compared to those of fall pumice EU3base, EU3top and EU4 show moderate variations overall (Fig. 10a). Normalized N_{V70}^{corr} values increase slightly throughout the sequence containing the gray pumice, and show no change at transitions between fall units and PDC deposits. High density (low vesicularity) clasts in EU3 times typically show lower number densities except for BO, where the low vesicularity end-member has even lower N_{Vf}^{corr}. The positive correlation between vesicularity and number density throughout gray pumice deposits favors a scenario in which vesicular magma experienced more vigorous nucleation than less vesicular magma. Interpreted in terms of decompression rates (Fig. 10b), this phenomenon can be explained as follows: zones of higher density/lower vesicularity within the ascending magma column are decompressed more slowly than zones of lower density. Spatially, this means that there must be a specific conduit configuration or process allowing a horizontal density gradient to form. We later argue that such zoning develops through the combination of velocity gradients and resulting shear localization within the ascending magma. Note that the overall decompression curve calculated for the magmatic phase of the eruption (Fig. 10b) seems to correlate well with estimates of column height variations (Fig. 1b) until the generation of PC2. Column height then decreases while number densities increase moderately.

The ubiquitous incidence of dense bands and trains of irregular/elongate vesicle trains within pumice clasts (fall+PDC, Fig. 5) suggests that shearing occurred within the

conduit during magma ascent. The diverse textures indicate different responses of the deforming magma to applied stresses. Less obvious shearing textures include vesicles that are progressively deformed, for which sharp deformation boundaries are difficult to define (Fig. 6d). On the other hand, some dense shear bands show abrupt transitions from undeformed to intensely sheared bubbles (Fig. 6e). In many cases (Figs. 6e and 6f), small vesicles seem to have nucleated within the dense band. This implies that at least some shear zones had formed prior to the last nucleation events. Vesicle trains also exhibit textural variations with “type 1” being fairly elongate with smooth outlines (Fig. 6b) and “type 2” displaying more equant shapes with irregular outlines (Fig. 6c). Possibly, deformed bubble trains could result from shearing induced coalescence while more equant trains could be generated by heterogeneous bubble nucleation and growth along inactive (i.e. “healed”) shear zones. Interestingly, dense bands and bubble trains can occur together at the clast scale (Fig. 6b), suggesting that narrow shear zones can be active within a small portion of the magma at different stages. Based on the various textures and their distributions within 79AD pumice clasts we propose a formation cycle for shear zones (Fig. 13). Initially, the presence of a lateral velocity gradient within the conduit (i.e. maximum velocity at the center, minimum at both conduit margins) leads to the formation of numerous millimeter-scale shear zones. These zones first appear as domains where equant vesicles become progressively deformed on the scale of a few mm. As shearing progresses, these zones narrow and the transition between undeformed and deformed bubbles becomes more abrupt. Vesicles are forced into coalescence within this narrow zone and may form elongated trains. As coalescence progresses, connectivity increases until exsolved gases are able to escape by bubble collapse along the deforming

zone. Shear zones now appear as dense, vesicle-poor bands that may end up undergoing further vesiculation (i.e. as indicated by the presence of numerous tiny vesicles) or heal and progressively disappear.

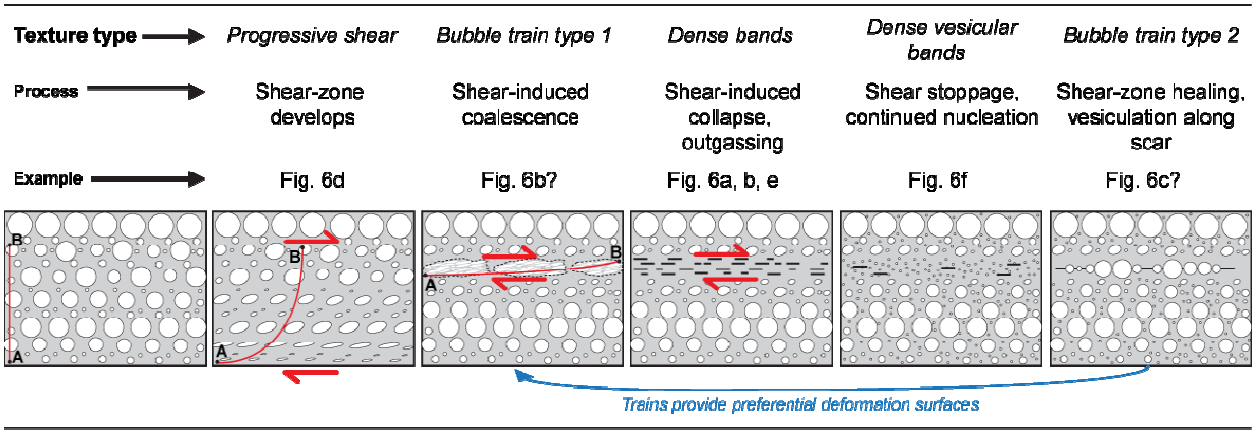

Figure 13: Hypothetic model for formation, evolution and demise of shear-zones. Vesicles are drawn according to their elongation, and the shape complexity commonly observed is not depicted. Connected points A and B mark the deformation profile within the three first sketches. Different textures are displayed along with the process responsible for their formation as well as Fig. 6 examples. Shear-localization initiates within a zone a few tens of vesicles in width. Larger bubbles are more readily deformed and coalesce as shear continues. Coalescence continues until bubbles are connected and gases escape. Collapsed bubbles form a dense band with lineations marking their prior presence. If shear delocalizes and stops, the bands can heal and nucleation continues. Along the preferential weakness zones still available, bubbles may expand along lines forming undeformed vesicle trains. These trains can in turn serve as new preferential sites for shear-localization and favor new outgassing cycles (blue arrow). It is possible that healed shear bands could also provide sites for nucleation and growth of new bubbles that may end up aligned in non-deformed trains.

4.3. Crystallization of leucites and other phases

Leucite crystals increase in size, and somewhat in number throughout the magmatic phase of the eruption. No change was observed between leucite size and number at the transition from fall pumice to PDC units. There is also a lack of correlation between leucite number density and vesicle number density (and thereby decompression rate), providing strong evidence that leucites in the gray magma did not form during ascent. The same conclusion was first suggested by Gurioli et al. (2005) and later

confirmed by Shea et al. (2009) for leucites within the white magma via laboratory decompression experiments. Hence, following the model proposed in this previous study, leucites nucleated in the magma storage area shortly prior to and during the eruption (i.e. as overlying magmas were progressively being tapped), most likely during a slow decompression phase before entering the conduit. The fact that leucites are found in slightly greater numbers and sizes as the eruption progresses simply reflects the longer time spent in the storage region prior to acceleration during decompression.

Finally, all pumice clasts from both white and gray phases of the eruption contain oxide microlites which probably served as nucleation sites for bubbles (Fig. 7) (Shea et al. 2010b). The only other microlite phases (sanidine and plagioclase) are found only in the last PDC of the magmatic phase, BO (Fig. 5). Their unique presence within this unit supports a model in which certain portions of the magma ascended slowly and/or stalled within the conduit for an extended time period and crystallized both phases. This hypothesis is supported by the lower N_{Vf}^{corr} value measured for this particular sample (BO high density, 22-4-17).

5. Discussion

5.1. Bubble nucleation, growth and maturation cycles within 79AD magmas

The comparison of vesicle texture data from both fall and PDC deposits within the white and gray pumice units of the magmatic phase of the 79AD eruption indicates that there is no fundamental difference in their degassing behavior. In both the phonolitic

white magma and the tephriphonolitic gray magma, nucleation was influenced by the ubiquity of tiny oxide microlites within pumice clasts. These crystals, particularly magnetite, play a significant role in reducing the degree of supersaturation needed to trigger nucleation (Hurwitz and Navon 1994; Mourtada-Bonnefoi and Laporte 2002; Mangan and Sisson 2005; Cluzel et al. 2008). Experiments involving decompression of EU2-derived melts by Larsen (2008) and later by Shea et al. (2010b) demonstrated that heterogeneous nucleation occurs within phonolitic magmas at 79AD eruption conditions (~0.25 MPa/s), and even at much higher decompression rates (3-17 MPa/s). Judging from the omnipresence of titanomagnetite within gray pumice (Figs. 5 and 7), we postulate that heterogeneous nucleation dominates during degassing of the 79AD gray magma as well. A simple calculation using Eq. (1) shows that extreme decompression rates on the order of 90-100 MPa/s are needed to produce the bubble number densities measured in EU3 pumice if values of surface tension for homogeneous nucleation in phonolites are applied (σ_{HOM}~0.09 N m^{-1}, Iacono Marziano et al. 2007). Using surface tension values that assume heterogeneous nucleation, peak rates calculated for the gray magma (~13 MPa/s) are still high for natural eruption conditions (equivalent to 500 m/s assuming a lithostatic pressure gradient). Thus, we cannot entirely discard the possibility that disequilibrium degassing and some degree of homogeneous nucleation may have taken place during the final stages of vesiculation prior to fragmentation, and that the values calculated represent "effective" decompression rates. Further decompression experiments on gray pumice are required to verify this hypothesis.

As in the white magma (cf. Gurioli et al. 2005a), bubble nucleation does not occur as one or a few pulses but is sustained during ascent. CVSDs obtained in both PDC and

fall pumice from white and gray magmas are best described by power-law relationships with exponents greater than 3. High *d* values testify primarily to high nucleation rates (e.g. Blower et al., 2001), and, to a second order, to the maturing of vesicle textures, as medium to large bubble populations are lost due to collapse and outgassing. While the type of nucleation (i.e. heterogeneous) and the duration of nucleation (i.e. continuous) were comparable throughout ascent of EU3 fall and EU3 PDC parent magmas, important differences exist in the respective proportion of clasts that exhibit mature vesicle textures and higher densities. PDC pumice systematically shows higher exponents than fall pumice, except for the TC sample. In the absence of a direct correlation between *d* and N_{Vcorr} (Fig. 12b), the high exponents in PDC magmas indicate higher numbers of "mature" clasts with lower vesicularities (Figs. 3 and 4) compared to fall units. Still, taken individually, both PDC and fall clasts exhibit mature textures and glass walls that thicken with increasing clast density (Fig. 12a). Hence, the transition from fall-to-PDC-producing columns was not triggered by radically different degassing processes within the conduit, but rather by the changing relative proportions of different density/vesicularity end-members in the conduit, as discussed further below.

The absence of measurable proportions of isolated vesicles within pumice from both fall and PDC phases of the gray magma compared to EU2 samples (Fig. 9) implies that medium and large-sized vesicles in the gray magma developed quasi-complete connectivity. The development of connected vesicles through diffusive bubble growth, expansion and coalescence depends on the relationship between the decompression ($\tau_{dec}=\Delta P/\Delta t$), the diffusive ($\tau_{dif}=L^2/D$), and the viscous relaxation timescales ($\tau_{vis}=4\mu/P_0$), where ΔP and Δt are the total decompression and total ascent time, L is bubble radius, D

is diffusivity, μ is the initial melt viscosity, and P_0 the initial pressure (Lensky et al., 2004; Gonnerman and Manga, 2007). For a bubble sizes typical of the range measured for coalescing vesicles in EU2 and EU3 samples (~40-100 µm in radius, c.f. Fig. 7), diffusivities used in previous calculations, melt viscosities of 10^3 and 10^2 Pa s for EU2 and EU3 respectively, initial pressures of 100 MPa we find that generally $\tau_{dec} > \tau_{dif} > \tau_{vis}$ for the gray magma, meaning that degassing occurs at equilibrium conditions, whereas for the white magma $\tau_{dif} > \tau_{dec} > \tau_{vis}$ implying that the time needed for diffusion of volatiles may be greater than the time available for decompression in the case of larger bubbles. Thus, degassing would prerably occur through enhanced nucleation rather than diffusive growth by the time bubbles reach certain sizes in the white magma. In turn this behavior would lead to the production of more mature textures with enhanced connectivity within the gray magma compared to the white, which is confirmed by pycnometry measurements (Fig. 9).

Interestingly, Klug and Cashman (2002) found that Crater Lake pumice from fall phases of the Mazama eruption had higher connectivity than PDC pumice, which is in stark contrast with pumice from the 79AD eruption. They interpreted their data to reflect less time for bubbles to grow and for connectivity to develop during PDC phases, ultimately resulting in lower vesicularities at fragmentation. In 79AD pumice, PDC phases typically possess high fractions of dense clasts and more mature vesicle textures reflecting prolonged ascent times compared to fall pumice. Hence, it appears that both prolonged and abridged ascent paths can produce higher density clasts after fragmentation and trigger the destabilization of the eruptive plume.

5.2. Leucite crystallization

Leucite microphenocrysts within the 79AD pumices show moderate increases in size and numbers throughout the magmatic phase. Modal size increases by merely 5-10 μm from PC1 to BO (Fig. 11b). Leucites in the white magma were inferred by Shea et al. (2009) to have crystallized during slow decompression of the magma chamber less than 5 days before the eruption. Data for the gray magma agree well with the latter model: leucite crystals increased only slightly in size and numbers due to increased holding time spent within the decompressing chamber. If minimum leucite growth rates of 10^{-7} mm s^{-1} determined by Shea et al. (2009) can be applied to the gray magma, it would have taken ~14-20 h for leucites to grow an additional 5-10 μm from EU2 to the end of EU3. Note that this value is slightly higher than the time-interval determined by Sigurdsson et al. (1985; 1989) for the time between EU2 and the beginning of EU4 (12 h), which is not surprising considering the growth rates are minimum values.

5.3. The role of small-scale shear zones within the conduit

Within 79AD phonolites, no tube/fibrous pumice clasts are found, but evidence of deformation prior to fragmentation is ubiquitous in the form of mm-scale planar features (cf. Fig. 6). Our proposed model for the formation of these textures involves phases of shear-initiation with wide zones of progressive vesicle deformation towards the shear zone, then thinning by increasing bubble coalescence and collapse (Fig. 13). The presence of shear zones and bands depicting different stages of this process within a single clast, suggests continuous strain localization and transfer: whenever a shear zone

vanishes and heals, stress is transferred to form a new shear zone nearby. Trains of undeformed vesicles may even form within areas of healed shear bands, and further provide new slip surfaces if deformation continues. As noted by Wright and Weinberg (2009), important feedback processes are expected to occur during the evolution of shear zones. At the early stages of strain localization, vesicles are dominantly equant and possess low capillary numbers $Ca = \frac{L\dot{\gamma}\mu_S}{\sigma} << 1$ (where L is bubble radius, $\dot{\gamma}$ is strain rate, μ_S is shear viscosity and σ is melt-vapor surface tension; Rust and Manga 2002; Llewellin et al. 2002), thus opposing significant resistance to the surrounding stresses. As vesicles are sheared, Ca values increase and bubbles increasingly accommodate deformation by free slip. The combination of bubble deformation and shearing-induced coalescence enhances viscosity reduction along these slip surfaces, and shear-zones become narrower, accommodating increasingly higher strain rates. As vesicles become interconnected within the shear-zone, permeability develops and outgassing through the newly created pathways can occur. Once shear zones are vesicle-free, stresses will be transferred nearby to create new slip bands and the initial shear zone will effectively heal. New, undeformed vesicles can then subsequently nucleate within the dense, healed zones.

Marti et al. (1999) noted that shear zones appear in magmas of various compositions. While their occurrence in phonolites confirms this, there may be some non-negligible differences in strain-localization mechanisms that are dependent on magma composition/viscosity and crystallinity. Hypothetically, more viscous magmas like rhyolites or rhyodacites would tend to develop larger-scale, wider zones of shear resulting in the formation of tube or banded pumice (e.g. Polacci et al. 2001), whereas

less viscous phonolites would experience the formation of numerous narrow zones that accommodate variations in ascent velocity within the conduit. However, tube pumices of trachytic composition fairly similar to Vesuvius phonolites were also found in the Campanian Ignimbrite (3-5% more SiO_2 and 1-2% less alkalis in the trachytic ignimbrite, Polacci et al. 2003), hence composition alone cannot explain the presence or absence of larger shear zones. The main difference between the latter two pumices is their crystal content; Campanian pumice contains less than 5% crystals, whereas 79AD pumice contains 20-40%. In the case of the rhyolitic Ramadas pumice, Marti et al. (1999) suggested that garnets acted as dislocation points facilitating propagation of shear movement. Leucites could potentially achieve the same effect, facilitating shear propagation and ultimately resulting in the formation of more numerous but thinner shear bands. This view agrees well with the formation of tube pumice from the crystal poor (i.e. <10%) Mt Mazama rhyodacitic magmas (Klug et al. 2002), but opposes the finding of numerous homogeneously foliated pumice clasts produced by crystal-rich (40-50%) magmas with rhyolitic melt compositions at Pinatubo (Polacci et al. 2001). Thus, the combined effects of crystals and melt properties such as viscosity probably need to be taken into account in the formation of shear zones. While physical and numerical models that investigate conduit shearing have already predicted the formation of wide shear zones during ascent (e.g. Mastin 2005; Hale and Mulhaus 2007), future models that include space-time variations of ascent velocity, *Ca* numbers, viscosity and crystal content for different magma types could help elucidate whether the density and the width of shear zones can be correlated with crystallinity and viscosity.

5.4. Conduit model for ascent and vesiculation of the 79AD gray magma

We have deduced that degassing processes were relatively similar throughout PDC and fall samples from the gray magma phase of the eruption, that more dense clasts are found within PDC deposits, that shear zones appear in most pumices, and that decompression rates generally increased but varied little from fall to PDC. Furthermore, the overall negative correlation observed between clast density and vesicle number density supports slower decompression of higher density clasts. Altogether, these observations require a conduit model that accounts for both decompression rates and density variations. If we assume that collected pumices acquire their final texture during fragmentation (e.g. Houghton and Wilson 1989; Klug et al. 2002), then varying magma densities/vesicularities were acquired within the conduit below fragmentation. Here, we propose that the range of clast densities measured within deposits from the various phases of the eruption correspond to both spatial and temporal degassing variations within the conduit (Fig. 14). In EU3 units, low density clasts result from fragmentation of magma in the central section of the conduit, where decompression timescales were shorter (less time for maturing of textures), and where larger vesicles suffered less shearing-induced coalescence and collapse. The high N_{Vcorr} and decompression rates measured within these clasts reflect their central position in terms of the velocity profile across the conduit. Conversely, high density, low vesicularity pumice would be produced by fragmentation of more marginal magma. The lower decompression rates recorded within these clasts argue for their more peripheral position as ascent velocities are expected to be lower, and residence times longer. The abundance of small-scale shear zones within high density pumice, as well as the presence of collapse textures outside shear zones, suggests that

coalescence and collapse have occurred to a greater extent in high density samples. The occurrence of variations in the relative proportions of low, modal and high density magma throughout the eruption can be accommodated by the progressive build-up near the margins of denser zones, as well as changes in the depth of fragmentation. Changes in the extent of lateral density gradients through time can explain adequately the production of eruptive plumes with varying proportions of dense clasts. The formation of dense zones favors dominantly stable plumes, while the clearing and eruption of these zones favor partial destabilization of the column by adding dense clasts into the system. Such cycles of build-up and clearing of denser magma could lead to the production of multiple partial collapses such as PC2, PC3, and PC4 (Fig. 14).

In addition to temporal density variations by formation of lateral vesicularity gradients, as magma travels upwards within the conduit, zones of denser magmas become thicker from the margins towards the center, creating vertical density gradients as well. The PDC generated during the total collapse of the column (TC) involved very few dense clasts (cf. Fig. 4). According to our model, if the magma is fragmented a greater depths, the denser margins are narrower and, overall, less dense magma is tapped. Hence, it is likely that the fragmentation level was deeper during production of TC (Fig. 14). This assertion is well supported by the provenance of lithic components in the deposits: Barberi et al. (1989) found that most units contained carbonate lithics of relatively shallow origins (~1.5-2.5 km), but found marbles, skarns and cumulates of deeper origins in deposits corresponding to TC and subsequent EU4.

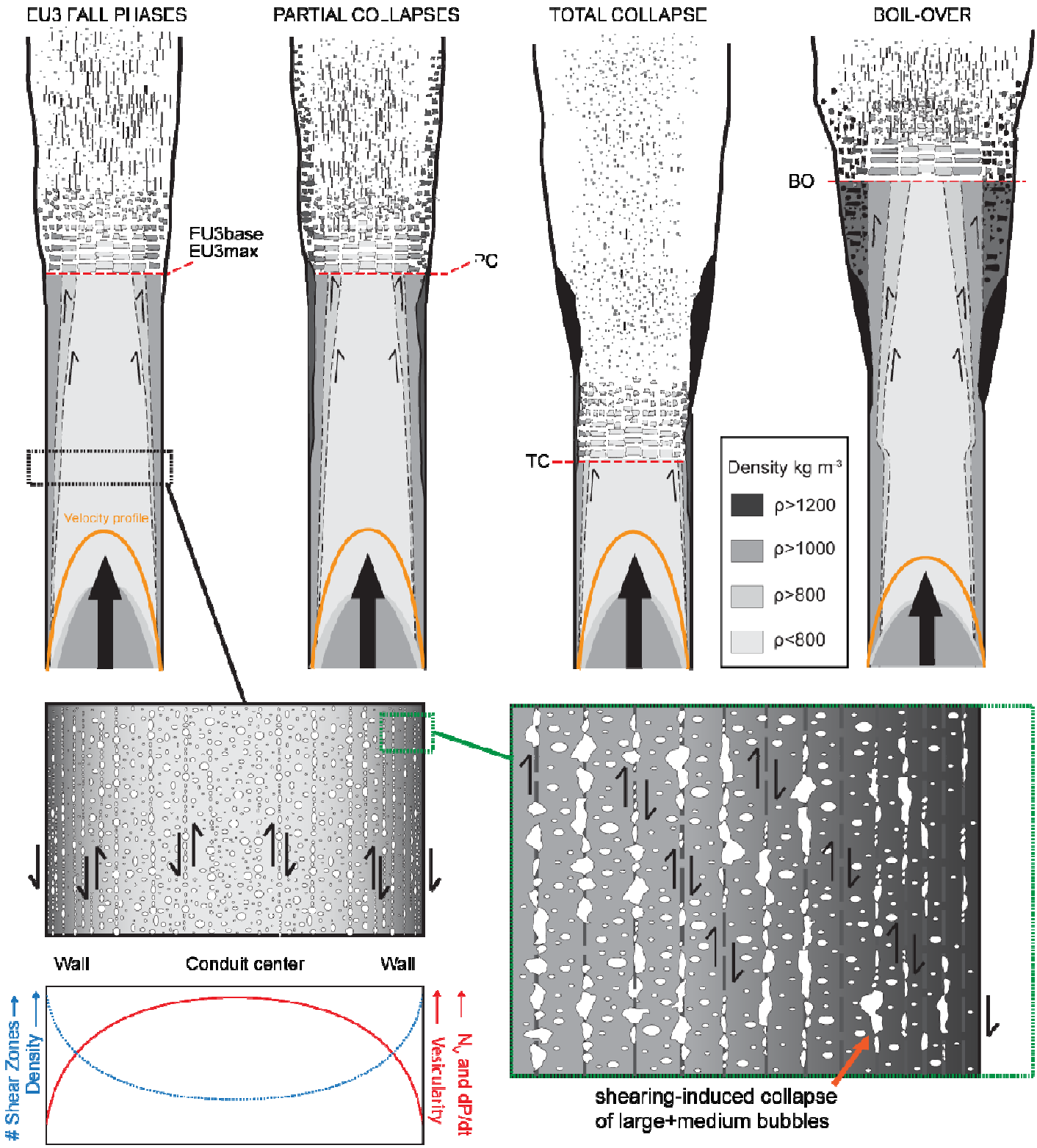
EU3 FALL PHASES
PARTIAL COLLAPSES
TOTAL COLLAPSE
BOIL-OVER
EU3base
EU3max
PC
TC
BO
Velocity profile
Density kg m-3
ρ>1200
ρ>1000
ρ>800
ρ<800
Wall
Conduit center
Wall
Shear Zones
Density
Vesicularity
Nv and dP/dt
shearing-induced collapse
of large+medium bubbles

← (p. 207) **Figure 14:** Conduit model during eruption of the 79AD gray magma. Denser clasts produced with low vesicle number densities typically originate from fragmentation of the slower-moving outer portions of the ascending magma, while lower density pumices are generated by fragmentation of the faster-decompressing central portion. Both maturing of bubbles unaided by shearing and forced maturing of bubbles by shearing contribute to forming these dense marginal zones. Temporal variations in the extent of these dense zones explain the inclusion of higher fractions of dense clasts during partial collapses, while combinations of changing fragmentation depth and vertical build-up of dense zones adequately explain the production of TC and BO. Zoomed insets show the details of how shear-zones affect the magma density by inducing bubble coalescence and collapse. A conceptual plot of density, vesicularity, decompression rates, number density and number of shear zones variations with lateral position in the conduit is shown below. Variations with conduit and how vesicle number densities are associated with the velocity profile imposed by shearing. Note that the horizontal scale for the conduit sketches is greatly exaggerated and that conduit radius increases from EU3base to BO as calculated in Table 3.

In stark contrast with TC, unit BO has a complex and extremely broad density distribution with a high fraction of dense clasts. This could imply that the magma travelled more vertical distance and had enough time to build-up wider dense zones. The fragmentation level, during production of BO, would have therefore been much shallower. The longer timescale available for maturing of bubble textures is reflected by the generally lower decompression rates calculated within clasts from this unit (Fig. 10). Additionally, sanidine and plagioclase microlites were found only in this deposit suggesting stalling or extremely slow ascent in a least some of the densest material involved in BO. Only lithics of shallow provenance (<1.5 km?) such as lavas and other volcanic rocks are found within BO (Cioni, unpublished data), reinforcing the idea that fragmentation occurred closer to the surface than during TC or the other PDCs. As fragmentation deepened during TC, some magma may have been left around the conduit margins and crystallized sanidine and plagioclase. When the fragmentation level rose after TC, some of the fresh ascending magma may have cleared the dense, degassed, microlite-rich magma (Fig. 14).

While this general model seems to be applicable to the gray pumice phase of the eruption, the end products of vesiculation and conduit shear may have been different during eruption of the white pumice. In EU1, EU2, and PC1 clast densities/vesicularities are not as well correlated with vesicle number densities; low density clasts show the lowest N_{Vf}^{corr} values in both EU2 and PC1 (Fig. 10). Due the more evolved nature of the white magma compared to the gray magma, in addition to the large temperature difference, the timescales of decompression, diffusive growth and viscous relaxation were likely fairly different resulting in more complex vesiculation histories, and the formation of different temporal and spatial density variations.

5.5. Mechanisms responsible for transitions from stable to collapsing eruptive columns

During the magmatic phase of the 79AD eruption, the column collapsed at least five times, either partially (PC1, PC2, PC3, PC4) or completely (TC). The sixth PDC investigated herein (BO) was likely produced by a collapsing jet or fountain (Cioni et al. 2004). Here, we attempt to link some of the parameters proposed as causes of column collapse (i.e. conduit radius and magma discharge rate variations) with other properties (i.e. clast density, vesicle number density). Variations in the pre-eruptive water content dissolved in the melt during the course of an eruption have also been postulated to affect strongly the stability of columns (e.g Neri and Dobran 1994). For instance, cooling or decompression-induced crystallization can cause the volatile content in the residual melt to increase. Ultimately, the increase in dissolved water enhances the stability of columns

by increasing exit velocity at the vent (Neri et al. 2002b). We consider that this is probably the case at Vesuvius since the crystallization of additional leucites from EU3base to BO (increase from 20-25 to ~35% in volume), if anything, would have increased the residual water content and favored the formation of a stable column. On the other hand, leucite crystallization during the slow decompression of gray magma probably affected the bulk viscosity of the magma (Table 3, Fig. A1 in the additional material). Bulk viscosity during the transition from white to gray magma was dominantly controlled by temperature differences between the upper thermally stratified portion of the chamber (EU1 and EU2 magmas) and the lower gray magma. In contrast, from EU3base to EU3 top, viscosity slightly increased due to crystallization which may have somewhat affected rates of magma degassing.

As initially suggested by Sigurdsson et al. (1985), increases in magma discharge rates (MDR) could potentially explain the global shift from dominantly convective to collapsing plumes. Based on calculations of column height (Fig. 1b), Carey and Sigurdsson (1987) derived MDR values that show a strong increase from ~7×10^{6} kg s^{-1} during EU1 to ~1.5×10^{8} kg s^{-1} prior to PC2 (Fig. 15a, Table 3). Subsequently, because column height calculated from inter-PDC fall units decreased after PC2, their values of MDR also decreased to ~10^{8} kg s^{-1} after PC3, and to ~10^{7} kg s^{-1} after TC.

Table 3: Summary of main eruptive parameters adopted for the different phases.

	White magma		Gray magma		References
Parameters	*EU1*	*EU2*	$EU3_{base\text{-}max}$ [i]	$EU3_{top}$	
ρ_{MAGMA} [a]	2520 kg m^{-3}	2550 kg m^{-3}	2625 kg m^{-3}	2625 kg m^{-3}	This study
T [b]	840˚C	900-925˚C	1050˚C	1050˚C	Cioni et al. (1995, 1998, Shea et al. (2009)
$X_{crystals}$ [c]	23.3%	20%	28.3%	37%	Shea et al. (2009), This study
At P=100 MPa [d]					
μ_{m+c}	3.4×10^3 Pa s	1.5×10^3	2.4×10^2	8.6×10^2	Shaw (1972)
μ_{m+c+b} [1]	3.0×10^3	1.0×10^3	4.0×10^2	8.0×10^2	Lejeune and Richet (1995)
μ_{m+c+b} [2]	4.0×10^3	2.0×10^3	4.2×10^2	9.0×10^2	Mangan et al. (1998)
At P=15 MPa					
μ_{m+c}	1.3×10^5	3.2×10^4	4.2×10^3	7.9×10^3	
μ_{m+c+b} [1]	3.0×10^4	8.0×10^3	1.0×10^3	3.0×10^3	
μ_{m+c+b} [2]	5.0×10^5	1.0×10^5	1.0×10^4	2.0×10^4	
$D_{conduit}$ [e]	35 m	40 m (43)	50 m (51)	65 m	Mastin and Ghiorso (2000), Neri et al. (2002b)
MDR [f]	7×10^6 kg s^{-1}?	2×10^7	1.4×10^8	8×10^7	Carey and Sigurdsson (1987)
V_{exit} [g]	145 m s^{-1}	160 m s^{-1} (185)	141 m s^{-1} (156)	138 m s^{-1}	Mastin and Ghiorso (2000), Neri et al. (2002b)
H_2O [h]	4.5-6 wt%	4.5-6 wt%	2.7-3.5 wt%	2.7-3.5 wt%	Cioni et al. (1995), Cioni (2000), Larsen (2008)
SiO_2	54.91 (0.26)	55.41 (0.38)	54.73 (0.48)	54.88 (0.34)	Cioni et al. (1995)
TiO_2	0.31 (0.14)	0.26 (0.11)	0.54 (0.05	0.56 (0.03	Larsen (2008)
Al_2O_3	22.30 (0.23)	21.97 (0.45)	19.36 (024)	18.57 (0.46)	Shea et al. (2009)
FeO*	2.16 (0.13)	2.90 (0.38)	4.60 (0.33)	4.81 (0.26)	
MnO	0.24 (0.08)	0.24 (0.12)	0.14 (0.01)	0.13 (0.01)	
MgO	0.23 (0.03)	0.65 (0.07)	1.60 (0.31)	2.31 (0.41)	
CaO	3.11 (0.22)	3.69 (0.25)	5.35 (0.30)	5.87 (0.63)	
Na_2O	6.22 (0.19)	5.32 (0.21)	4.49 (0.29)	4.26 (0.42)	
K_2O	9.89 (0.42)	9.17 (0.39)	9.04 (0.14)	8.37 (0.64)	
P_2O_5	0.09 (0.04)	0.12 (0.05)	0.18 (0.03)	0.23 (0.03)	

a. Vesicle-free magma density obtained by He-pycnometry on powdered samples (cf. Table 2).
b. Magma temperature
c. Total crystal content (microphenocrysts+phenocrysts)
d. Magma viscosity (μ_{m+c} is viscosity of melt+crystals, μ_{m+c+b} [1] is viscosity of melt+crystals+bubbles assuming bubbles have Ca<1, μ_{m+c+b} [2] is viscosity of melt+crystals+bubbles assuming bubbles have Ca>>1). Calculations were performed for pressures of 100 MPa at lower conduit conditions and at 15 MPa, near fragmentation level.
e. Conduit diameter, f. mass discharge rate, and g. exit velocity. Values of conduit diameter and exit velocity were computed using Conflow (Mastin, 2005). For comparison, values calculated by Neri et al. (2002b) for the 79AD eruption are shown in parentheses.
h. Dissolved water contents, and major oxide analyses normalized to 100 wt% (dry).
i. Deposits EU3base and EU3 max are lumped together here since their chemistry or crystal content is about the same.

The models utilized to calculate MDR, however, assume a sustained plinian column and any mass/energy loss from the production of PDCs cannot be accounted for. Hence, Carey and Sigurdsson's estimates of MDR should be accurate until PC1 but progressively worsen (i.e. underestimate) as more PDCs were generated. In fact maximum decompression rates trends follows closely MDR values up to PC1 and then deviate, continuing to rise while MDR decreases (Fig. 15a). Hence, we propose that MDR did not necessarily decrease after PC1 during the eruption but, rather, that values may have continued to slightly increase, paralleling decompression rate behavior.

Overall, for the four parameters considered here (density, mass discharge rate, conduit diameter, decompression rate), several combinations of collapse mechanisms can be considered for the different transitions (Fig. 15).

- *Mechanism A, density: transitions from fall deposit phases to partial collapses PC1, PC3, PC4*: Compared to the fall samples that precede them (EU2, EU3base, EU3top respectively), these PDCs all contain higher fractions of dense clasts (Fig. 15b), and were therefore derived from magmas that possessed wider "dense" zones of less vesicular magma within the conduit (Fig. 14). Vesicle number densities and inferred decompression rates for fall and partial collapse PDC samples stay rather constant except for the shift from white pumice (EU2) to gray pumice PC1 (cf. Fig. 10). An increase in the proportion of mean and high density clasts could thus have altered the dynamics of the rising plume, and caused the passage from a stable to transitional (i.e. partially collapsing) column. We cannot completely discard the idea that the decrease in dissolved water content during the shift from white to gray magma (PC1) may have played a role in the generation of a transitional column by decreasing exit velocity.

Even so, both gray and white eruptive phases experienced extended periods of stable, convective plumes with likely constant volatile contents; thus the odds that the mingling of the gray and the white magmas resulted in dissolved H_2O contents and favored column collapse are low.

- *Mechanism B, density and discharge rate combined: transition from EU3max to PC2*: MDR increases abruptly from EU2 to EU3 (from ~10^7 to 10^8 kg s^{-1}) and then much more gradually from EU3base to EU3top.

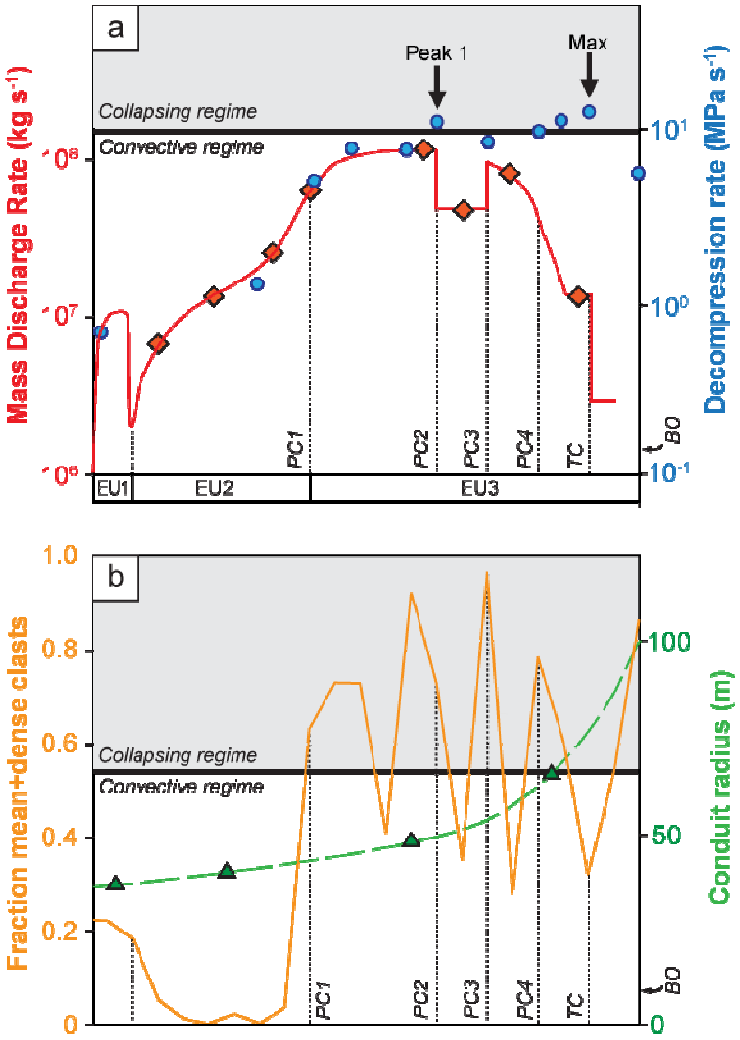

Figure 15: Column collapse mechanisms during the magmatic phase of the 79AD eruption. (a) Variations in mass discharge rate (from Carey and Sigurdsson 1987) and maximum decompression rates calculated from high density clasts (EU1, EU2, PC1) for the white pumice and from low density clasts (EU3base to BO) for the gray pumice. (b) Evolution of the fraction of mean and dense clasts (cf. Figure 4) and changes in conduit diameter inferred from physical models. The boundaries between collapsing and convective regimes are conjectured.

If, as stated above, MDR mimicked decompression rate behavior and continued to rise, partial collapse PC2 was produced during the first peak in discharge rate ("Peak 1" in Fig. 15a). In contrast, decompression rates for EU3max were lower than for PC2, suggesting that perhaps MDR was low enough at this point to allow clasts in the column to efficiently mix with atmospheric air and cause buoyancy. When the MDR increased, this was no longer the case and the column partially collapsed. Therefore, in this case, density increases during EU3max and PC2 times may have combined with the abrupt increase in discharge rate during PC2 to partly destabilize the eruptive plume.

- *Mechanism C, discharge rate increase and conduit widening combined: transitions from fall deposit EU3top to total collapse TC*: In contrast to partial collapse phases, pumice clasts sampled within TC do not show evidence of strong variations in density (Fig. 3). An increase in mean density clasts was observed (Fig. 4 and Fig. 15b) but, overall, the proportion of high density pumice is similar to fall samples EU3base, EU3top and subsequent EU4. In contrast, decompression rates increase from PC3 to TC, and reach the maximum value measured (~13 MPa/s, Fig. 15a). If discharge rates followed the same pattern, then the total column collapse could have been partly caused by the second, highest peak in MDR. In addition, it has been shown that the lithic content increased from EU2 to EU4 (Barberi et al., 1989), suggesting that by EU3top times the conduit had been significantly eroded, thereby increasing in diameter. Calculations of conduit diameter variations using the conduit model Conflow (Mastin and Ghiorso 2000), together with the constraints given by decompression rates yield dimensions of 35-65 m from EU1 to EU3top (Table 3, Fig.

15b). Several authors (e.g. Cioni et al. 1992) have also shown that by EU4, the conduit had been further enlarged and the upper portions of the reservoir regions had begun collapsing. Hence, the total collapse of the eruptive column was likely triggered by the combination of peaking MDR and widening of the conduit walls. Minor increases in modal and high density clast fraction compared to other fall deposits may also have aided in generating instabilities in the eruptive column but are probably much less significant than in previous cases.

- *Mechanism D, density increase and conduit widening combined: generation of low energy collapsing fountain and BO*: This PDC was generated at the very end of the total column collapse phase and contains the highest fraction of dense clasts measured with a very broad pumice density distribution (cf. Fig. 3). The high lithic content of this deposit (70%, Cioni et al. 2004) implies that by BO times, the conduit had broadened significantly, though MDR was waning. Decompression rates calculated for this unit are still fairly elevated (4 MPa s^{-1}), but represent the lowest values measured in all PDC samples (Fig. 15a). In sum, the high content of dense juveniles and lithics, coupled with the enlarged conduit probably combined to generate a small, fully collapsing low energy plume which was rapidly channeled and traveled only short distances from the vent (Cioni et al. 2004). The very dense clasts (ρ > 1.2 g cm^{-3}) with sanidine and plagioclase microlites within this unit were probably formed during prolonged residence within the conduit margins. Newly ascending magma may have entrained this part of the magma column depleted in medium and large bubbles. The latter would then have further vesiculated, forming numerous tiny bubbles during accelerating ascent.

6. Conclusions

Peaks in proportions of dense clasts occurred during four out of the six transitions from fall-to PDC-producing columns. Assuming that pumice textures from this eruption were frozen at or near fragmentation, these peaks raise the question of which conduit processes could be responsible for the increase in overall density, and in cases where density peaks were absent, which other processes could result in the destabilization of the eruptive column.

Pumice textures, in particular vesicle size distributions and number densities, illustrate that all EU3 magmas underwent similar phases of degassing and partial outgassing, but that the spatial and temporal extent of these processes may have been different: the formation of numerous localized shear zones during ascent of bubble-rich magmas particularly closer to conduit margins favored outgassing and ultimately production of denser samples at the fragmentation level. Hence, it is the respective proportions and evolution of shear zones (i.e. position and extent within the conduit) during the various fall and PDC-producing phases that could be responsible for the observed density gradients. If such lateral gradients and the abundance of shear zones also evolve progressively from the reservoir to fragmentation, the passage from products richer in lighter clasts to denser layers can be explained by both variations in the depth of the fragmentation level, as well as temporal changes in marginal build-up of denser magma portions. A similar model can be invoked for the white magma; however the different magmatic properties may have resulted in a slightly different localization of denser outgassed zones throughout the conduit.

The study of six different PDC deposits within the magmatic portion of the stratigraphy also revealed that stable to collapsing column transitions occurred in stages that do not show peaks in clast density. Several other mechanisms, such as increases in discharge rates or widening of the conduit, can combine with magma density variations to potentially trigger such transitions; the 79AD eruption illustrates the complex interplay of these factors. Accordingly, our results show that, while increases in clast density were the principal trigger for partial collapses PC1, PC3, and PC4, production of PC2 likely reflected a first peak in discharge rate combined with the presence of dense clasts. The conditions leading to total collapse TC were in turn favored by both the widening of the conduit/vent system and increasing discharge rate. Finally, the last small-scale collapse of the magmatic phase (BO) occurred when discharge rates were low but the extremely high clast densities, combined with the lower decompression rates and the larger conduit together led to the formation of a boiling-over fountain.

Acknowledgments

The authors acknowledge the NSF grant EAR 0537950. Jessica Larsen, Andrew Harris, Margherita Polacci are thanked for their help with sample collection in the field. We are grateful to both Thomas Giachetti and Tim Druitt for their much needed help in setting up He-pycnometer measurements, as well as Cyrille Galven from the Laboratoire des Fluorures at the University of Le Mans for use of their instruments. Clara Margalef is thanked for help with sample preparation. We thank Julia Hammer, Sarah Fagents and John Allen for insightful comments.

Appendix A1: Viscosity variations during the 79AD magmatic phase

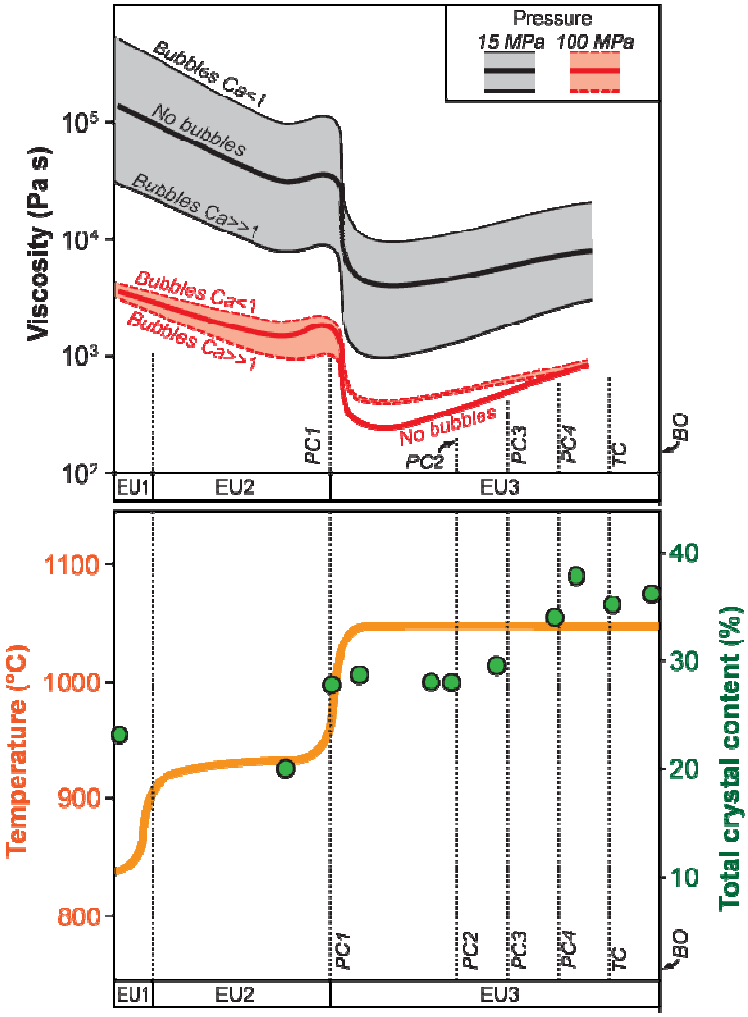

Figure A1: Variations of viscosity (thick black and red lines=melt+crystals, thin surrounding lines represent possible variations when sheared or non-sheared vesicles are included), temperature and crystals content within samples from the eruptive stratigraphy. Temperature exerts the dominant control on viscosity throughout the eruption, however, the increase that follows the white/gray transition is due to leucite crystallization during slow decompression of the magma prior to fast conduit ascent. Viscosity (cf. Table 3 for references) was calculated both at depth (100MPa) and towards fragmentation (15 MPa).

CHAPTER 6. PERSPECTIVES AND FUTURE WORK

Throughout the various investigations presented in this dissertation, several comments were made illustrating some of the current flaws pertaining to the experimental procedures utilized, the assumptions required for texture characterization or the lack of data for the gray magma phase of the 79AD eruption. This last chapter describes some possible improvements to the methods described throughout this dissertation, and further work that could address some important remaining questions.

1. Phase equilibria for the white magma

Chapter 2 focused on leucite crystallization within the white, phonolitic portion of the erupted magma during ascent, storage or slow decompression from the reservoir. This particular magma is extremely important in determining the storage conditions prior to the eruption, which are still a matter of debate. Our preliminary phase stability data suggest that leucites are only stable at pressures < 100-125 MPa, which agrees with estimates from melt inclusion data (Cioni, 2000) and the depth of origin of erupted lithics (Barberi et al., 1989). However, our experiments were all performed at X_{H2O}=1 and other authors (cf. Blundy and Cashman, 2008 and references therein) have shown that the presence of CO_2 can significantly modify the inferred storage depth (i.e. by shifting stability curves towards higher pressures). Because Vesuvius magma reservoirs are encased within carbonate rocks, it is quite possible that magmas inherit some CO_2 through dissolution and assimilation. Cioni (2000) showed that CO_2 was absent soon after decompression was initiated. It remains uncertain whether CO_2 was outgassed or never existed in 79AD phonolites to begin with. Scaillet et al. (2008) carried out phase

stability experiments using EU2 phonolitic starting material at various saturation conditions and determined that, based on the stability of amphibole and leucites, the magma was water-undersaturated and initial storage conditions were close to 200 MPa. However, their water-saturated experiments yield very different results at the pressure range tested within our leucite crystallization range for similar conditions. This is likely to be due to differences in sample preparation and experimental techniques; Scaillet et al. (2008) use powdered samples which they fuse at high temperatures prior to the experiments to homogenize the melt. This may however destroy any crystal nuclei that were initially present and would have served as nucleation sites. Our technique avoids this problem, by using samples that are more lightly crushed and not subject to fusing. In all cases, to truly constrain storage conditions using phase equilibria, chemical analyses are required to determine best-matching oxide proportions in all phases. Hence, with Jessica Larsen (co-PI on the NSF project that funded this PhD), we decided to initiate a better constrained phase equilibria study for EU2. Analyses have already been performed for water-saturated experiments; however, water-undersaturated runs are still needed in the future to complete the X_{oxides}-P-T-X_{H2O} space. Unfortunately, the same cannot be achieved easily for the gray magma (tephriphonolite) because it resulted from the complete mixing of a tephritic magma with the phonolite, thus numerous crystal phases are not in chemical equilibrium with the surrounding melt. Even lightly crushing the samples would eventually result in chemical contamination by mixing crystals and glass.

2. The timing of leucite crystallization

Through our study of leucite crystallization within the EU2 magma, it became obvious that the crystals did not form during ascent in the conduit, like plagioclase in many calc-alkaline melts. Leucites require more time to nucleate and seem to form in clusters or as aggregates of skeletal crystals when decompression is rapid or temperatures low. While we now know that 4-5 days are sufficient in most cases to obtain leucite size distributions and habits matching natural samples, we do not possess good constraints on the exact timing. What is the maximum decompression rate that can be applied for leucites to crystallize with textural features matching those from natural samples? Since the study was published last year, it has come to light through textural investigations of vesicles in experiments that the early stages of ascent were likely to involve slow decompression. Hence, as we suggested initially in Chapter 2, leucites may have formed during these initial stages rather than during storage for longer time periods. Experiments imposing slower initial decompression rates could therefore be performed to investigate whether these crystal phases really need steady environments or whether they are able to grow in the conduit at conditions of moderate undercooling.

3. Improvement of vesiculation experiments

In chapter 4, decompression experiments aiming to mimic magmatic ascent were presented. It was noted that vesicle volume distributions in natural samples were much broader and more complex than those obtained from the experiments, even though number densities were similar. Unlike rhyolites, phonolites and tephriphonolites appear

to nucleate without requiring supersaturation and bubble expansion/growth can continue throughout the entire ascent path. Hence, vesicle volume and size distributions can provide us with a direct link not only to the decompression rates but also to the entire decompression path (i.e. the evolution of ascent rates from reservoir to the fragmentation level). From the study of experimental textures in Chapter 3, fall textures in Chapter 4 and PDC textures in Chapter 5, we recognized that in order to replicate magmatic ascent, laboratory experiments need to be significantly improved; decompression needs to be continuous (i.e. not stepped) and evolving towards accelerating rates (i.e. instead of using one integrated decompression rate). In theory, for magmas that vesiculate "easily" (i.e. no supersaturation necessary), the ascent style could be determined from the number density curves for various vesicle sizes: if each vesicle size class nucleated successively, the largest vesicles would be the first to appear and the smallest the last. Thus, if we can convert the number densities of vesicles for each of those size classes to decompression rates (i.e. using Toramaru's equations, see Chapters 4 and 5), then we can determine the ascent path and the evolution of ascent rates. This type of analysis could therefore be utilized on natural samples prior to deciding what type of ascent is to be imposed during laboratory experiments.

4. Implementation of additional FOAMS modules

Since its creation, FOAMS has been tested/utilized by several students from different universities (Natalie Yakos and Wendy Stovall, University of Hawaii; Ian Schipper and Livia Colo, University of Florence). FOAMS is available freely and our plan is to keep

updating and fixing errors in the next few years. Future versions of FOAMS will include a new module that measures glass wall thickness in the loaded sample images. The code is already written (utilized in chapter 5) and should be implemented by the end of 2010. Briefly, the centroid of selected objects (i.e. vesicles) is determined by averaging the half-distance between numerous intersections through each object, and lines of pixels are measured between the centroids of two adjacent bubbles. The user may choose to only measure the glass portion (in which case the pixels corresponding to any other phase are removed from the connecting pixel line) or the entire distance between vesicle edges. This type of glass wall measurement should be performed on bubble images that have not been decoalesced, in which walls have not been drawn to separate vesicles. Otherwise glass thickness will be biased by the number of pixels used to reconnect glass septa.

The second major improvement needed for FOAMS is building in the capacity to measure vesicles in deformed samples. Non-deformed samples may have slightly elongate vesicles but they typically fail to follow a unique direction (i.e. possess unique shape factor) which makes the use of non-spherical stereological correction parameters inadequate. On the other hand, samples that have been sheared along one direction such as tubular or foliated pumice or lava flow interiors do generally have vesicles that obey a unique set of deformation parameters. The extent of deformation and the correction factors depend on vesicle size (large bubbles deform to a greater extent than small ones). Hence, there is a need for these sets of correction parameters for various values of vesicle elongation and size. The easiest way to obtain such parameters is through numerical modeling. Virtual vesicular rocks need to be created with ellipsoids of different shapes

and sizes. Intersections would then be made and curves of normalized vesicle size versus intersection probability would be obtained. The testing and implementation of the FOAMS "deformed samples" module will be pursued with the collaboration of Thomas Giachetti from the University of Clermont-Ferrand (France) who has also written extensive codes for vesicle analysis in Matlab®.

5. The "conduit model" for Vesuvius

In chapter 5, we presented a new model for the ascent and degassing of magma during the 79AD eruption. According to our results, denser portions of the gray magma experienced lower decompression rates whereas lower density portions underwent much faster ascent. This trend is reversed in the white magma. In our conduit model, the bubble textures in marginal regions had more time to mature and ultimately outgas. In the case of the white magma, ascent was sufficiently slow that even central portions of the magma could eventually collapse, even though they record the highest decompression rates. While our data support these interpretations, further proof could be obtained by measurement of water dissolved in pumice glass. If our model is accurate, dense gray pumice would show slightly lower water contents than lighter clasts due to more extensive degassing. This could be verified by performing H_2O measurements using FTIR or the electron microprobe. In June of 2010, water will be analyzed in samples from the phreatomagmatic phase of the eruption (see section below). We also hope to perform additional analyses within pumice from the magmatic phase.

6. The phreatomagmatic phase of the 79AD eruption

In chapter 5, a detailed investigation of vesicle and leucite textures within products of the magmatic phase of the 79AD eruption (EU1-EU3) was presented, leading to characterization of the various factors that lead to some of the transitions from stable to collapsing eruptive columns. One of the additional tasks within the scope of this project was to perform the same type of study on products of the phreatomagmatic phase (EU4-EU8) to compare with those obtained in the magmatic phase. More specifically, we wish to examine whether the extensive distribution tails in density histograms measured in EU5, EU6, EU7 and even EU8 layers are due to early quenching (i.e. arrested vesiculation) or late maturing of textures (i.e. outgassing). To achieve this, we plan to perform volatile analyses in the groundmass glass of pumice clasts from the various units. We will measure volatile contents (H_2O and possibly CO_2) using the FTIR available at the University of Clermont-Ferrand in France. If early quenching related to magma-water interaction occurred, then high volatile contents should be preserved within the glass. Images collected at the SEM for the various samples (EU4-EU8) will undergo rectification and be processed through FOAMS.

REFERENCES

Adams, N.K., Houghton, B.F., Fagents, S.A., Hildreth, W., 2006. The transition from explosive to effusive eruptive regime: the example of the 1912 Novarupta eruption, Alaska. Geol. Soc. Am. Bull. 118, 620–634. doi 10.1130/B25768.1

Alberico, I., Lirer, L., Petrosino, P., Santacroce, R., 2002. A methodology for the evaluation of volcanic risk in Campi Flegrei. J. Volcanol. Geotherm. Res. 116, 63-78.

Allen, S.R., 2005. Complex spatter- and pumice-rich pyroclastic deposits from and andesitic caldera-forming eruption: the Siwi pyroclastic sequence, Tanna, Vanuatu. Bull. Volcanol. 67, 27-41.

Andronico, D., Cioni, R., 2002. Contrasting styles of Mount Vesuvius activity in the period between the Avellino and Pompeii Plinian eruptions, and some implications for assessment of future hazards. Bull. Volcanol. 64, 372-391.

Arrighi, S., Principe, C., Rosi, M., 2001. Violent strombolian and subplinian eruptions at Vesuvius during post-1631 activity. Bull. Volcanol. 63, 126-150.

Armienti, P., Pareschi, M.T., Innocenti, F., Pompilio, M., 1994. Effects of storage and ascent on the kinetics of crystal growth. Contrib. Mineral. Petrol. 115, 402-415.

Armienti, P., Francalanci, L., Landi, P., 2007. Textural effects of steady-state behavior of the Stromboli feeding system. J. Volcanol. Geotherm. Res. 160, p. 86-98.

Bagdassarov, N., Dorfman, A., Dingwell, D., 2000. Effect of alkalis, phosphorus, and water on the surface tension of haplogranite melt. Am. Mineral. 85, 33–40.

Bai, L., Baker, D.R., Rivers, M., 2008. Experimental study of bubble growth in Stromboli basalt melts at 1 atm. Earth Planet. Sci. Lett. 267, 533-547. doi 10.1016/j.epsl.2007.11.063

Barberi, F., Bizouard, B., Clocchiatti, R., Metrich, N., Santacroce, R., Sbrana, A., 1981. The Somma-Vesuvius chamber: A petrological and volcanological approach. Bull. Volcanol. 44, p. 295–315.

Barberi, F., Leoni, L., 1980. Metamorphic carbonate ejecta from Vesuvius Plinian eruptions: evidence of occurrence of shallow magma chamber. Bull. Volcanol. 43, p. 107–120.

Barberi, F., Cioni, R., Rosi, M., Santacroce, R., Sbrana, A., Vecci, R., 1989. Magmatic and phreatomagmatic phases in explosive eruptions of Vesuvius as deduced by grain-size and compositional analysis of pyroclastic deposits. J. Volcanol. Geotherm. Res. 38, 287–307.

Barberi, F., Macedonio, G., Pareschi, M.T., Santacroce, R., 1990. Mapping the tephra fallout risk: An example from Vesuvius (Italy). Nature 344, 142–144.

Baxter, P.J., Aspinall, W.P., Neri, A., Zuccaro, G., Spence, R.J.S., Cioni, R., Woo, G., 2008. Emergency planning and mitigation at Vesuvius: a new evidence-based approach. J. Volcanol. Geotherm. Res. 178, 454-473.

Bertagnini, A., Landi, P., Rosi, M., Vigliargio, A., 1998. The Pomici di Base Plinian eruption of Somma-Vesuvius. J. Volcanol. Geotherm. Res. 83, 219–239.

Bigelow, J., 1856. On the death of Pliny the Elder. Mem. American Acad. Arts Sci. 6, 223-227.

Blong, R.J., 1984. Volcanic Hazards: A Sourcebook on the Effects of Eruptions. Sydney, Academic Press. 424 pp.

Blower, J.D., Keating, J.P., Mader, H.M., Phillips, J.C., 2001. Inferring volcanic degassing processes from vesicle size distributions. Geophys. Res. Lett. 28, 347–350. doi 10.1029/2000GL012188

Blower, J.D., Keating, J.P., Mader, H.M., Phillips, J.C., 2002. The evolution of bubble size distributions in volcanic eruptions. J. Volcanol. Geotherm. Res. 120, 1–23.

Blundy, J., Cashman, K.V., 2008. Petrologic Reconstruction of Magmatic System Variables and Processes. Rev. Mineral. & Geochem. 69, 179–239.

Burgisser, A., Gardner, J.E., 2005. Experimental constraints on degassing and permeability in volcanic conduit flow. Bull. Volc. 67, 42–56.

Burnard, P., 1999. Eruption dynamics of “popping rock” from vesicle morphologies. J. Volcanol. Geotherm. Res. 92, 247–258.

Cabane, H., Laporte, D., Provost, A., 2005. An experimental study of Ostwald ripening of olivine and plagioclase in silicate melts: implications for the growth and size of crystals in magmas. Contrib. Mineral. Petrol. 150, p. 37–53.

Capasso, L., 2000. Herculaneum victims of the volcanic eruptions of Vesuvius in 79 AD. The Lancet 356, 1344–1346.

Carey, S., Sigurdsson, H., 1987. Temporal variations in column height and magma discharge rate during the 79 A.D. eruption of Vesuvius. Geol. Soc. Am. Bull. 99, 303–314.

Carey, S., Sigurdsson, H., Gardner, J.E., Criswell, W., 1990. Variations in column height and magma discharge during the May 18, 1980 eruption of Mount St. Helens. J. Volcanol. Geotherm. Res. 43, 99–112.

Carey, R.J., Houghton, B.F., Thordarson, T., 2008. Contrasting styles of welding observed in the proximal Askja eruption deposits I: Regional welding. J. Volcanol. Geotherm. Res. 171, 1–19. doi 10.1016/j.jvolgeores.2007.11.020.

Carey, R.J., Houghton, B.F., Thordarson, T., 2009. Abrupt shifts between wet and dry phases of the 1875 eruption of Askja volcano: Microscopic evidence for macroscopic dynamics. J. Volcanol. Geotherm. Res. 184, 256–270.

Carta, S., Figari, R., Sartoris, G., Sassi, E., Scandone, R., 1981. A statistical model for Vesuvius and its volcanological implications. Bull. Volcanol. 44, 129–151.

Cashman, K.V., 1988. Crystallization of Mount St Helens 1980-1986 dacite: A quantitative textural approach. Bull. Volcanol. 50, p. 194–209.

Cashman, K.V., Marsh, B.D., 1988. Crystal size distribution (CSD) in rocks and the kinetics and dynamics of crystallisation II. Makaopuhi lava lake. Contrib. Mineral. Petrol. 99, 292–305.

Cashman, K., 1992. Groundmass crystallization of Mount St Helens dacites, 1980-1986: a tool for interpreting shallow magmatic processes. Cont. Mineral. Petrol. 109, 431–449.

Cashman, K.V., 1993. Relationship between plagioclase crystallization and cooling rate in basaltic melts. Cont. Mineral. Petrol. 113, 126–142.

Cashman, K. V., Mangan, M.T., 1994. Physical aspects of magmatic degassing II: Constraints on vesiculation processes from textural studies of eruptive products, in Volatiles in Magmas. ed. M. Carroll, p. 447–478, Min. Soc. Am..

Cashman, K.V., Mangan, M.T., Newman, S., 1994. Surface degassing and modifications to vesicle size distributions in active basalt flows. J. Volcanol. Geotherm. Res. 62, 45–68.

Cashman, K.V., Blundy, J., 2000. Degassing and Crystallization of Ascending Andesite and Dacite. Phil. Trans.: Math., Phys. Eng. Sci. 358, pp.1487–1513.

Castro, J.M., Mercer, C., 2004. Microlite textures and volatile contents of obsidian from the Inyo volcanic chain, California. Geophys. Res. Lett. 31, L18605.

Cigolini, C., Laiolo, M., Bertolino, S., 2008. Probing Stromboli volcano from the mantle to paroxysmal eruptions. In: Annen, C. & Zellmer, G. F. (eds), Dynamics of Crustal Magma Transfer, Storage and Differentiation. Geol. Soc. Lond. Spec. Pub. 304, 33–70.

Cioni, R., Marianelli, P., Sbrana, A., 1992. Dynamics of the AD 79 eruption: stratigraphic, sedimentological and geochemical data on the successions from the Somma–Vesuvius southern and eastern sectors. Acta Vulcanol. 2, 109–123.

Cioni, R., Civetta, L., Marianelli, P., Metrich, N., Santacroce, R., Sbrana, A., 1995. Compositional layering and syn-eruptive mixing of periodically refilled shallow magma chamber: the A.D. 79 Plinian eruption of Vesuvius. J. Petrol. 36, p. 739–776.

Cioni, R., Marianelli, P., Santacroce, R., 1998. Thermal and compositional evolution of the shallow magma chamber of Vesuvius: Evidence from pyroxene phenocrysts and melt inclusions. J. Geophys. Res., 103(B8), 18277–18294.

Cioni, R., Santacroce, R., Sbrana, A., 1999. Pyroclastic deposits as a guide for reconstructing the multi-stage evolution of the Somma-Vesuvius caldera. Bull. Volcanol. 60, 207–222.

Cioni, R., 2000. Volatile content and degassing processes in the 79AD magma chamber at Vesuvius (Italy). Contrib. Mineral. Petrol. 140, 40–54.

Cioni, R., Gurioli, L., Sbrana, A., Vougioukalakis, G., 2000. Precursors to the Plinian eruptions of thera (late bronze age) and vesuvius (AD 79): Data from archaeological areas. J. Volcanol. Geotherm. Res. 177, 719–724.

Cioni, R., Longo, A., Macedonio, G., Santacroce, R., Sbrana, A., Sulpizio, R., Andronico, D., 2003a. Assessing pyroclastic fall hazard through field data and numerical simulations: Example from Vesuvius. J. Geophys. Res. 108, B2-2063.

Cioni, R., Sulpizio, R., Garruccio, N., 2003b. Variability of the eruption dynamics during a Subplinian event: the Greenish Pumice eruption of Somma-Vesuvius (Italy). J. Volcanol. Geotherm. Res. 124, 89-114.

Cioni, R., Gurioli, L., Lanza, R., Zanella, E., 2004. Temperatures of the A.D. 79 pyroclastic density current deposits (Vesuvius, Italy). J. Geophys. Res. 109, B02207.

Cioni, R., Bertagnini, A., Santacroce, R., Andronico, D., 2008. Explosive activity and eruption scenarios at Somma-Vesuvius (Italy): Towards a new classification scheme. J. Volcanol. Geotherm. Res. 178, 331–346.

Civetta, L., Galati, R., Santacroce ,R., 1991. Magma mixing and convective compositional layering within the Vesuvius magma chamber. Bull. Volcanol. 53, 287–300.

Clarke, A.B., Voight, B., Neri, A., Macedonio, G., 2002. Transient dynamics of vulcanian explosions and column collapse. Nature 415, 897–901.

Cluzel, N., Laporte, D., Provost, A., Kannewischer, I., 2008. Kinetics of heterogeneous bubble nucleation in rhyolitic melts: implications for the number density of bubbles in volcanic conduits and for pumice textures. Contrib. Mineral. Petrol. 156, 745–763.

Costa, A., Blake, S., Self, S., 2006. Segregation processes in vesiculating crystallizating magmas. J. Volcanol. Geotherm. Res. 153, 287-300.

Costa, A., Dell'Erba, F., Di Vivo, M.A., Isaia, R., Macedonio, G., Orsi, G., Pfeiffer, T., 2009. Tephra fallout hazard assessment at the Campi Flegrei caldera (Italy). Bull. Volcanol. 71, 259–273.

Couch, S., Sparks, R.S.J., Carroll, M.R., 2003, The Kinetics of Degassing-Induced Crystallization at Soufriere Hills, Montserrat. J. Petrol. 44, 1477–1502.

Crisp, J., Cashman, K.V., Bonini, J.A., Hougen, S.B., Pieri, D.C., 1994. Crystallization history of the 1984 Mauna Loa lava flow. J. Geophys. Res. 99, B4 7177–7198.

Daniele, P., Lirer, L., Petrosino, P., Spinelli, N., Peterson, R., 2009. Applications of the PUFF model to forecasts of volcanic clouds dispersal from Etna and Vesuvio. Comput. Geosci. 35, 1035–1049.

Degruyter, W., Bachmann, O., Burgisser, A., 2010. Controls on magma permeability in the volcanic conduit during the climactic phase of the Kos Plateau Tuff eruption (Aegean Arc). Bull. Volcanol. 72, 63–74.

De Vivo, B., Rolandi, G., Gans, P.B., Calvert, A., Bohrson, W.A., Spera, F.J., Belkin, H.E., 2001. New constraints on the pyroclastic eruptive history of the Campanian volcanic Plain (Italy), Mineral. Petrol. 73, 47–65.

Di Girolamo, P., 1968. Petrografia del Somma-Vesuviu: le serie piroclastiche. Accad. Sci. Fis. e Mat. Rend. 4 (35).

Di Muro, A., Neri, A., Rosi, M., 2004. Contemporaneous convective and collapsing eruptive dynamics: the transitional regime of explosive eruptions. Geophys. Res. Lett. 31, 1–4.

Dobran, F., Neri, A., Todesco, M., 1994. Assessing the pyroclastic flow hazard at Vesuvius. Nature 367, 551–554.

Doell, R.R., Dalrymple, G.B., 1973. Potassium-Argon Ages and Paleomagnetism of the Waianae and Koolau Volcanic Series, Oahu, Hawaii. Geol. Soc. Am. Bull. 84, 1217–1241.

Eberl, D.D., Drits, V.A., Srodon, J., 1998. Deducing the growth mechanisms for minerls from the shapes of crystal size distributions. Am. J. Sci. 298, 499–533.

Esposti Ongaro, T., Neri, A., Todesco, M., Macedonio, G., 2002. Pyroclastic flow hazard assessment at Vesuvius (Italy) by using numerical modeling. II. Analysis of flow variables. Bull. Volcanol. 64, 178–191.

Esposti Ongaro, T., Neri, A., Menconi, G., De'Michieli Vitturi M., Marianelli, P., Cavazzoni, C., Erbacci, G., Baxter, P.J., 2008. Transient 3D numerical

simulations of column collapse and pyroclastic density current scenarios at Vesuvius. J. Volcanol. Geotherm. Res. 178, 378–396.

Formenti, Y., Druitt, T.H., 2003. Vesicle connectivity in pyroclasts and implications for the fluidization of fountain-collapse pyroclastic flows, Montserrat (West Indies). Earth Planet. Sci. Lett. 214, 561–574.

Gaonac'h, H., Lovejoy, S., Stix, J., Scherzter, D., 1996a. A scaling growth model for bubbles in basaltic lava flows. Earth Planet. Sci. Lett. 139, 395–409.

Gaonac'h, H., Stix, J., Lovejoy, S., 1996b. Scaling effects on vesicle shape, size and heterogeneity of lavas fromMount Etna. J. Volcanol. Geotherm. Res. 74, 131–153.

Gaonac'h, H., Lovejoy, S., Schertzer, D., 2005. Scaling vesicle distributions and volcanic eruptions. Bull. Volcanol. 67, 350–357.

Gardner, C.A., Cashman, K.V., Neal, C.A., 1998. Tephra-fall deposits from the 1992 eruption of Crater Peak, Alaska: implications of clast textures for eruptive processes. Bull. Volcanol. 59, 537–555.

Gardner, J.E., Rutherford, M.J., Carey, S., Sigurdsson, H., 1995. Experimental constreaints on pre-eruptive water contents and changing magma storage prior to explosive eruptions of Mount St Helens volcano. Bull. Volcanol. 57, 1–17.

Gardner, J.E., Hilton, M., Carroll, M.R., 1999. Experimental constraints on degassing of magma: isothermal bubble growth during continuous decompression from high pressure. Earth Planet. Sci. Lett. 168, 201–218.

Gardner, J.E., Hilton, M., Carroll, M.R., 2000. Bubble growth in highly viscous silicate melts during continuous decompression from high pressure. Geochim. Cosmochim. Acta. 64, 1473–1483.

Gardner, J.E., Denis, M.-H., 2004. Heterogeneous bubble nucleation on Fe–Ti oxide crystals in high-silica rhyolitic melts. Geochim. Cosmochim. Acta 68, 3587–3597.

Gardner, J.E., 2007. Heterogeneous bubble nucleation in highly viscous silicate melts during instantaneous decompression from high pressure. Chem. Geol. 236, 1–12. doi:10.1016/j.chemgeo.2006.08.006

Geshwind, C., Rutherford, M.J., 1995. Crystallization of microlites during magma ascent: the fluid mechanics of recent eruptions at Mount St. Helens. Bull. Volcanol. 57, 356–370.

Giachetti, T., Druitt, T.H., Burgisser, A., Arbaret, L., Galven, C., (in press) Bubble nucleation, growth and coalescence during the 1997 Vulcanian explosions of Soufriere Hills Volcano, Montserrat. J. Volcanol. Geotherm. Res.

Gonnermann, H.M., Manga, M., 2007. The fluids mechanics of volcanic eruptions. Ann. Rev. Fluid Mech. 39, 321–356.

Gorshkov, G.S., 1959. Gigantic eruption of the Volcano Bezymianny. Geol. Soc. Spec. Publ. 21, 77–109.

Gualda, G.A.R., Rivers, M., 2006. Quantitative 3D petrography using x-ray tomography: Application to Bishop Tuff pumice clasts. J. Volcanol, Geotherm. Res. 154, 48–62.

Gurioli, L., Cioni, R., Sbrana, A., Zanella, E., 2002. Transport and deposition of pyroclastic density currents over an inhabited area: the deposits of the 79AD eruption of Vesuvius at Herculaneum, Italy. Sedimentol. 49, 929–953.

Gurioli, L., Pareschi, M.T., Zanella, E., Lanza, R., Deluca, E., Bisson, M., 2005a. Interaction of pyroclastic density currents with human settlements: Evidence from Pompeii. Geology 33, 441–444.

Gurioli, L., Houghton, B.F., Cashman, K.V., Cioni, R., 2005b. Complex changes in eruption dynamics during the 79 AD eruption of Vesuvius. Bull. Volcanol. 67, 144–159.

Gurioli, L., Harris, A.J.L, Houghton, B.F., Polacci, M., Ripepe, M., 2008. Textural and geophysical characterization of explosive basaltic activity at Villarrica volcano, J. Geophys. Res., 113:B08206. doi:10.1029/2007JB005328

Hale, A.J., Mühlhaus, H-B., 2007. Modelling shear bands in a volcanic conduit: Implications for over-pressures and extrusion rates. Earth Planet. Sci. Lett. 263, 74–87.

Hamilton, W., 1768. An account of the Eruption of Mount Vesuvius, in 1767: In a letter to the earl of Morton, president of the royal society, from the honourable William Hamilton, his majesty's envoy extraordinary at Naples. Phil. Trans. 58, 1–14.

Hamilton, W., 1780. An account of an eruption of Mount Vesuvius, which happened in August, 1779. Phil. Trans. Roy. Soc. Lond. 70, 42-84.

Hammer, J.E., Cashman, K.V., Hoblitt, R.P., Newman, S., 1999. Degassing and microlite crystallization during pre-climactic events of the 1991 eruption of Mt. Pinatubo, Philippines. Bull. Volcanol. 60, 355–380.

Hammer, J.E., Cashman, K.V., Voight, B., 2000. Magmatic processes revealed by textural and compositional trends in Merapi dome lavas. J. Volcanol. Geotherm. Res. 100, 165–192.

Hammer, J.E., Rutherford, M.J., 2002. An experimental study of the kinetics of decompression-induced crystallization in silicic melt. J. Geophys. Res. 107(B1), 1–24.

Hammer, J.E., 2004. Experimental nucleation data applied to classical theory. Am. Mineral. 89, p. 1673–1679.

Harms, E., Gardner, J.E., Schmincke, H.-U., 2004. Phase equilibria of the Lower Laacher See tephra (East Eifel, Germany): constraints on pre-eruptive storage conditions of a phonolitic magma reservoir. J. Volcanol. Geotherm. Res. 134, 135–148.

Heiken, G., 1978. Plinian eruptions in the Medicine Lake Highland, California, and the nature of underlying magma. J. Volcanol. Geotherm. Res. 4, 375–402.

Heim, A., 1873. Der Vesuv im April 1872. Zeitschrift der Deutschen Geologischen Gesellschaft 25: 1-52.

Hess, K.-U., Dingwell, D.B., 1996. Viscosities of hydrous leucogranitic melts: A non-Arrhenian model. Am. Mineral., 81, p. 1297–1300.

Higgins, M.D., 1994. Numerical modeling of crystal-shapes in thin sections: Estimation of crystal habit and true size. Am. Mineral. 79, 113–119.

Higgins, M.D., 2000. Measurement of crystal size distributions. Am. Mineral. 85, 1105–1116.

Hobbs, W.H., 1906. The grand eruption of Vesuvius in 1906. J. Geol. 14, 636–655.

Hon, K., Kauahikaua, J., Denlinger, R., Mackay, K., 1994. Emplacement and inflation of pāhoehoe sheet flows; observations and measurements of active lava flows on Kilauea Volcano, Hawaii. Geol. Soc. Am. Bull. 106, 351–370.

Houghton, B. F., Wilson, C.J.N., 1989. A vesicularity index for pyroclastic deposits, Bull. Volcanol. 51, 451– 462.

Hurwitz, S., Navon, O., 1994. Bubble nucleation in rhyolitic melts: Experiments at high pressure, temperature, and water content. Earth Planet. Sci. Lett. 122, 267–280.

Iacono Marziano, G., Schmidt, B.C., Dolfi, D., 2007. Equilibrium and disequilibrium degassing of a phonolitic melt (Vesuvius AD 79 “white pumice”) simulated by decompression experiments. J. Volcanol. Geotherm. Res. 161, p. 151–164.

Ippolito, F., 1950. Sul meccanismo del seppellimento di Pompei e di Ercolano. Pompeiana 1950, 387–395.

Jaupart, C., 1996. Physical models of volcanic eruptions. Chem. Geol 128, 217–227. doi:10.1016/0009-2541(95)00175-1.

Johnston-Lavis, H.J., 1884. The Geology of Monte Somma and Vesuvius, being a Study in Volcanology, Quart. J. Geol. Soc. 40, 35-119.

Kaminski, E., Jaupart, C., 1997. Expansion and quenching of vesicular magma fragments in Plinian eruptions. J. Geophys. Res. 102, B6 12,187-12,203.

Ketcham, R. A., 2005. Computational methods for quantitative analysis of three-dimensional features in geological specimens. Geosphere 1, 32–41.

Ketcham, R. A., Carlson, W.D., 2001. Acquisition, optimization and interpretation of X-ray computed tomographic imagery: Applications to the geosciences. Comput. Geosci. 27, 381–400.

Kirkpatrick, T.J., 1981. Kinetics of Crystallization of Igneous Rocks. Rev. Mineral. 8, 321–398.

Klug, C., Cashman, K.V., 1994. Vesiculation of May 18, 1980, Mount St. Helens magma, Geology, 22, 468– 472.

Klug, C., Cashman, K.V., 1996. Permeability development in vesiculating magmas: implications for fragmentation. Bull. Volcanol. 58, 87-100.

Klug, C., Cashman, K.V., Bacon, C., 2002. Structure and physical characteristics of pumice from the climactic eruption of Mount Mazama (Crater Lake), Oregon. Bull. Volcanol. 64, 486– 501.

Larsen, J.F., Gardner, J.E., 2000. Experimental constraints on bubble interactions in rhyolite melts: implications for vesicle size distributions. Earth Planet. Sci. Lett., 180, 201– 214.

Larsen, J.F., Denis, M.-H., Gardner, J.E., 2004. Experimental study of bubble coalescence in rhyolitic and phonolitic melts. Geochim. Cosmochim. Acta. 68, 333–344.

Larsen, J.F., Gardner, J.E., 2004. Experimental study of water degassing from phonolite melts: implications for volatile oversaturation during magmatic ascent. J. Volcanol. Geotherm. Res. 134, 109–124.

Larsen, J.F., 2005. Experimental study of plagioclase rim growth around anorthite seed crystals in rhyodacite. Am. Mineral. 90, 417–427.

Larsen, J.F., 2008. Heterogeneous bubble nucleation and disequilibrium H2O exsolution in Vesuvius K-phonolite melts. J. Volcanol. Geotherm. Res. 275, 278–288.

Lautze, N. C., Houghton, B. F., 2007. Linking variable explosion style and magma textures during 2002 at Stromboli volcano, Italy. Bull. Volcanol. 69, 445– 460.

Lensky, N.G., Navon, O., Lyakhovsky, V., 2004. Bubble growth during decompression of magma: experimental and theoretical investigation. J. Volcanol. Geotherm. Res., 129, 7–22.

Le Pennec, J-L., Hermitte, D., Dana, I., Pezard, P., Coulon, C., Cocheme, J-J., Mulyadi, E., Ollagnier, F., Revest, C., 2001. Electrical conductivity and pore-space topology of Merapi lavas: implications for the degassing of porphyritic andesite magmas. Geophys. Res. Lett. 28, 4283–4286.

L'Heureux, I., 2007. A new model of volatile bubble growth in magmatic system: Isobaric case. J. Geophys. Res. 112, B12,208.

Lirer, L., Pescatore, T., 1968. Studio sedimentologico delle piroclastici del Somma-Vesuvio. Accad. Sci. Fis. e Mat. Rend. 3a (7).

Lirer, L., Pescatore, T., Booth, B., Walker, G.P.L., 1973. Two Plinian Pumice-Fall Deposits from Somma-Vesuvius, Italy. Geol. Soc. Am. Bull., 84, p. 759–772.

Lirer, L., Munno, R., Petrosino, P., Vinci, A., 1993. Tephrostratigraphy of the AD 79 pyroclastic deposits in perivolcanic areas of Mt. Vesuvio (Italy). J. Volcanol. Geotherm. Res. 58, 133–139.

Lirer, L., Petrosino, P., Alberico, I., 2010. Hazard and risk assessment in a complex multi-source volcanic area: the example of the Campania Region, Italy. Bull. Volcanol. Published online, doi: 10.1007/s00445-009-0334-2.

Llewellin, E.W., Mader, H.M., Wilson, S.D.R., 2002. The rheology of a bubbly liquid: R. Soc. Lond. Proc. A 458, 987–1016.

Lofgren, G.E., 1974. An experimental study of plagioclase crystal morphology: isothermal crystallization. Am. J. Sci. 274, 243–273.

Lovejoy, S., H. Gaonac'h, and D. Schertzer, 2004. Bubble distributions and dynamics: The expansion-coalescence equation. J. Geophys. Res. 109, B11203, doi:10.1029/2003JB002823.

Luongo, G., Perrotta, A., Scarpati, C., De Carolis, E., Patricelli, G., Ciarallo, A., 2003. Impact of the AD 79 explosive eruption on Pompeii, II. Causes of death of the inhabitants inferred by stratigraphic analysis and areal distribution of the human casualties. J. Volcanol. Geotherm. Res. 126, 169–200.

Lyakhovsky, V., Hurwitz, S., Navon, O., 1996. Bubble growth in rhyolitic melts: experimental and numerical investigation. Bull Volcanol. 58, 19–32.

Macedonio, G., Pareschi, M. T., Santacroce, R., 1988. A numerical simulation of the Plinian fall phase of 79 A.D. eruption of Vesuvius. J. Geophys. Res. 93, 14,817–14,827.

Macedonio, G., Pareschi, M.T., Santacroce, R., 1990. Renewal of volcanic activity at Vesuvius: Tephra fallout. J. Volcanol. Geotherm. Res. 40, 327–342.

Maiuri, A., 1977. Herculaneum. Instituto Poligrafico dello Stato (Roma).

Mangan, M., 1990. Crystal size distribution systematic and the determination of magma storage times: The 1959 eruption of Kilauea volcano, Hawaii. J. Volcanol. Geotherm. Res. 44, 295–302.

Mangan, M. T., Cashman, K.V., 1996. The structure of basaltic scoria and reticulite and inferences for vesiculation, foam formation, and fragmentation in lava fountains. J. Volcanol. Geotherm. Res. 73, 1–18.

Manga, M., Castro, J., Cashman, K.V., 1998. Rheology of bubble bearing magmas. J. Volcanol. Geotherm. Res. 87, 15–28.

Mangan, M.T., Sisson, T.W., 2000. Delayed, disequilibrium degassing in rhyolite magma: Decompression experiments and implications for explosive volcanism. Earth Planet. Sci. Lett. 183, 441–455.

Mangan, M.T., Sisson, T.W., Hankins, W.B., 2004. Decompression experiments identify kinetic controls on explosive silicic eruptions. Geophys. Res. Lett., 31, L08605.

Mangan, M.T., Sisson, T.W., 2005. Evolution of melt-vapor surface tension in silicic volcanic systems: experiments with hydrous melts. J. Geophys. Res. 110, B01202

Marianelli, P., Metrich, N., Santacroce, R., Sbrana, A., 1995. Mafic batches at Vesuvius: a glass inclusion approach to the modalities of feeding stratovolcanoes. Contrib. Minerl. Petrol. 120, 159–169.

Marsh, B.D., 1988. Crystal size distribution (CSD) in rocks and the kinetics and dynamics of crystallization: I. Theory. Contrib. Mineral. Petrol. 99, 277–291.

Marsh, B.D., 1998. On the interpretation of Crystal Size Distributions in magmatic systems. J. Petrol. 39, 553–600.

Martel, C., Schmidt, B.C., 2003. Decompression experiments as an insight into ascent rates of silicic magmas. Contrib. Mineral. Petrol. 144, 397–415.

Marti, J., Soriano, C., Dingwell, D.B., 1999. Tube pumices as strain markers of the ductile-brittle transition during magma fragmentation. Nature 402, 650–653.

Massol, H., Koyaguchi, T., 2005. The effect of magma flow on nucleation of gas bubbles in a volcanic conduit. J. Volcanol. Geotherm. Res. 143, 69–88.

Mastin, L.G., Ghiorso, M.S., 2000. A Numerical Program for Steady-State Flow of Magma-Gas Mixtures Through Vertical Eruptive Conduits. USGS Open-File Report, 00-209.

Mastin, L.G., 2002. Insights into volcanic conduit flow from an open-source numerical model, Geochem., Geophys., Geosyst. 3, 7.

Mastin, L.G., 2005. The controlling effect of viscous dissipation on magma flow in silicic conduits. J. Volcanol. Geotherm. Res. 143, 17–28.

Mastrolorenzo, G., Pappalardo, L., 2006. Magma degassing and crystallization processes during eruptions of high-risk Neapolitan-volcanoes: Evidence of common equilibrium rising processes in alkaline magmas. Earth Planet. Sci. Lett. 250, 164–181.

Mele, D., Sulpizio, R., Dellino, P., La Volpe, L., 2009. Stratigraphy and eruptive dynamics of a long-lasting Plinian eruption of Somma-Vesuvius: the Pomici di Mercato (8900 years B.P.). Bull. Volcanol., submitted.

Mock, A., Jerram, D.A., 2005. Crystal size distributions (CSD) in three dimensions: insights from the 3D reconstruction of a highly porphyritic rhyolite. J. Petrol. 46, 1525–1541.

Mongrain, J., Larsen, J.F., King, P.L., 2008. Rapid water exsolution, degassing, and bubble collapse observed experimentally in K-phonolite melts. J. Volc. Geotherm. Res., 173, 178–184.

Moore, G., Vennemann, T., Carmichael, I.S.E., 1995. Solubility of water in magmas to 2 kbar. Geology, 23, 1099–1102.

Morgan, D.J, Jerram, D.A., 2006. On estimating crystal shape for crystal size distribution analysis. J. Volcanol. Geotherm. Res., 154, 1–7.

Morgan, D.J., Blake, S., Rogers, N.W., De Vivo, B., Rolandi, G., Davidson, J.P., 2006. Geology 34, 845–848.

Mourtada-Bonnefoi, C.C., Laporte, D., 1999. Experimental study of homogeneous bubble nucleation in rhyolitic magmas. Geophys. Res. Lett. 26, 3505–3508.

Mourtada-Bonnefoi, C.C., Laporte, D., 2002. Homogeneous bubble nucleation in rhyoliticmagmas: an experimental study of the effect of H2OandCO2. J.Geophys. Res. 107, B4. doi:10.1029/2001JB00290.

Mourtada-Bonnefoi, C.C., Laporte, D., 2004. Kinetics of bubble nucleation in a rhyolitic melt: an experimental study of the effect of ascent rate. Earth Planet. Sci. Lett. 218, 521–537.

Mues-Schumacher, U., 1994. Chemical variations of the 79AD pumice deposits of Vesuvius. Eur. J. Mineral. 6, 387–395.

Muncill, G.E., Lasaga, A.C., 1988. Crystal-growth kinetics of plagioclase in igneous systems: isothermal H2O-saturated experiments and extension of a growth model to complex silicate melts. Am. Mineral. 73, 982–992.

Nakada, S., Shimizu, H., Ohta, K., 1999. Overview of 1990–1995 eruptions at Unzen Volcano. J Volcanol Geotherm Res 89, 1–22.

Namiki, A., Manga, M., 2006. Influence of decompression rate on the expansion velocity and expansion style of bubbly fluids. J. Geophys. Res., 111, B11208, doi:10.1029/2005JB004132.

Navon, O., Lyakhovsky, V., 1998. Vesiculation processes in silicic magmas. In: Gilbert, J.S., Sparks, R.S.J. (Eds.), The Physics of Explosive Volcanic Eruptions. Geol. Soc. Lond. Spec. Pub. 145, pp. 27–50.

Neri, A., Dobran, F., 1994. Influence of eruption parameters on the thermofluid-dynamics of collapsing volcanic columns. J. Geophys. Res. 99, 11833–11857.

Neri, A., Macedonio, G., 1996. Numerical simulations of collapsing volcanic columns with particles of two sizes. J. Geophys. Res. 101, 8153–8174.

Neri, A., Papale, P., Macedonio, G., 1998. The role of magma composition and water content in explosive eruptions: II. Pyroclastic dispersion dynamics, J. Volcanol. Geotherm. Res. 87, 95–115.

Neri, A., Di Muro, A., Rosi, M., 2002a. Mass partition during collapsing and transitional columns by using numerical simulations. J. Volcanol. Geotherm. Res. 115, 1–18.

Neri, A., Papale, P., Del Seppia, D., Santacroce, R., 2002b. Coupled conduit and atmospheric dispersal dynamics of the AD 79 Plinian eruption of Vesuvius. J. Volcanol. Geotherm. Res., 120, 141–160.

Neri, A., Esposti Ongaro, T., Monconi, G., De' Michieli Pitturi, M., Cavazioni, C., Erbacci, G., Baxter, P.J., 2007. 4D Simulation of esplosive eruption dynamics at Vesuvius. Geophys. Res. Lett. 34, doi: 10.1029/2006GL028597.

Nicholis, M.G., Rutherford, M.J., 2004. Experimental constraints on magma ascent rate for the Crater Flat volcanic zone hawaiite. Geology 32, 489–492.

Noguchi, S., Toramaru, A., Shimano, T., 2006. Crystallization of microlites and degassing during ascent: Constraints on the mechanical behavior of magma during the Tenjo Eruption on Kozu Island, Japan. Bull. Volcanol. 68, 432–449.

Nunziante, L., Fraldi, M., Lirer, L., Petrosino, P., Scotellaro, S., Cicirelli, C., 2003. Analysis of AD 79 eruption pyroclastic currents impact and present risk assessment for buildings at Vesuvio. Bull. Volcanol. 65, 154–176.

Okumura, S., Nakamura, M., Tsuchiyama, A., 2006. Shear-induced bubble coalescence in rhyolitic melts with low vesicularity. Geophys. Res. Lett. 33, L20316, doi:10.1029/2006GL027347.

Okumura, S., Nakamura, M., Tsuchiyama, A., Nakano, T., Uesugi, K., 2008. Evolution of bubble microstructure in sheared rhyolite: formation of a channel-like bubble network. J. Geophys. Res. 113, B07208.

Orsi, G., Gallo, G., Heiken, G., Wohletz, K., Yu, E., Bonani, G., 1992. A comprehensive study of pumice formation and dispersal: The Cretaio tephra of Ischia (Italy). J. Volcanol. Geotherm. Res. 53, 329–354. doi: 10.1016/03770273(92)90090-Z.

Orsi, G., Di Vito, M.A., Isaia, R., 2004. Volcanic hazard assessment at the restless Campi Flegrei caldera. Bull. Volcanol. 66, 514–530.

Papale, P., Dobran, F., 1993. Modeling of the ascent of magma during the plinian eruption of Vesuvius in A.D. 79. J. Volcanol. Geotherm. Res. 58, p. 101–132.

Papale, P., Neri, A., Macedonio, G., 1998. The role of magma composition and water content in explosive eruptions. 1. Conduit dynamics. J. Volcanol. Geotherm. Res. 87, 75–93.

Park, Y., Hanson, B., 1999. Experimental investigation of Ostwald-ripening of forsterite in the haplobasaltic system. J. Volcanol. Geotherm. Res. 90, p.103–113.

Piochi, M., Mastrolorenzo, G., Pappalardo, L., 2005. Magma ascent and eruptive processes from textural and compositional features of Monte Nuovo pyroclastic products, Campi Flegrei, Italy. Bull.Volcanol. 67, 663–678.

Pioli, L., Pistolesi, M., Rosi, M., 2007. Pumice textures as an indicator of magma mingling and fragmentation processes at Stromboli volcano (Italy). Eos Trans. AGU, 88(52), Fall meet. Suppl., Abstract V22A-02.

Polacci, M., Papale, P., 1997. The evolution of lava flows from ephemeral vents at Mount Etna: insights from vesicle distribution and morphological studies. J. Volcanol. Geotherm. Res. 76, 1–17.

Polacci, M., Papale, P., Rosi, M., 2001. Textural heterogeneities in pumices from the climactic eruption of Mount Pinatubo, 15 June 1991, and implication for magma ascent dynamics. Bull. Volcanol. 63, 83–97.

Polacci, M., Pioli, L., Rosi, M., 2003. The Plinian phase of the Campanian Ignimbrite eruption (Phlegrean Fields, Italy): Evidence from density measurements and textural characterization of pumice. Bull. Volcanol. 65, 418–432. doi: 10.1007/s00445-002-0268-4.

Polacci, M., Baker, D.R., Mancini, L., Tromba, G., Zanini, F., 2006. Three-dimensional investigation of volcanic textures by X-ray microtomography and implications for conduit processes. Geophys. Res. Lett., 33, L13312.

Polacci, M., Baker, D. R., Bai, L., Mancini, L., 2008. Large vesicles record pathways of degassing at basaltic volcanoes. Bull. Volcanol., 70, 1023-1029. doi:10.1007/s00445-007-0184-8.

Polacci, M., Baker, D.R., Mancini, L., Favretto, S., Hill, R.J., 2009. Vesiculation in magmas from Stromboli and implications for normal Strombolian activity and paroxysmal explosions in basaltic systems. J. Geophys. Res. 114, B01206. DOI 10.1029/2008JB005672

Principe, C., Tanguy, T-C., Arrighi, S., Paiotti, A., Le Goff, M., Zoppi, U., 2004. Chronology of Vesuvius' activity from A.D. 79 to 1631 based on archaeomagnetism of lavas and historical sources. Bull. Volcanol. 66, 703–724.

Proussevitch, A. A., Sahagian, D.L., 1996. Dynamics of coupled diffusive and decompressive bubble growth in magmatic systems. J. Geophys. Res. 101, 17447–17455.

Proussevitch, A., Ketcham, R.A., Carlson, W.D., Sahagian, D., 1998. Preliminary results of X-ray CT analysis of Hawaiian vesicular basalts. Eos, 79 (17), 360.

Proussevitch, A.A., Sahagian, D.L., Tsentalovich, E.P., 2007a. Statistical analysis of bubble and crystal size distributions: Formulations and procedures. J. Volcanol. Geotherm. Res. 164, 95–111. doi:10.1016/j.jvolgeores.2007.04.007.

Proussevitch, A.A., Sahagian, D.L., Carlson, W.D., 2007b. Statistical analysis of bubble and crystal size distributions: Application to Colorado Plateau basalts. J. Volcanol. Geotherm. Res. 164, 112–126. doi:10.1016/j.jvolgeores.2007.04.006.

Rittman, A., Ippolito, F., 1947. Sulla stratigrafia del Somma-Vesuvio: Napoli, Atti Fondaz. Polit. Messog. d'Italia (7).

Rittmann, A., 1950. L'eruzione Vesuviana del 79, studio magmatico e vulcanologico. Pompeiana 1950, 456–474.

Rolandi, G., Paone, A., Di Lascio, M., Stefani, G., 2008. The 79 AD eruption of Somma: The relationship between the date of the eruption and the southeast tephra dispersion. J. Volcanol. Geotherm. Res. 169, 87–98.

Rolandi, G., 2010. Volcanic hazard at Vesuvius: An analysis for the revision of the current emergency plan. J. Volcanol. Geotherm. Res. 189, 347–362.

Romano, C., Giordano, D., Papale, P., Mincione, V., Dingwell, D.B., Rosi, M., 2003. The dry and hydrous viscosity of alkaline melts from Vesuvius and Phlegrean Fields. Chem. Geol. 202, 23–38.

Rosi, M., Principe, C., Vecci, R., 1993. The 1631 Vesuvius eruption. A reconstruction based on historical and stratigraphical data. J. Volcanol. Geotherm. Res. 58, 151–182.

Rossano, S., Mastrolorenzo, G., De Natale, G., 1998. Computer simulations of pyroclastic flows on Somma-Vesuvius volcano. J. Volcanol. Geotherm. Res. 82, 113–137.

Rossano, S., Mastrolorenzo, G., De Natale, G., 2004. Numerical simulation of pyroclastic density currents on Campi Flegrei topography: a tool for statistical hazard estimation. J. Volcanol. Geotherm. Res. 132, 1–14.

Rust, A.C., Manga, M., 2002. Effects of bubble deformation on the viscosity of dilute suspensions. J. Non-Newtonian Fluid. Mech. 104, 53–63.

Rust, A.C., Manga, M., Cashman, K.V., 2003. Determining flow type, shear rate and shear stress in magmas from bubble shapes and orientations. J. Volcanol. Geotherm. Res. 122, 111–132.

Rust, A.C., Cashman, K.V., 2004. Permeability of vesicular silicic magma: inertial and hysteresis effects. Earth Planet. Sci. Lett. 228, 93–107.

Rutherford, M.J., Sigurdsson, H., Carey, S., Davis, A., 1985. The May 18, 1980, eruption of Mount St. Helens 1. Melt composition and experimental phase equilibria. J. Geophys. Res. 90, B4 2929-2947.

Rutherford, M.J., 1996. Conditions in the pre-eruption 79AD Vesuvius magmas: controls on magmatic and eruption processes, *in* Vesuvius Decade Volcano, Workshop Handbook, IAVCEI-CEV, IAVCEI-CMVD, 17–22 September 1996.

Rutherford, M.J., Gardner, J.E., 2000. Rates of Magma Ascent. In: Sigurdsson, H. (Ed.), Encyclopedia of Volcanoes. Academic Press, pp. 207–218.

Rutherford, M.J., Devine, J.D., 2003. Magmatic conditions and magma ascent as indicated by hornblende phase equilibria and reactions in the 1995-2002 Soufriere Hills magma. J. Petrol. 44, 1433-1454.

Sable, J.E., Houghton, B.F., Wilson, C.J.N., Carey, R.J., 2006. Complex proximal sedimentation from Plinian plumes: the example of Tarawera 1886. Bull. Volcanol. 69, 89–103.

Sahagian, D.L., Proussevitch A.A., 1998. 3D particle size distributions from 2D observations: stereology for natural applications. J. Volcanol. Geotherm. Res. 84, 173–196.

Saltikov, S.A., 1967. The determination of the size distribution of particles in an opaque material from a measurement of the size distribution of their sections. In: Elias, H. Ed., Stereology. Springer-Verlag, NY, pp. 163–173.

Santacroce, R., Cioni, R., Marianelli, P., Sbrana, A., Sulpizio, R., Zanchetta, G., Donahue, D.J., Joron, J.L., 2008. Age and whole rock-glass compositions of proximal pyroclastics from the major explosive eruptions of Somma-Vesuvius: a review as a tool for distal tephrostratigraphy. J. Volcanol. Geotherm. Res. 177, 1–18. doi:10.1016/j.jvolgeores.2008.06.009

Savelli, C., 2001. Two-stage progression of volcanism (8-0 Ma) in the central Mediterranean (southern Italy). J. Geodyn. 31, 393–410.

Scaillet, B., Pichavant, M., 2004. Crystallization conditions of Vesuvius phonolites. Geophys. Res. Abstr. 6, p. 03764.

Scaillet, B., Pichavant, M., Cioni, R., 2008. Upward migration of Vesuvius magma chamber over the past 20,000 years. Nature 455, 216–220.

Scandone, R., 1996. Factors controlling the temporal evolution of explosive eruptions. J. Volcanol. Geotherm. Res. 72, 71–93.

Scandone, R., Giacomelli, L., 2001. The slow boiling of magma chambers and the dynamics of explosive eruptions. J. Volcanol. Geotherm. Res. 110, 121–136.

Shaw, H.R.,1972, Viscosities of magmatic silicate liquids: an empirical method of prediction. Am. J. Sci. 272, 870–893.

Shea, T., Larsen, J.F., Gurioli, L., Hammer, J.E., Houghton, B.F., Cioni, R., 2009. Leucite crystals: surviving witnesses of magmatic processes preceding the 79AD eruption at Vesuvius, Italy. Earth Planet. Sci. Lett. 281, 88–98, doi: 10.1016/j.epsl.2009.02.014.

Shea, T., Houghton, B., Gurioli, L., Cashman, K., Hammer, J., Hobden, B., 2010a, J. Volcanol. Geotherm. Res., Textural studies of vesicles in volcanic rocks: an

integrated methodology. J. Volcanol. Geotherm. Res. 190, 271–289. doi: 10.1016/j.jvolgeores.2009.12.003.

Shea, T., Gurioli, L., Larsen, J.F., Houghton, B.F., Hammer, J.E., Cashman, K.V., 2010b. Linking experimental and natural vesicle textures in Vesuvius 79AD white pumice. J. Volcanol. Geotherm. Res. 192, 69-84. doi:10.1016/j.jvolgeores.2010.02.013

Sheridan, M.F., Barberi, F., Rosi, M., Santacroce, R., 1981. A model for Plinian eruptions of Vesuvius. Nature 289, p. 282–285.

Sheridan, M.F., Malin, M.C., 1983. Application of computer assisted mapping to volcanic hazard evaluation of surge eruptions: Vulcano, Lipari, and Vesuvius. J. Volcanol. Geotherm. Res. 17, 187–202.

Shin, H., Lindquist, W.B., Sahagian, D.L., Song S.R., 2005. Analysis of the vesicular structure of basalt. Comput. Geosci. 31, 473–487.

Sigurdsson, H., Cashdollar, S., Sparks, R.S.J., 1982. The eruption of Vesuvius in AD 79: reconstruction from historical and volcanological evidence. Am. J. Archaeo. 86, 39–51.

Sigurdsson, H., Carey, S., Cornell, W., Pescatore, T., 1985. The Eruption of Vesuvius in A.D. 79. Nat. Geog. Res. 1, p. 332–387.

Sigurdsson, H., Carey, S., 1989. Plinian and co-ignimbrite tephra fall from the 1815 eruption of Tambora Volcano. Bull. Volcanol. 51, 243–270.

Sigurdsson, H., Cornell, W., Carey, S., 1990. Influence of magma withdrawal on compositional gradients during the AD 79 Vesuvius eruption. Nature 345, 519–521.

Simakin, A.G., Armienti, P., Epel'baum, M.B., 1999. Coupled degassing and crystallization: experimental study at continous pressure drop, with application to volcanic bombs. Bull. Volcanol. 61, 275–287.

Song, S.R., Jones, K.W., Lindquist, W.B., Dowd, B.A., Sahagian, D.L., 2001. Synchrotron X-ray computed microtomography: Studies on vesiculated basaltic rock. Bull. Volcanol. 63, 252–263.

Sparks, R.S.J., Wilson, L., 1976. A model for the formation of ignimbrite by gravitational column collapse. J. Geol. Soc. Lond. 132, 441–451.

Sparks, R.S.J., 1978. The dynamics of bubble formation and growth in magmas: a review and analysis. J. Volcanol. Geotherm. Res. 3, 1–37.

Sparks, R.S.J., Murphy, M.D., Lejeune, A.M., Watts, R.B., Barclay, J., Young, S.R., 2000. Control on the emplacement of the andesite lava dome of the Soufriere Hills volcano, Montserrat by degassing-induced crystallization. Terra Nova 12, 14–20.

Sulpizio, R., Cioni, R., Di Vito, M.A., Mele, D., Bonasia, R., Dellino, P., 2010. The Pomici di Avellino eruption of Somma-Vesuvius (3.9 ka BP) part I: stratigraphy, compositional variability and eruptive dynamics. Bull. Volcanol., in press.

Suzuki, Y., Gardner, J.E., Larsen, J.F., 2007. Experimental constraints on syn-eruptive magma ascent related to the phreatomagmatic phase of the 2000AD eruption of Usu volcano, Japan. Bull. Volcanol. 69, 423–444.

Tanguy, J-C., Ribiere, C., Scarth, A., Tjetjep, W.S. 1998. Victims from volcanic eruptions; a revised database. Bull. Volcanol. 60, 137–144.

Todesco, M., Neri, A., Esposti Ongaro, T., Papale, P., Macedonio, G., Santacroce, R., Longo, A., 2002. Pyroclastic flow hazard assessment at Vesuvius (Italy) by using numerical modeling. I. Large-scale dynamics. Bull. Volcanol. 64, 155–177.

Toramaru, A., 1989. Vesiculation process and bubble size distributions in ascending magmas with constant velocities. J. Geophys. Res. 94, (B12) 17523–17542.

Toramaru, A., 1990. Measurement of bubble size distributions in vesiculated rocks with implications for quantitative estimation of eruption processes. J. Volcanol. Geotherm. Res. 43, 71–90.

Toramaru, A., 1995. Numerical study of nucleation and growth of bubbles in viscous magmas. J. Geophys. Res. 100, 1913–1931.

Toramaru, A., 2006. BND (bubble number density) decompression rate meter for explosive volcanic eruptions. J. Volcanol. Geotherm. Res. 154, 303–316.

Turnbull, D., Fisher, J.C., 1949. Rates of nucleation in condensed systems, J. Chem. Phys. 17, 71–73.

Underwood, E.E., 1970. Quantitative Stereology. Addison-Wesley, Reading, 274 pp.

Valentine, G.A., Wohletz, K.H., 1989. Numerical models of plinian eruption columns and pyroclastic flows. J. Geophys. Res. 94, 1867–1877.

Vergniolle, S., 1996. Bubble size distribution in magma chambers and dynamics of basaltic eruptions. Earth Planet. Sci. Lett., 140, 269–279.

Voorhees, P.W., 1992. Ostwald ripening of two-phase mixtures. Annu. Rev. Mat. Sci. 22, 197–215.

Walker, G.P.L., 1981. The Waimihia and Hatepe plinian deposits from the rhyolitic Taupo Volcanic Centre. NZ J. Geol. Geophys. 24, 305–324.

Watson, E.B., 1994. Diffusion in volatile-bearing magmas. Rev. Mineral. 30, 371–411.

Wilson, L., Sparks, R.S.J., Walker, G.P.L., 1980. Explosive volcanic eruptions—IV. The control of magma properties and conduit geometry on eruption column behavior. Geophys. J. Roy. Astr. Soc. 63, 117–148.

Woods, A.W., Bower, S.M., 1995. The decompression of volcanic jets in a crater during explosive volcanic eruptions. Earth Planet. Sci. Lett. 131, 189–205.

Wright, H.M.N., Roberts, J.J., Cashman, K.V., 2006. Permeability of anisotropic tube pumice: Model calculations and measurements. Geophys. Res. Lett. 33, L17316.

Wright, H.M.N., Cashman, K.V., Rosi, M., Cioni, R., 2007. Breadcrust bombs as indicators of Vulcanian eruption dynamics at Guagua Pichincha, Ecuador. Bull. Volcanol. 69, 281–300.

Wright, H.M.N., Weinberg, R.F., 2009. Strain localization in vesicular magmas: Implications for rheology and fragmentation. Geology 37, 1023-1026.

Yamada, K., Tanaka, H., Nakazawa, K., Emori, H., 2005. A new theory of bubble formation in magma. J. Geophys. Res. 110, B02203.

Zanella, E., Gurioli, L., Pareschi, M. T., Lanza, R., 2007. Influences of urban fabric on pyroclastic density currents at Pompeii (Italy): 2. Temperature of the deposits and hazard implications. J. Geophys. Res. 112, B05214, doi:10.1029/2006JB004775.